

IPICYT
**INSTITUTO POTOSINO DE INVESTIGACIÓN
CIENTÍFICA Y TECNOLÓGICA, A.C.**

POSGRADO EN CIENCIAS APLICADAS

**Novel curved and strained carbon-based
nanostructures: a theoretical study of their electronic
properties and their response to laser excitations**

Tesis que presenta

Felipe Valencia Hernández

Para obtener el grado de

Doctor en Ciencias Aplicadas

En la opción de

Nanociencias y Nanotecnología

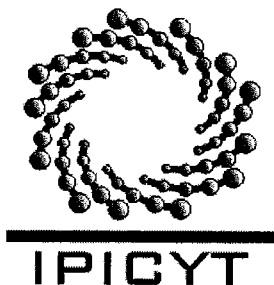
Codirectores de la Tesis:

Dr. Humberto Terrones Maldonado

Dr. Mauricio Terrones Maldonado

Dr. Aldo Humberto Romero Castro (CINVESTAV)

San Luis Potosí, S.L.P., Junio de 2005.



Instituto Potosino de Investigación Científica y Tecnológica, A.C.

Acta de Examen de Grado

COPIA CERTIFICADA

El Secretario Académico del Instituto Potosino de Investigación Científica y Tecnológica, A.C., certifica que en el Acta 013 del Libro Primero de Actas de Exámenes de Grado del Programa de Doctorado en Ciencias Aplicadas en la opción de Nanociencias y Nanotecnología está asentado lo siguiente:

En la ciudad de San Luis Potosí a los 3 días del mes de junio del año 2005, se reunió a las 10:00 horas en las instalaciones del Instituto Potosino de Investigación Científica y Tecnológica, A.C., el Jurado integrado por:

Dr. Aldo Humberto Romero Castro	Presidente	CINVESTAV
Dr. Mauricio Terrones Maldonado	Secretario	IPICYT
Dr. Florentino López Urías	Sinodal	IPICYT
Dr. Humberto Terrones Maldonado	Sinodal	IPICYT
Dr. Jesús Dorantes Dávila	Sinodal externo	IF-UASLP

a fin de efectuar el examen, que para obtener el Grado de:

DOCTOR EN CIENCIAS APLICADAS
EN LA OPCIÓN DE NANOCIENCIAS Y NANOTECNOLOGÍA

sustentó el C.

Felipe Valencia Hernández

sobre la Tesis intitulada:

Novel curved and strained carbon-based nanostructures: a theoretical study of their electronic properties and their response to laser excitations

que se desarrolló bajo la dirección de

Dr. Humberto Terrones Maldonado
Dr. Mauricio Terrones Maldonado
Dr. Aldo Humberto Romero Castro (CINVESTAV)

El Jurado, después de deliberar, determinó

APROBARLO

Dándose por terminado el acto a las 13:10 horas, procediendo a la firma del Acta los integrantes del Jurado. Dando fé el Secretario Académico del Instituto.

A petición del interesado y para los fines que al mismo convengan, se extiende el presente documento en la ciudad de San Luis Potosí, S.L.P., México, a los 3 días del mes junio de 2005.




Mtra. Ma. Elisa Lucio Aguilar
Jefa del Departamento de Asuntos Escolares

THESIS COMMITTEE

Aldo Humberto Romero.

President.

Mauricio Terrones Maldonado.

Secretary.

Humberto Terrones Maldonado.

Synodal.

Florentino López Urías.

Synodal.

Jesus Dorantes Davila.

Synodal.

APPROVAL

Of a Thesis submitted by

Felipe Valencia

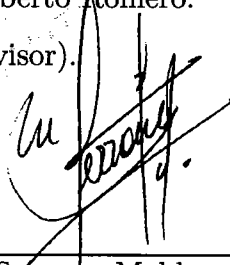
This thesis has been read and found satisfactory by the advisors.



Aldo Humberto Romero

Aldo Humberto Romero.

(Co-supervisor).



Mauricio Terrones Maldonado

Mauricio Terrones Maldonado.

(Co-supervisor)



Humberto Terrones Maldonado

Humberto Terrones Maldonado.

(Co-supervisor)

Dedicated to

those three women who make sense to my life: Esther, Toña and Laura. And, if you found that kind of boring I will add: To Rafael, my litter brother, to ACB who may never know- and shall never care- to Caya -my girl for such a long gone time- to Claudia, who made this years much easier and to Lola, my girl and partner.

Novel Curved and strained novel carbon-based nanostructures : A theoretical study of their electronic properties and their response to laser excitations.

Felipe Valencia H.

Submitted for the Doctorate degree.

May 2005

Abstract

In this thesis we review and discuss, from a theoretical point of view, the physical properties of a wide variety of carbon-based nano-materials. This work is focused on systems in which the atomic structures exhibit one - or a combination - of the following features: i) negative curvature, ii) highly strained C-C bonds, or iii) localized bond strain due to mechanical defects. The electronic and structural properties of these systems have been calculated using first principles and tight-binding approaches.

The mechanical stability of negatively curved graphitic crystals (the Triply Periodic Graphitic Surfaces, also known as Schwarzites) is reviewed for a representative variety of flavors. It is shown that, for small crystals, identification could be achieved using vibrational spectroscopy; whereas larger systems would be practically indistinguishable from amorphous phases of graphite-like materials. The electronic properties of such systems and their response to optical excitations are related to the local atomic environment and different families could be characterized using Electron Energy Loss Spectroscopy (EELS). In contrast to other curved carbons, such as single walled carbon nanotubes, metallicity is only possible for structures containing seven membered rings. Atomic doping also could be achieved by substitutions of Boron or Nitrogen atoms, or by the introduction of pyridine-like groups.

One and two dimensional networks built from the cubic cubane cage have been

also investigated. These networks are shown to be mechanically stable. Their electronic properties are intrinsically related to those of the cubane molecule and, large electronic gaps have been observed. The introduction of electronically rich linkers could be used to reduce the gap without affecting significantly their mechanical stability.

In addition, the interaction of laser pulses with graphitic carbon nanostructures is studied in detail. Novel paths for defect healing are shown to be available using the contribution of the electronic entropy to the system's free energy. These studies suggest that it may be possible to anneal selectively defects (e.g. pentagon-heptagon pairs) using femtosecond laser pulses, in order to modify the electronic and mechanical properties of carbon nano-systems. We have extended the calculation framework for laser-matter interactions, in order to allow for the study of systems with more than one atomic species (e.g. binary semiconductors).

These studies, originally designed for systems containing a single atomic species, has been extended so that further investigations, binary semiconductors would be possible.

Acknowledgments

I was introduced to the study of condensed matter systems by Prof. Jairo Giraldo (*Universidad Nacional de Colombia*). I lack words to express my gratitude for his scientific advice, teaching and personal guidance, during my undergraduate years. He also taught me many other important things; among them, the joy of scientific research, and the importance of hard work.

I learned to appreciate the beauty of quantum mechanics thanks to Professor Efrain Barbosa (*Universidad Nacional de Colombia*). He also taught me to keep the mind and eyes opened, and I hope never to forget that advise.

Professor Martín García, *Kassel Universitât*, and Doctor Harald Jeshcke, *Frankfurt Universitât*, provided me with invaluable help and direction concerning the theoretical description of laser-matter interaction. My work in that field is based upon their original ideas, schemes, and computational codes.

Professors M. Kiwi, R. Ramirez and A. Toro-Labbe from *Pontificia Universidad Católica de Chile*, and Miss. Barbara Herrera, from the same institution, have been collaborators in the studies on cubyl-cubane related systems.

Professor E. Hernandez at *l' Institut de Ciencia de Materials de Barcelona*, ICMAB, provided me with both software, feedback, and discussions in the study of nanoporous carbon models and, in general, in many aspects of tight-binding modeling of solids.

I acknowledge all the advise and help I have received from my supervisors, including the judicious reading of this work; they are not to be blamed for any remaining errors.

Professor A. Romero taught me almost everything I know about material's modeling. Most of the methods used in this work were suggested by him. He also

instilled in me a philosophy of life; taught me the ethics of scientific work, and the importance of scientific collaboration. He offered me wise advice, strong support, and generous friendship, ever from the first years of my graduate studies. Professor H. Terrones suggested most of the work performed on negatively curved structures. He provided me not only with many valuable comments during my ph.D research, but also friendship, and even economical support (through the SNI system of researcher's assistant, which is also acknowledged). Professor M. Terrones, cleverly pointed out to me many important facts, especially but not restricted to, those related with the experimental facts. He also suggested several interesting research directions. Hopefully, some day I will have the chance to express my gratitude for their advise and friendship, with more than these few words.

The IPICyT's staff in general (both researches, students and clerical workers) is also acknowledged.

I acknowledge IPICyT for providing me with a Ph.D. scholarship and also with most of the computational resources. Resource allocation in the Centro Nacional de Supercomputo is also acknowledged. Support from CONACyT, Mexico, through grants W-8001, 36365-E, G-25851-E, 37589-U, and J-42647-F, is acknowledged.

THANKS!

List of publications

THEORETICAL CHARACTERIZATION OF SEVERAL MODELS OF NANOPOROUS CARBON, **F. Valencia**, A. H. Romero, E. Hernandez, M. Terrones, and H. Terrones, *New Journal of Physics*, 3, 123 (2003).

AB INITIO STUDY OF CUBYL CHAINS AND NETWORKS, **F. Valencia**, A. H. Romero, M. Kiwi, R. Ramirez, A. Toro-Labbé, *J. Chem. Phys.*, 121, 9172 (2004).

POLYCUBANES LINKED WITH C₂, N₂, NO AND NS: FROM INSULATING TO METALLIC BEHAVIOR, **F. Valencia**, A. H. Romero, M. Kiwi, R. Ramirez, A. Toro-Labbé, *Phys. Rev. B*, 71, 033410 (2005).

FEMTOSECOND LASER NANOSURGERY OF DEFECTS IN CARBON NANOTUBES, A. H. Romero, M. E. García, H. O. Jeschke, **F. Valencia**, H. Terrones, M. Terrones, *accepted for publication in Nanoletters*, 2005.

A DENSITY FUNCTIONAL THEORY STUDY OF CUBANE OLIGOMERS, B. Herrera, **F. Valencia**, A. H. Romero, M. Kiwi, R. Ramirez, A. Toro-Labbé, *to be submitted to Chemical Physics Letters* 2005.

ULTRAFAST RESPONSE OF DEFECTIVE GRAPHITIC SYSTEMS: LASER INDUCED VIBRATIONS AND INVERSE STONE-WALES TRANSITIONS, **F. Valencia**, A. H. Romero, M. E. García, H. O. Jeschke, *in production* 2005.

And little he knew of the things that ink may do, how it can mark a dead man's thoughts for the wonder of later years, and tell of happenings that are gone clean away, and be a voice for us out of the dark of time, and save many a fragile thing from the pounding of heavy ages; or carry us, over the rolling centuries, even a song from lips long dead on forgotten hills...

Lord Dunsany

Foreword

*The thing that hath bee, it is that which shall be;
and that which is done is that which shall be done.*

Ecclesiastes

Much have been said about nanotechnology elsewhere (and almost anywhere) therefore little more will be stated in this preface. These few words, mainly related to carbon nanostructures and matter-light interaction, have also been discussed in the available literature. However, they have been useful for the author when he was writing this thesis and, hopefully, will be useful for the casual reader.

Carbon nanotechnology is becoming important in the modern developments. From amorphous carbon to nanotubes, and from ultrahard polycrystalline diamonds to active foams, new technological possibilities and theoretical challenges have raised during the past two decades. When we think about carbon being the basis of organic life - and one of the most commonly used and studied elements - we sometimes forget about its enormous versatility. C-C bonds do exhibit three fundamental kinds of orbital hybridization: linear sp , sp^2 and sp^3 ; all of the latter play a crucial role in the always fascinating world of carbon chemistry.

The semiconducting character of silicon has placed it on top of the electronic devices since the fabrication of the first transistor. Meanwhile, the mechanical strength and bond flexibility of carbon has been widely exploited for the production of catalytic devices, active filters and metal composites. Within the nanotechnology framework, novel and efficient ways to tailor the electronic properties of carbon-based systems have opened new avenues for developing ultra-miniaturized electronics. Pristine and doped carbon fullerenes and nanotubes have been proposed as

good candidates in nano-electronic devices. Recently, significant advances in the generation of hetero-junctions have been accomplished.

The discovery of carbon fullerenes and the identification of nanotubes marked the starting point of a new era of carbon-based systems. The physico-chemical properties of these systems could be strongly dependant upon the global geometric properties and localized structural defects; curvature and strain play a major role in the material's behavior. Therefore, dimensionality, curvature and strain are parameters that could be varied in order to construct and predict carbon based nanodevices.

Synthesis and characterization should advance together in material engineering. Acquiring the complete information regarding these novel materials is needed, but this step is, by no means, trivial. Structures tailored at the atomic level now require advanced tools with atomic resolution.

An important question arises: is it possible to acquire information about these novel materials from optical measurements? Before this question is answered, we could mention that light has always been the humans favorite source of information. Just remember what the semitic God created in the first place. Vision and "High Resolution Vision", a.k.a. microscopy, are "short wavelength" phenomena, i.e. visible light wave-lengths are much smaller than the scatterers (visible objects) and it is clear that many of the optical features could be described accurately by means of purely classical electrodynamics. But most interesting is that the scenario could be completely changed when studying nanostructures. Even visible (above 380 nm) and ultraviolet (above 10 nm) wave lengths are far too large at the atomic scales.

Still the answer to the question posed earlier is affirmative. The wavelengths of visible and near ultraviolet light are usually larger than (or at least comparable with) the dimensions of the system and, generally, nanoparticles lie below the resolution of any optical microscope. However, there are various reasons for studying the optical response in nanosized systems. First, nanoparticles are usually larger than the De-Broglie wavelength of energetic electrons (not very energetic, only a few KeV), which interact with matter similarly to the interaction of light with the continuous media, and that is related to the same microscopic quantities: polarizability, susceptibility

and dielectric function. Secondly, absorption of intense energy light, such as X-Ray Absorption, is also related to small atomic lengths. In a third place, the system response is no longer described by the classical electromagnetic theory but by the quantum (or at least semiclassical) description of light-matter interactions. This latter condition means, for very small particles, that slight geometrical changes are able to induce significant variations in the optical response; a feature that has been exploited to obtain information about the morphology of clusters interacting with light of long wavelength. Fourth, and last for us, as shall be discussed in this thesis, the application of ultrashort (in time scale) and very energetic laser pulses could induce local atomic rearrangements, a fact that is related to highly non-thermal phenomena (electrons and ions having dramatically different temperatures and localized electronic excitations).

Almost in perfect timing with the nano and femto revolution, advances in computer hardware and methods employed in computer physics allows one to investigate the nature of the chemical bonds in nanostructured materials, the related physical properties and , to some extent, the output of several experimental characterization techniques such as spectroscopy. Given enough computational power, this theoretical study can be performed without resorting to empirical data by means of what are usually called *ab-initio* or *first principles* methods, being the Density Functional Theory used in this work one of the most popular nowadays . When computer resources are restricted, it is necessary to use simpler approximations retaining the quantum nature inherent to the atomic interactions¹. The Tight Binding approximations are the most celebrated simplified descriptions of the chemical binding, and they have also been widely used throughout this work.

In this thesis you will find a theoretician's, and specifically a computer physicist, point of view regarding novel nanostructured carbon allotropes in which curvature and strain play a significant role. In addition, their characterization using Electron

¹This condition is ever reached, although the limiting size of the system depends upon the available resources at any given research center. The cost of first principles calculations increases dramatically with the number of atoms. Therefore, there are many interesting problems where ab-initio calculations are prohibitively expensive

Energy Loss Spectroscopy (EELS) and vibrational spectroscopy, as well as how their electronic properties could be modified by doping is studied in this work. Finally we will discuss a novel route to perform specific atomic structural changes using ultra short laser pulses (e.g. femto-second laser pulses).

Due to my theoretical background, a considerable amount of space is devoted to description of theoretical methods and the validity of the approximations employed. I do hope that the reader finds this work relevant, especially from the physics point of view, so that this account is worthy for a wider audience.

Contents

Abstract	v
Acknowledgments	vii
List of Publications.	ix
1 Introduction	1
1.1 The carbon polymorphism: valence-bond description of the covalent carbon bonds.	1
1.2 Strain in carbon-based structures.	7
1.2.1 Cubane oligomers	8
1.3 Curved carbon systems.	10
1.4 Inducing structural changes using femtosecond laser irradiation. . . .	12
1.5 Scope of this work.	14
2 Relevant features of functionalized cubyl-cubane polymers.	16
2.1 Essentials of cubane and cubyl-cubane oligomers.	16
2.2 One and two dimensional arrays of cubyl-cubane networks.	18
2.2.1 Vibrational spectra	25
2.2.2 Electronic Properties	29
2.3 Building networks with cubane units: Finite size effects.	31
2.4 Effects of functionalization on electronic properties.	37
3 Crystalline models for nanoporous carbons, pure carbon and doped structures.	54
3.1 The world of nanoporous carbons.	54

3.2	The Schwarzite models.	56
3.3	Structure and energetics.	58
3.3.1	Local atomic environment: bond lengths and bond angles . . .	61
3.3.2	Topological properties	63
3.3.3	Solvent accessible surfaces.	65
3.3.4	Total energies.	67
3.4	Elastic Properties.	70
3.5	Electronic properties.	73
3.6	Electron Energy Loss Spectra.	82
3.7	Vibrational spectra.	87
3.8	Doping Schwarzites with boron and nitrogen: substitutional and pyridine-like defects.	91
3.9	A note on synthesis attempts	98
4	Laser pulses interacting with matter.	99
4.1	Overview.	99
4.2	A practical realization: Tight-binding modeling plus molecular dynamics.	101
4.2.1	Evolution of the occupation numbers	101
4.2.2	Free energy and ionic motion	102
4.2.3	The charge transfer problem	104
4.3	Extending the model I: Polarization Effects	105
4.4	Extending the model II: Multiple atomic species	113
4.5	Extending the model III: Full density matrix approach, <i>a modest proposition</i>	115
4.5.1	Basic equations for the time evolution of the reduced density matrix operator in the localized orbitals basis set	116
4.5.2	Collision Part	118
4.5.3	Energy and Forces	119
4.5.4	Some Implementation Tips	119

5	Releasing strain and relaxing the curvature via a laser induced process.	122
5.1	Motivation.	122
5.2	Ultrafast response of defective graphitic systems	123
5.2.1	Graphene.	124
5.2.2	Single Walled Carbon nanotubes.	131
5.2.3	SW transformations in Fullerenes	137
5.3	Ultrafast response of fullerenes inside nanotubes.	140
6	Conclusions and outlook	143
6.1	Further work	145
6.1.1	Polycubane polymers.	145
6.1.2	Negatively curved carbon structures.	145
6.1.3	Laser-matter interaction.	146
6.1.4	Synthetic paths for Schwarzite structures	146
	Bibliography	147
	Appendix	166
A	Essentials on many electrons physics.	166
A.1	The many body problem of condensed matter.	166
A.2	Un-coupling the fast electrons from the slow ions: The adiabatic approximation.	168
A.3	General description of the electronic sub-system	170
A.4	Single particles in an effective field: the Hartree-Fock method.	174
A.5	Beyond Hartree-Fock: Particle's correlation.	180
A.6	Quasiparticles	181
B	Density Functional Theory.	187
B.1	The Basic concepts and principles.	187
B.2	Solving the equations, the Kohn-Sham method.	191
B.3	Applications of DFT	195

B.4	Interpretation of the Kohn-Sham orbitals	195
B.5	The Local Density Approximation.	196
B.6	Generalized Gradient Approximations.	197
B.7	Basis sets for the one-electron wavefunction.	198
B.8	Pseudopotentials.	199
C	Tight-binding modeling.	202
C.1	Essentials.	203
C.2	Transferability of the tight-binding parameters.	205
D	Periodic systems.	208
D.1	A review on basic concepts.	209
D.2	Single particle equations in the periodic system: the Bloch's Theorem.	210
D.3	The band-structure of solids and the density of states.	212
D.4	Lattice dynamics: phonons.	214
E	Optical response.	217
E.1	Microscopic description of the interaction with external fields. Linear Regime	217
E.2	The dielectric function in a Tight-Binding Approximation.	219
E.3	Dielectric Loss of fast electrons passing through a material system. . .	220
F	Simplified evolution of the occupation number in a tight-binding approach	223

List of Figures

1.1	Schematic representation of the covalent bonding between two equivalent atoms (A , and B). The nuclei are at a distance R_{AB} . The lower lying states (core levels), retain their atomic character; whereas states extended between the two nuclei (molecular orbitals) define the molecular bonding.	2
1.2	The formation of hybrid orbitals in carbon. The electronic configuration of the external ($n = 2$) shell, changes from the ground state ($2s^2 2p^2$), to an excited ($1s 2p^3$), from where the orbital hybridization proceeds.	4
1.3	Representation of the hybrid carbon orbitals. The original s and p_z orbitals are shown at the top of the picture. At the bottom panels, we show molecular and solid state (only possible for sp^2 and sp^3) representatives for each kind of hybridization.	5
1.4	Representation of the σ and Π bonds in carbon. The + and - symbols, represent the sign of the wavefunctions in the respective lobules. . . .	6
1.5	Molecular models for some systems involved in the formation of cubane oligomers, starting from the simple cubane molecule. The dehydrocubane (cubene) intermediate state, is highly reactive and is the desired monomer. Diiodo-bicubyl is the first step in the formation of chains.	9

1.6	Geometrical interpretation of the metallic or semiconductor behavior of Single Walled carbon Nanotubes. The chiral vector \vec{c}_k defines the type of rolling. The tubule will display metallic behavior when the plane defined by \vec{c}_k in the reciprocal space, contains the point at which the conduction and valence bands of graphene are in contact (K point). Adapted from ref. [24].	11
1.7	Molecular representations for some Schwarzite crystals. (a) Eight cells of the balanced P structure. (b) Eight cells of the balanced D structure. (c) Eight cells of the balanced G structure. (d) The cubic cell of the Schoen IWP-G structure.	13
2.1	The cubane molecule, C_8H_8	17
2.2	Proposed linear cubyl chains models. (a) Joining through the cube diagonal. (b): Ladder configuration. (c): With rotated cubyl units.	19
2.3	Energy <i>vs.</i> deformation curves for the straight cubyl chain (a), the ladder-like chain (b), and BFGS relaxation path for the staggered configuration of cubyl units. The reference “0” energy is the optimal energy for each model.	22
2.4	A two dimensional cubyl network (a) and its corresponding Brillouin zone (b).	24
2.5	Energy <i>vs.</i> isometric deformation for the bidimensional cubyl network. The reference “0” energy is the minimum energy.	25
2.6	Left Panel: Vibrational spectra (Γ point) for the 2D network (top), 1D chain(middle) and isolated cubane molecule (bottom). Right panel: vibrations at the X point for the 2D network (top) and 1D chain (middle).	27
2.7	Electronic band structure for an individual cubyl chain (middle panel), and a network (right panel) compared to the electronic levels of the cubane molecule (left panel). The special points in the First Brillouin Zone of the two dimensional network are depicted in Fig. 2.4. $E = 0$ always corresponds to the highest occupied energy level.	30

- 2.8 Electronic density of states for the cubane molecule (bottom), the cubyl chain (middle) and the cubyl 2D network (top). The zero level of energy is the Fermi level, defined to be in the middle of the gap. Shadowing indicates occupied states. 31
- 2.9 Electronic density of states ($e-dos$) for cubyl-cubane oligomers, calculated within a tight-binding approach. Continuous line: chain of 10 cubyl-cubane units; dotted line: 5 cubyl-cubane units; dashed line: one single cubane molecule. The small changes between the 5 and 10 units chains imply that these oligomers are rapidly approaching the 1D crystalline polymer behavior. The zero energy level is the highest occupied energy level in each case. 33
- 2.10 The planar average of the Kohn-Sham potential in the direction perpendicular to a 2D cubane network. The vacuum level is the value of this potential in the middle of the cell. 35
- 2.11 Effect of the chain deflection on the energy and electronic properties of cubyl-cubane oligomers. Upper panel: elastic stiffness against bending, as function of the number of cubane units. Lower panel: electronic density of states for a 14-units oligomer before and after bending; the black line corresponds to the straight rod, and the red line to a 10° bent rod. 38
- 2.12 Cubyl-cubane chains bridged by: (a) Ethyne, (b) Benzyne, and (c) diethyne radical groups. The reference points X1 and X2 signaling the extremes of the radical groups are shown in each case. 40
- 2.13 Electronic properties (left:band structures, and right: $e-dos$) for polycubanes with hydrocarbon molecules as dopants. (a) Ethyne-bridged polymers, (b)benzyne-bridged polymers and (c) diethyne-bridged polymers. The Fermi level is located $E = 0$. Occupied states are shadowed in the $e-dos$ 43
- 2.14 Electronic properties (left:band structures, and right: $e-dos$) for polycubane networks with alkyne molecules as dopants. (a) is for the ethyne bridged network , (b) for diethyne bridging. 44

2.15	Molecular models of polycubanes containing C ₂ , N ₂ , NO and NS molecules as dopants. Black spheres represent Nitrogen atoms, pale gray and light gray spheres represent Oxygen and Sulphur atoms, respectively.	45
2.16	Electronic density of states of polycubanes with C ₂ , N ₂ , NO and NS molecules as dopants. The Fermi Level is at $E = 0$. Occupied states are shadowed.	46
2.17	Band structure of polycubanes with C ₂ , N ₂ , NO and NS molecules as dopants.	47
2.18	HOMO of polycubanes with C ₂ , N ₂ , NO and NS molecules as dopants	49
2.19	LUMO of polycubanes with C ₂ and N ₂ molecules as dopants, and the first state of the second conduction band for the case of NO and NS molecules.	50
2.20	ELF for polycubanes with C ₂ (a), N ₂ (b), NO (c) and NS (d) molecules as dopants.	52
3.1	Cubic crystal cells for the Schwarzite models comprising only of hexagonal and octagonal rings. Blue boxes around each structures represent the borders of the unit cell. (a) Structures with 6-8-8 atomic environment. (b) Balanced structures dividing the space in two equivalent regions.	59
3.2	Cubic crystal cells for the Schwarzite models comprising hexagonal, heptagonal, octagonal and pentagonal (only for IWP-G) rings. Blue boxes represent the borders of the unit cell.	60
3.3	Geometrical parameters used in the evaluation of the local Gaussian curvature, in the negatively-curved crystals. The surface area assigned to each vertex is one third of the shadowed area.	64
3.4	Simplified scheme for quantification of molecular surfaces. A probe sphere rolls over the Van der Waals representation of the atoms in the molecule. The center of the probe sphere defines the Solvent Accessible Surface.	65

- 3.5 Solvent Accessible surfaces for the D688, P688, G688, P8BAL, G8BAL and D766 Schwarzite crystals; and van der Waals surfaces for the D8BAL, NP7PAR, P688, IWP-G, NP8BAL, and P7PAR models. . . . 66
- 3.6 Total energies per atom for the studied crystals, measured from the value for a graphene layer. The corresponding curve for diamond is shown for comparison. Curves and labels for the balanced (8BAL-) structures are shown in blue. Structures containing heptagons are highlighted in red. 68
- 3.7 Total energy of the negatively curved crystals, with respect to the graphene layer, as function of the average local Gaussian curvature. The dashed line correspond to a crude linear regression. In the estimation of $|K_I|$, a constant surface element $S_I = 1.75\text{\AA}^2$, corresponding to the perfect graphene bond lengths has been used. 69
- 3.8 The behavior of the Bulk modulus as a function of atomic density of the cell for. It is clear that most of the models follow an exponential law. D-like negatively-curved structures are always stronger than could be expected from this “typical” behavior. 72
- 3.9 Electronic densities of states (e-DOS) for the different negatively curved structures, calculated using the Seifert parametrization [109]. Densities are normalized to the unity in the range of available energies. The reference, “0”, level is the Fermi level. The calculated e-DOS for graphene is shown in the first panel. A Lorentzian broadening of 0.1eV was used in the calculation. 76
- 3.10 Electronic densities of states, normalized to the unity, the reference level is the Fermi level, now using the Pettifor parametrization [65]. The calculated e-DOS for graphene is shown for comparison. The Lorentzian broadening was 0.1eV. 77
- 3.11 Upper panel: Electronic density of states for G688, calculated within the Tight-Binding framework, both before -to the left- and after -to the right- relaxation. Lower panel: same as above within the GGA framework. 78

3.12	Electronic density of states for polybenzene -D688- before (upper panel) and after(lower panel) relaxation. The Fermi level is located at “0” energy. The corresponding distributions of distance to nearest and next nearest neighbors, are shown representing the geometrical rearrangement.	80
3.13	Same as fig. 3.12 but for the P688 structure.	80
3.14	Same as fig. 3.12 but for the G688 structure.	81
3.15	The K-shell core EEL spectra, measured from the K-shell edge, calculated within the projected density of states approximation, for the 8BAL family of negatively curved structures.	83
3.16	The K-shell core EEL spectra, measured from the K-shell edge, calculated within the projected density of states approximation, for the 688 family of negatively curved structures. The densities of states are convoluted with a Lorentzian function, whose full width at half maximum is 1eV.	83
3.17	The K-shell core EEL spectra, measured from the K-shell edge, calculated within the projected density of states approximation, for the negatively curved structures containing heptagons.	84
3.18	The low energy loss spectra, with the zero loss part excluded and calculated within the Tight-Binding RPA approach, for the 688 family of negatively curved structures. The graphene and diamond spectra are shown for comparison.	86
3.19	The low energy loss spectra, with the zero loss part excluded and calculated within the Tight-Binding RPA approach, for the 8BAL family of negatively curved structures.	86
3.20	The low energy loss spectra, with the zero loss part excluded and calculated within the Tight-Binding RPA approach, for the negatively-curved structures containing heptagons.	87

- 3.21 Vibrational Density of states for nine Schwarzite models, normalized to the unity. The spectra shown for P8BAL and larger structures, actually correspond only to gamma point vibrations. A Lorentzian broadening of 3cm^{-1} was used in the calculation of the densities. . . . 88
- 3.22 Temperature dependence of the thermodynamic variables for polybenzene (D688) structure 90
- 3.23 The low temperature region of the C/T^3 curves for the carbon Schwarzites, calculated from the vibrational densities of states. (a) For the highest density frameworks (688 structures), (b) for the low density crystals. . . 90
- 3.24 Electronic density of states for the D688 structure with Boron (left panel) and Nitrogen (right panel) substitution. Energies are measured with respect the Fermi level. The contributions of the Π states to the partial densities of states are also shown. Calculations were performed using the Seifert parametrization [109] 92
- 3.25 Representation of the HOMO (a) and LUMO (b) orbitals for the D688 structure, and orbitals near the Fermi level for the N enriched (c) and B enriched (species). In the color map, higher densities are colored in red. 93
- 3.26 Electronic density of states (e-DOS) for P8BAL (a), NP8BAL (b) and D8BAL(c) with a Nitrogen in substitution, calculated with the Seifert parametrization [109]. The Fermi level is located at “0” energy. 95
- 3.27 Molecular models for unrelaxed pyridine-like defect on the P8BAL (a), and D8BAL(b) frameworks. 95
- 3.28 Energy vs. volume (normalized to the optimal volume) for the D8BAL structure with a pyridine-like defect. Points are the calculated data and the curve is a fit to the Birch-Murnaham equation. 96
- 3.29 Left panel: Electronic density of states for the D8BAL structure with a pyridine-like defect, calculated using the Seifert parametrization. Partial contributions from the Π carbon and nitrogen states are also shown. Right panel: optimized geometry for this framework 97
- 3.30 Same as figure 3.29 for the P8BAL framework. 97

-
- 4.1 Schematic representation of the laser induced processes: the system is moving in a time dependent free energy surface which vary significantly during the pulse duration. Eventually, the system reaches a new equilibrium position. 100
- 4.2 Excess force field configuration after laser irradiation in a simple cubic carbon cluster. 109
- 4.3 The overall excess force magnitude for different polarization directions in a cubic carbon cluster, $P=(0,0,0)$ stands for not-polarized light. . 110
- 4.4 Top: Final force configuration for a capped nanotube for electric field parallel to the main axis (a), or perpendicular to it (b). Differences are significant only at the atoms bound to the pentagonal cap. Bottom: Velocity autocorrelation functions for both cases. 111
- 4.5 Initial and final charge configurations for a capped nanotube during with different directions of the electric field. 112
- 4.6 Binding energies for the methane molecule as function of the C-H bond length, calculated using the tight binding parametrization of ref. [65] with and without considering LCN. 115
- 5.1 Top, snapshots of the Minimum Energy Path calculated for inverse SW transition in graphene using the CI-NEB. (a) The defective system with heptagon-pentagon pairs, (b) Transition State exhibiting sensible compression of the rotated dimer. (c) Perfect graphene layer. Bottom, the corresponding potential energy showing the barrier . . . 125
- 5.2 Snapshots of the graphene response to a laser pulse, the laser peak occurs at 100fs, and it's intensity profile -envelope function- is shown to the right. The rotated dimer is shown in blue. When the absorbed energy is 0.77eV per atom (4% of the electrons are excited), low frequency vibrations are excited and strong motions near the defect are noticeable. Color mapped surfaces below each snapshot show the dramatized version of the Z-motion for the subjacent surface. . . . 127

- 5.3 Power spectra calculated after laser irradiation for different absorbed energies. The spectrum for the thermalized sample is shown for comparison. The spectrums are normalized to 1 in the region between 0 cm^{-1} and 4000 cm^{-1} . Most of the spectral power for the thermalized case lies in the region above 1000 cm^{-1} where the laser irradiated samples do not exhibit any significant feature. 128
- 5.4 Evolution of the dihedral angle between the rotated dimer and an adjacent pentagon with time and absorbed energy. Dark points are the calculated data and the smooth surface is a guide to the eye. Arrows are used to emphasize the quite linear dependency between the value of the angle's minimum (maximum) just before (after) laser irradiation and the absorbed energy. 129
- 5.5 Frontal and lateral snapshots for the laser induced S-W transition. When 1.32eV per atom are absorbed (6% of the electrons are excited) the strong motions are followed by bond breaking, out of plane rotation and, finally defect healing. The rotated dimer is shown in blue. 130
- 5.6 The free energy U, that ions would feel moving along the inverse SW transition paths at several electronic temperatures. To the left: the laser induced path; to the right: the CI-NEB path with energies calculated in the Tight Binding approach. 131
- 5.7 Snapshots of the response of a (7,7)-CNT to a femtosecond laser pulse leading to the healing of the SW defect. The relevant processes and the times at which they happen (measured with respect to the maximum of the pulse) are indicated. 133
- 5.8 The calculated electronic densities of states along the trajectory points selected for the snapshots in figure 5.7. The initial and final steps show clearly the expected behavior for a defective and perfect nanotube. The Fermi level is located at "0" energy. 135

-
- 5.9 Kinetic energy evolution during the simulation time for a (7,7) nanotube under laser irradiation for two different values of the absorbed energy. At 1.7eV/atom the inverse SW transition occurs. At 1.6eV/atom the system reaches a metastable state with the dimer pushed into the tube. The configuration of the defect neighborhood at the point where the initial vibrations disappear is also displayed 136
- 5.10 Snapshots from the response of a C_{2v} fullerene to a laser pulse. Initial lattice temperature is 300 K. Configurations after laser irradiation are shown at different absorbed energy values. The rotated dimer is shown in blue and pentagons in red. 138
- 5.11 Snapshots of the ultrafast response of two neighboring fullerenes under the action of a 20fs and 1.96eV laser pulse. The results shown are for $T_{init}=300K$. Several facing conditions are examined. In the bottom panel, 7- and 9- membered rings appearing in the dimer, are colored in blue and red, respectively. 142

List of Tables

2.1	C-C bond lengths in the chain and network models. 1α -pos Å and 2α -pos Å stands for bonds at α positions with 1 or 2 intercage bonds, when it applies. far and far for bonds far [⊥] from the intercage bond parallel or perpendicular to the chain axis, when this concept applies otherwise we report the value as far(par). Values for linear oligomers with 2,3 and 4 cubyl units (2C, 3C and 4C respectively) and for a 2x2, 3x2 4x2 and 3x3 planar oligomers are reported in order to follow the evolution of the structure with size. For the sake of comparison: the calculated C-C bond in the cubane molecule was 1.571Å	26
2.2	Comparison between the limiting values of the electronic properties reported in ref [59] and our corresponding crystal models. Label (a) stands for our plane waves calculations with the PW91 exchange-correlation. Label (b) stands for the B3LYP localized basis set calculations performed by Herrera [59]. Values for the isolated cubane molecule are also reported.	36
2.3	Distances and energetics of the lowest polymer unit cells considered in this work. X1 denotes the first atom on the linker group and X2 the last one (Fig. 2.12). X12 is a relevant length of the linker group: the ethyne bond length, the bond length in the benzyne ring, the N-N, N-O, and N-S distances respectively. bW corresponds to the valence bandwidth. The elastic constant $K = \frac{d^2E}{d\zeta^2}$ where $\zeta = a/a_0$ is the deformation along the chain axis.	41

- 2.4 Electronic Lowdin charges for different atoms in the cubyl chains unit cells, and the corresponding spilling parameter for the partial charge decomposition. C1 and C4 are the cube diagonals in the growth direction with C1 bonded to X2 and C4 to X1. The subindexes *in* and *out* refer to the position of the atoms in or out the plane defined by the C-X1-X2 bonds, if this plane is defined at all (N₂, NO and NS doping), the superindexes *1* and *2* signals whether those atoms are closer to X1 or to X2. 51
- 3.1 Geometrical parameters for the studied structures before and after relaxation. The bond lengths in Å, angles in degrees, and their respective abundances (the values within round parentheses) are reported. In order not to overload the table, whenever the number of bond angles/lengths was larger than three, we report only the mean value, the mean squared deviation and the number of different values found (within square brackets). 62
- 3.2 Average absolute values for the Gaussian curvature ($\overline{|K_I|}$), at the carbon-atom sites for the Schwarzites structures. Values for the unrelaxed crystals are also reported. The corresponding value for the Buckminsterfullerene C₆₀ is shown for comparison. 63
- 3.3 Solvent Accessible Surfaces for the Schwazite crystals, calculated using a probe radius of 1.4Å. The value for graphene is shown for comparison. 67
- 3.4 Energies per atom, relative to the value in a graphene layer. The corresponding value for diamond is also shown for comparison. . . . 67
- 3.5 Lattice constants and elastic constant for the studied models. Values computed for diamond are shown for comparison. Values of the upper and lower bounds to the isometric shear modulus *G* are, intentionally, reported with a larger number of significative figures just to reflect the small differences. 74

3.6	Electronic band gap energies (Δ_1) calculated for different negatively curved structures. The superindexes S and P stand for the Seifert and Pettifor parametrizations. The values calculated for diamond is shown for comparison. For the Seifert parametrization, we have also registered the values obtained for the unrelaxed structures. For the IWP-G structure we report the value of the band overlap.	75
3.7	Vibrational contribution to the Total Energy E , Free Energy F , Entropy S and Specific Heat C at 300K for the studied models	89

Chapter 1

Introduction

“LISTEN to me,” said the Demon as he placed his hand upon my head. “The region of which I speak is a dreary region in Libya, by the borders of the river Zaire. And there is no quiet there, nor silence.
Silence, a Fable, Edgar Allan Poe.

Carbon is a fascinating element. Depending on the molecular or crystal structure, carbon-based materials could display dramatically different electronic properties. Therefore, it is becoming one of the most widely used elements to create new prototypes of nanoelectronic devices. In particular, since the discovery of fullerenes in 1985 [1], various carbon structures exhibiting novel electronic and mechanical properties have been identified. Our work is related to the properties of curved and strained carbon-based structures. Therefore, before entering into the discussion of our results, let us state what do we mean by *strain* and *curvature*, and why those two concepts are relevant in the physico-chemistry of carbon.

1.1 The carbon polymorphism: valence-bond description of the covalent carbon bonds.

Let us consider the covalent bond between carbon atoms. By definition, covalency implies that the interaction with the nearest neighbors is of prime relevance. Under this consideration, a transparent understanding of the covalent bonding in molecules,

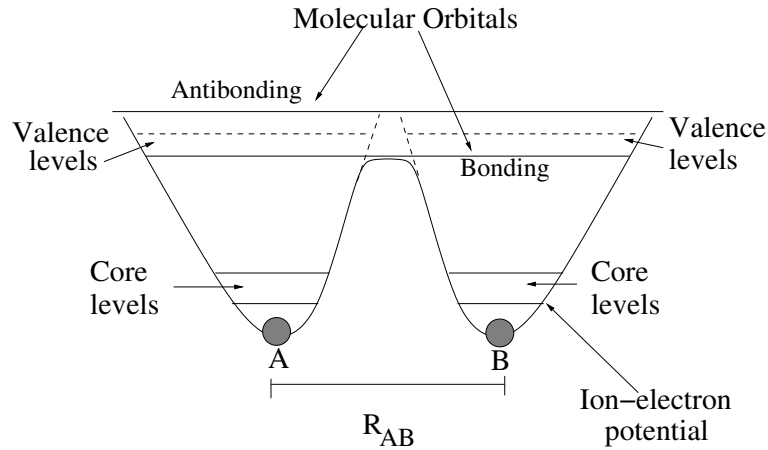


Figure 1.1: Schematic representation of the covalent bonding between two equivalent atoms (A , and B). The nuclei are at a distance R_{AB} . The lower lying states (core levels), retain their atomic character; whereas states extended between the two nuclei (molecular orbitals) define the molecular bonding.

clusters and solids, could be achieved considering the simplest case of a single electron shared by two equivalent nuclei. This scenario is sketched in figure 1.1; two identical atoms (A and B) are bound together, at a given distance (R_{AB} . The deep-lying states of the system, are localized about each nuclei (thus, they are referred as *core levels*); the states involved in the chemical bonding are referred as *valence levels*. The binding electron, is described by the *molecular orbitals*. A physically appealing approximation for the wavefunction describing the shared electron (molecular orbital), is the linear combination combination of atomic orbitals (**LCAO**), expressed as:

$$\Phi_{mo} = \frac{\phi_A \pm \phi_B}{\sqrt{2}}, \quad (1.1)$$

where Φ_{mo} describes a molecular orbital, and ϕ_A , ϕ_B , are the wavefunctions for valence states localized at the centers A and B , respectively. The Hamiltonian for the molecule, in this single-electron approximation, is of the form:

$$H = T + V(r_A) + V(r_B) + V(R_{AB}), \quad (1.2)$$

where $V(r_A)$ and $V(R_B)$, are the Coulomb interactions between the electron and

the nuclei, T is the kinetic energy operator, and $V(R_{AB})$ is the Coulomb interaction among the nuclei. Therefore the energies for the molecular orbitals are given by the expression:

$$E_{mo} = \frac{\langle \phi_A | H | \phi_A \rangle \pm \langle \phi_B | H | \phi_B \rangle + 2 \langle \phi_A | H | \phi_B \rangle}{2 \pm 2 \langle \phi_A | \phi_B \rangle} \equiv \frac{E_A \pm V_{AB}}{1 \pm S_{AB}}, \quad (1.3)$$

where we have used the fact that ϕ_A , and ϕ_B , represent the same orbitals, but centered at different positions; and defined the interaction potential

$$V_{AB} = \langle \phi_A | H | \phi_B \rangle,$$

and the orbital overlap

$$S_{AB} = \langle \phi_A | \phi_B \rangle.$$

Therefore, using this simplistic description, one can relate the binding energy to the overlap between the valence orbitals involved in the bond. The lowest energy level in Eq. 1.3 is referred as *bonding orbital*, and that with the highest energy as *antibonding*. The symmetries associated to the valence levels, define the orientations for which the overlap is maximized. This requirement on the overlap, explains the strongly directional character of the covalent bonding.

For carbon, the ground state atomic configuration in a single-electron (Hartree-Fock) picture, is: $1s^2, 2s^2, 2p^2$. The s - orbitals have spherical symmetry, meanwhile p - orbitals exhibit elongated shapes. The simplest prescription defining the valence electrons (un-paired electrons in an open atomic shell), would allow only for two covalent bonds per carbon atom. However, carbon-based structures display three- and four-fold coordinated atoms. The establishment of these covalent bonds, requires overlap between *hybrid* orbitals. In figure 1.2, the formation of these hybrid atomic orbitals for carbon is sketched. The resultant orbitals and related molecular and solid systems, are depicted in figure 1.3.

The sp hybrid orbitals, are oriented at 180° , thus they describe the bonding in linear carbon chains (ethynes). The sp^2 hybrids, are 120° apart from each other, and provide an explanation for geometry of three-fold coordinated systems (alkanes, and graphitic structures). The sp^3 hybridization, explains the formation of tetrahedrally

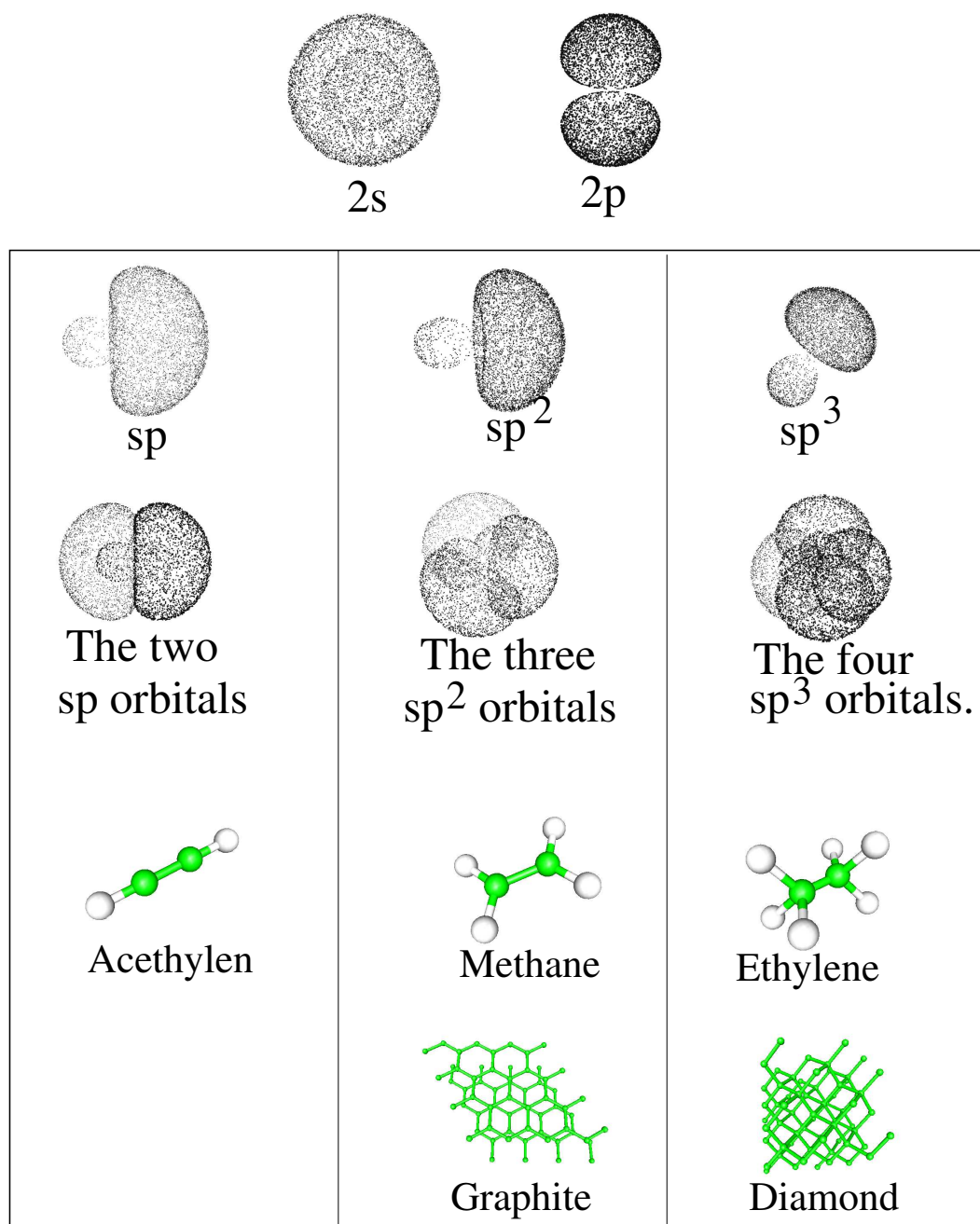


Figure 1.3: Representation of the hybrid carbon orbitals. The original s and p_z orbitals are shown at the top of the picture. At the bottom panels, we show molecular and solid state (only possible for sp^2 and sp^3) representatives for each kind of hybridization.

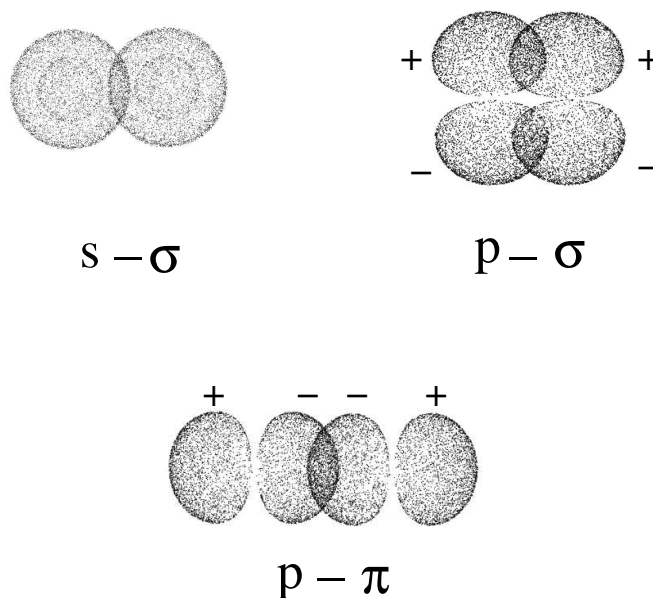


Figure 1.4: Representation of the σ and Π bonds in carbon. The + and - symbols, represent the sign of the wavefunctions in the respective lobules.

that graphite (an sp^2 hybridized system) behaves as a semimetal, whereas diamond (sp^3 hybridization) is a good insulator.

The description presented in this section, constitutes the classical *valence-bond* theory for the chemical bonding, as presented in any standard text-book [2]. Besides the many intrinsic drawbacks of this theory (among all, the full neglect of many-body effects), it provides a very useful classification scheme for carbon-based structures. Many of the geometrical, mechanical, and electronic properties, of carbon materials could be related to the kind of hybridization, and to the presence of Σ or Π bonds. The rationale underlying the success of such simple model, is the strong covalent character of carbon-carbon bonds. The discussion of, for instance, covalent bonds in hydrocarbons, follows the same principles stated for carbon-carbon bonds. The amazing polymorphism of carbon is, thus related to the possibility of different types of hybridization.

1.2 Strain in carbon-based structures.

In the previous section, we have stated that the type of hybridization defines the optimal bond-angles in carbon-based structures. Reciprocally, the number of nearest neighbors in the structure (the coordination), defines the type of hybridization required to establish the bonds. It would seem, using the simple valence-bond theory discussed above, that carbon-based structures could display only 180° , 120° , and 109.5° bond angles. Indeed, the vast majority of hydrocarbons, and carbon-based materials, displays the geometric, and electronic properties expected for sp , sp^2 or sp^3 hybridizations.

However, in various molecules, the C-C bond angles deviate notoriously from the optimal values expected from their coordination (on the basis of the standard hybridizations). A major contribution to the understanding of carbon physics, has been made by chemists (note that nowadays the gap between chemistry and physics is becoming smaller, but it was not so 20 or 10 years ago). During the past decades, chemists were synthesizing very exciting hydrocarbons a long time before physicists became aware of them. In particular, hydrocarbons in which the C-C bond angles deviate notoriously from the optimal values expected from their coordination (on the basis of the standard hybridizations analysis), have been synthesized [3–10].

In order to describe the establishment of covalent bonds at these *non-conventional* angles, it is sufficient to construct combinations of atomic orbitals, other than sp , sp^2 or sp^3 hybrids; the formation of these novel orbitals is referred as *non-standard hybridization*. There are various interesting features associated with non-standard hybridized molecules. Their cohesive energies are smaller, when compared to those for conventionally hybridized molecules. Therefore, a significant amount of energy may be liberated in chemical reactions transforming non-conventional bonds into normal hybridized ones. This energy difference is referred as *strain energy*, and the systems exhibiting non-conventional angles, are referred as *strained* systems. The chemical reactivities, an electronic properties, of strained molecules also differ from those of conventional hydrocarbons; these variations are thus considered to be effects of the bond strain.

The cubane molecule [3] represents a major breakthrough in the field of strained

molecules. Cubane was the first non-conventional tetra-coordinated bonded hydrocarbon to be synthesized. This molecule displays large formation energy (about 144Kcal/mol), and strain energy (166Kcal/mol). However, the absence of an *easy* path for the transformation towards more stable hydrocarbons, provides the surprising thermal stability of the cubane molecule, and the molecular cubane solid [11–13]; cubane decomposition occurs only at temperatures above 220 Celsius degrees. From the purely esthetic point of view, it is interesting to mention that cubane is the hydrocarbon-realization of a Platonic solid. Following the synthesis of cubane, other two *Platonic hydrocarbons* has been synthesized; tetrahedrane [5] (stabilized by using four tert-butyl substituents), and dodecahedrane [10]. However, the strain energy and thermal stability of cubane, make this molecule more appealing for further technological developments. Furthermore, the cubane synthesis could be realized with high yields; cubane displays the largest strain energy for an hydrocarbon available at milligram quantities [14].

Strained hydrocarbons, in particular cubane, have been proposed as the basis for a new generation of propellants and explosives [14–16, 18].

Strained bonds also appear during the structural transformations of graphitic systems. An strickling example (one that we will mention further during this work), is the celebrated Stone and Wales transformation, which introduces two heptagon-pentagon pairs in a perfect hexagonal arrangement [19]. The transition path consist of a $\frac{\pi}{2}$ rotation of one dimer, during this rotation, the system visits configurations with strained bonds.

1.2.1 Cubane oligomers

From the nanoscience point of view, cubane molecules could be seen as very strained hydrocarbon clusters. In 1999, Eaton and his co-workers, demonstrated that cubane molecules could be used as building blocks for polymer chains [17]. The reaction of 1,4-diiodocubane (the cubane molecule with iodine substituents at the diagonals), with phenyllithium, produces a high yield of 4-phenylcubyl-iodine (a cubane molecule with a phenyl substituent and a iodine substituent) [17]. The

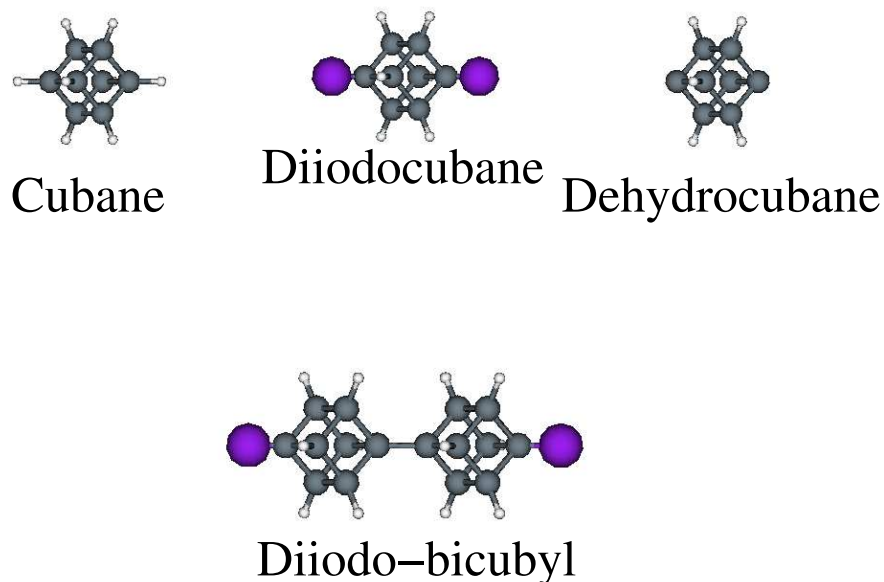


Figure 1.5: Molecular models for some systems involved in the formation of cubane oligomers, starting from the simple cubane molecule. The dehydrocubane (cubene) intermediate state, is highly reactive and is the desired monomer. Diiodo-bicubyl is the first step in the formation of chains.

1,4-dehydrocubane (cubane with two hydrogen atoms removed from the diagonals, dubbed *cubene*), appears as an intermediate state during this reaction. Cubene is a very reactive system, and it can not be isolated. This dehydrocubane system, is the precursor for cubane polymerization. The techniques developed by the Eaton's group, allow for coupling of dehydrocubanes, first towards the simple diiodo-bicubyl dimer, and then to chains up to 5-cubane units [17]. *In vivo* polymerization is hindered by the poor solubility of larger chains. However further improvements in the synthetic paths may allow for larger polymer chains, made of these cubic hydrocarbon clusters. Figure 1.5 depicts some of the systems involved in the formation of cubyl-cubane chains.

The large electronic band-gap of solid cubane [20], suggest that cubane polymers

would be transparent in the visible and ultraviolet region of the spectrum. Theoretical investigations on hypothetical polymers made of fully dehydrogenated cubanes, predict low electronic band gaps for these structures [21]. However, dehydrogenated cubane networks would be very reactive species, and saturation of the bonds may lead to a significant increase in the electronic band-gap. A significant amount of work has to be done in the field of cubane polymerization. From the purely theoretical point of view, extensive investigations of the mechanical and electronic properties of cubane oligomers are required, a task that we have partially achieved in this work.

1.3 Curved carbon systems.

Curved surfaces decorated with atoms from the IV group in the periodic table, such as carbon fullerenes [1] crystals and silicon clathrates [22], have been studied during the past two decades. The decoration of these surfaces does not require non-conventional hybridizations; the bond angles remain close to 120° (for sp^2 networks), or 109.5° (for sp^3 hybridization). In order to build positively curved surfaces from sp^2 and sp^3 hybridized atoms, the introduction of pentagonal rings is required. In general, the presence of pentagonal rings posses specific electronic and vibrational properties. The vast amount of void space in fullerene crystalline packings, suggests the possibility of doping, thus resulting in changes of the electronic properties [23]. But it is not only the existence of pentagonal rings, usually referred as defects, what induces electronic changes in graphene sheets. As a matter of fact, many of the intriguing features of carbon nanotubes (cylindrically rolled graphene layers), and fullerenes (hollow carbon cages), can be understood in terms of global geometrical parameters. This is specially true for single walled carbon nanotubes (SWCNT), in which the diameter and chirality determine whether the system behaves as a semiconductor or as a metal [24] (see figure 1.6). This geometrical description constitutes an amazing work of physics and lead scientists, at the beginning of the 90's decade, to propose other novel curved atomic arrangements.

The physico-chemical properties of fullerenes, and SWCNT with small diameters, are dramatically different from those of graphite. In particular, these novel nano-

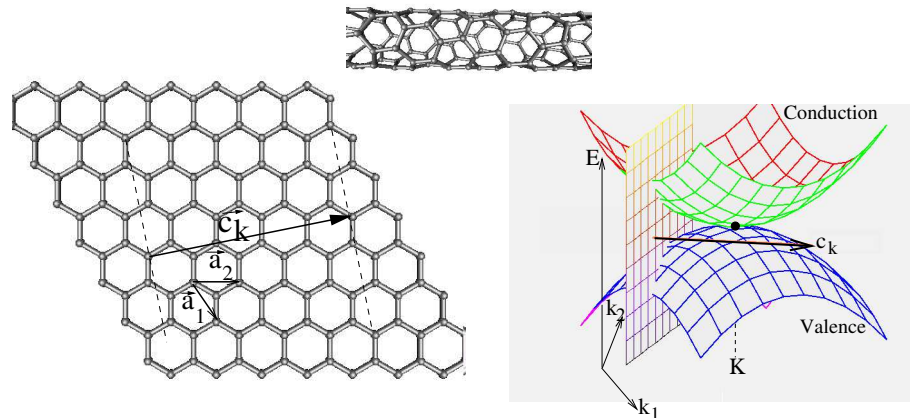


Figure 1.6: Geometrical interpretation of the metallic or semiconductor behavior of Single Walled carbon Nanotubes. The chiral vector \vec{c}_k defines the type of rolling. The tubule will display metallic behavior when the plane defined by \vec{c}_k in the reciprocal space, contains the point at which the conduction and valence bands of graphene are in contact (K point). Adapted from ref. [24].

structures have been found to exhibit catalytic activity, for instance in the cracking of hydrocarbons, whereas graphite is generally regarded as an inert surface. The increase in the chemical activity is, therefore, related to the curvature of these systems. As a matter of fact, fullerenes and nanotubes with large diameters, do not display notorious chemical activity.

From the many possible curved surfaces, *minimal surfaces* possess particularly interesting properties. These surfaces are solutions to the *Plateau's problem*; and are the surfaces with minimal area for a given boundary. The mean curvature must be zero, and the Gaussian curvature negative, for a surface to be minimal. In 1890 H. A. Schwarz solved the Plateau's problem for skew quadrilateral boundaries. The Schwarz structures could be periodically repeated in the three spatial directions, and are thus known as *Triply periodic minimal surfaces (TPMS)*. TPMS display labyrinthine structures, dividing the space into inter-penetrating subspaces. Following the ideas of Schwarz, other mathematicians have constructed periodical minimal surfaces [28]. The topology of various physical systems is described by minimal surfaces; soap films, zeolites, and liquid crystals, among others.

1.4. Inducing structural changes using femtosecond laser irradiation. 12

In 1991, Mackay and Terrones demonstrated that TPMS could be decorated using sp^2 hybridized carbons [25–27], and gave to those crystals the name of *carbon Schwarzites* (see figure 1.7). Schwarzites open the possibility of enhanced chemical activity, preserving mechanical robustness in the three dimensions (note that nanotubes are very strong in the axial direction, but the interactions among nanotubes in a bundle are weak, van der Waals, forces). Various Schwarzite crystals have been reported in the literature [29–31]; their cohesive energies are within acceptable ranges (below, or close to, the cohesive energy of the Buckminster fullerene). This type of materials can be generated by introducing five-, seven-, and eight-membered rings. Huang, Ching, and Lenosky [32], used a first principle approach to study the electronic properties of Schwarzite structures comprising only hexagons and heptagons. The purely topological effects on the band structure have been investigated, solving the single-particle Schrödinger equation for electrons constrained to move on the surface [33]. The question regarding the interplay between the topological properties, the existence of octagonal and heptagonal rings, and the electronic properties remains unsolved.

Various experimental reports [34–36], suggest that disordered Schwarzite phases have been synthesized. Schwarzite fragments are also believed to induce magnetism in all-carbon structures [37, 38]. Extensive studies aimed to the experimental identification of Schwarzite structures are required. In our work, we have performed an extensive theoretical study of various Schwarzitic crystals, especially focused in characterization techniques. Our results should be relevant in the study of novel negatively curved carbon structures; such as ordered microporous carbons [36], and spongy carbons [34, 35].

1.4 Inducing structural changes using femtosecond laser irradiation.

By now, we have become aware that both strain and curvature are able to modify the electronic properties of carbon-based structures. Various possible applications have been proposed for the novel carbon materials, but a significant amount of work

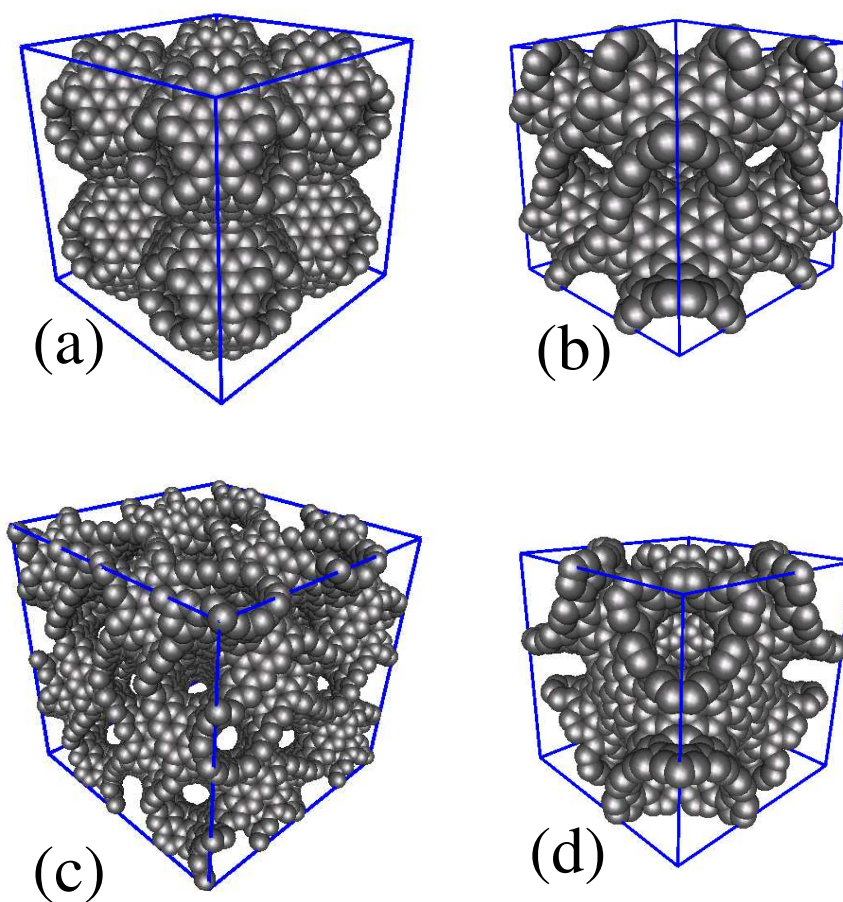


Figure 1.7: Molecular representations for some Schwarzite crystals. (a) Eight cells of the balanced P structure. (b) Eight cells of the balanced D structure. (c) Eight cells of the balanced G structure. (d) The cubic cell of the Schoen IWP-G structure.

must be carried out in order to witness real industrial applications. One of the most difficult issues concerning carbon nanostructures is that they can be very sensitive to symmetry and geometrical defects. For example, the inclusion of pentagonal rings can induce a transition from semiconducting to metallic behavior in SWCNTs. Is it possible to manipulate the location of those defects thus changing the local strain?.

Ultrashort (femtosecond) laser pulses, have proved to be convenient tools for structural modifications at the atomic level [39]. The increase in the electronic entropy, allows the system to overcome the energetic barriers associated with less probable configurations [40]. Therefore, laser pulses could induce structural transitions which are very difficult under thermal conditions [40–42].

For carbon-based systems, laser induced fragmentation of fullerenes [43], selective cap opening in nanotubes [44], and laser graphitization of diamond [45,46], have been studied. In this work we discuss how the ultrashort laser pulses induce strain release processes in graphitic systems, in which 5-7-7-5 defects are transformed into 6-6-6-6 rings. We also study the possibility of laser induced fullerene annealing, a possible path towards more complex carbon structures.

1.5 Scope of this work.

In the main body of this work, we present theoretical results on various carbon systems using different methods. Chapter 2 deals with polymer chains built from cubane molecules; their mechanical and electronic properties, and the effects of doping with functional groups. Chapter 3 is related to Schwarzite structures and their relation with experimentally synthesized nanoporous carbons. Finally, chapter 4 and 5 are concerned with the use of ultrashort laser pulses for inducing new structural changes which release strain in the nanostructures, using Stone-Wales type transformations responsible of annealing heptagon-pentagon pairs within carbon nano-structures.

The appendices provide more detailed information on the general background on many-electron systems, suitable methods for describing covalent solids used throughout this work (Density Functional Theory and Tight binding approximations), and

the theoretical description of matter-light interactions. The mathematical derivation of important formulas and related issues used in the main body are also described in detail in the appendices.

Chapter 2

Relevant features of functionalized cubyl-cubane polymers.

Pleased to meet you,

hope you guessed my name

Sympathy For The Devil, The Rolling Stones.

In this chapter we propose novel one- and two- dimensional materials using the cubane molecule as a building block, and study their electronic and mechanical properties. The proposed models are crystalline polymers and polymeric networks simulated as perfectly periodic systems. It is envisaged that these proposed materials could be used in the construction of nanoelectronic devices.

2.1 Essentials of cubane and cubyl-cubane oligomers.

The cubane molecule, C_8H_8 (see figure 2.1), was first synthesized in 1964 by the Eaton's group [3], and it is still considered a paradigm in highly strained molecules. The C-C-C bond angles of 90° are quite far from the 109.4° ; commonly observed in stable sp^3 hybridized hydrocarbons. A large energy value of about 166 Kcal/mol is associated with this high strain. Despite this, the molecule remains stable because,

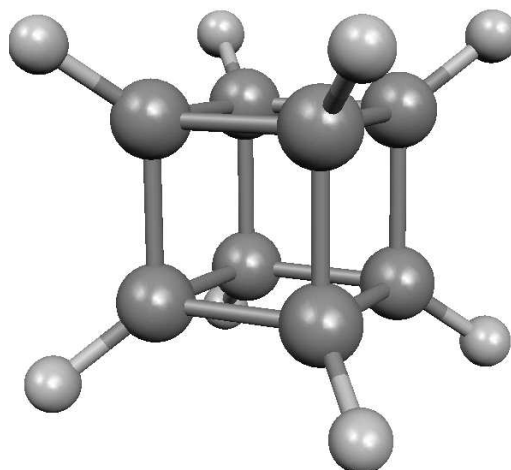


Figure 2.1: The cubane molecule, C_8H_8 .

according to Eaton himself, there is no easy path for the atoms to re-accommodate¹. The relevance of cubane research is best underlined by Eaton's words : *Cubane is the most highly strained, kinetically stable ring system available in quantity . We have used it as the source of even more highly strained compounds including 1(9)-homocubene (the most highly twisted olefin), cubene, (the most highly pyramidalized olefin), and such intriguing species as 1,4-dehydrocubane, cubyl cation (the "least likely" cation), and the cubylcarbinyl radical (the fastest rearranging saturated radical). These have "record" properties and as such have proven to be of fundamental importance in developing an understanding of bonding in strained systems.* Therefore, besides the proposed practical applications, most of them related to the explosive industry, cubane and other related molecules are chemical and physically interesting system. Indeed the synthesis, again by Eaton's group, of octanitrocubane [16,18], believed to be one of the most powerful developing explosives, was listed in the Chemical Society's *Chemistry* magazine as one of the chemistry-related milestones of the year 2000.

From the theoretical point of view, most of the studies have been on solid cubane or in the single molecule itself [11, 13, 47, 48]. The molecule has been characterized

¹This forbidden path stability mechanism would deserve a larger discussion, but that is far from the main field of this thesis.

using different theoretical methods and most of them agree with experimental observations [49–52]. The C-C distance is of the order of 1.57 Å, C-H distance is of the order of 1.11 Å, and the C-C vibrational modes are higher than any other hydrocarbon mainly due to the strain present on the molecule. The electronic gap has been calculated to be at least 4.5eV [47] (a value of about 8.3eV is also accepted in the literature [47]) corresponding to a good insulator with very localized orbitals.

Searching for new paths to increase the available strain energy, Eaton’s group has developed techniques that allow the polymerization of cubane and the exchange of hydrogen atoms for electronic enriched groups. The polymerization is an extra bonus in the cubane chemistry, and synthesis of large cubyl-cubane rods and surface-like materials has been also carried out by Eaton’s group in a controlled fashion. Rods as large as 15 Å long have been produced although there are still some problems related to the solubility of oligomers with more than three units that require the attachment of extra molecules in the chain [17]. The synthetic path includes the ability to insert functional groups within the oligomers [17]. We believe that this process could be a new route for obtaining electronic devices in the nanometric scale, and this possibility is discussed in the present chapter.

Here we study possible chains and networks made from cubane molecules, with the inclusion of functional groups. In addition, the electronic properties are shown to be attached to those of the molecule itself. The introduction of doping groups allows tuning of those electronic properties.

2.2 One and two dimensional arrays of cubyl-cubane networks.

Let us first consider a chain of cubyl-cubane units joined along the cube diagonals, as shown in the first panel of Figure 2.2. Hydrogen atoms have been removed at both sides of this diagonal in order to allow for the intercube C-C carbon bond².

²The resulting radical anion is referred in the literature as *1-4 dehydrocubane* [17]. However, throughout our discussion we will refer to this building blocks as cubanes or cubyl-cubanes, except

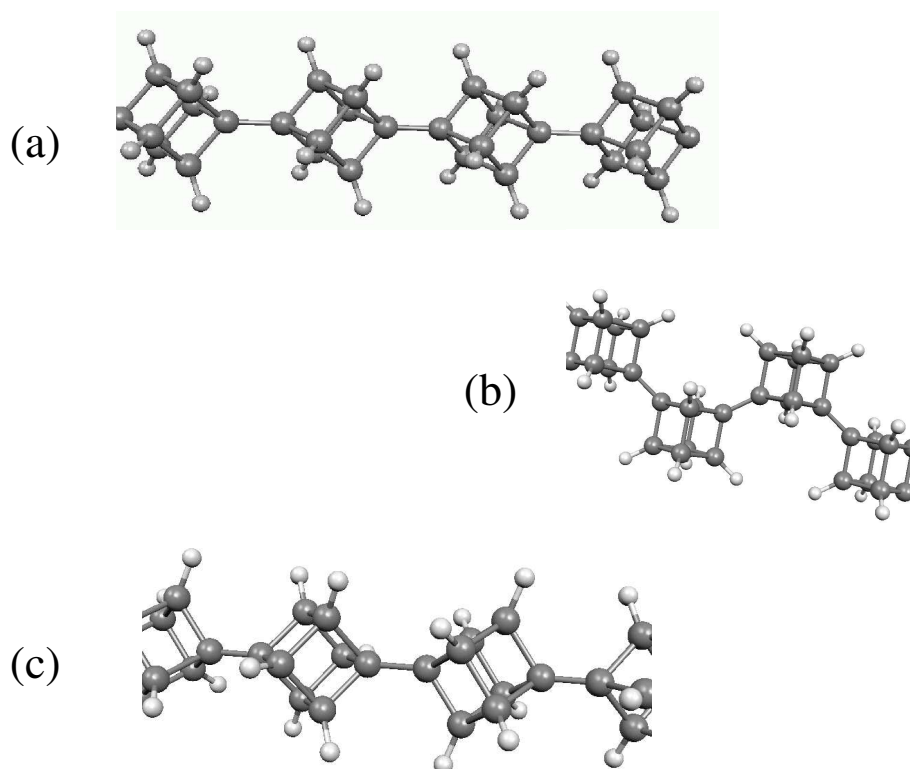


Figure 2.2: Proposed linear cubyl chains models. (a) Joining through the cube diagonal. (b): Ladder configuration. (c): With rotated cubyl units.

If the chain is large enough, it can be considered as a one dimensional periodic system in which the unit cell comprises only of one cubyl unit. This primitive cell is rather small and it is possible to study the electronic properties of the large chain within DFT theory without severe computational burden. The question of whether the crystalline approximation is valid for reasonably sized systems will be addressed in section 2.3.

For this study we have chosen a plane wave approach using pseudopotentials. The exchange-correlation energy is treated within the Perdew-Wang Generalized Gradient Approximation (PW91) scheme [57], pseudopotentials were of the Ultrasoft Vanderbilt kind [58]. Kinetic energy cutoffs of 20 Ry for the wavefunctions and 120 Ry for the charge densities were used, respectively. This level of theory is accurate enough for the description of the geometry, electronic properties and vibrational

when there is place for confusion.

spectra of the cubane molecule. By performing a local minimization of the C_8H_8 molecule, we have found C-C distances of 1.571 Å, C-H distances of 1.098 Å, C-C-C bond angles of 90° , and C-C-H bond angles of 125.3° , that are in good agreement with other theoretical approximations and experimental data [3,47]. These results will be used for comparison with the proposed models. Although symmetry was not imposed during the relaxation procedure, we have found only minor deviations from the full cubic symmetry represented by tiny dispersions around the mean angles and distances (0.0002 Å for C-C distances, 0.015° for C-C-C bond angles and 0.1° for C-C-H bond angles).

Let us now consider the polymerization of cubyl molecules, and how the chain properties are modified when compared to the isolated molecule. We set up our model polymer assuming cubyl-cubane symmetry to be the same as that of the cubane molecule: i.e. we have used perfectly cubic building blocks. The lattice parameter is initialized at a value for which the intercage C-C bond is close to lengths of the intra-cage bonds. Relaxation of the model to the local minimum is achieved varying the lattice parameter and internal coordinates (using the Broyden-Goldfarb-Shanno, BFGS [60], method)³. Total Energies per atom were converged up to 0.01eV, a criteria that was kept during the remaining calculations.

The final geometry, depicted in figure 2.2, corresponds to a chain with periodicity of $c_o = 4.2\text{Å}$ (c_o is the lattice parameter). The intercage bond is significantly shorter than the cage-bonds (1.462 Å vs. 1.567 Å and 1.581 Å) meaning that this cubyl-cubyl bond is stronger than the bonds within the molecule itself. This inter-cage bond makes an angle of 125.6° with the neighboring C-C bonds (from now on referred as the α -positioned bonds, in the usual chemical notation), i.e. fairly the same value corresponding to the C-C-H bonds. The connection is, therefore, made smoothly along the cube diagonals.

Setting this rather strong bond requires accommodation of the cubyl units, as the shared atoms (those forming the inter-cage bond) can be thought to be pulled towards each other. The six cage bonds at α -positions with the intercage bond are

³Eight special k-points were used in this step for sampling the Brillouin Zone. This number was proven to assure good convergence both in energies and forces.

longer than those far apart from that bond (those are the 1.567Å and 1.581Å bonds previously mentioned). The angles between two α -positioned bonds shift towards 90.5° with a consistent shift in the opposite angles in the same cube face to 80.5°, all the remaining bonds stay near their original 90° value. C-H distances and C-C-H angles remain unchanged by the intercage bonding. All these changes are consistent with the image of pulling the cubyl blocks through the diagonal, and the rather small changes from the cubane structure reflects the mechanical strength of the cubane unit. Despite the differences in the corresponding theoretical framework, the results are also consistent with our calculations on cubyl-cubane oligomers [59],

It is interesting to have a measure of the mechanical strength of the whole chain. For this we have defined an elastic constant that is the measure of the curvature in the Energy *vs.* deformation curve (see figure 2.3) $K = \frac{d^2E}{d\varsigma^2}$, where $\varsigma = c/c_o$. This definition yields a value of $K = 191$ eV for the simple cubyl chain, meaning that a large amount of energy is needed to stretch the chain. In order to rationalize this number, a large cubyl rod would exhibit a Young modulus between 200-400 GPa in the axial direction, depending on the definition of the cross section (i.e. on the actual experimental setup). The strength under bending will be addressed later in the context of finite size effects.

This kind of straight chain is not the only one that can be made from the cubyl units. In our study on cubyl-cubane oligomers [59], we have also examined ladder-like connections in which the chain axis does not coincide with one of the cube diagonals [59]. Extrapolation of this kind of oligomers leads to the model depicted in the second panel of figure 2.2. In this case, we have two cubyl units per cell and the chain axis lies parallel to one of the cube faces. We have performed the same relaxation procedure mentioned above, but using half the number of k-points. The final structure posses a lattice parameter of $a_o = 6.85$, and an intercage bond of 1.471 Å . Besides the intercage bond, the ladder-like chains exhibit three kinds of intracubyl bonds: (i) α -positioned bonds performing 1.580Å lengths;

(ii) Bonds lying parallel to the chain axes and located far from the intercage bond, performing 1.569Å lengths;

(iii) Bonds lying perpendicular to the chain axis and located far from the in-

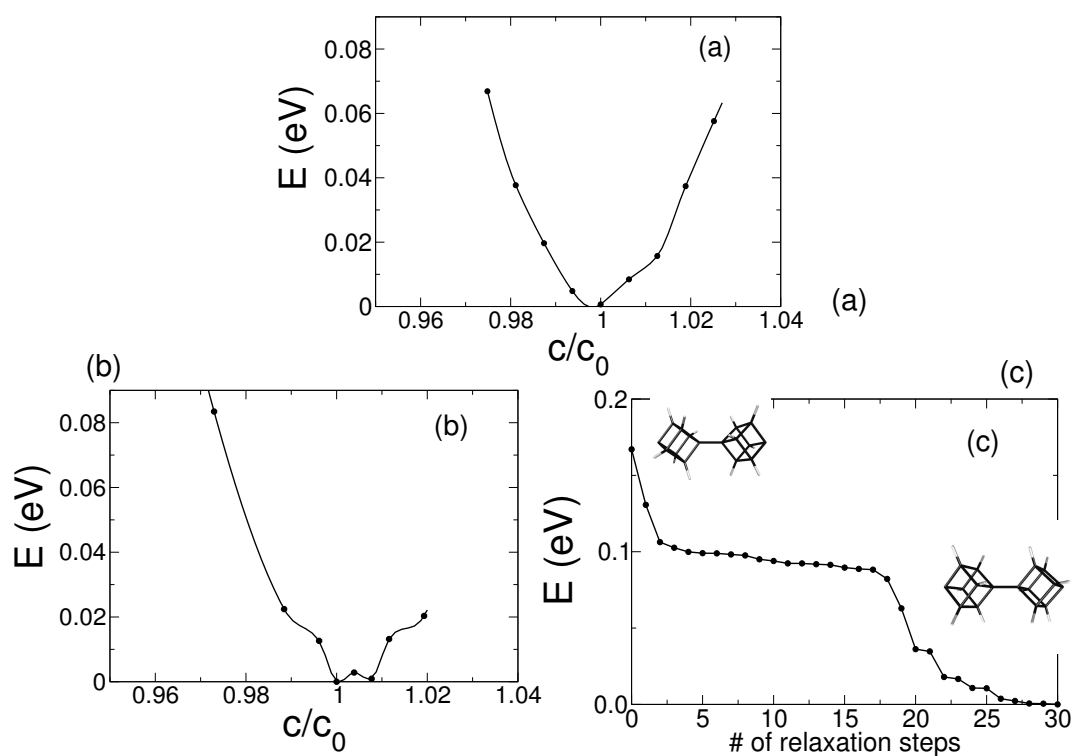


Figure 2.3: Energy *vs.* deformation curves for the straight cubyl chain (a), the ladder-like chain (b), and BFGS relaxation path for the staggered configuration of cubyl units. The reference “0” energy is the optimal energy for each model.

tercage bond , performing 1.567Å lengths;

Therefore we can confirm that α -positioned bonds get stretched during the onset of the inter-cubyl one. Bond angles between inter-cage and α -positioned bonds, inter-cage bonds are shifted to 89.5° , a shift that is compensated by rearrangement of the other C-C-C angles that remain closer to 90° . This is consistent with the “pulling the diagonal” effect, the difference being that now we are pulling an “accordion”. These results are also consistent with our results on stair-like oligomers [59]. The shape of the Energy vs. deformation curve (see figure 2.3) makes it rather difficult to define a simple elastic constant as we did for the straight chain, but it is clear from the curve that this model would be mechanically softer.

It is remarkable that the binding energies, defined as the difference between the chain energy and the atomic energies $E_b = E_{chain} - E_{atoms}$, per cubyl unit of these two models are mainly the same $E_b = 89.6$ eV, thus demonstrating that the binding energy is mainly determined by the inter-cubyl bond rather than by the detailed chain structure; also signaling the strong molecular character of these chains.

It is also possible to figure out a chain whereby the C-H bonds are no longer in the eclipsed configuration, but in an staggered configuration (as in the ethane molecule). This model was also treated (see figure 2.2) using the same theory level, and it was found to lie in a very unstable patch of the Potential Energy Surface, so that the BFGS relaxation resulted in a stable eclipsed chain (see figure 2.3); that is just the same straight chain we discussed above. The barrier for rotation is rather small (about 0.15 eV), therefore rotation of cubyl-cubane monomers could be expected to occur in cubyl-cubane polymers, a fact that is recognized in the experimental literature [17]. Neither the mechanical strength nor the electronic properties depend strongly upon the relative orientation of the C-H bonds, and we will use for our discussion the eclipsed configuration.

Before analyzing the electronic properties of the cubyl chain, let us introduce the two dimensional network of cubyl-cubane units shown in figure 2.4. The primitive vectors of this structure lie parallel to two cube diagonals, forming an oblique lattice, whose Brillouin zone is also shown in figure 2.4. We performed the lattice vector and internal coordinates relaxation. Taking advantage of the system symmetry, we

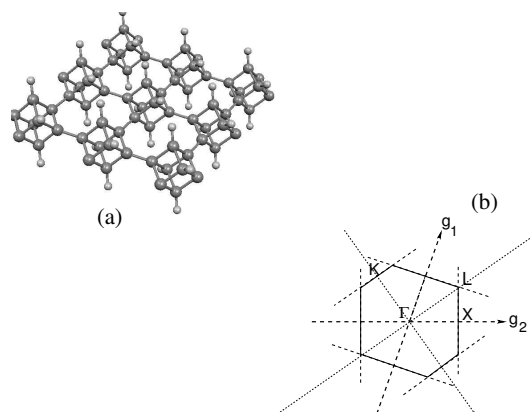


Figure 2.4: A two dimensional cubyl network (a) and its corresponding Brillouin zone (b).

have considered that the two lattice vectors have always the same length, a_o . This procedure leads us to a model with $a_o = 4.23$ and a geometry with four different C-C bond lengths: 1.449\AA for the intercage bond, 1.60\AA for the cubyl bonds α -positioned with respect to two intercage bonds, 1.579\AA for bonds α -positioned only with one intercage bond and 1.555\AA for bonds far from the intercage bonds. Meanwhile for 1D cases, the C-H bonds remained unchanged; now these bonds are slightly affected by the network setup. A minor compression of the C-H bond length to 1.097\AA comes together with distortion of C-C-H angles. Whenever the C-C bonds include one of the shared atoms, C-C-H angles shift to 124° , otherwise they shift to 125.1° . The inter-cubyl angles also exhibit a larger distortion than in the 1D cases: angles including a bond far from the inter-cage shift to 90.8° with a consequent shift of the opposite angles towards 89.2° . Of course, these changes are still small, and the cubyl structure remains very near to that of the perfect cubane molecule.

The positive curvature of the energy as a function of the area is indicative of the 2D network stability. Defining now an elastic constant using the curvature of the energy *vs.* area plot (see figure 2.5): $K' = \frac{d^2 E}{d\sigma^2}$, where $\sigma = a/a_0$, we obtained $K' = 108$ eV, which is related to the energy delivered by the system when the network is subject to an isotropic deformation along the unit cell vectors. Under orthorhombic deformations of the lattice vectors, it is observed that the energy is well fitted by a quadratic function $E = E_o + \frac{1}{2} C z^2$, where the deformation parameter

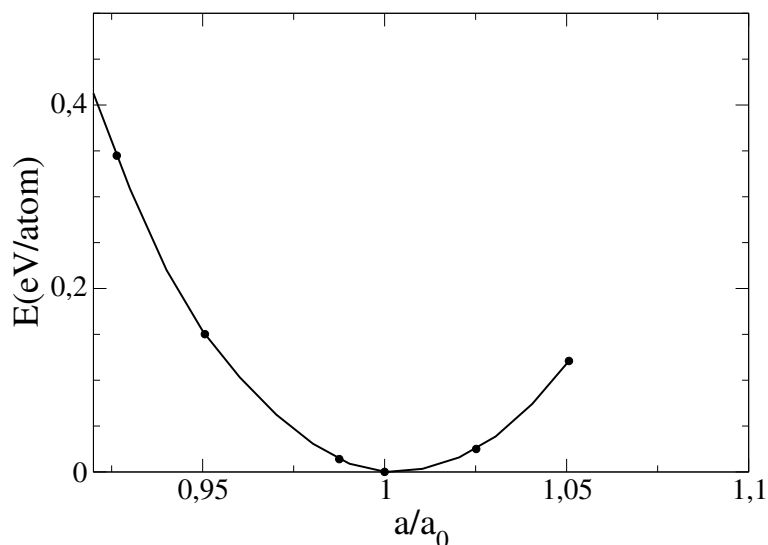


Figure 2.5: Energy *vs.* isometric deformation for the bidimensional cubyl network. The reference “0” energy is the minimum energy.

is related to the ratio between the lengths of the basis vectors in the plane: $z = 1 - \frac{a}{c}$ and the constant $C = 74.38$ eV, thus showing that the system is stable under this non isometric strain.

Table 2.1 summarizes the most significant geometrical parameters obtained for these models, i.e. the C-C bond distances, In the table we also report result for cubyl-cubane oligomers, that will be discussed in the next section.

2.2.1 Vibrational spectra

Further confirmation of the mechanical stability of a system can be achieved by calculating the vibrational spectra: stable systems will exhibit only positive vibrational frequencies. We have performed such calculations within the DFT perturbation theory scheme, first in the Γ point (localized, in phase vibrations) and then in the X point (counter-phase vibrations). The reliability of our calculations for the vibrational spectra was confirmed by previous calculations on the vibrations for the cubane molecule. The above mentioned minor deviations from the full cubic symmetry in the calculated geometry, lead to degeneracy removal in the expected 18 vibrational modes. Nevertheless, both symmetries and frequencies are in very

Species	Intercage (Å)	1α -pos (Å)	2α -pos (Å)	far [⊥] (Å)	far	a_o (Å)
2C	1.483Å	1.565Å	1.560Å	...
3C	1.487Å	1.570Å	...	1.560Å	1.560Å	...
4C	1.476Å	1.579Å	...	1.569Å	1.569Å	...
stair model	1.471Å	1.580Å	...	1.569Å	1.567Å	6.85Å
straight model	1.462Å	1.581Å	1.567Å	4.20Å
2x2	1.479Å	1.577Å	1.609Å	...	1.570Å	...
3x2	1.478Å	1.578Å	1.609Å	...	1.563Å	...
4x2	1.487Å	1.564Å	1.582Å	...	1.557Å	...
3x3	1.478Å	1.577Å	1.587Å	...	1.568Å	...
network	1.449Å	1.579Å	1.600Å	...	1.555Å	4.23Å

Table 2.1: C-C bond lengths in the chain and network models. 1α -pos Å and 2α -pos Å stands for bonds at α positions with 1 or 2 intercage bonds, when it applies. far^{||} and far for bonds far[⊥] from the intercage bond parallel or perpendicular to the chain axis, when this concept applies otherwise we report the value as far(par). Values for linear oligomers with 2,3 and 4 cubyl units (2C, 3C and 4C respectively) and for a 2x2, 3x2 4x2 and 3x3 planar oligomers are reported in order to follow the evolution of the structure with size. For the sake of comparison: the calculated C-C bond in the cubane molecule was 1.571Å

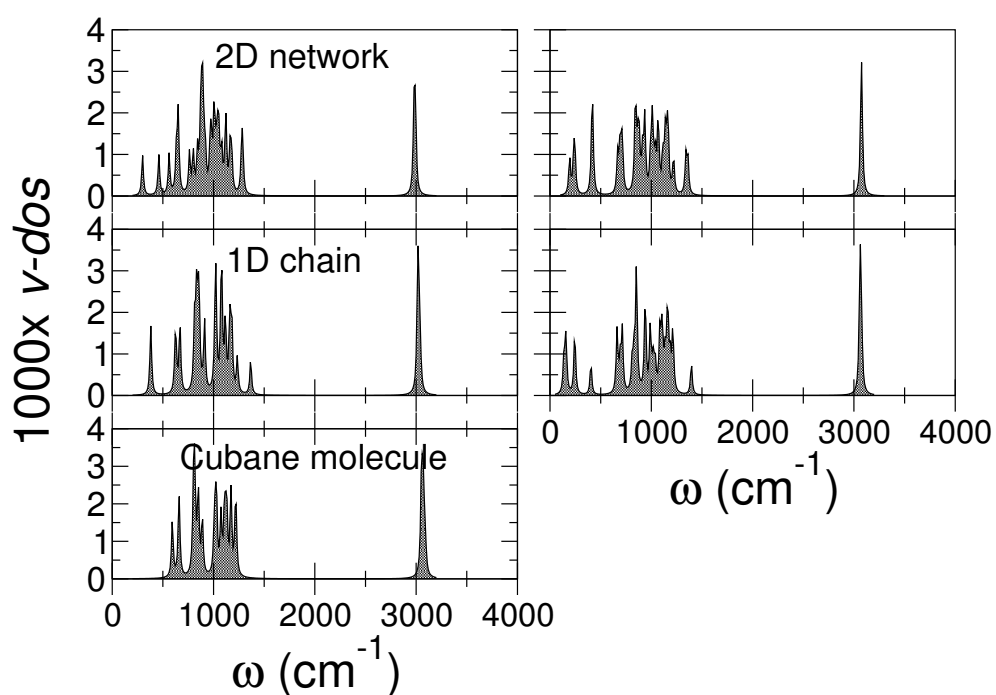


Figure 2.6: Left Panel: Vibrational spectra (Γ point) for the 2D network (top) , 1D chain(middle) and isolated cubane molecule (bottom). Right panel: vibrations at the X point for the 2D network (top) and 1D chain (middle).

good agreement with other theoretical and experimental reports [12,47].

The first remarkable result is that, neglecting the first three spurious modes coming from the coupling with the periodic images in the simulation box, the vibrations confirmed the mechanical stability of our chains and networks. Secondly, it is interesting to note that most of the vibrations preserve their molecular character, revealing very little dispersion (only small differences between the Γ and X counterparts were observed). As expected, this is specially true for the high energy optical modes, corresponding to C-H bond stretching.

Let us first analyze the modes intrinsically associated with the chain formation, later we will discuss those that reveal an strong molecular character. For the linear chain, the acoustic mode is, at Γ , the in-phase rotation of cubyl units around the chain axis; this mode shifts towards 136 cm^{-1} at the X point developing a significant dispersion. Coupled rotations in a plane perpendicular to the chain axis are the first optical modes with frequencies around 380 cm^{-1} at Γ and 152 cm^{-1} and 159 cm^{-1} at X, being the most dispersive of all the calculated modes. Finally, another mode comprising the intercage bond stretching appears around 1350 cm^{-1} at Γ and disperses to 1450 cm^{-1} at X. All of these *chain* modes involve only slight changes in the cubyl geometry.

For the less dispersive modes, we have that the breathing mode (that in the cubane molecule appears around 1008 cm^{-1}) are hindered by the intercage bond, and its strength is fragmented in rather complex molecular expansions and compressions (half breaths), C-C-C bending modes (600 and 650 cm^{-1} in the molecule) are slightly blue shifted, meanwhile C-C stretching (around 800 , 850 and 900 cm^{-1}) and C-C-H bending modes (up to 1222 cm^{-1}) get red shifted. All of these models exhibit low dispersion, as expected from their molecular character

The two acoustic modes in the cubyl network come from cubyl motion both out- and in-plane. This kind of modes exhibit a large dispersion going towards 234 cm^{-1} and 246 cm^{-1} , respectively. The first optical modes are rotation modes, which can be around any one of two axis: one in-plane and the other perpendicular to the network. These modes lie around 299 cm^{-1} , 460 cm^{-1} and 560 cm^{-1} , respectively (left top in Fig. 2.6) at Γ and exhibit a significant dispersion going to 193 cm^{-1} ,

414 cm^{-1} and 415 cm^{-1} at the X point. Again there is a peak associated with strong atomic motions along the network axes (cube diagonals) which lies around 1278 cm^{-1} and shifts towards 1350 cm^{-1} at the X point.

Concerning the molecular-like modes of the 2D-network, we have observed some C-C stretching modes shifted to the 900 cm^{-1} region, and some C-C-H bending modes shifted to the 1000 cm^{-1} region increasing the vibrational density of states (*vdos*) between 900-1000 cm^{-1} . C-H stretching modes are also red shifted in this case.

In summary: vibrational spectra confirms the mechanical stability of these models, pure chain and network vibrations exhibit significant dispersion. Still, the spectra is dominated by the single molecule behavior, with only minor modifications, revealing the very molecular character of this models.

2.2.2 Electronic Properties

The electronic band structures of the different cubane systems are shown in Fig. 2.7, and the corresponding density of states for the lowest energy configuration is depicted in Fig. 2.8. In Fig. 2.7, the band structure of the different cubane networks is compared with the electronic levels of the single cubane molecule. As expected, there is a clearcut change of the electronic gaps, from 5.43 eV for HOMO-LUMO gap of the cubane molecule, to a 4.87 eV band gap for the 1D cubyl chain, and a 3.78 eV band gap for the 2D network. As expected, the results indicate that dimensionality contributes to the electronic delocalization.

An increase in the band structure curvature as function of dimensionality is clearly noticeable, both in the valence and in the conduction bands. This increase implies a decrease of the effective electron mass, especially close to the Fermi level. The lower electronic level retains its molecular character, as can be seen from the very low dispersion of the band structure. This is also true for other electronic bands (Figs. 2.7 and 2.8), in particular for the first virtual modes of the 1-D chain. This means that electronic conduction would be rather difficult, even promoting electrons across the large band gap (for the sake of comparison: the calculated value for diamond in the same theory level is about 4.1 eV). In the two dimensional

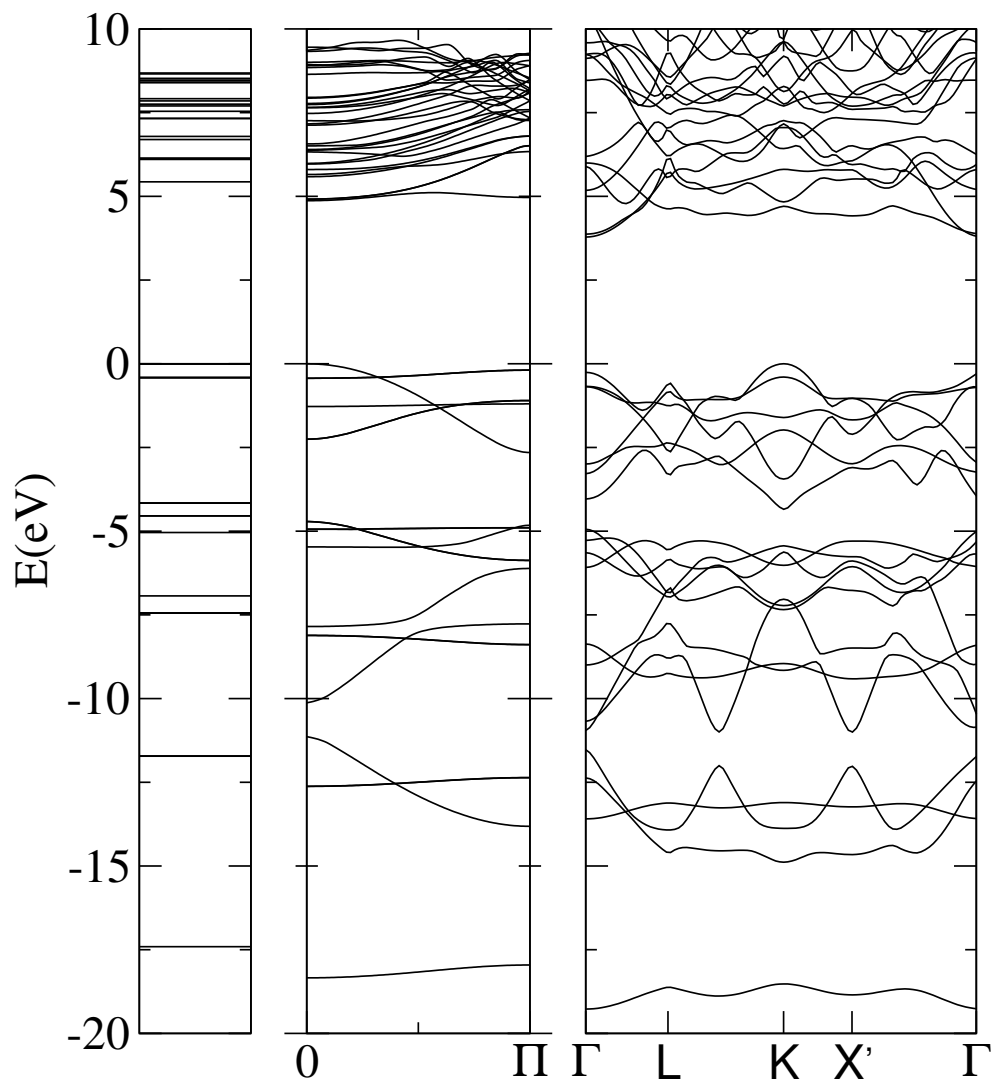


Figure 2.7: Electronic band structure for an individual cubyl chain (middle panel), and a network (right panel) compared to the electronic levels of the cubane molecule (left panel). The special points in the First Brillouin Zone of the two dimensional network are depicted in Fig. 2.4. $E = 0$ always corresponds to the highest occupied energy level.

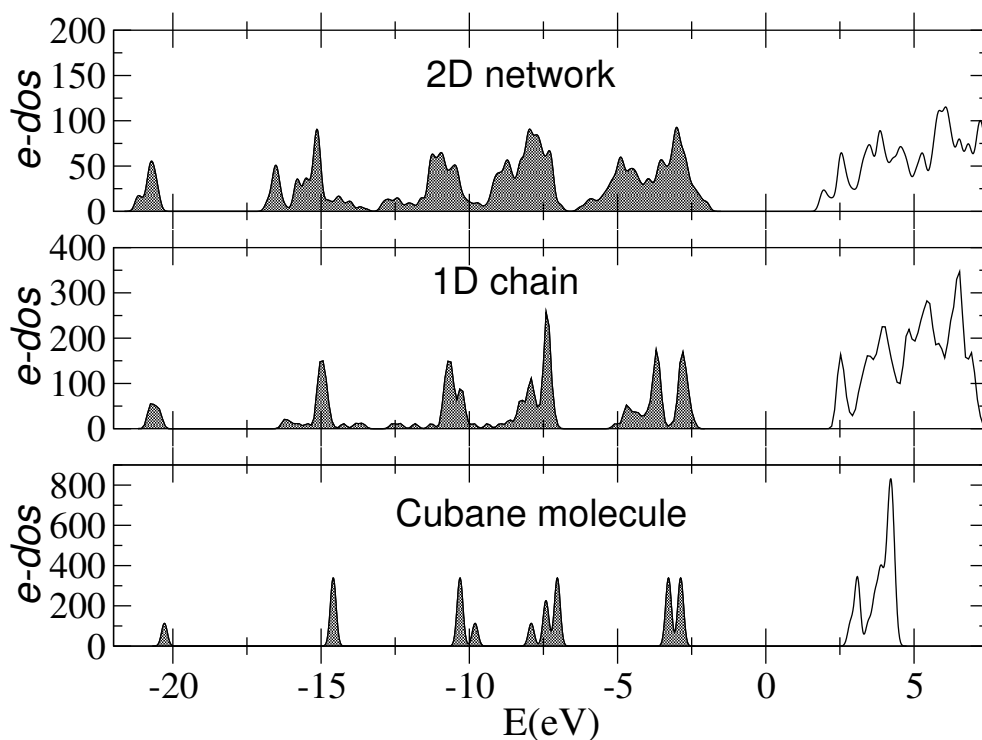


Figure 2.8: Electronic density of states for the cubane molecule (bottom), the cubyl chain (middle) and the cubyl 2D network (top). The zero level of energy is the Fermi level, defined to be in the middle of the gap. Shading indicates occupied states.

network we have an indirect gap and a larger dispersion at the Γ point for the first virtual electronic states. We find much more valence states available near the Fermi energy, which also increases the surrounding density of states (Fig. 2.8). Inclusion of dopants or functional groups within the chain and/or network could lead to semiconductor character, and even to metallic behavior, according to our calculations [61], as we will see below.

2.3 Building networks with cubane units: Finite size effects.

Perfect periodicity is only an approximation to treat a real problem with a large number of atoms. However this assumption, simplifies the problem both conceptually and computationally and often yields to qualitatively correct results. It is,

therefore, important to check the validity of this approximation for real oligomers. Within this context, we will focus now on effects arising from the finite size of cubyl-cubane chains.

Let us first consider the results summarized on Table 2.1, in which the geometry of various oligomers can be compared to that of the crystalline polymer. Most of the calculations reported for the oligomers were carried out by Barbara Herrera [59], at the Pontificia Universidad Catolica de Chile as part of our collaboration project. These calculations were performed using the hybrid B3LYP [62,63] functional and a Gaussian basis set (6-311G**) with the Gaussian 98 code [64]. It is remarkable that trends in the reported ladder-like oligomers coincide quite well with the infinite stair-like model described above, demonstrating that the geometry is already converging to that of an infinite crystal model even for a small number of monomers (the largest linear oligomer discussed in ref [59] has only 4 units). The same is true for the surface-like oligomers, although in those cases the convergence seems to be slower.

Now we focus on the electronic properties of the oligomers. Full DFT calculations for an increasing number of monomers are considerably expensive. In order to avoid these costly computations, we performed tight-binding calculations using the Pettifor parametrization for hydrocarbons [65]. This tight-binding approach allows us to treat a larger number of cubyl units retaining an adequate description of the electronic properties.

A series of hydrogen saturated oligomers was constructed, using the relaxed building block of the straight chain model. The evolution of the electronic densities of states (e-DOS) as the number of cubyl-cubane units increases is shown in Fig 2.9. The electronic properties reach the crystalline limit for oligomers comprising about five cubyl-cubane units. This rather small size lies well within the capabilities of the reported synthetic paths [17].

The calculations performed by Herrera [59] showed that the evolution of Electron Affinities (EA) and Ionization Potential (IP) with increasing oligomer sizes can be accurately fitted to power laws of the form [66]:

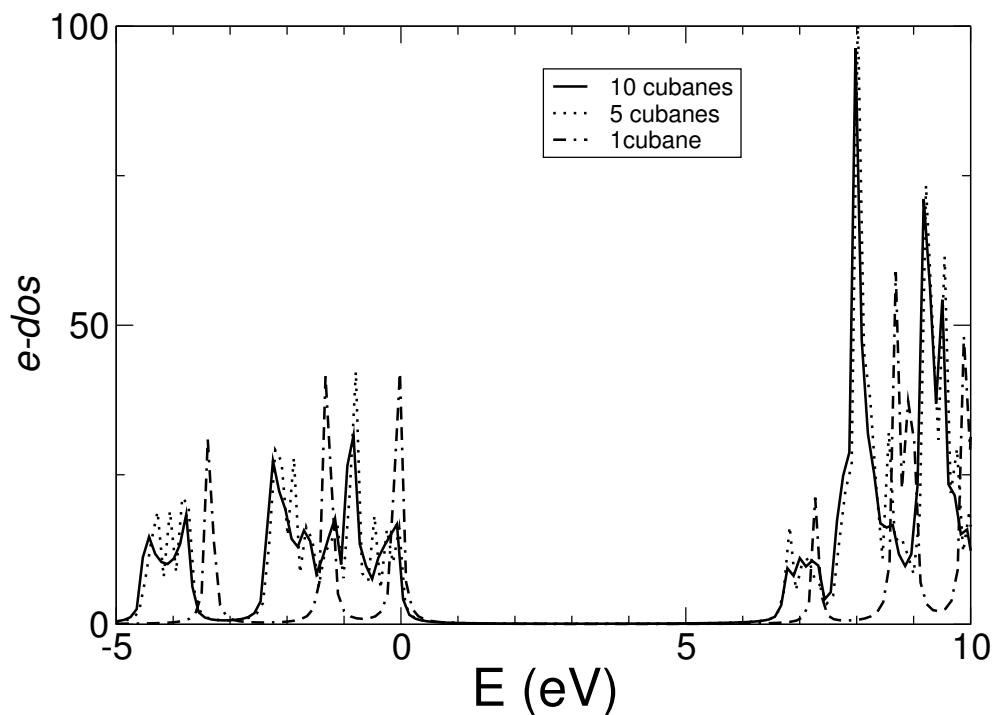


Figure 2.9: Electronic density of states ($e-dos$) for cubyl-cubane oligomers, calculated within a tight-binding approach. Continuous line: chain of 10 cubyl-cubane units; dotted line: 5 cubyl-cubane units; dashed line: one single cubane molecule. The small changes between the 5 and 10 units chains imply that these oligomers are rapidly approaching the 1D crystalline polymer behavior. The zero energy level is the highest occupied energy level in each case.

$$IP(n) = IP(\infty) + A_{IP}n^{-1/3} \quad (2.1)$$

and

$$EA(n) = EA(\infty) + A_{EA}n^{-1/3}, \quad (2.2)$$

where the constants A_{EA} and A_{IP} arise from the screening effects in these finite systems [66], The corresponding limiting values are $EA=0.03\text{eV}$ and $IP=4.58\text{ eV}$. Those values may be regarded as the limits of the corresponding properties for an infinite number of monomers (infinite polymer). Therefore it is relevant to compare these results with the corresponding values using our periodic models (the *infinite case* ionization potential must be compared with the system's Work Function (W)). In quantum chemical calculations with localized basis sets, as those reported in [59], the potentials can be calculated using the approximations:

$$EA = -E_{LUMO} \quad \text{and} \quad IP = -E_{HOMO}$$

In our plane waves calculations the Kohn-Sham potential (V_{KS}) does not vanish in vacuum and the energy associated with an isolated electron is given by a vacuum level

$$V_{vac} = V_{KS}(R \rightarrow \infty)$$

where R is the distance from the reference point to any atom in the system. Therefore, within the same approximations, we have

$$W = V_{vac} - E_{HOMO} \quad (2.3)$$

and

$$EA = V_{vac} - E_{LUMO} \quad (2.4)$$

The *farrest possible* distance to take as the vacuum level is half the distance between periodic images, i.e. half of the simulation cell parameter in the direction perpendicular to the growing plane (plane perpendicular to the growing axes) in the case of the 2D network (one dimensional chains). The vacuum level converges more

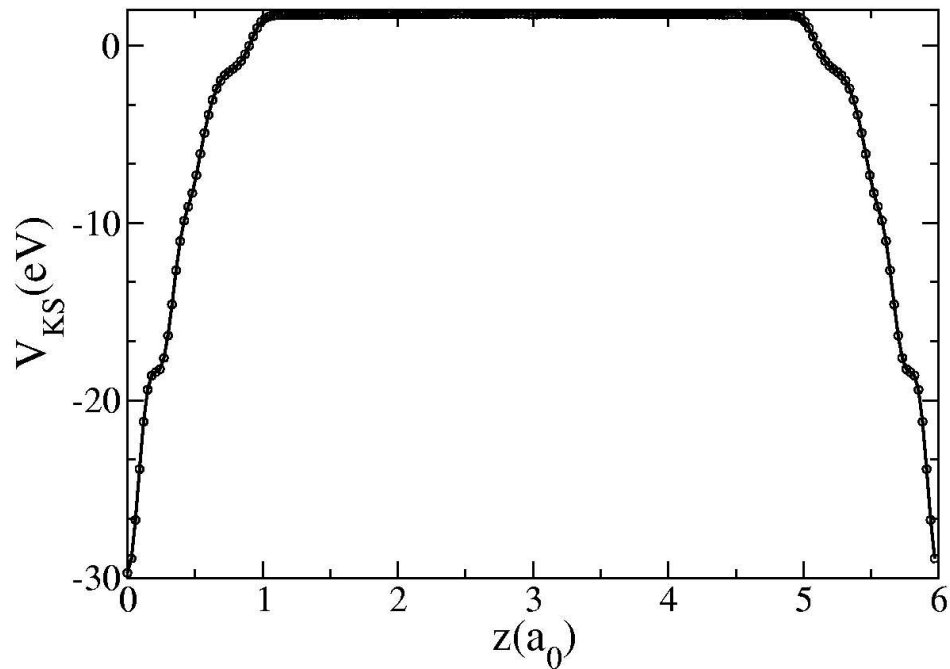


Figure 2.10: The planar average of the Kohn-Sham potential in the direction perpendicular to a 2D cubane network. The vacuum level is the value of this potential in the middle of the cell.

slowly with the empty simulation cell space than the geometries and band structures. We have performed self consistent calculations using the optimized geometries and larger empty spaces to obtain well converged values for V_{vac} . As shown in fig. 2.10 for the 2D network; a perpendicular distance of six times the a_0 cell parameter is enough to get well converged value.

Table 2.2 shows the results for these electronic properties. The band gap of the crystalline polymers, and HOMO-LUMO gap for the cubyl-cubane oligomers, are also reported in Table 2.2. The values correspond to our plane wave pseudopotentials calculations, and the Gaussian basis-set calculations performed by Herrera [59], respectively.

The first outstanding feature in Table 2.2 is the sensitive difference between the gaps calculated with the two methods, due to the well known deficiencies of DFT calculations to extract exact values for electronic band gaps. The Ionization Potential for the cubane molecule is clearly less sensitive to the actual model, because

	cubane(a)	cubane(b)	Inf. limit(b)	1D chain (a)	2D network(b)
EA(eV)	0.64	1.58	0.03	0.52	0.76
IP(eV)	6.07	6.84	4.58	5.30	4.74
Gap(eV)	5.43	8.44	4.59	4.87	3.78

Table 2.2: Comparison between the limiting values of the electronic properties reported in ref [59] and our corresponding crystal models. Label (a) stands for our plane waves calculations with the PW91 exchange-correlation. Label (b) stands for the B3LYP localized basis set calculations performed by Herrera [59]. Values for the isolated cubane molecule are also reported.

the interpretation of the exact DFT HOMO level as the Ionization Potential has a real physical basis. It is also clear that the band gap reduction between the isolated molecule and the infinite limit is quite more dramatical than the reduction obtained with the 1D and 2D models; the same being true for the changes in the remaining properties. Increasing the dimensionality in our crystalline polymer models (1D vs 2D) results in values closer to the infinite monomers limit. Therefore, it is very likely that the differences are not only due to the use of different DFT flavors; the infinite monomers limit may correspond to the properties of a 3D bulk material (e.g. the super-cubane structure [67]) rather than to a 1D or 2D polymer.

Until now we have considered only straight cubyl-cubane rods. Now we consider the effects related to bending of the above discussed cubyl-cubane oligomers. For this purpose, we have altered the finite chains by rotating each cubyl unit by an angle ϕ with respect to the previous one, preserving the cubyl geometries and intercage bond lengths. We have considered angles below 10° . Energetic and electronic properties of these altered chains were studied within the same tight-binding approach as in the previous step. In all these cases, the strain energy associated to this kind of bending increases quadratically with the bending angle ϕ , so that the associated elastic constants

$$K_{bend} = \frac{1}{2} \frac{d^2 E_{strain}^{cu}}{d\phi^2}$$

where E_{strain}^{cu} is the strain energy per cubyl-cubane unit, are always positive (see

the left part of Fig. 2.11). It is also interesting to notice that the electronic density of states is only slightly sensitive to the chain curvature, as seen on the right side of Fig 2.11. For larger bending angles, larger effects on the electronic properties may arise.

In summary, the calculated geometrical parameters and electronic properties converge rather fast as function of the oligomers size. Therefore, the perfect crystalline polymer model can provide a good description for real oligomers with realizable sizes.

2.4 Effects of functionalization on electronic properties.

In the previous section we have seen that a polymer formed by cubane molecules is an strong insulator with electronic band gap of about 83% of the HOMO-LUMO gap of the cubane molecule (4.5eV and 5.4 eV respectively). It was also demonstrated that the electronic properties of cubyl-cubane oligomers approach the infinite chain behavior within reasonable oligomers sizes (about five units). Therefore, properties predicted for perfectly periodic systems could be obtained in finite systems, and further calculations on long chains are not required.

Now we will explore the possibility of manipulating the electronic properties by doping the system. The electronic properties of the doped models are studied within the same DFT framework used for the pristine models.

First let us consider carbon based functional groups, particularly alkyne chains (ethyne and diethyne radical anions) and benzene rings (the radical anion benzyne). The selection of these functional groups was based on the following:

(i) Chemical paths leading to various ethyne-bridged oligomers and polymers have been reported [68–72].

(ii) Intercalation of alkyne spacers within the cubane framework, leading to an expanded cubane molecule, has also been realized [73].

(iii) The alkyne chains exhibit a triple bonded character and a *sp* hybridization. The mixing of this *sp* hybridized chains with the mostly *sp*³ cubyl units, can be

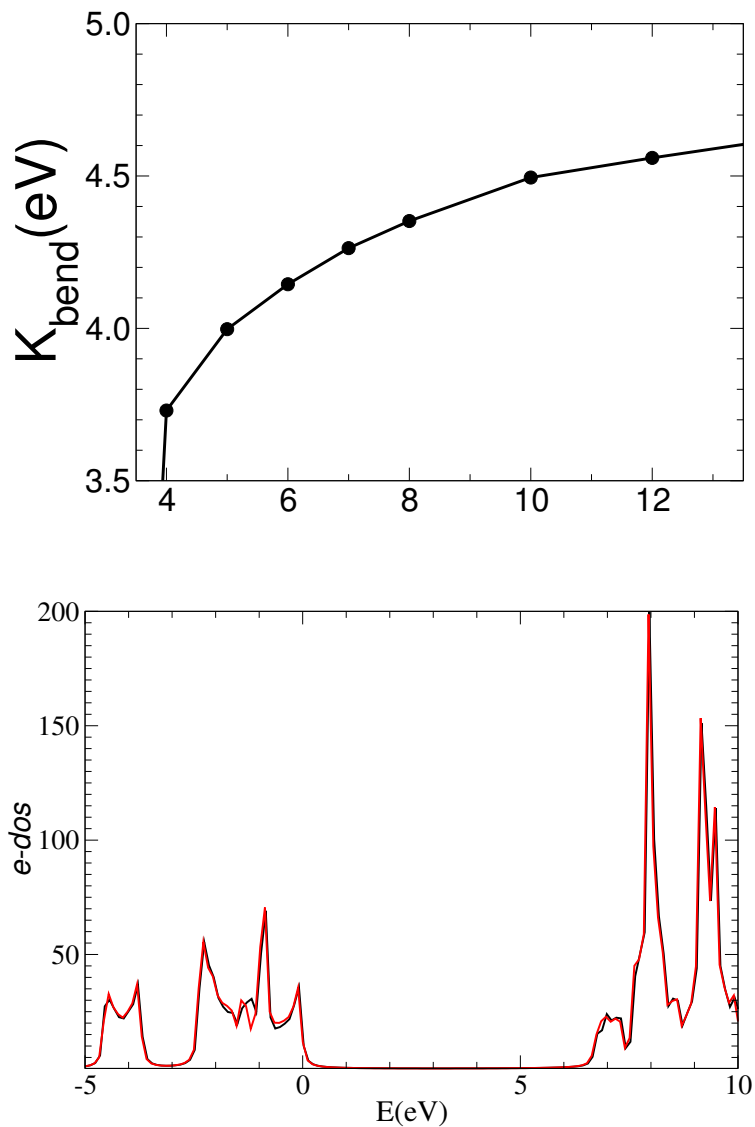


Figure 2.11: Effect of the chain deflection on the energy and electronic properties of cubyl-cubane oligomers. Upper panel: elastic stiffness against bending, as function of the number of cubane units. Lower panel: electronic density of states for a 14-units oligomer before and after bending; the black line corresponds to the straight rod, and the red line to a 10° bent rod.

expected to lead to sensitive changes in the e-dos and, specifically, to a decrease in the electronic band gap.

(iv) Iodine terminated cubyl-cubane dimers with benzyne intercalation (p-bis(4-iodocubyl)benzene) can be produced with high yields (about 70%) as part of the oligomerization reaction [17]. Iodine terminals are key factors in the polymerization process, therefore benzyne intercalated rods could be synthesized [17].

(v) Benzyne exhibits delocalized electronic states, a Π bonding character and a sp^2 hybridization. Therefore, benzene inclusions may help to the electronic delocalization in the system, resulting in the reduction of the band gap.

In order to check the validity of the stated suggestions regarding the electronic properties, we have constructed ethyne-, benzyne-, and diethyne-bridged models (Fig. 2.12). On these novel polymers, we have performed the geometrical relaxation procedure described in the previous section, and studied the corresponding electronic properties.

We are not going into the detailed description of the output geometries, they are only slightly distorted with respect to the cubyl chain configuration (Fig. 2.12). The most relevant geometrical parameters - v.gr., the lengths of the bonds between the cubyl-cubane cages and the linkers, the ethyne bond length, the benzyne ring bond length and the lattice parameters - are reported in table 2.3. These structures are also mechanically stable, at least under axial stresses, and from their corresponding E vs a_o curves it is possible to define an elastic constant just in the same way we did for the straight chain. The values of these constants are: 441eV ($a_o = 6.85 \text{ \AA}$) for one ethyl inclusion, 305eV for diethyne inclusion ($a_o = 9.41 \text{ \AA}$) and 225eV for the benzyne inclusion ($a_o = 8.58 \text{ \AA}$), meaning that it is harder to stretch these structures than the original straight chain. We believe that this increase in the stretching energy is due to the fact that the carbon-carbon bonds between the cubyl units and the included molecules are stronger than the original intercage bond. As a matter of fact, one can see in table 2.3 that in the structures containing one and two alkynated species the cubyl-alkyne C-C bond (performing 1.418 \AA and 1.412 \AA) is shorter than the corresponding intercage bond in the straight cubyl chain. For benzyne, this distance is a little larger (1.481 \AA) but the rigidity of the benzyne

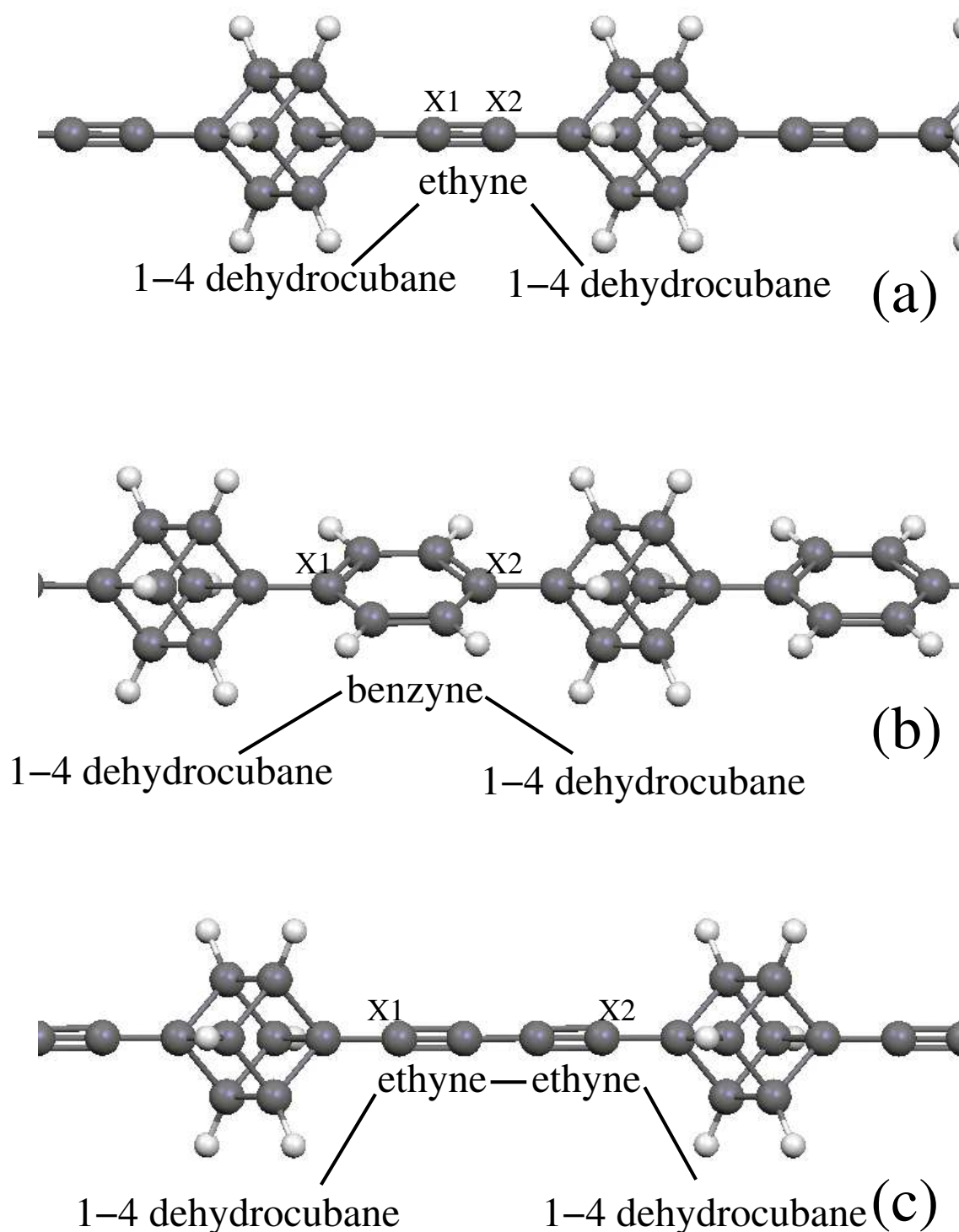


Figure 2.12: Cubyl-cubane chains bridged by: (a) Ethyne, (b) Benzyne, and (c) diethyne radical groups. The reference points X1 and X2 signaling the extremes of the radical groups are shown in each case.

Doping	Cub-X1 [Å]	Cub-X2 [Å]	X12 [Å]	Alat [Å]	bW [eV]	K(eV)
C ₂	1.418	1.418	1.227	6.85	0.43	441
2-C ₂	1.412	1.412	1.232	9.41	0.33	305
benzyne	1.481	1.481	1.406	8.59	0.38	225
N ₂	1.413	1.413	1.268	6.22	0.11	246
NO	1.372	1.404	1.416	6.12	0.055	180
NS	1.391	1.751	1.644	6.62	0.048	158

Table 2.3: Distances and energetics of the lowest polymer unit cells considered in this work. X1 denotes the first atom on the linker group and X2 the last one (Fig. 2.12). X12 is a relevant length of the linker group: the ethyne bond length, the bond length in the benzyne ring, the N-N, N-O, and N-S distances respectively. bW corresponds to the valence bandwidth. The elastic constant $K = \frac{d^2 E}{d\zeta^2}$ where $\zeta = a/a_0$ is the deformation along the chain axis.

bonds (performing 1.406 Å) lengths, contributes to the overall strength.

Therefore, the inclusion of this hydrocarbon groups does not compromise the mechanical strength of the cubyl chains. We now focus on the electronic properties. Figure 2.13 depicts the band dispersion and electronic densities of states of these model polymers. The effects of doping can be stated from the comparison between these doped chains and the pristine model (figures 2.8 and 2.7). The lower states remain almost unchanged, preserving their molecular (almost no dispersion) character. The dispersive occupied states are also very similar to their counterparts in the straight chain. A clear gap reduction occurs with the inclusion of alkyne chains and benzyne, this reduction arises from the presence of little dispersive states within the straight chain gap, near the top of the valence band and the bottom of the conduction band. Inclusion of alkenes and benzyne does not modify the molecular character of the band structure. Most of the modifications in this aspect are related to the formation of a 1-D solid.

Electronic band gaps are still large: over 3.37 eV, and we must recall that our model underestimates the diamond band gap which is about 4.1 eV in the same

theory level. The widths of the valence bands are rather small (around 0.4eV). These model polymers, thus, perform large effective masses. Indeed, the effective masses measured at the top of the valence band are $-1.49m_e$, $-1.22m_e$ and $-1.12 m_e$ for ethyne- benzyne- and diethyne- bridged polymers, respectively.

Now let us see how the same kind of doping operates in the two dimensional chains. We have excluded the benzyne molecule, because it does not seem to perform better than the simple alkyne chains and requires more computational effort. The intercalation of alkyne chains results in a rather significant decrease of the band gap, again related to the presence of intermediate states, but now those states exhibit a significant band dispersion. The systems can be regarded as a real semiconductor with an indirect (Γ to L) band gap (Fig. 2.14). Note that a typical measure for the Hubbard contribution to the e-e interaction is the width of the valence band; therefore the increase in the electronic dispersion should be reflected in an increase of the e-e interaction.

Concerning the mechanical stability, it is again possible to define elastic constants from the Energy *vs.* area curves, performing $K' = 106$ eV for ethyne inclusions and $K' = 170$ eV for diethyne. The trends in the elastic properties are, thus, similar as those shown by the one dimensional chains.

An step forward consist in the introduction of different electronically rich systems. In this context, we have considered doping with nitril groups (N_2), oxynitril (NO) and sulfunitril (NS). Cubane molecules with hydrogen substituted by nitrogen rich groups have been synthesized [16] and, thus, chemical reaction paths leading to nitril bridged polymeric chains may be available in the near future. Optimization of the models proceeds in the same way that for the other structures. In order to fulfill our energy convergence criteria, stated at the beginning of this section, we have used kinetic energy cutoffs of 30 Ry for NO 34Ry for NS, and 10 special k-points in the 1D-Brillouin zone.

For one dimensional cases, this doping procedure still produces mechanically stable models. The inclusion of N_2 produces only minor changes to the cubyl geometry, similar to the hydrocarbon molecules cases. For NO and NS groups, the cubyl unit is strongly pulled by the doping group. As consequence of this pulling, some of the

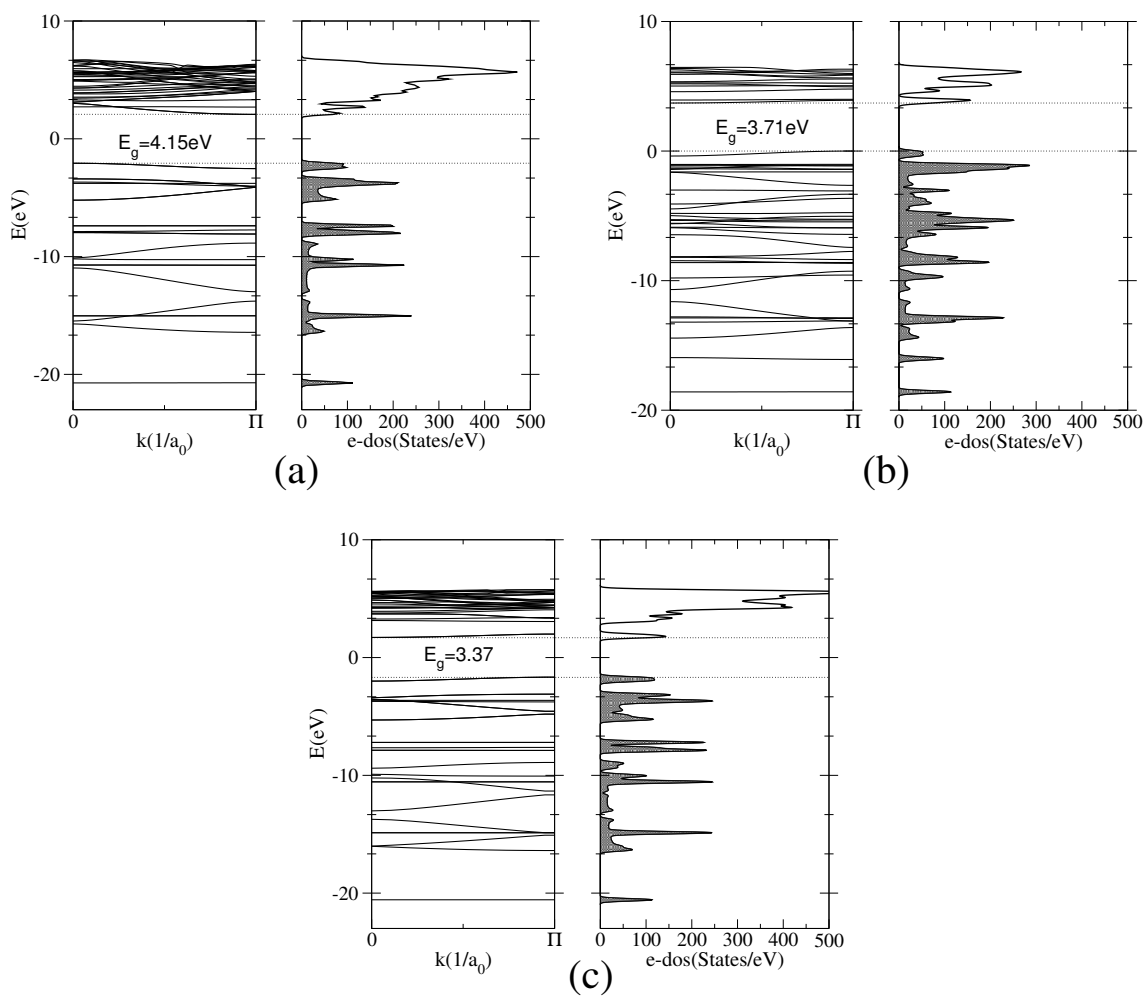


Figure 2.13: Electronic properties (left: band structures, and right: e-dos) for poly-cubanes with hydrocarbon molecules as dopants. (a) Ethyne-bridged polymers, (b) benzyne-bridged polymers and (c) diethyne-bridged polymers. The Fermi level is located $E = 0$. Occupied states are shadowed in the e-dos.

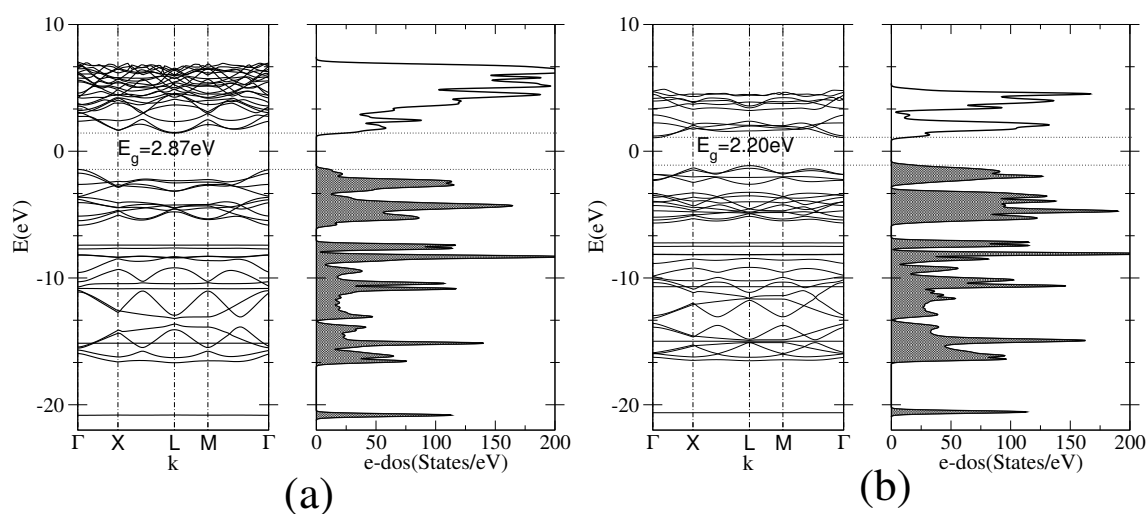


Figure 2.14: Electronic properties (left:band structures, and right:e-dos) for poly-cubane networks with alkyne molecules as dopants. (a) is for the ethyne bridged network , (b) for diethyne bridging.

cubyl-cage bonds get elongated. Polymers bridged with NO exhibit C-C bonds as large as 1.62 Å in the cubyl-cubane cages. Similarly, for NS doping, bonds up to 1.61 Å length are present. The average bond length is always very close to 1.573 Å (fluctuations around 0.05Å), which is similar to the value for the cubane molecule, and to the average value in the straight chains. Again, the most relevant geometrical parameters can be found in Table 2.3 (some others are reported in figure 2.15).

For nitrogen containing dopants, the polymer main axis is no longer aligned with the cubyl-cubane diagonal (Fig 2.15), as it was the case for ethyne and benzyne bridging (Fig 2.12). The angles between the growth axis and the cubane diagonal are 5.1°, for N_2 , 7.5°, for NS, and 8.4° for NO linkers. The respective lattice parameters reflect the linear addition of the bridging groups, as in the case of alkyne inclusions.

Nitrogen contains lone-pair electrons which are good electron donors, so one could expect it to provide useful chemical and electronic properties. As a matter of fact, and as can be seen from figures 2.16 and 2.17, the modifications in the band structure and density of states lead by the N_2 inclusion are quite more significant than those lead by the C_2 doping. There is a noticeable broadening of the e-dos near the HOMO level, and also a very well defined peak in the conduction region

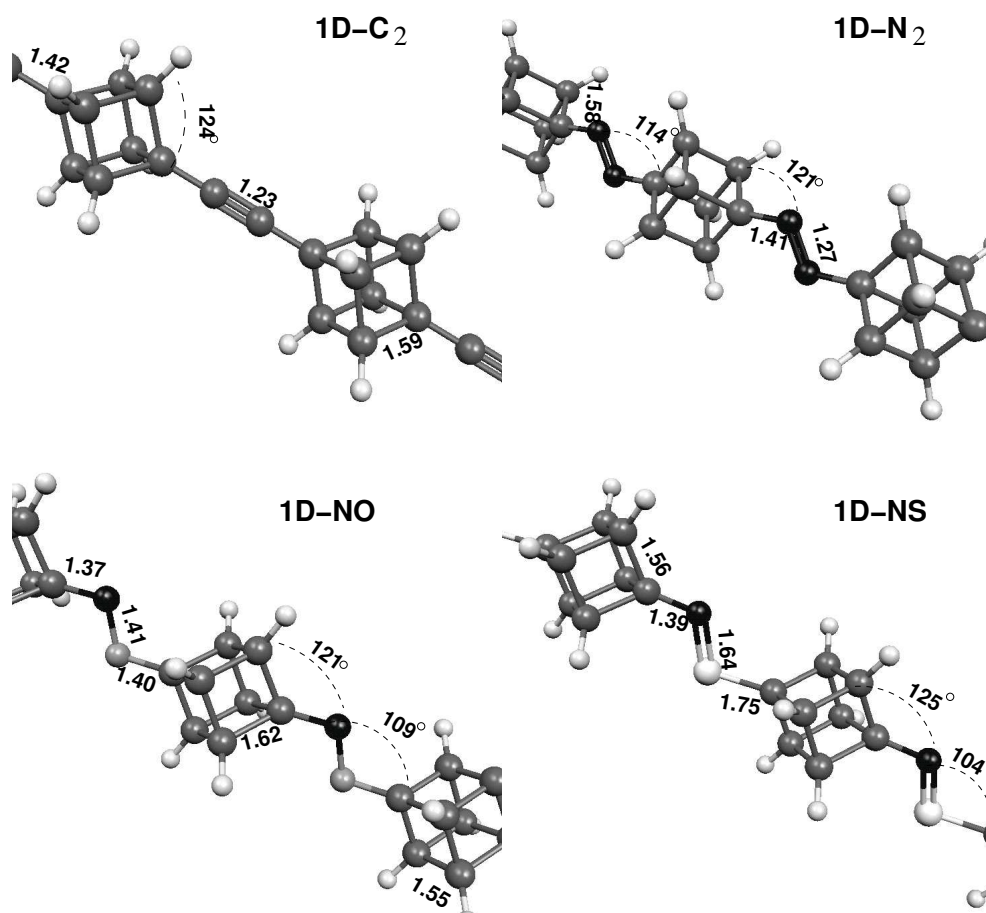


Figure 2.15: Molecular models of polycubanes containing C₂, N₂, NO and NS molecules as dopants. Black spheres represent Nitrogen atoms, pale gray and light gray spheres represent Oxygen and Sulphur atoms, respectively.

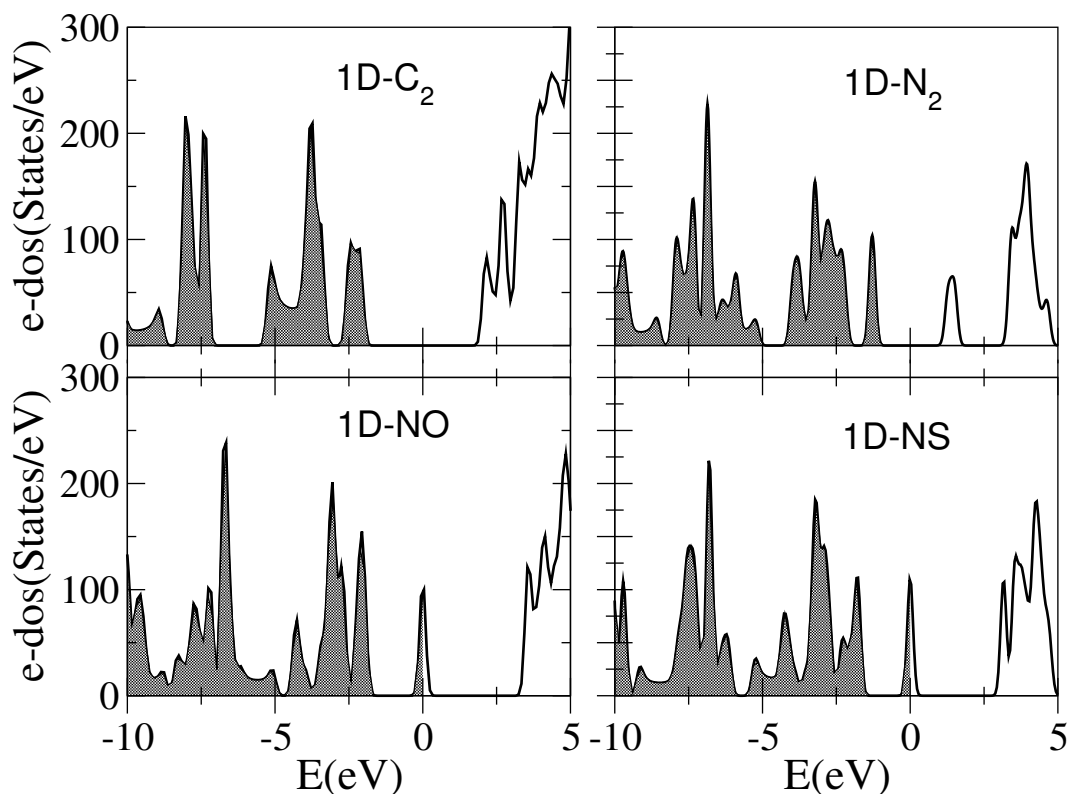


Figure 2.16: Electronic density of states of polycubanes with C_2 , N_2 , NO and NS molecules as dopants. The Fermi Level is at $E = 0$. Occupied states are shadowed.

which helps closing the band gap. The latter reaches now 2.43eV. However, the effective masses in both the valence and the first conduction region are very large: $-6.99m_e$ and $2.62m_e$ respectively (calculated at the top of the valence band, and at the bottom of the first conduction band). N_2 doped polycubanes would exhibit semiconductor behavior. The observed splitting of the valence band may show relevant in the electron-phonon interaction. Although the elastic constant for the N_2 bridged polymer is a slightly smaller, when compared to the alkyne case, is still very strong.

The polymers resulting from doping with NO and NS are gap-less. The conduction band is half-filled, as depicted in Figs. 2.16 2.17. Very little dispersion is observed in the conduction band, consequently, effective masses are even larger than for the remaining models ($17.2m_e$ for NS and $16.38m_e$ for NO). The appearance of a non-symmetric group helps the formation of a conjugated polymer with metallic

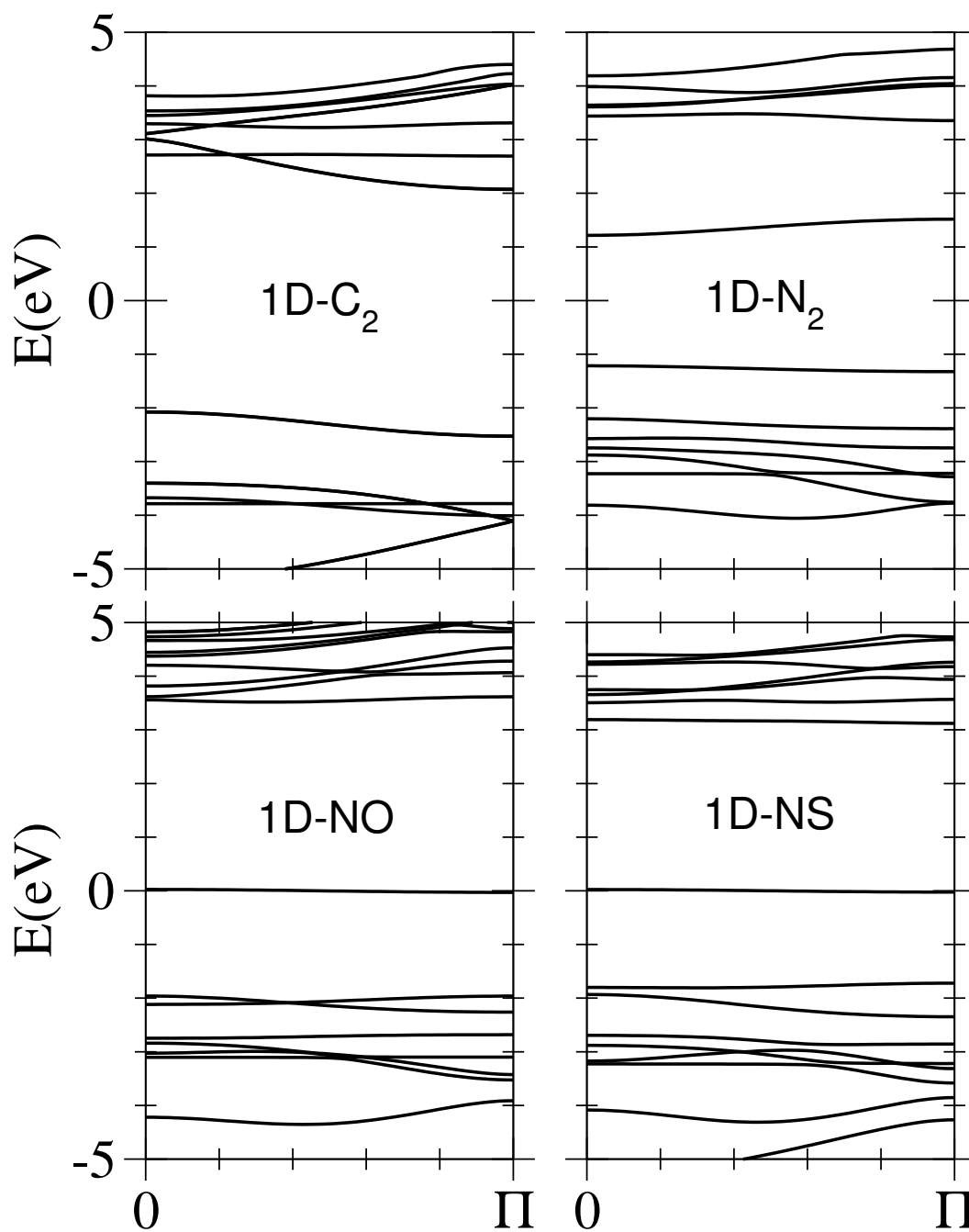
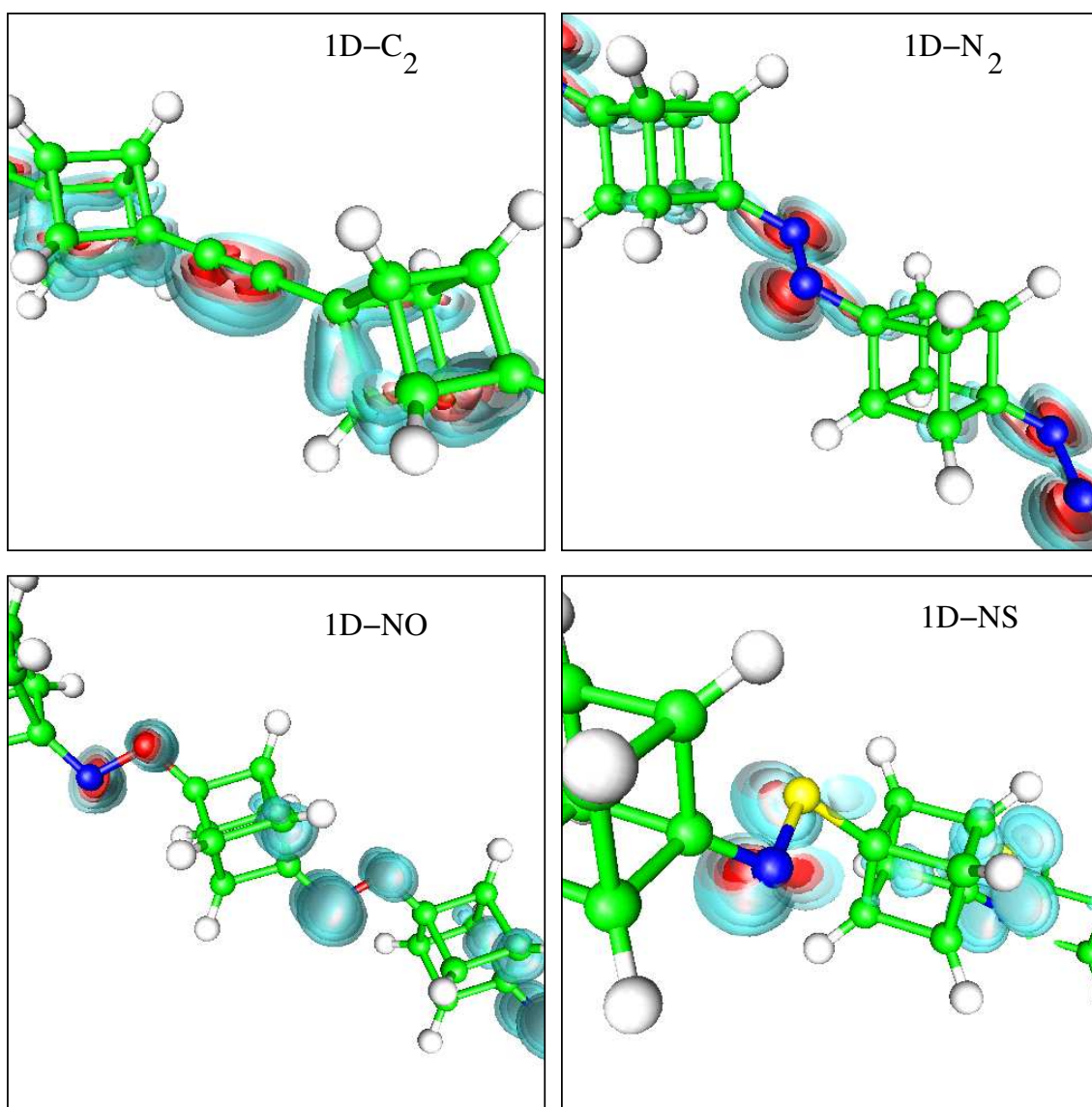


Figure 2.17: Band structure of polycubanes with C_2 , N_2 , NO and NS molecules as dopants.

properties. A synthesized NS chain polymer was the first metallic polymer reported in the literature [74] with alternate bonding and with unequal bond lengths. This feature is also present in the polycubanes with NS and NO doping. The elastic constants for NS and NO containing polycubanes are smaller than in the remaining models.

The electronic properties can be better characterized by looking at the last occupied Kohn-Sham state (HOMO) as shown in Fig 2.18. The behavior on every system is rather different. In the case of C₂, the appearance of π bonding is dominating this state; the charge is shared between the ethyne bonding and the α positioned bonds. N₂, NO and NS doped polymers exhibit very localized orbitals centered on the included functional group, providing more electronic density to the atoms joining the cubanes. When electrons get excited, they occupy the LUMO orbital (the case of N₂ and C₂ doping), or get promoted to the second conduction band (the case of NO and NS) represented in Fig 2.19. As it was the case for the HOMO orbital, the behavior is rather different depending on the doping. For C₂ enriched polycubanes, the charge is localized around the π bond formed by the ethyne group, but also in the center of the cubane. This is a rather particular feature that we did not find in any other polycubane. This behavior indicates a very delocalized state on the whole chain, and can be related to the e-dos depicted on Fig. 2.16. As a matter of fact, C₂ enriched polycubane displays a wide conduction band, corresponding to more dispersive and delocalized states. For N₂, the charge is again localized on the nitril group, which is an indication of the localization given by the N₂ bonding. In the case of NO and NS, there are contributions arising from the localization on the dopants and on the cubane, which is an indication of its metallic behavior. Charge delocalization in this second conduction band is clearly observed in NO enriched cubanes, meanwhile the first state in the second conduction band of NS enriched cubanes is still very localized, a feature that is also observable from the e-dos.

In order to have a measure of the charge distribution in the cubyl chains and, then, a better understanding of the bond character, we have calculated the Lowdin charges, which are reported in table 2.4. For the sake of comparison, charges for the pristine chain are also reported in the table. We have subtracted the nominal

Figure 2.18: HOMO of polycubanes with C₂, N₂, NO and NS molecules as dopants

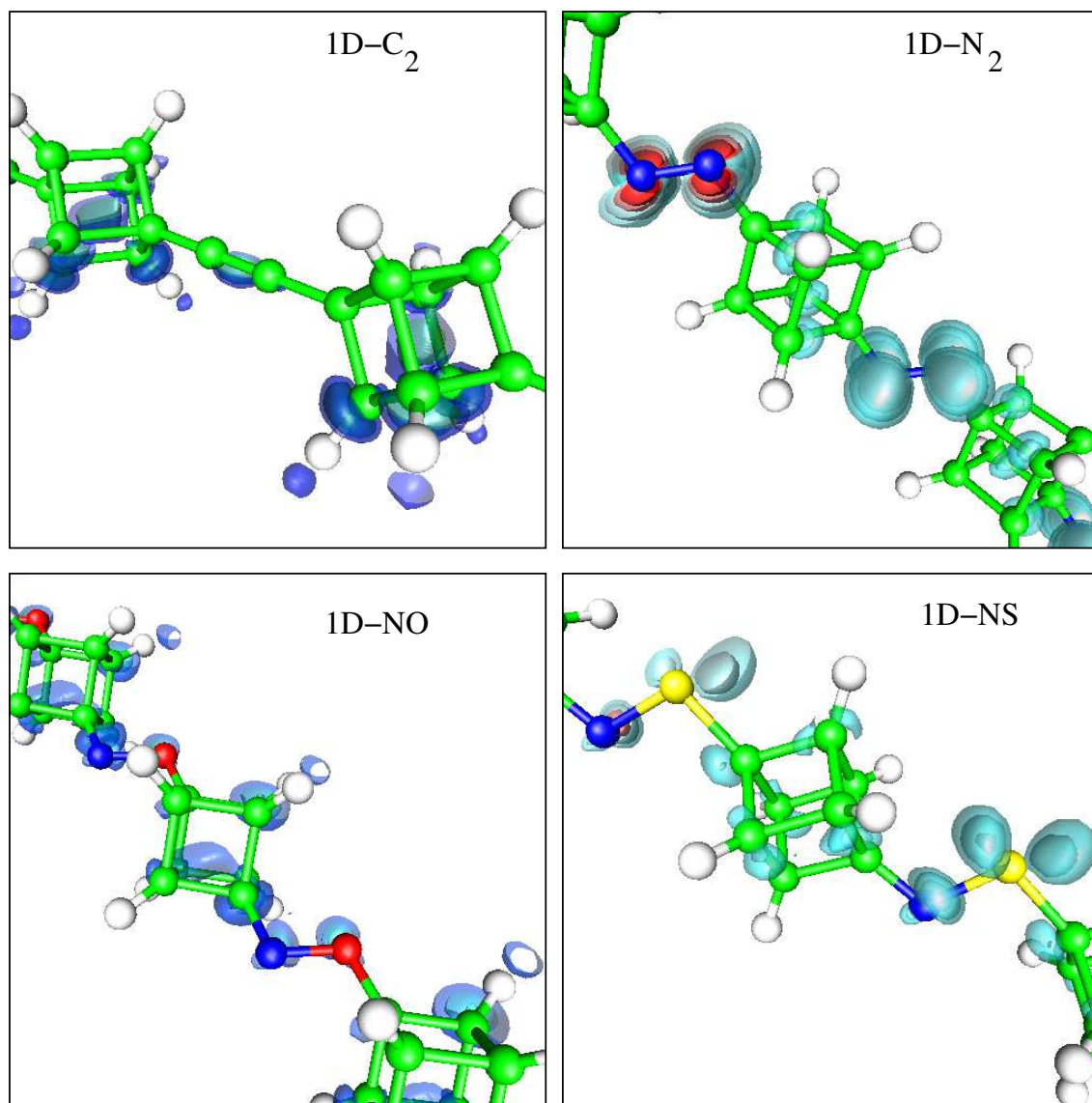


Figure 2.19: LUMO of polycubanes with C₂ and N₂ molecules as dopants, and the first state of the second conduction band for the case of NO and NS molecules.

X1X2	C1	C4	C _{out} ¹	C _{out} ²	C _{in} ¹	C _{in} ²	X1	X2	H _{out} ¹	H _{out} ²	H _{in} ¹	H _{in} ²
...	-0.059	-0.059	0.133	0.133	0.133	0.133	-0.182	-0.182	-0.182	-0.182
CC	-0.047	-0.047	0.112	0.112	0.112	0.112	0.024	0.024	-0.197	-0.197	-0.197	-0.197
N ₂	-0.176	-0.175	0.113	0.113	0.151	0.151	0.085	0.085	-0.198	-0.198	-0.203	-0.203
NO	-0.256	-0.176	0.127	0.139	0.109	0.129	0.141	0.139	-0.202	-0.205	-0.201	-0.200
NS	0.062	-0.169	0.142	0.119	0.117	0.118	0.449	-0.545	-0.198	-0.203	-0.200	-0.194

Table 2.4: Electronic Lowdin charges for different atoms in the cubyl chains unit cells, and the corresponding spilling parameter for the partial charge decomposition. C1 and C4 are the cube diagonals in the growth direction with C1 bonded to X2 and C4 to X1. The subindexes *in* and *out* refer to the position of the atoms in or out the plane defined by the C-X1-X2 bonds, if this plane is defined at all (N₂, NO and NS doping), the superindexes 1 and 2 signals whether those atoms are closer to X1 or to X2.

valence, so that the data shown in table 2.4 must be read as the fraction of electrons gained or lost by each atom. According to the corresponding spilling parameters, the Lowdin projections account for roughly the 99% of the total electronic charge and, thus, the reported electron fraction gains and losses are reasonable.

In every case, charge is transferred from the H atoms to *p* – *like* states in their neighboring C atoms. The *s* – *like* to *p* – *like* charge ratios in the carbon atoms remain close to 1/3, indicating *sp*³ hybridization. The C-C, N-N and N-O bonds in the doping groups are mainly covalently attached, with little charge being transferred from one atom to the other. For the N-S bond a significant amount of charge goes from the S to the N atom. The C_{cage}-C_{ethyne} bond exhibits a slight charge transfer from the cage to the ethyne group. This charge transfer between the cage atoms and the attached functional groups is more significant when N and O are included, whereas S donates a slight amount of charge to the bonded C atom.

Visualization of the above bonding mechanism can also be achieved using the electron localization function (ELF). ELF is a measure of the probability to find an electron with the same spin in the neighborhood of a given electron, it is defined so that its value is 0.5 when electrons are completely delocalized [76]. In figure 2.20, a

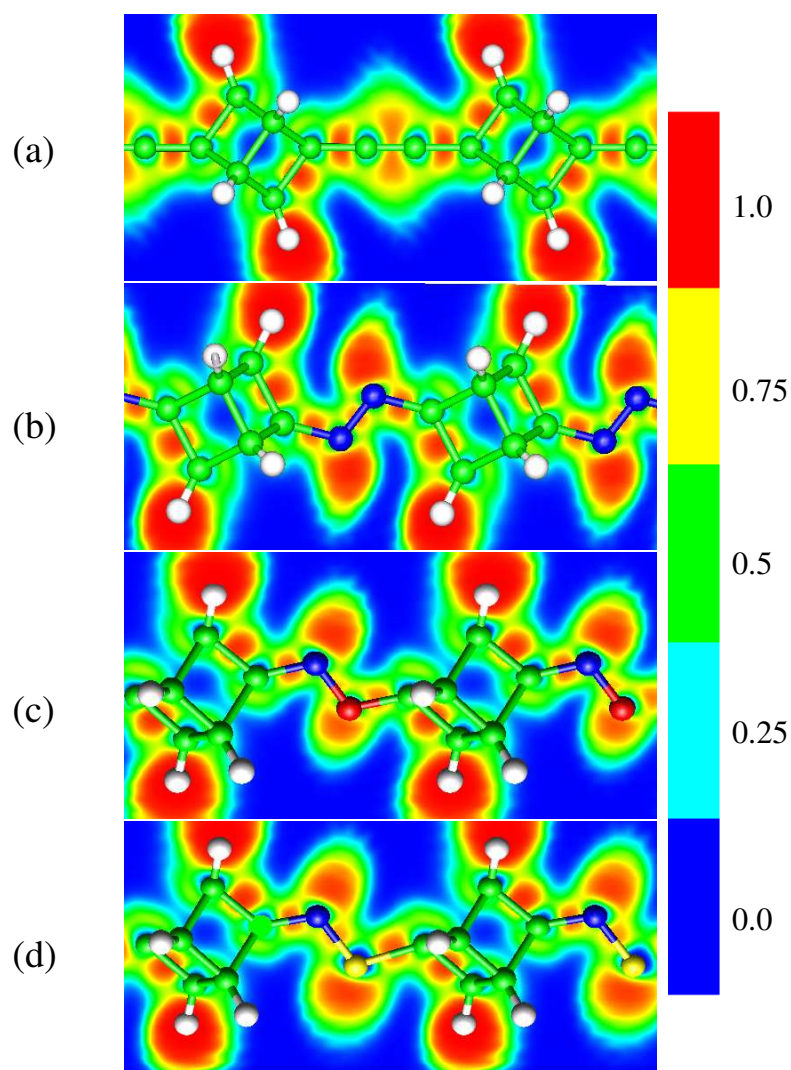


Figure 2.20: ELF for polycubanes with C₂ (a), N₂ (b), NO (c) and NS (d) molecules as dopants.

contour plot for the ELF of these species is expressed, projected in the plane of the bond between the cubyl unit and the dopant molecules⁴.

Cubyl networks, on their own, cannot stand the pulling force driven by the dopants containing nitrogen. One of the cube sides is opened and the cubic geometry collapses.

⁴ELF calculations were performed using Martin Troulliers pseudopotentials [77] with a BLYP hybrid functional which is usually considered a good one for describing bond topologies. A kinetic energy cutoff of 60Ry was used.

In summary: It would be possible to manipulate the electronic properties of polymeric cubyl chains and networks by the introduction of dopant molecules. As a matter of fact, cubyl polymers seem to provide a rather stable frame for the inclusion of a wide variety of molecules: alkynes, benzyne, nitril, oxynitril and sulfonytril. These doped systems preserve the mechanical stability of the chain, which is mainly provided by the mechanical strength of the cubyl unit and the formation of covalent bonds with Nitrogen, Sulphur and Oxygen atoms. These models exhibit small band dispersions both in the valence and conduction bands, and perhaps they could exhibit unusual electron-phonon coupling interactions. In particular, electron-phonon interaction could be enhanced by the splitting of the valence band observed for doped chains.

Chapter 3

Crystalline models for nanoporous carbons, pure carbon and doped structures.

While I nodded, nearly napping, suddenly there came a tapping,

The Raven, E. A. Poe

3.1 The world of nanoporous carbons.

The production and characterization of porous forms of carbon have been, for quite a long time now, active fields of research, mainly in due to their applications as active filters and gas storage devices [78–82]. While traditional porous carbons exhibit rather disordered pore structures, the recent implementation of template techniques for the fabrication of nanostructured materials [78, 79, 83] brought a new perspective to the field. Carbonization of various precursors impregnated in ordered porous frameworks, allows for the synthesis of nanoporous carbons with a periodic pore structure [36, 78–82, 88, 89, 106]. These novel materials are very good candidates for the fabrication of electrochemical double layer capacitors (EDLCs), hydrogen storage devices, and electro-catalytic components [36, 78–82, 88, 89, 106]. Therefore, ordered nanoporous carbons are particularly appealing for digital communication devices and fuel-cell technologies.

Zeolites (crystalline aluminosilicate materials with pore sizes ranging from 3 Å to 13 Å) and mesoporous silicates (amorphous solids with ordered pore structures) have been used as templates. Ordered mesoporous silicates are available using liquid crystals as templates [93]. It is shown that the pore sizes, and pore topology, of the resulting carbon products could be controlled. The zeolite and silicates can be removed using hydrofluoric acid (HF); thus leaving the carbon network intact [36]. After removal of the template material, two different behaviors have been observed: some materials retain the structure achieved during the templated carbonization step, and others develop internal structural transformations [36, 78–82, 88, 89]. In each case, the final result is a thermally and mechanically stable carbon material with periodically arranged pores. Possible modifications induced on carbon networks by zeolite frameworks have also been discussed in the literature [92].

Carbonization of carbon-coated crystalline frameworks (zeolites) is a promising method for the synthesis of novel periodic graphitic systems comprising of sp^2 hybridized atoms. Terasaki's *et. al.* work on carbon coated Zeolite “Y” [36], demonstrated the lack of evidence for graphitic planes after thermal annealing at 900K, and strong evidence of sp^2 bond hybridization in the solid state NMR spectra. These results support the idea that ordered aromatic rings, arranged on curved surfaces, conform this particular nanoporous carbon [36]. Another synthetic route, comprising the Chemical Vapor Deposition (CVD) of carbon nanostructures, has also shown evidence of 3D connected sp^2 hybridized networks with a rather disordered structure [35]. The complete characterization of these materials is still needed.

In an attempt to elucidate the actual structure and physical properties of nano and microporous carbons, theoretical investigations are required. Here we attempt the comprehensive characterization of various negatively-curved carbon crystals, with cubic unit cells. Mechanical and electronic properties of these models are discussed. The results obtained for these crystalline models, could give insights on the properties of ordered nanoporous carbons with very small pore diameters, as those reported in references [36], [35]¹.

¹For mesoporous carbons, which are more probably build from amorphous carbons and several graphitic layers, other theoretical approaches have been already reported in the literature [96]

Elastic constants, which provide valuable information about mechanical stability, electronic and vibrational densities of states (DOS) have been calculated for these carbon systems. Optical spectroscopy studies, such as Electron Energy Loss Spectroscopy (EELS), can also be very useful and we have calculated them using a Tight-Binding and RPA approach. We also report on the thermodynamical properties calculated from the vibrational-DOS. It is important to stress out that, besides the curvature of the system, proper relaxation of the structures is essential for obtaining an adequate description of the electronic properties.

Due to the large amount of atoms per unit cell in the studied structures, most of our results are obtained using the tight-binding method. But whenever we found necessary to confirm our conclusions - and it was computationally feasible - plane wave Density Functional Theory (DFT) calculations in both the Local Density Approximation (LDA) and Generalized Gradient Approximation (GGA) were also performed using the PWSCF package [97] and the CASTEP package [98].

The systems that will be described in detail in the next section, can be regarded both as models for explaining nanoporous carbons found experimentally, or as novel structures that await to be synthesized. We also attempt to generate information on the specific surface area of these structures (the utmost important quantity for gas storage devices), and on the effects of doping with Boron and Nitrogen.

3.2 The Schwarzite models.

The fascinating catalytic and electronic properties of carbon nanotubes, fullerenes, and other carbon nanostructures exhibiting sp^2 hybridization, have been recognized since the early 90's. These properties are different from those observed for the *mother* graphite structure. The presence of five-membered rings plays an important role in the onset of these differences. Still, even nanotubes without pentagonal rings exhibit a rich chemical and physical behavior that arises from their curvature. The C-C bond in a graphene layer is one of the strongest bonds in nature (that is why carbon nanotubes possess extremely high Young moduli), but graphite, nanotube bundles and fullerene crystals are, mostly, bound by weak van der Waals forces.

In this context, one may ask: Would it be possible to construct a 3D arrangement of covalently bound carbon atoms with the same properties as nanotubes?. Such structure would be mechanically resilient upon tension and shear stresses. Along this line of thought, Mackay and Terrones [25–27] showed, in 1991 and followed by many other authors [29–31], that it is indeed possible to construct triply periodic carbon structures using sp^2 hybridized networks. The requisite is to decorate, using carbon atoms, negatively-curved surfaces (i.e. surfaces where the the principal Gaussian curvatures have opposite signs). Initially, they used the concept of minimal surfaces, studied by the great mathematician H. A. Schwarz in the XIX century, and named them *Schwarzite Structures*. In order to decorate such surfaces, the introduction of heptagonal and octagonal carbon rings is needed.

Schwarzite structures (or just Schwarzites) are ordered nanoporous and crystalline systems, similar to a zeolite structure. They exhibit complex pore structures, and one of the earliest models was dubbed *the plumber's nightmare*.

For a full review of the notation employed, interested readers are referred to the original references [25–27, 29–31], specially, see [99] and [100–102]. The crystallographic and geometrical description of these surfaces can be regarded as a whole new field, termed *flexocrystallography*. The pores in Schwarzite structures can be arranged in a diamond like architecture: hence they are called **D** structures. If the pores are arranged in a Gyroid fashion, they are referred as **G** structures. When the pores form a primitive cubic structure, they are referred as **P** structures [25, 99].

The D, G, and P, Triply Periodic Minimal Surfaces (TPMS) divide the space in two equivalent subspaces, and for this reason they are referred as balanced (**BAL**) structures. When these TPMS are decorated with carbon atoms, they generate the **D8BAL**, **G8BAL**, **P8BAL** and **NP8BAL** structures; the prefix **N** stands for *New* and is used to distinguish between the two different P balanced systems.

There are periodic graphitic structures in which each carbon atom is shared by two octagons and one hexagon (vertices type **688**), thus generating the following crystals: **D688**, **G688** and **P688**. Similarly, Schwarzites in which each atom is shared by two hexagons and one heptagon are referred as **766** structures; from this family we have studied the **D766** structure.

Finally, it is also possible to build up periodic surfaces which are parallel (**PAR**) to a balanced one and, therefore, divide the space into two inequivalent subspaces; decoration of these surfaces with carbon, requires the introduction of heptagonal rings, originating the **D7PAR**, **G7PAR**, **P7PAR** and **NP7PAR** systems . Figures 3.1 and 3.2 depict these eleven Schwarzite crystals.

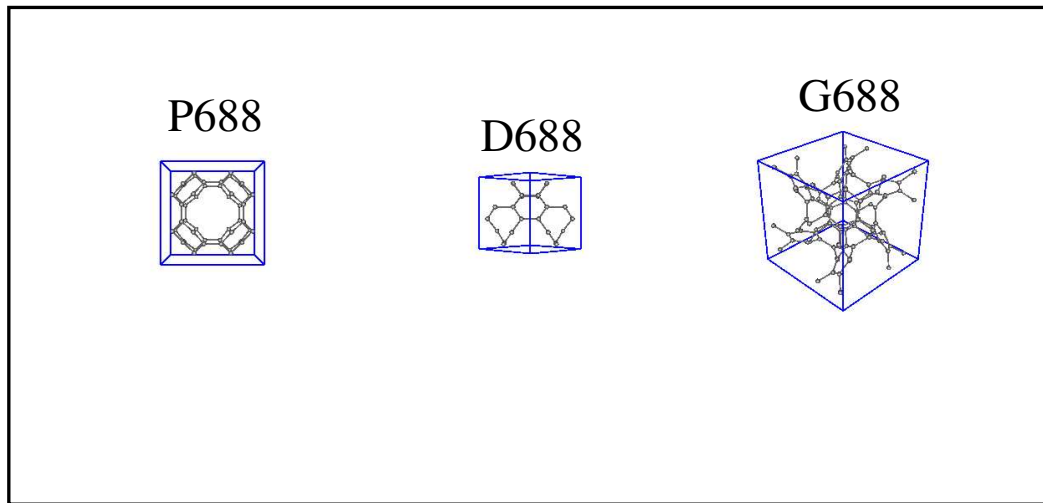
Previous theoretical work on Schwarzites have demonstrated that they may be stable under experimental conditions, this fact, together with the interconnected channel structure that can be obtained, lead us to believe that they are excellent candidates, for ordered microporous carbons in which the pore diameters are really small ($<8 \text{ \AA}$).

Schwarzites are not only interesting as models for nanoporous carbons, they may also be of technological advantage. However, from the theoretical stand point, the interplay between global curvature and the existence of high-membered rings is still an open question.

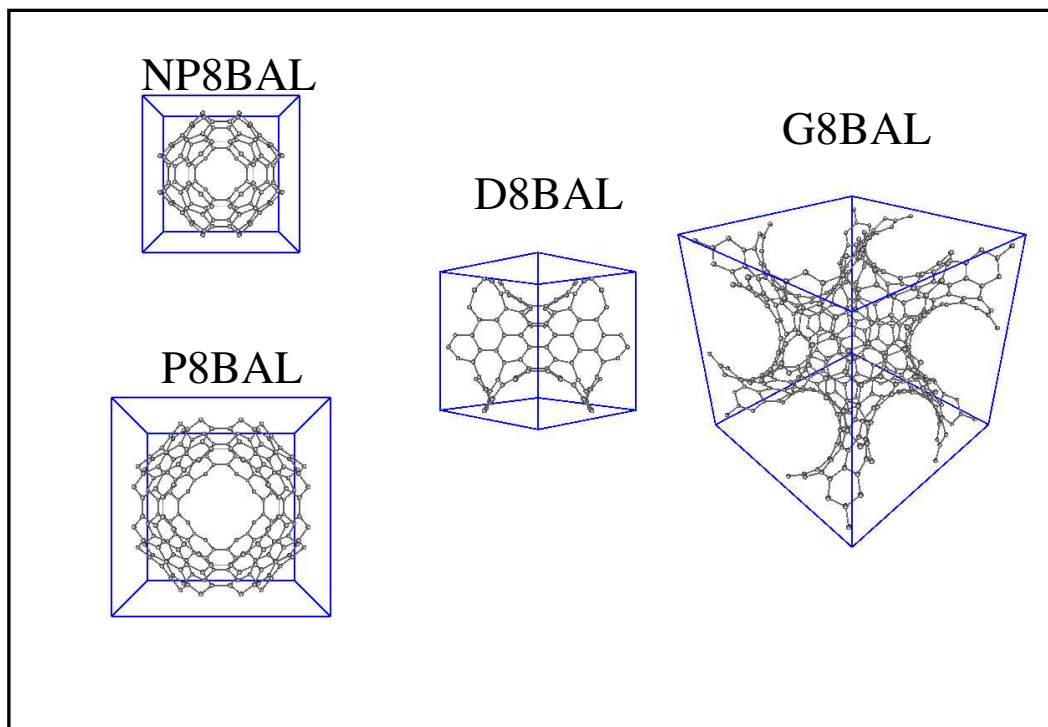
To summarize this section, let us quote Milani's work [35]: *“These carbon sponges should also be good candidates for the investigation of negatively curved carbon networks and, in particular, of the long sought topological structure of random Schwarzites”*. We will only add that if random Schwarzites are interesting, crystalline Schwarzites may be even more interesting.

3.3 Structure and energetics.

First of all, we determined the equilibrium structures by relaxing the lattice constant and the atomic coordinates of each studied model. Energies were calculated using a Tight-Binding approach with the Seifert parametrization [107, 109]. The internal coordinates at each given lattice parameter were relaxed using the Conjugate Gradient method [107]. Brillouin zone sampling was accomplished using Monkhorst-Pack (**MP**) meshes [110] of special $k - points$. The $k - point$ grids provide convergence in the total energies below the 1meV/atom threshold; which is accurate enough to follow the changes in energy with volume and geometry. For the largest (D766 and IWP-G) cells, Γ point sampling revealed enough to fulfill this convergence criterion,



(a)



(b)

Figure 3.1: Cubic crystal cells for the Schwarzite models comprising only of hexagonal and octagonal rings. Blue boxes around each structures represent the borders of the unit cell. (a) Structures with 6-8-8 atomic environment. (b) Balanced structures dividing the space in two equivalent regions.

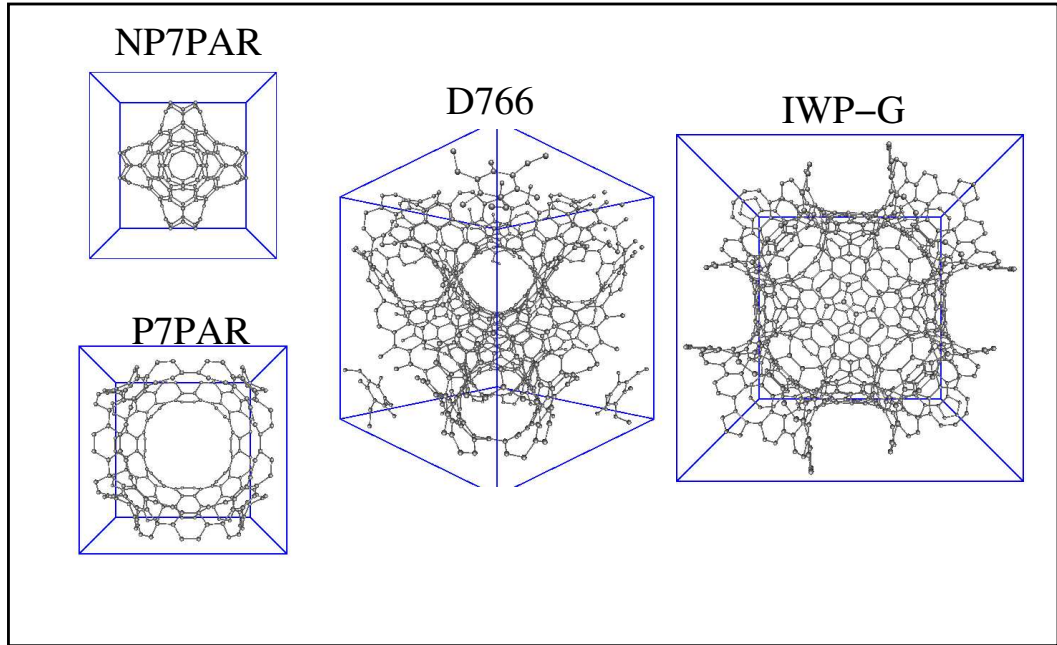


Figure 3.2: Cubic crystal cells for the Schwarzite models comprising hexagonal, heptagonal, octagonal and pentagonal (only for IWP-G) rings. Blue boxes represent the borders of the unit cell.

but in general denser grids were required.

Fitting the Energy vs. Volume curves to the Birch-Murnaham formula [103]:

$$\begin{aligned}
 E = E_0 + \frac{9}{8}B_0V_0 \left[\left(\frac{V_0}{V} \right)^{2/3} - 1 \right]^2 + \frac{9}{16}B_0V_0(B_p - 4) \left[\left(\frac{V_0}{V} \right)^{2/3} - 1 \right]^3 \\
 + \gamma_4 \left[\left(\frac{V_0}{V} \right)^{2/3} - 1 \right]^4 + \dots
 \end{aligned} \tag{3.1}$$

we found the equilibrium energy, E_0 lattice parameter, $a = (V_0)^{1/3}$, bulk modulus, B_0 , and the derivative of the bulk modulus with pressure, B_p , for each structure. For most of the studied crystals the first three terms in (3.1) are sufficient to obtain a good fit, and we only found necessary the fourth order term for the IWP-G structure. The internal coordinates are further relaxed at the value of lattice parameter obtained from the fit.

3.3.1 Local atomic environment: bond lengths and bond angles

Sketches of the structures obtained after relaxation can be viewed in fig. 3.1 and 3.2. Simple inspection of the relaxed geometries does not reveal notorious changes with respect to the original models. Nevertheless, the relaxation procedure leads to a rather significant rearrangement of the bonds, as can be observed from table 3.1, where both lengths and angles after and before relaxation are reported.

Concerning the correctness of the calculated geometries, it is important to remark that the tight-binding model we have used, reproduces accurately the geometries for diamond and graphene. The calculated lattice parameters are 3.57\AA for diamond and 2.46\AA for graphene, which are in very good agreement with experimental data. The bond lengths and bond angles in carbon Schwarzites are close to those of the graphene layer, as can be seen from the bond lengths and angles reported in table 3.1. Furthermore, we also carried out Density Functional Theory (DFT) calculations on the energetics and density of states for D688 P688, and G688, in order to test our Tight-Binding results. Within a plane wave pseudopotential framework [97], we performed both LDA calculations using the Perdew-Zunger [111] exchange correlation functional with a Von Barth-Car [112] pseudopotential, and GGA calculations with the Perdew-Wang91 [57] exchange correlation formula and an ultrasoft [58] pseudopotential. Due to the increase in the computational effort in the DFT calculations, we have chosen an accuracy goal of 0.05 eV/atom in the total energy, which is sufficient as long as we are not interested in detailed geometrical optimization. This accuracy threshold was reached with a kinetic energy cutoff of 58 Ry and 4 special k points for the Brillouin zone integration (the Monkhorst-Pack $2\times 2\times 2$ mesh) for the LDA calculation, and with an energy cutoff of 20 Ry and 10 k points for the GGA calculation. The output forces from those calculations are about 10 times larger in the unrelaxed models, when compared to the tight-binding optimized structures. These results are, therefore, consistent with the relaxation trends observed in our tight-binding approach.

Structure	#atm/cubic cell	Bond length (Å) unrelaxed	Bond length(Å) relaxed	Angle unrelaxed	Angle relaxed
D688	24	(19)1.421 (8)1.423	(15)1.399 (12)1.494	{6}120.00°±0.016°	{4}119.99±0.010
P688	48	(60)1.462	(12)1.348 (48)1.489	(96)114.09° (48)120.00°	(48)113.89° (96)122.71°
G688	96	(48)1.400 (72)1.457	(72)1.409 (48)1.492	(96)117.49° (96)117.94° (96)119.98°	(96)114.31° (96)119.96° (96)121.99°
D8 BAL	96	{7}1.447±0.021	{5}1.427±0.029	{40}119.94°±5.12°	{6}119.97°±5.86°
NP8 BAL	104	{14}1.472± 0.026	{10}1.477±0.032	{49}114.41°±19.8°	{21}119.44°±2.69°
NP7 PAR	120	{12}1.4312± 0.006	{10}1.443±0.047	{27}118.35°±3.74°	{13}118.48°±4.81°
P8 BAL	192	(96)1.439 (168)1.451	{5}1.427±0.021	{7}119.48°±2.07°	{9}119.68°±2.69°
P7 PAR	216	{7}1.447±0.012	{8}1.428±0.025	{19}119.68°±3.83°	{15}119.60°±3.44°
G8 BAL	384	{6}1.447±0.014	{6}1.428±0.016	{45}119.73°±4.48°	{12}119.77°±4.16°
D766	672	{11}1.425±0.023	{8}1.429±0.020	{21}119.56°±2.10°	{21}119.71°±3.74°
IWP-G	744	291.448±0.035	{34}1.429±0.023	{98}118.35°±12.86°	{185}119.45°±7.12°

Table 3.1: Geometrical parameters for the studied structures before and after relaxation. The bond lengths in Å , angles in degrees, and their respective abundances (the values within round parentheses) are reported. In order not to overload the table, whenever the number of bond angles/lengths was larger than three, we report only the mean value, the mean squared deviation and the number of different values found (within square brackets).

Table 3.2: Average absolute values for the Gaussian curvature ($\overline{|K_I|}$), at the carbon-atom sites for the Schwarzites structures. Values for the unrelaxed crystals are also reported. The corresponding value for the Buckminsterfullerene C_{60} is shown for comparison.

Structure	$\overline{ K_I }(\text{\AA}^{-2})$ unrelaxed	$\overline{ K_I }(\text{\AA}^{-2})$ relaxed	Structure	$\overline{ K_I }(\text{\AA}^{-2})$ unrelaxed	$\overline{ K_I }(\text{\AA}^{-2})$ relaxed
C_{60}	0.077	0.077	NP7PAR	0.147	0.133
D688	0.000	0.000	NP7PAR	0.15	0.13
P688	0.215	0.013	P8BAL	0.030	0.020
G688	0.088	0.072	G8BAL	0.013	0.011
D8BAL	0.003	0.0018	D766	0.027	0.015
NP8BAL	0.12	0.038	IWP-G	0.11	0.037

3.3.2 Topological properties

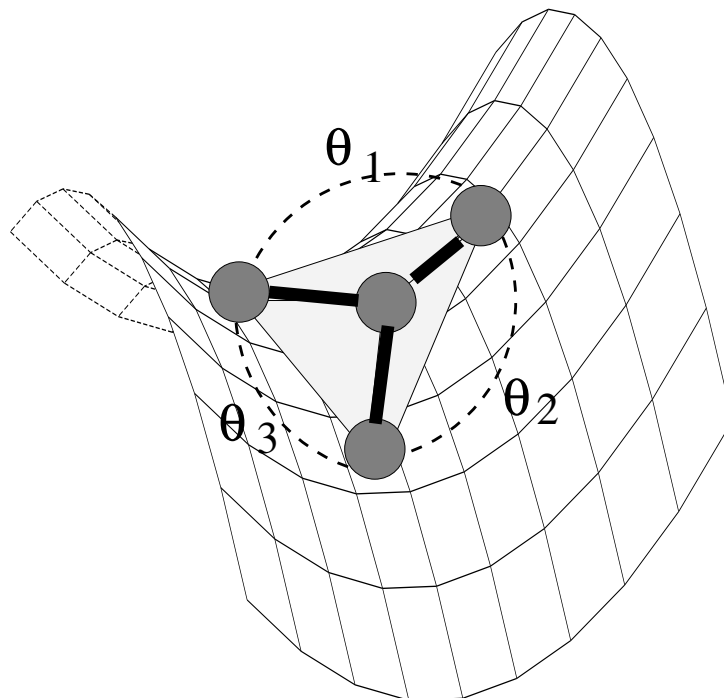
The carbon atoms on these negatively-curved surfaces, are the vertices of finite meshes. The local Gaussian curvature (K_G) of these grids, can be estimated discretizing the Gauss-Bonnet formula [113, 114]:

$$K_G(I) \cdot S_I = \frac{2\Pi - \sum_{i=1}^3 \Theta_i}{S_I},$$

where I is the vertex (site) index. The quantity $2\Pi - \sum_{i=1}^3 \Theta_i$, with Θ_i 's depicted in figure 3.3, is known as the *angle-excess*. The surface area assigned to each vertex (S_I), is $\frac{1}{3}$ -th of the total area of the three triangles formed by each vertex and its nearest neighbors (shadowed areas in fig. 3.3).

The average absolute values for the Gaussian curvature ($\overline{|K_I|}$), are reported in Table 3.2. These values are reduced after relaxation. Therefore, we can state that the relaxation leads carbon bonds towards arrange more flat configurations.

Figure 3.3: Geometrical parameters used in the evaluation of the local Gaussian curvature, in the negatively-curved crystals. The surface area assigned to each vertex is one third of the shadowed area.



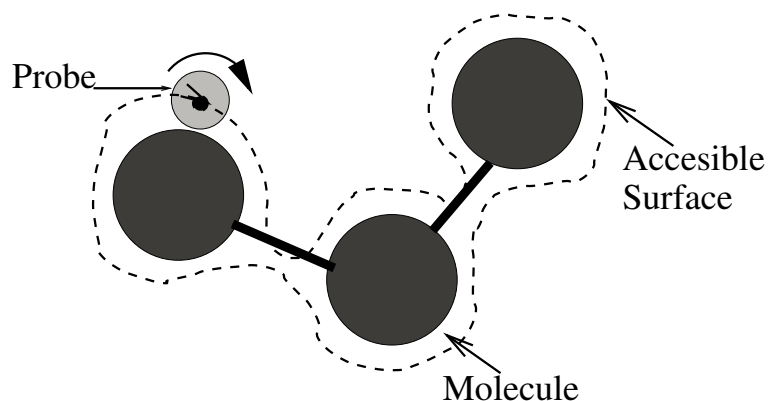


Figure 3.4: Simplified scheme for quantification of molecular surfaces. A probe sphere rolls over the Van der Waals representation of the atoms in the molecule. The center of the probe sphere defines the Solvent Accessible Surface.

3.3.3 Solvent accessible surfaces.

In 1983, M. L. Connolly designed a simple method to quantify the surface area of proteins and nucleic acids [115]. In his work, the area of a molecular system accessible to a solvent is measured as the surface generated by a probe sphere rolling over Van der Waals spheres representing the atoms (see fig. 3.4). The obtained measure is known as the Solvent Accessible Surface (**SAS**), or Connolly surface. Improvements over the original Connolly's algorithm have been developed by several authors, especially by M.F. Sanner [116]. The Sanner formulation for the SAS, is one of the standard methods for visualization and quantification of molecular surfaces [116,117].

The SAS lacks any information regarding the chemical interactions between the molecular framework and specific adsorbate. Notwithstanding, this geometric concept has been successfully applied to the realization of novel materials with exceptional dye uptake capability [118]. Materials with high SAS, are likely to exhibit large effective areas for gas storage and dye uptake [118].

We have calculated the SAS for the Schwarzite crystals, using the M. F. Sanner program [116]. A probe radius of 1.4\AA was used (this is a common value in the literature, corresponding to the Van der Waals radius of the water molecule). The calculations for the D688, P688, G688, P8BAL, G8BAL and D766 models, were

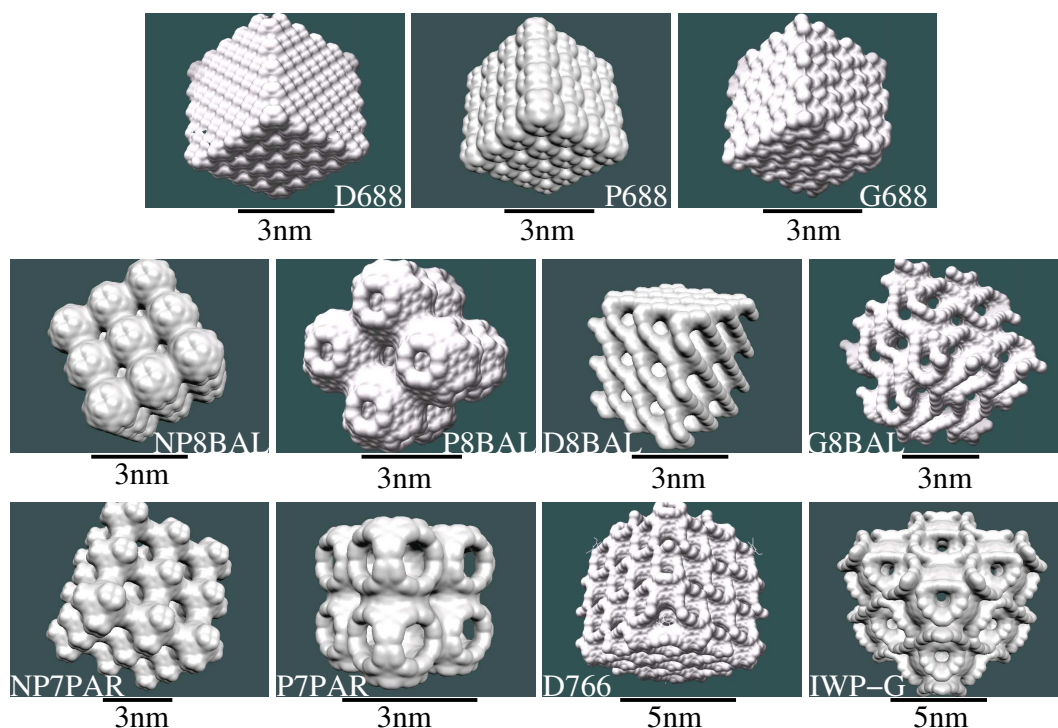


Figure 3.5: Solvent Accessible surfaces for the D688, P688, G688, P8BAL, G8BAL and D766 Schwarzite crystals; and van der Waals surfaces for the D8BAL, NP7PAR, P688, IWP-G, NP8BAL, and P7PAR models.

performed using cubic supercells of the Schwarzite crystals of at least 3nm length in each side. The expected SAS for the negatively-curved models is taken as the average value of the atomic SAS for the inner-most atoms, in order to separate the effects of the cluster surface. For the D8BAL, NP7PAR, P688, IWP-G, NP8BAL, and P7PAR crystals, the Sanner algorithm was not able to render the SAS in large supercells, and we used smaller clusters for the quantification of the SAS. The molecular surfaces, depicted in fig.3.5, were rendered using the CHIMERA package [117]. In the cases for which the Sanner algorithm failed, we show the van der Waals surfaces (each atom is represented by a van der Waals sphere), rendered using the MOLEKEL package [119].

The D688, P688 and G688 crystals exhibit closed surfaces at the supercell's boundary. Their internal channels are, consequently, inaccessible to the probe sphere. The remaining crystals are open frameworks, with corresponding high values of SAS. Table 3.3 summarizes our results for the Solvent Accessible Surfaces.

Structure	SAS (m ² /gr)	Structure	SAS (m ² /gr)
Graphene	2572	NP7PAR	1704
D688	0.0	P8BAL	1881
P688	0.0	P7PAR	1820
G688	0.0	G8BAL	1606
D8BAL	1431	D766	1640
NP8BAL	1798	IWP-G	1627

Table 3.3: Solvent Accessible Surfaces for the Schwazite crystals, calculated using a probe radius of 1.4Å. The value for graphene is shown for comparison.

3.3.4 Total energies.

The calculated total energies per atom, measured with respect to the corresponding value for the graphene structure, are reported in Table 3.4. As can be seen in this table, diamond is slightly above graphene in energy. The Schwarzite structures lie between 0.2 eV and 0.5eV per atom above graphene - or diamond-. The energies calculated for P688 and polybenzene (D688) structures are in good agreement with those reported in O' Keeffe's et al. work [29].

Structure	Energy(eV)	Structure	Energy(eV/atom)
Diamond	0.035	NP7PAR	0.476
D688	0.262	P8BAL	0.236
P688	0.525	P7PAR	0.263
G688	0.482	G8BAL	0.269
D8BAL	0.277	D766	0.308
NP8BAL	0.338	IWP-G	0.378

Table 3.4: Energies per atom, relative to the value in a graphene layer. The corresponding value for diamond is also shown for comparison.

Considering all the studied structures, P8BAL shows the lowest energy, 0.236 eV/atom, although the difference with polybenzene is only about 0.026 eV/atom. The C_{60}

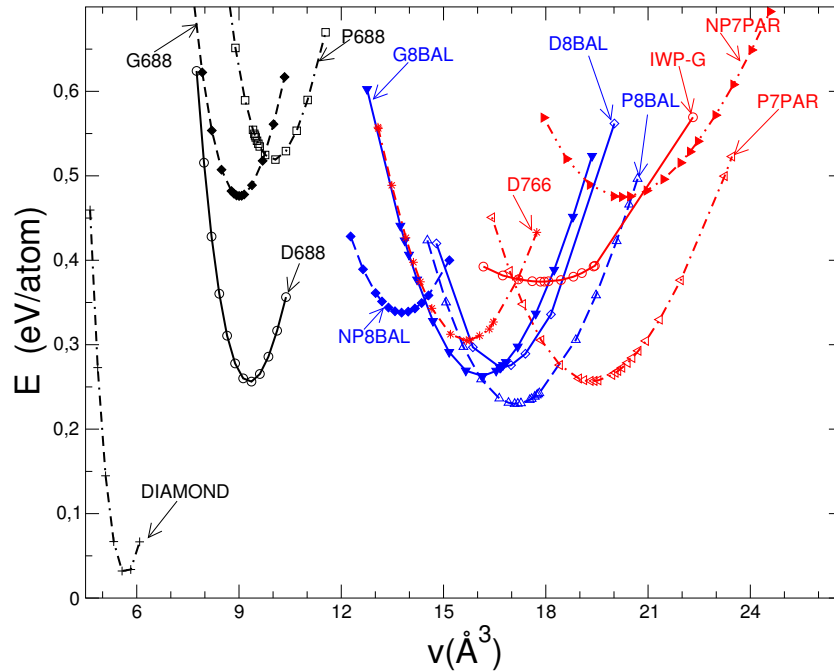


Figure 3.6: Total energies per atom for the studied crystals, measured from the value for a graphene layer. The corresponding curve for diamond is shown for comparison. Curves and labels for the balanced (8BAL-) structures are shown in blue. Structures containing heptagons are highlighted in red.

buckyball lies about 0.44 eV/atom above the graphene layer (see for example ref [29]) so that most of the studied models are at least energetically viable. The P688 structure exhibits the largest energy difference with respect to graphene (0.525 eV/atom). Only the P688, the G688 (0.482 eV/atom), and the NP7PAR (0.476 eV/atom) crystals are above the energy corresponding to the C_{60} structure. It is also remarkable that all the negatively curved D structures, despite their different curvatures, exhibit similar energies, meanwhile G- and P curved structures can be constructed with rather different energetic behavior.

The evolution of the energy with the average local Gaussian curvature, is depicted in figure 3.7. In general, energies increase with the curvature. The P688 structure displays a significant deviation from the overall trend.

The fact that the energy of Schwarzite structures should follow an overall linear trend with the Gaussian curvature, has been discussed in the literature [106]. It is

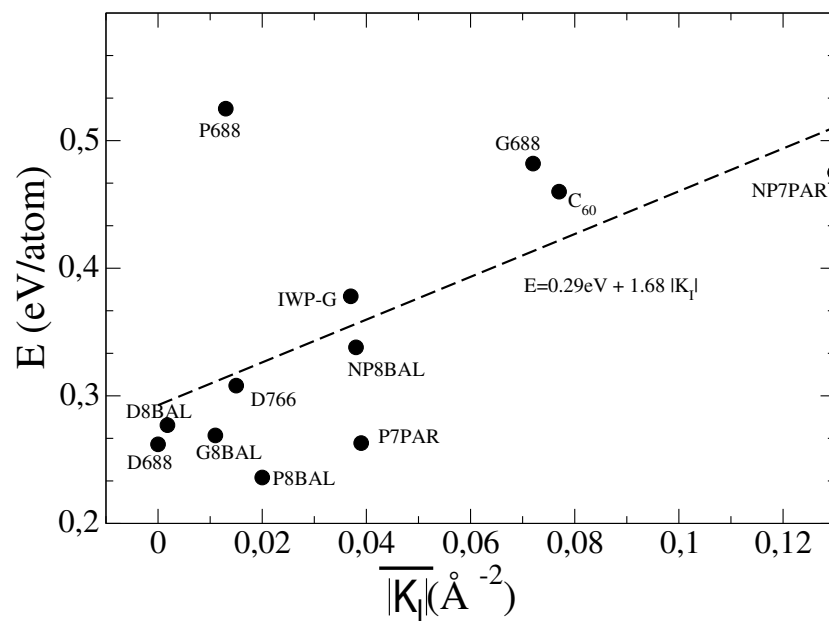


Figure 3.7: Total energy of the negatively curved crystals, with respect to the graphene layer, as function of the average local Gaussian curvature. The dashed line correspond to a crude linear regression. In the estimation of $|K_I|$, a constant surface element $S_I = 1.75\text{\AA}^2$, corresponding to the perfect graphene bond lengths has been used.

related to a general form for the energy of membranes and foams (Helfrich's energy, see ref. [106] and references therein):

$$E = \int_S (\gamma + \kappa_1 H_m^2 + \kappa_2 K), \quad (3.2)$$

where H_m and K are the mean and Gaussian curvature, and γ is the surface density of energy for graphene. For minimal surfaces, the mean curvature is zero, and a linear behavior of the energy with the curvature is expected (provided that the surface atomic density is constant, a fact that is approximately verified in our studied crystals). The value for the slope, in the crude linear regression depicted in fig. 3.7, is close to the value of 1.5eV extracted from first principles calculations of the cohesive energy of schwarzites (see [106]). However, the actual value of the energy would depend upon other factors, such as the number of n-membered rings in the cell (n=5,6,7,8), and the distribution of Gaussian curvatures. It is also important to regard that the assignation of the surface element corresponding to each site is somehow arbitrary.

3.4 Elastic Properties.

For cubic systems there are three independent elastic constants: C_{11} , C_{12} , and C_{44} -usually referred to as the trigonal shear modulus-. The first two can be written in terms of the bulk modulus, $B_o = (C_{11} + 2C_{12})/3$, and the tetragonal shear modulus, $(C_{11} - C_{12})$. These elastic constants for a given material provide valuable information related to mechanical stability of the system. For mechanically stable cubic systems, all of the above mentioned elastic moduli must be strictly positive.

As stated above, the bulk modulus is extracted from the Birch-Murnaham equation. The remaining elastic moduli were calculated by straining the lattice vectors and relaxing the internal coordinates. For the tetragonal shear modulus we used volume conserving orthorhombic deformations [103]; for cubic structures this kind of strain produces energy changes given by:

$$\Delta E(x) = V(C_{11} - C_{12})x^2 + O[x^4] \quad (3.3)$$

where x is the strain. For the trigonal shear modulus, volume conserving monoclinic deformations, inducing energy changes of the form:

$$\Delta E(x) = \frac{V}{2} C_{44} x^2 + O[x^4] \quad (3.4)$$

were used. The deformation parameter, x , used in our calculations ranges between 0 and 0.06 for both moduli. Bulk and shear moduli calculated in the present work are shown in table 3.5. We must note that the agreement between the calculated values for diamond data ($B_0 = 543\text{GPa}$, $C_{11} - C_{12} = 951\text{GPa}$, $C_{44} = 576\text{GPa}$), is similar to that achieved using the LDA approximation.

In polycrystalline samples, neither the tetragonal nor the trigonal shear modulus can be directly measured. Instead, one could study the isometric shear modulus G . Although there is no simple relationship between the elastic constants and G , bounds can be calculated from them [103], and we have also included those limiting values in table 3.5. It is also possible to characterize the mechanical properties of a given material in terms of the Young modulus E_y and Poisson ratio ν , which can be related to the Bulk and shear moduli [103]. Taking the value of G as the average between the obtained lower and upper bounds, we have estimated those parameters, as well as the first Lamé constant (I), and included them in table 3.5.

As expected, all the Schwarzites are, softer compared to diamond, but still strong: the bulk moduli are (except for the IWP-G) larger than the value for silicon in the diamond phase². All the shear moduli are larger than zero, meaning that these structures would be mechanically stable.

One of the main features of these negatively curved surfaces, is that shear moduli are noticeable smaller than bulk moduli. Therefore, these materials would be much softer under shear than under compression. This fact can be understood in terms of the different energies required for bond rotations and bond compressions³. In these single-layered decorated surfaces, shear strain would comprise mostly bond

²In the diamond phase, the bulk modulus of silicon is 98GPa, and between 80-100 GPa in typical LDA calculations. This structures is the hardest phase of silicon, much softer structures like the silicon clathrates [22] are still mechanically stable.

³In graphitic networks, bond rotations are generally less expensive than compression-stretching of the bonds [120].

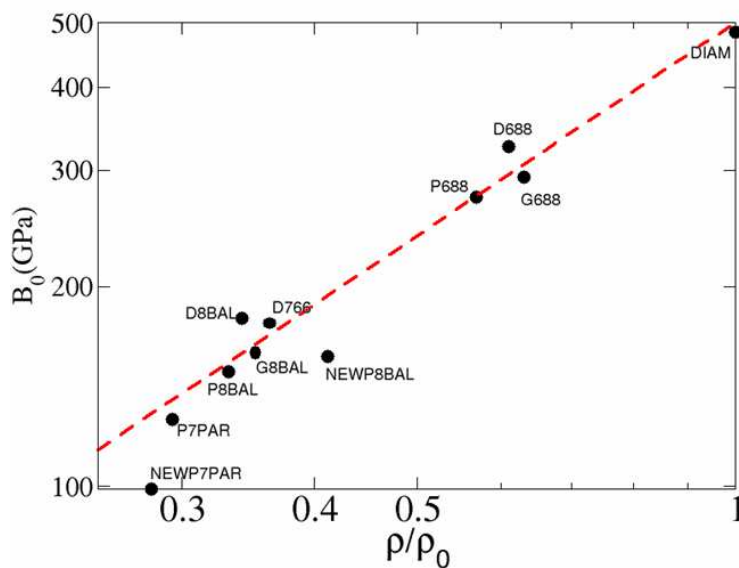


Figure 3.8: The behavior of the Bulk modulus as a function of atomic density of the cell for. It is clear that most of the models follow an exponential law. D-like negatively-curved structures are always stronger than could be expected from this “typical” behavior.

rotations, whereas compression strains would induce larger changes in the bond lengths.

Of all the studied models, polybenzene exhibits the largest bulk and shear moduli and, therefore, it would be the most stable under mechanical stress. Because of this reason, and its relatively low energy, polybenzene could be thought of as the main candidate to be synthesized. This result is in agreement with those reported by other authors [29].

Bulk modulus increases with the atomic density. It is remarkable that B_0 follows an approximate power law of equation 3.8, $B_0 = C * \rho^\lambda$, where ρ is the cell atomic density of each model, and the exponent λ equals 1.071. Nevertheless, D688, D766 and D8BAL exhibit B_0 which are slightly larger than the calculated from the power law described above. IWP-G deviates strongly from this trend, and we have not included it in figure 3.8, for reasons that will be clarified later in this. NP7PAR also deviates from the power law, perhaps because it displays a very low atomic density.

It is important to note that the IWP-G structure, exhibits strong anharmonic

effects represented by a large fourth order coefficient in the Birch-Murnaham equation (3.1). This fourth order term displays values of $\gamma_4 = 55.5$ eV/atom, a really large contribution to the energy curve. Taking into account the flat behavior of the Energy vs. Volume curve (see figure 3.6), the fact that it crosses the corresponding curves of much more robust structures, and the relatively high energy of this structure, one can expect that IWP-G is unstable under mechanical stress, and therefore we have left this model aside in the calculation of the remaining elastic constants and vibrational properties.

The information on energetics, geometry and elastic constants confirms the mechanical stability of the Schwarzites models, except for the IWP-G structure. The material strength could be at least of the same order as that of silicon. It is important to remark that the concept of mechanical hardness is not directly related to that of mechanical strength (elastic properties). Even if these systems can be elastically deformed by relatively small stresses, they contain only covalent C-C bonds which lengths and angles are close to those of graphene. Therefore, the actual mechanical hardness could be rather high.

3.5 Electronic properties.

In table 3.6 the calculated fundamental electronic band gaps (Δ_1) are shown. Those gaps are calculated as the difference between the highest occupied energy level and the lowest unoccupied energy level in the k -point mesh used to sample the Brillouin zone. The band gap for diamond is remarkably overestimated in our calculations using the Seifert parametrization (about 42% over the actual value of 5.47 eV), and the same trend is to be expected for the remaining values. As a countercheck of these trends we have also calculated the band gaps within the orthogonal Pettifor parametrization [65], which provides a better value for diamond band gap (6.3 eV) and, in general, is considered to provide a better description of the unoccupied states. It is clear, from table 3.6, that both tight-binding models predict similar trends for the electronic gap.

In order to achieve a better description of the electronic properties, electronic

Structure	$a(\text{\AA})$	$B_0(\text{GPa})$	B_p	$C_{11} - C_{12}(\text{GPa})$	$C_4(\text{GPa})$	$G(\text{GPa})$	$E_y(\text{GPa})$	ν	$I(\text{GPa})$
Diamond	3.57	484	4.8	938	607	547.1-547.5	1193	0.09	119
D688	6.07	325	4.6	161	186	131.7-135.4	325	0.32	236
P688	7.83	273	4.4	101	79	66.1-66.3	184	0.39	229
G688	9.53	293	3.5	123	124	93.3-94.8	255	0.36	230
D8BAL	11.70	179	4.3	148	76	75.5	198	0.32	129
NP8BAL	11.28	157	140	1.78	85	78.7	202	0.29	104
NP7PAR	13.44	99	3.05	88	30	35.4	95	0.34	75
P8 BAL	14.87	149	0.8	61	82	54.3-56.8	148	0.33	112
P7 PAR	16.11	126	2.0	69	54	45.1-45.3	121	0.34	96
G8 BAL	18.37	159	1.3	115	78	69.0-69.1	182	0.31	113
D766	21.92	176	2.0	180	67	75.7-75.6	199	0.31	126
IWP-G	23.70	34	-9.8	

Table 3.5: Lattice constants and elastic constant for the studied models. Values computed for diamond are shown for comparison. Values of the upper and lower bounds to the isometric shear modulus G are, intentionally, reported with a larger number of significative figures just to reflect the small differences.

Structure	Δ_1^S (eV)	Δ_1^P (eV)	Δ_1^S (eV)
	relaxed	relaxed	unrelaxed
Diamond	7.80	6.3	7.80
D688	2.90	2.60	2.90
P688	0.04	0.011	0.10
G688	1.50	1.50	0.30
D8BAL	0.20	0.40	0.00
NP8BAL	0.04	0.10	0.28
NP7PAR	1.16	0.90	0.24
P8BAL	1.40	1.12	0.80
P7PAR	1.30	1.10	0.73
G8BAL	0.20	0.29	0.00
D766	1.30	1.00	1.00
IWP-G	-0.04	-0.02	-0.025

Table 3.6: Electronic band gap energies (Δ_1) calculated for different negatively curved structures. The superindexes S and P stand for the Seifert and Pettifor parametrizations. The values calculated for diamond is shown for comparison. For the Seifert parametrization, we have also registered the values obtained for the unrelaxed structures. For the IWP-G structure we report the value of the band overlap.

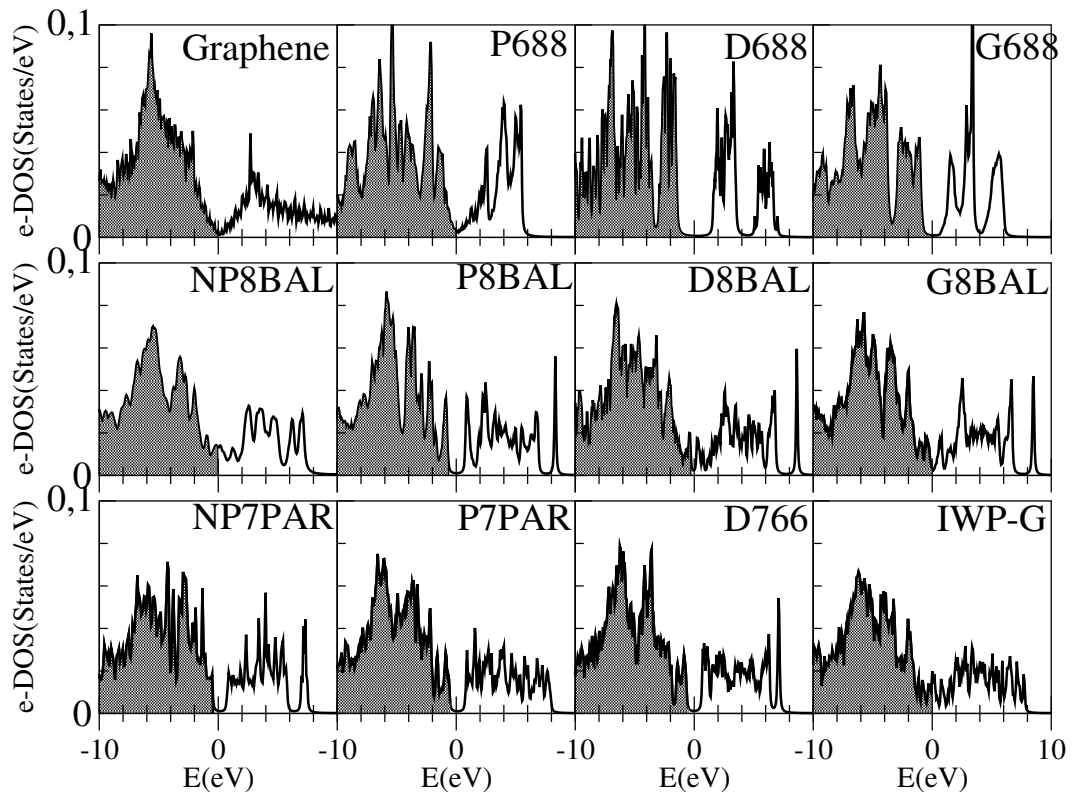


Figure 3.9: Electronic densities of states (e-DOS) for the different negatively curved structures, calculated using the Seifert parametrization [109]. Densities are normalized to the unity in the range of available energies. The reference, “0”, level is the Fermi level. The calculated e-DOS for graphene is shown in the first panel. A Lorentzian broadening of 0.1eV was used in the calculation.

densities of states (e-DOS) were calculated using the Seifert (Fig. 3.9) and Pettifor (Fig. 3.10) parametrizations.

These two tight-binding approaches yield similar behaviors for the e-DOS near the Fermi level (and in the region between $\sim -4\text{eV}$ to $\sim 4\text{eV}$). The Pettifor model predicts gaps in the valence band (about $\sim 5\text{eV}$ below the Fermi level) which are not present in the calculations using the Seifert parametrization. These valence band gaps could be related to a similar feature in the calculated graphene e-DOS (see Fig. 3.10). For the valence band of graphene, the e-DOS calculated using the Seifert parametrization, closely resembles the shape obtained using first principles calculations [121]. A comparison between the Seifert parametrization e-DOS and

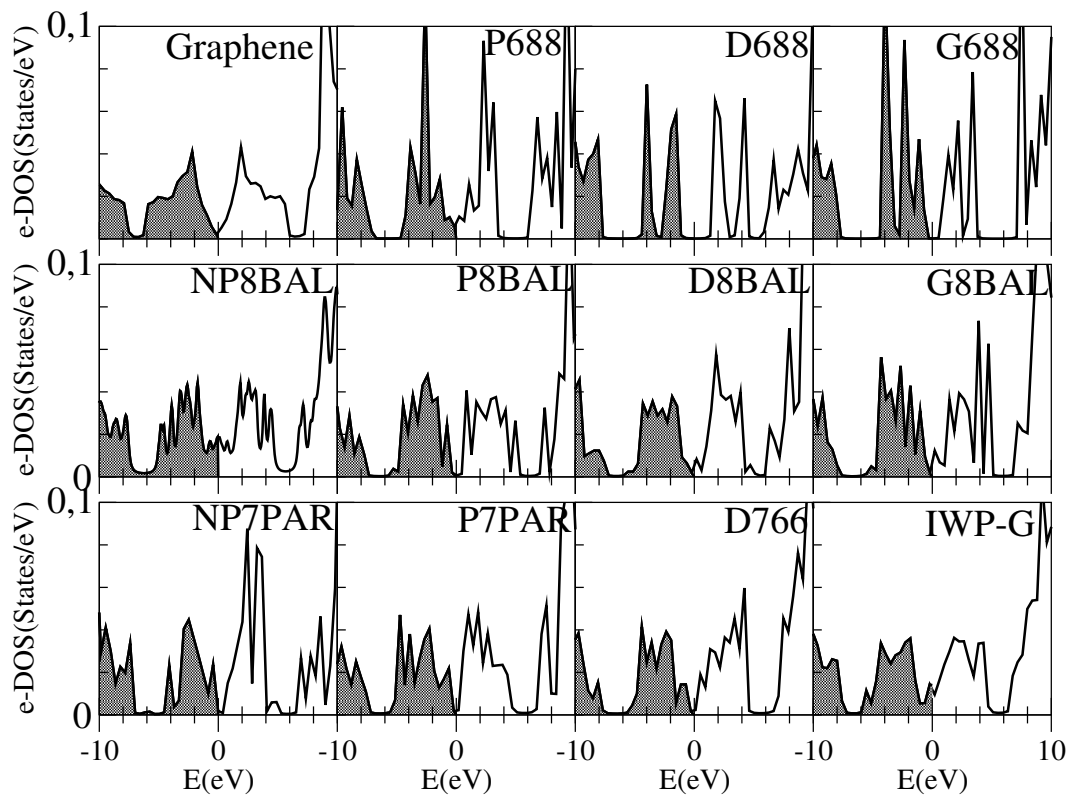


Figure 3.10: Electronic densities of states, normalized to the unity, the reference level is the Fermi level, now using the Pettifor parametrization [65]. The calculated e-DOS for graphene is shown for comparison. The Lorentzian broadening was 0.1eV.

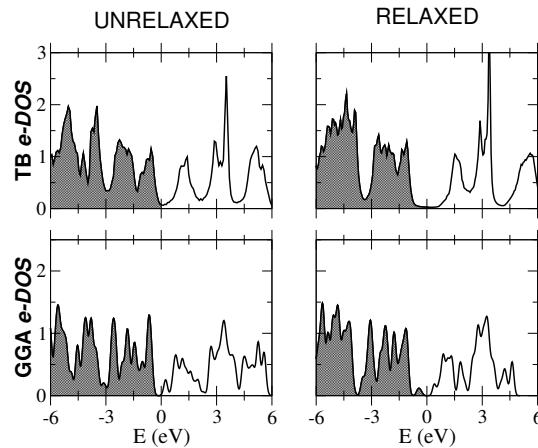


Figure 3.11: Upper panel: Electronic density of states for G688, calculated within the Tight-Binding framework, both before -to the left- and after -to the right- relaxation. Lower panel: same as above within the GGA framework.

the GGA e-DOS for the G688 structure is shown in figure 3.11. Despite its main deficiency (the clear overestimation of the band gap), the Seifert parametrization describes accurately the shape of the e-DOS both in the valence and in the conduction bands. Similar results were obtained for the D688 and P688 crystals. This agreement favors the Seifert model for the description of the valence bands. The energy gaps in the valence band, predicted using the Pettifor model, may be regarded as artifacts of this parametrization.

We can identify six structures as small band gap semiconductors: D688, G688, P8BAL, P7PAR, NP7PAR, and D766. For the P688, D8BAL, and G8BAL crystals, the shape of the e-DOS is typical of semimetallic species; electrons could overcome the small electronic band gap at finite temperature. The NP7PAR and IWP-G structures, display almost constant e-DOS near the Fermi level and they would behave like metals at normal experimental conditions. IWP-G exhibits the largest e-DOS at the Fermi level. Only for this crystal, overlap between valence and conduction bands was observed, a fact that could be related to the presence of pentagons in its structure. However, as we stated above, the mechanical stability of IWP-G would be seriously compromised under normal experimental conditions.

Is interesting to remark the similarities between the electronic structure of the

D8BAL and G8BAL. Besides being both semimetallic, further similarities can be established between some of their major characteristics. There is a strong and narrow peak around 8-9 eV, a broader peak near 7 eV and a third one around 3 eV, although in D8BAL this third peak appears to be segmented. This three peaks seems to be also present in the P8BAL structure, however their similarities are less clear, except for the 9 eV peak. It is noteworthy that the D, G and P triply periodic minimal surfaces are related by a bending transformation which preserves the metric and angles [26], [27]. Therefore a relationship among their properties can be established when these are decorated with carbon atoms.

The effect of relaxation on the electronic properties is poorly represented in table 3.6. Figs 3.12 to 3.14 show the e-DOS near the Fermi level, calculated using the Seifert parametrization⁴, and the geometrical arrangement, represented by the distribution of distance to the nearest and the next nearest neighbors, for some models exhibiting different electronic behavior.

Let us first consider the polybenzene structure. As seen in figure 3.12, the e-DOS is almost unaffected by the significant structural rearrangement. A similar behavior is exhibited by P8BAL, G8BAL and D766, where only minor density reaccommodation takes place after relaxation.

In the P688 structure, although relaxation brings a reduction in the electronic band gap, there is also a notorious reduction in the e-DOS near the Fermi level. The overall appearance of the e-DOS is quite different after relaxation. This fact may be related to the different angle distribution. The hexagonal rings in the original structure occur in almost flat planes, a fact that changes drastically after relaxation. The differences between the original and the relaxed geometries, are larger for the

⁴The major changes in the density arising from the geometry variations are accurately described using the Seifert parametrization, when compared to DFT results. In Fig. 3.11), the deepening of the valence band valley around 3 eV, the reduction in the valence states density near the Fermi level and the shift to the right of the first hump in the conduction states density, are observed in the Seifert tight-binding model and in the GGA calculations. It is also noteworthy that our GGA results underestimate the diamond band gap by about 25%, so that DFT results in figure 3.11 may also underestimate the semiconductor character of the relaxed G688 structure. Similar results were obtained also for the D688 and the P688 structures; and in the GGA and LDA approximations.

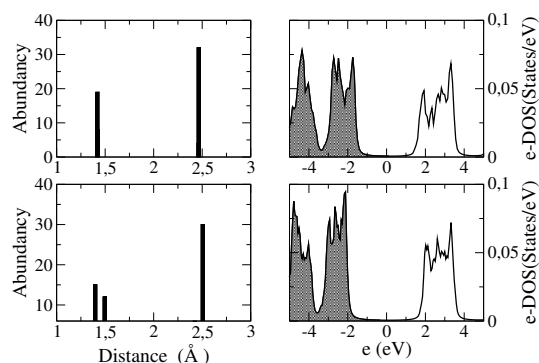


Figure 3.12: Electronic density of states for polybenzene -D688- before (upper panel) and after (lower panel) relaxation. The Fermi level is located at “0” energy. The corresponding distributions of distance to nearest and next nearest neighbors, are shown representing the geometrical rearrangement.

P688 structure, compared to the other negatively-curved crystals. Therefore the notorious changes in the e-DOS are understandable.

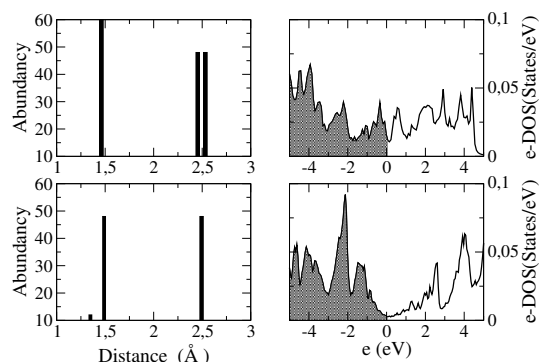


Figure 3.13: Same as fig. 3.12 but for the P688 structure.

In contrast with polybenzene, the G688 structure develops a large change in the e-DOS with a rather small geometrical rearrangement. As shown in figure 3.14, the e-DOS looks completely different after relaxation. In fact, G688 is the most striking case, and exhibits the largest change in the band gap (1.2 eV). The geometrical relaxation does not produce sensible changes like in P688, but leads a change in the ordering of the bond orders. The initial structure was constructed using two bond lengths: the largest corresponding to the bonds shared by one hexagonal and one octagonal ring, and the shortest corresponding to the bonds shared by two octagonal

rings. In the relaxed structures, the order changed, and the largest length is that corresponding to the bonds shared by two octagonal rings. That seems to be a unique behavior within the studied models, and may be the origin of the observed variations in the electronic properties.

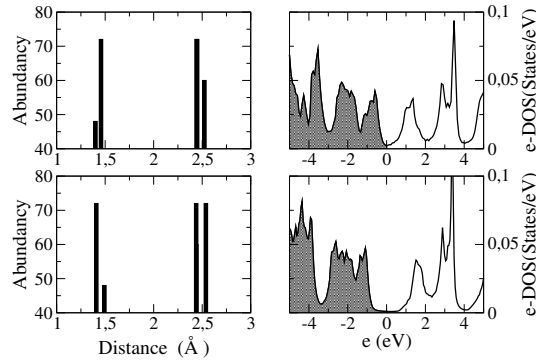


Figure 3.14: Same as fig. 3.12 but for the G688 structure.

From the remaining structures, it is only worth mentioning the opening of a the small gap in the D8BAL structure. In the initial structure, the conduction and valence bands are barely in contact. Therefore this gap-opening should be considered a slight modification of the electronic structure, commensurable with the small geometrical changes.

In most of the studied crystals, the relaxation procedure yields less conductive structures (with higher electronic band gaps, or reduced e-DOS near the Fermi level). Only for IWP-G and NP8BAL, there is an enhancement of the metallicity after relaxation. The enhancement of the metallic behavior in the latter crystals, could be related to the fact that the bond angles after relaxation are closer to those of a graphene (see Table 3.1).

In the work of Huang and Ching [32], it is stated that the electronic properties are more strongly dependent upon global geometrical properties than on the exact atomic positions. We agree with their statement. The changes in the e-DOS after relaxation are small for most of the studied crystals. Besides the discussed reinforcement of the semiconductor character (or weakening of the metallic character), the relaxation does not bring about dramatic changes. However, proper relaxation plays a relevant role in the theoretical characterization of these structures, because even

small atomic rearrangement could induce changes in system's topology. This is the case for the P688, the G688, the P7PAR, and the NP7PAR structures. Therefore, local relaxation of the coordinates should be considered in the study of negatively-curved carbon structures.

3.6 Electron Energy Loss Spectra.

Now let us see if electronic spectroscopy could provide additional information for the Schwarzite crystals, and further understanding of the relationship between the curvature and the bonding character in these structures. One property that help us in this context is the Energy Loss Spectrum (**EELS**). As a matter of fact, the low energy loss spectrum (**LEELS**) depends strongly upon collective electron motions (plasmons) that should be very sensitive to the global curvature of the structures, meanwhile the core energy loss spectrum (high energy loss) is intrinsically related to the local atomic environment.

The core EELS near the Carbon K-shell (Near Edge Loss Spectra, **NEELS**), probes the transitions between atomic s -states and the unoccupied states. Therefore, in the near edge region, the high energy EELS samples the density of empty states with p -symmetry (see appendix E). The onset for the energy loss, (the K-edge), depends only on the atomic species. According to X-Ray absorption fine-structure (**XAFS**) measurements, the K-edge for carbon is at 280 eV [122]. In the simplest approximation, the NEELS structure is thus, proportional to the p -projected density of states, shifted to the K-edge. Reliable calculations of the NEELS for carbon structures using this simple scheme, have been reported in the literature [123] . In this context, we have calculated the NEELS structure for the negatively-curved crystals from the p -projected density of unoccupied states, using the Pettifor parametrization. This density of p -empty states, was convoluted with a Lorentzian function of full width at half maximum of 1eV, in order to account for thermal effects and experimental resolution. The calculated spectra for the **688**, the **8BAL**, and heptagon-containing structures are reported in figures 3.16 to 3.17.

It is clear that these crystals posses an adequate EELS signature. Their NEEL

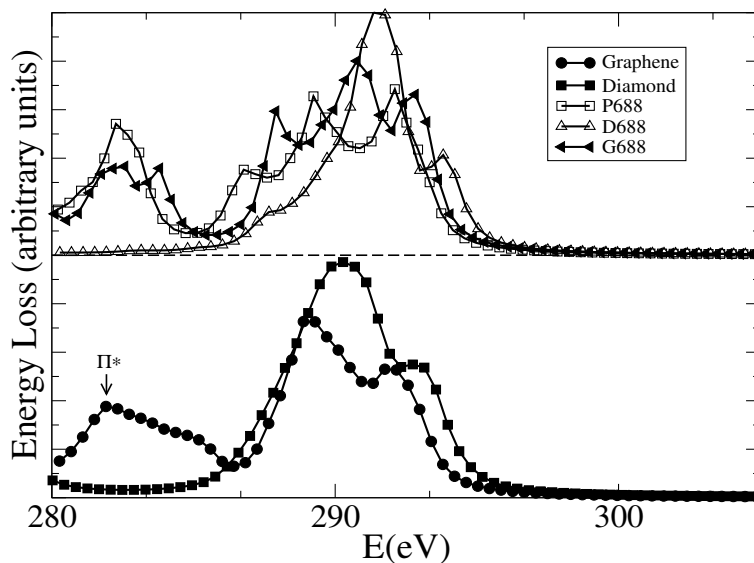


Figure 3.15: The K-shell core EEL spectra, measured from the K-shell edge, calculated within the projected density of states approximation, for the **8BAL** family of negatively curved structures.

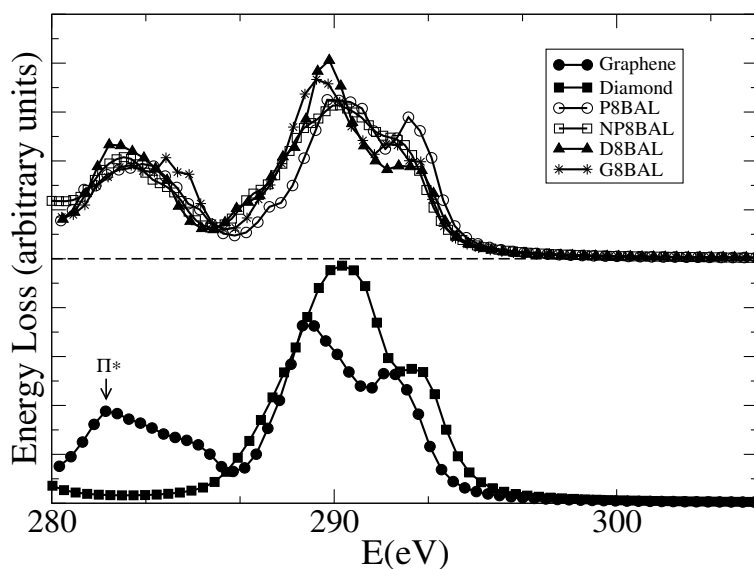


Figure 3.16: The K-shell core EEL spectra, measured from the K-shell edge, calculated within the projected density of states approximation, for the **688** family of negatively curved structures. The densities of states are convoluted with a Lorentzian function, whose full width at half maximum is 1eV.

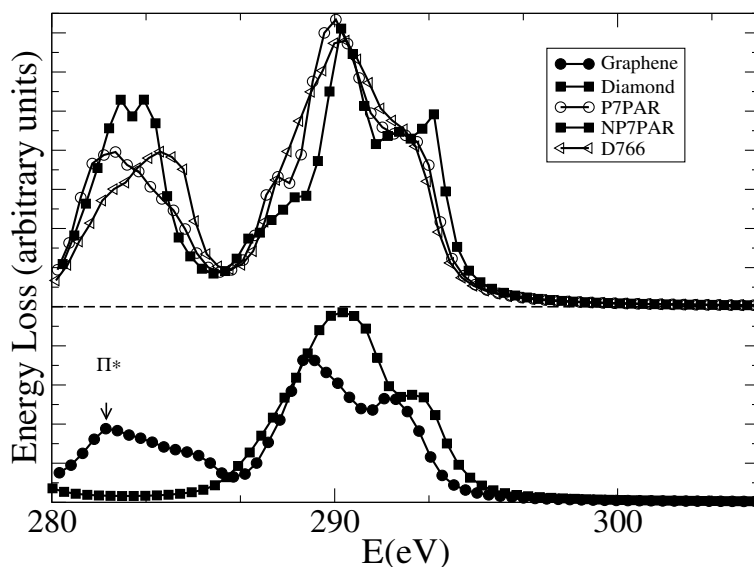


Figure 3.17: The K-shell core EEL spectra, measured from the K-shell edge, calculated within the projected density of states approximation, for the negatively curved structures containing heptagons.

spectra display peaks which are clearly distinguishable from those corresponding to graphene and diamond. This fact is particularly notorious for the 688- crystals, which exhibit a rich peak structure. For the 688 family it is remarkable that, although the local atomic environment of each structure is very similar (each atom being surrounded by the same number of hexagons and octagons), their peak structures are quite different; a fact that could be related to the positions of next nearest neighbors, and to the localization or delocalization of the electronic wavefunctions near the Fermi level. The spectrum for D688 is very similar to the diamond spectrum; nevertheless, the shift in the position of the first peak ($\sim 1.5\text{eV}$) could be experimentally resolved. The G8BAL spectrum is rather similar to that of graphene, a behavior that was expected because this structure exhibits large patches of hexagons covering its surface.

Resolutions below 1eV are rarely achieved in NEEL spectroscopy (XAFS techniques can usually reach this threshold [122]). However, some features of the calculated spectra (v.gr. the position of the strongest peaks), could be resolved in typical NEELS setups.

For the calculation of the LEELS, we have chosen a simple Tight-Binding/Random Phase Approximation approach as described in the theoretical framework (see appendix E). This is a crude approximation of the optical response, and it is known to fail in the description of the detailed absorption and reflection spectra. Fortunately, the position and evolution of the plasmon modes are not that sensitive to the detailed description of the electronic states. Of course, in order to achieve accurate agreement with experiments, higher theory levels should be implemented (for instance TDDFT [124]), but at this point we are only interested in the general trends, that can be studied within this simple theory level.

In the calculated LEEL spectra (figures 3.18 to 3.20), we observe various interesting features. But before analyzing them in detail, it is important to note that we restrict the discussion to the major features in those spectra: the TB/RPA model predicts within a reasonable accuracy the position of the diamond plasmon peak, but not the width of this plasmon mode. Therefore, we believe that the peaks positions (and perhaps even the peak structure in the graphene and graphene-like modes) are reliable, but the peak structure in the energy range of the diamond plasmon is not that accurate.

Let us summarize our low EELS results:

- (i). It is clear that the structures exhibit plasmon modes close to those of graphene and diamond, but developing noticeable energy shifts.
- (ii). Each structure exhibits a different LEEL spectrum.
- (iii). Comparing the LEELS data with the NEEL spectra, it is clear that even structures like G8BAL, which display a graphitic local environment, exhibit a diamond-like component in the low EEL spectra.

All of the above lead us to believe that, as expected, EELS techniques, can be useful in the identification of Schwarzite structures. These results also reveal the interplay between global curvature and local binding environment in Schwarzite models. The conclusions drawn from our simple TB/RPA approximation, lead us to believe that, a better (and necessarily computationally more expensive) description of the optical properties could be worthy, especially if it allows for an accurate description of other optical techniques (for instance reflectance and refractivity spec-

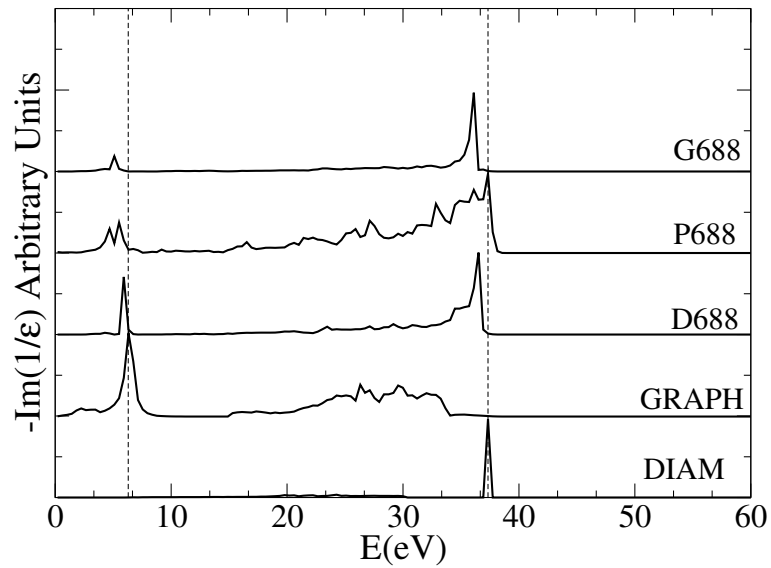


Figure 3.18: The low energy loss spectra, with the zero loss part excluded and calculated within the Tight-Binding RPA approach, for the **688** family of negatively curved structures. The graphene and diamond spectra are shown for comparison.

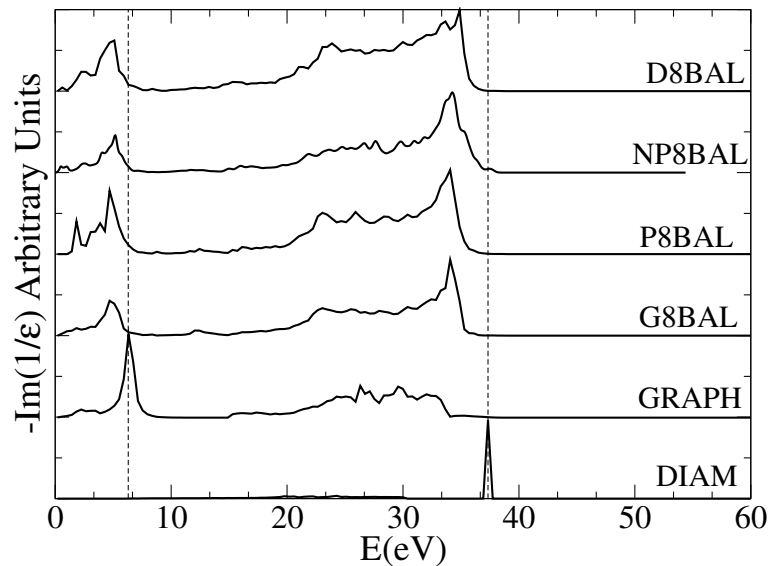


Figure 3.19: The low energy loss spectra, with the zero loss part excluded and calculated within the Tight-Binding RPA approach, for the **8BAL** family of negatively curved structures.

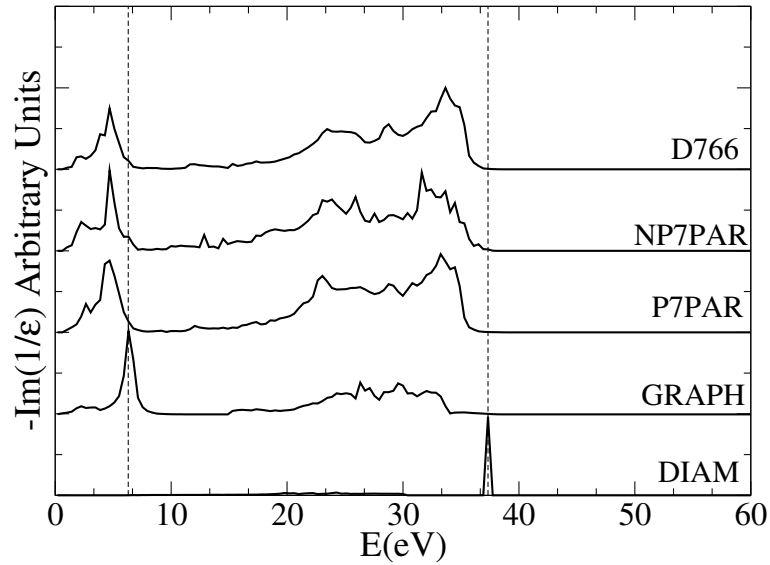


Figure 3.20: The low energy loss spectra, with the zero loss part excluded and calculated within the Tight-Binding RPA approach, for the negatively-curved structures containing heptagons.

tra), which may also uncover important information. Spectroscopic characterization of the peaks appearing below 10eV for P8BAL, D8BAL, P7PAR, and NP7PAR structures, is not possible at the present stage.

3.7 Vibrational spectra.

The vibrational densities of states computed in this work are shown in figure 3.21, where a Lorentzian broadening of 3cm^{-1} is used. The most remarkable feature in those v-DOS spectra is the appearance of vibrational gaps. For D688 there is a clear gap centered in 1670cm^{-1} and of 85cm^{-1} width. For P688 additional gaps appear: the first one centered in 1535.5cm^{-1} with a 50cm^{-1} width, another one 1642.5cm^{-1} with a 88cm^{-1} width, a third one centered at 1767cm^{-1} with a 141cm^{-1} width, the fourth is centered at 1817cm^{-1} with 41cm^{-1} width, finally a fifth, very narrow, gap appears centered at 1863cm^{-1} with only 3cm^{-1} width (possibly a calculation artifact). For G688 there are no longer gaps in the investigated region. For the larger structures, it is difficult to establish the existence of gaps because we

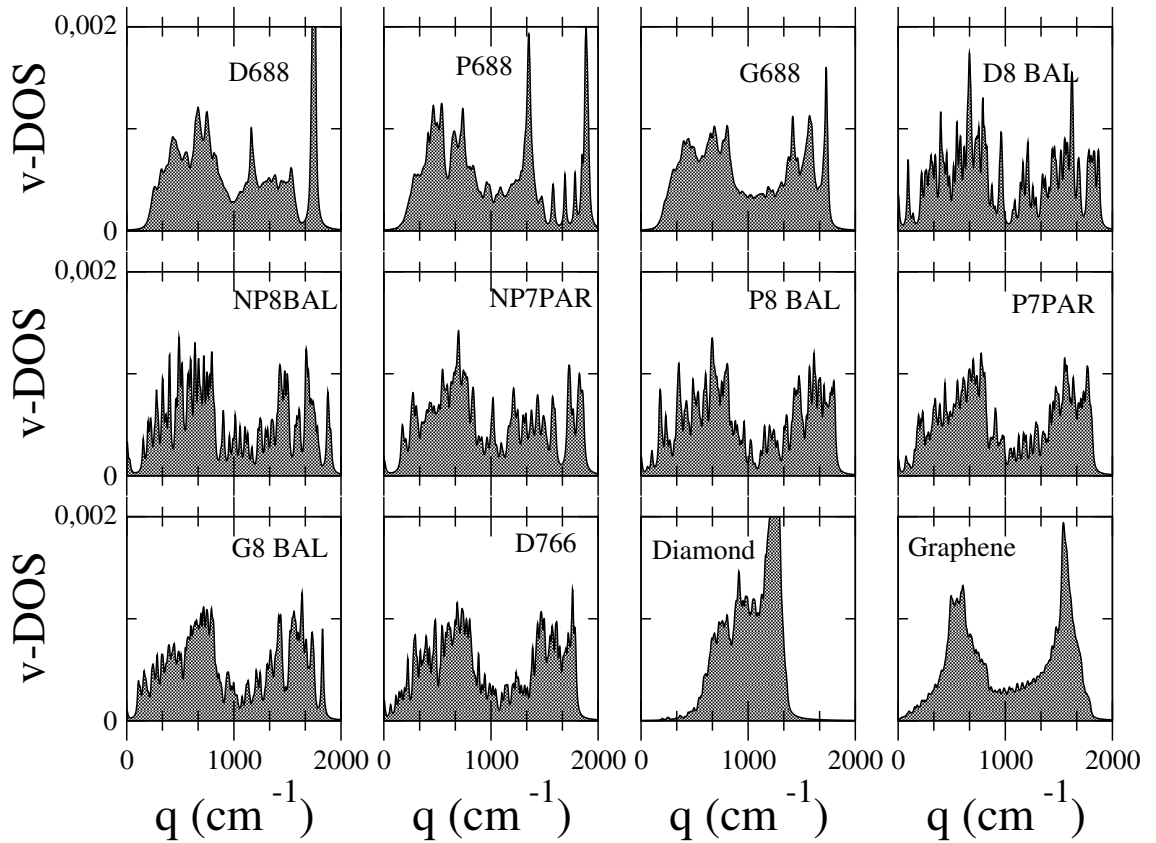


Figure 3.21: Vibrational Density of states for nine Schwarzite models, normalized to the unity. The spectra shown for P8BAL and larger structures, actually correspond only to gamma point vibrations. A Lorentzian broadening of 3cm^{-1} was used in the calculation of the densities.

are limited to the vibrations at the gamma point. These vibrations, seems to fill rather densely the range of allowed wave vectors and those structures are unlikely to develop vibrational gaps. As a matter of fact, with the used Lorentzian broadening, no clear gap structure appears for P8BAL, P7PAR and G8BAL (see fig. 3.21) .

As is to be expected for sp^2 hybridized networks, all these structures exhibit rather high v-dos near the main graphene peak (around 1540cm^{-1}), nevertheless this feature is no longer the most relevant in the v-dos spectra.

The vibrational spectra, can be experimentally investigated in a wide range of frequencies, using Inelastic Neutron Scattering. The rich peak structure of the smaller cells, suggest the use of vibrational spectroscopy in order to identify Schwarzite structures. However, when the number of atoms in the unit cell increases, that

Structure	$E(\text{KJ mol}^{-1})$	$F(\text{KJ mol}^{-1})$	$S(\text{J mol}^{-1}\text{K}^{-1})$	$C(\text{J mol}^{-1} \text{K}^{-1})$
D688	18.68	17.44	4.15	7.89
P688	18.52	17.28	4.24	7.96
G688	18.68	17.44	4.15	7.89
D8BAL	18.76	16.78	6.62	8.42
NP8BAL	18.74	16.87	6.23	8.49
NP7PAR	18.45	16.69	5.87	8.44
P8BAL	18.79	17.00	5.99	8.30
P7PAR	18.77	17.02	5.71	8.28
G8BAL	18.60	16.91	5.63	8.36
D766	18.68	16.91	5.89	8.34

Table 3.7: Vibrational contribution to the Total Energy E , Free Energy F , Entropy S and Specific Heat C at 300K for the studied models

identification would be more difficult: the overall shapes of the spectra are very similar to those observed for amorphous carbon structures. Still, there is some structure in the very low frequency region (below 400cm^{-1}) that could be experimentally measurable. More specific spectroscopic techniques, such as Raman and IR spectroscopy, may help in the experimental identification.

Now we turn our attention to the thermodynamic potentials for the carbon Schwarzkite structures. In table 3.7, we have reported the calculated values of the vibrational contribution to the Total Energy (E), Free Energy (F), Entropy (S), and specific Heat (C), at 300K, for the studied negatively-curved structures. One could distinguish clear similarities between G688 and D688 (actually both structures exhibit the same values). The lower density frameworks, exhibit higher specific heats, entropies and lower Free Energies.

The dependence of the thermodynamic potentials with temperature for the polybenzene structure is sketched in figure 3.22. The profiles are just the same for the remaining models. The behavior of these quantities, is very similar to that of other carbon structures, such as diamond and graphite. The heat capacity indicates that

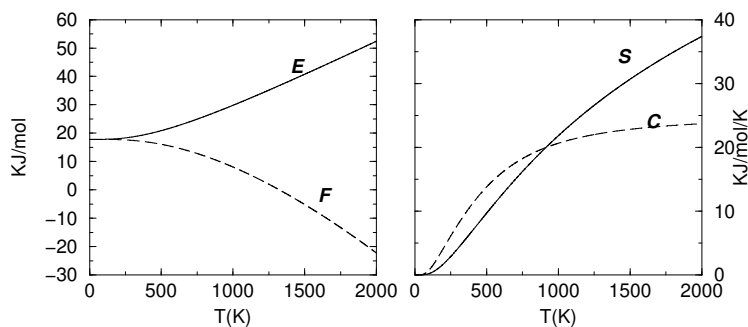


Figure 3.22: Temperature dependence of the thermodynamic variables for polybenzene (D688) structure

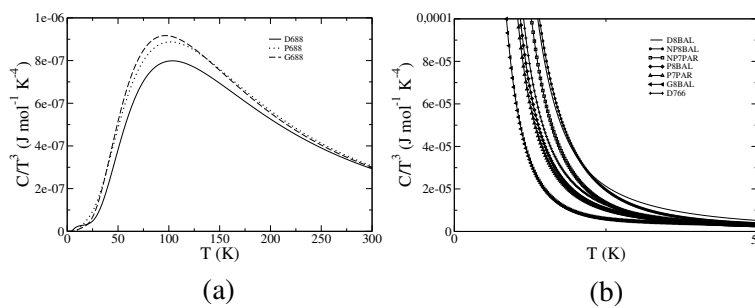


Figure 3.23: The low temperature region of the C/T^3 curves for the carbon Schwarzites, calculated from the vibrational densities of states. (a) For the highest density frameworks (688 structures), (b) for the low density crystals.

the D688 structure behaves as a Debye crystal at about 1000K; the same is true for the other studied structures.

The low temperature behavior of the C/T^3 curve is depicted in figure 3.23. The calculated specific heats fail to reproduce the expected $1/T^3$ law in the low temperature region. This flaw is related to the lack of states in the v-DOS in the very low energy region. Because of the size of the supercells (and q – point grids) used for the calculations, the densities of states near “0” frequency do not follow an w^2 law. The drawbacks of the very v-DOS in the low frequency region are, as expected, more notorious for the larger cells, for which we have access only to the Γ point vibrations.

3.8 Doping Schwarzites with boron and nitrogen: substitutional and pyridine-like defects.

Let us consider what can be obtained if Schwarzite structures are electronically enriched with the inclusion of Boron or Nitrogen atoms. Because the differences in the number of valence electrons, the electronic structure of these systems could be expected to be considerably modified, as is the case for doped carbon nanotubes [169].

First we studied the case of the polybenzene (D688) structure. The rather large electronic band gap makes this structure particularly appealing for doping, as large densities at the Fermi level could be expected whenever electrons are promoted to the conduction bands. We substitute a single carbon atom out of the 24 equivalent atoms in the unit cell of D688 either by Boron or Nitrogen. The structures have been relaxed, following the same methodology discussed previously, using again the Seifert set of tight-binding parameters [109]. For both Boron and Nitrogen substitutions, the mechanical stability of the structure is preserved, and only slight changes in the lattice parameters were observed. The internal coordinates remain unchanged. The Bulk modulus is 335GPa for Nitrogen inclusions, consistent with the decrease of the lattice parameter (about 1% less than in the pristine structure). For Boron, the bulk modulus decreases to 310GPa, consistent with the slight expansion of the lattice; the lattice parameter being decreased by about 1%. The mechanical properties are, therefore, dominated by those of the pure carbon cell.

As depicted in Fig. 3.24, effective doping is achieved via Nitrogen substitution with the expected large density of states at the Fermi level. The rationale of this result is the fact that the electronic density of states is mostly the same for the doped and the pristine structure; being mainly determined by the contribution from the Π -C partial density of states. The carbon structure acts, therefore, as a host for the Nitrogen impurity, thus shifting the Fermi level to the conduction band in order to allocate an additional electron.

The opposite behavior is observed for Boron inclusions. The electronic structure is also dominated by the pristine cell structure, and the Fermi level is slightly shifted

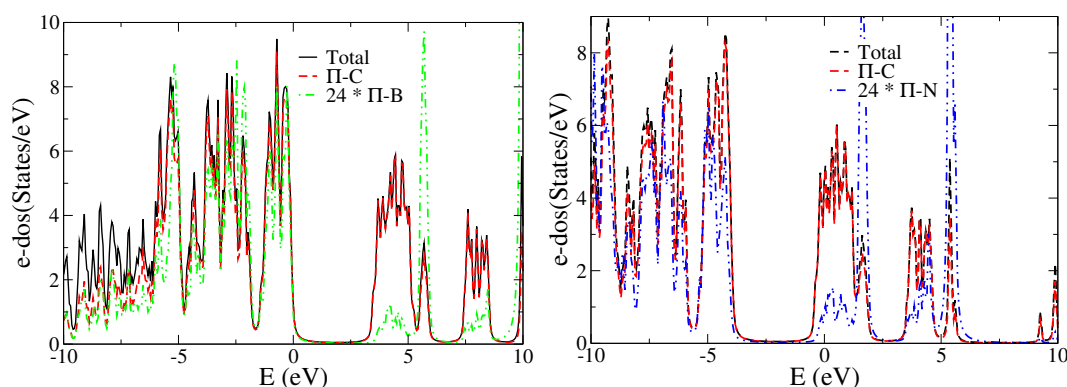


Figure 3.24: Electronic density of states for the D688 structure with Boron (left panel) and Nitrogen (right panel) substitution. Energies are measured with respect to the Fermi level. The contributions of the Π states to the partial densities of states are also shown. Calculations were performed using the Seifert parametrization [109]

to the left due to the lack of electrons. This means that the last valence band is partially filled.

DFT results calculations were performed for the polybenzene structure with Nitrogen and Boron substitution, within the same approach we used for the pristine cell (see section 3.3). These calculations confirmed the results obtained using the tight-binding approach. Because for carbon-based systems, the Kohn-Sham orbitals usually resemble the quasiparticle's amplitudes (see appendix A and B), the effects of the doping on the local electronic properties can be assessed by looking at the corresponding HOMO and LUMO orbitals. The HOMO orbital provide us information regarding the parts of the model that are more likely to be accessible via nucleophilic attacks. Similarly, the LUMO orbital is related to accessibility via electrophilic attacks. For the metallic systems, the HOMO and LUMO levels are the same, and what we show is just a plot of the density charge for orbitals near the Fermi level. The results using the PW91 exchange correlation energy [57] for the orbitals are shown figure 3.25. These orbitals are consistent with localization of the sites accessible to nucleophilic and electrophilic attacks, on the B and N atoms, so that B and N substitutions can be considered as really promoters of the chemical activity in the sites where they lie.

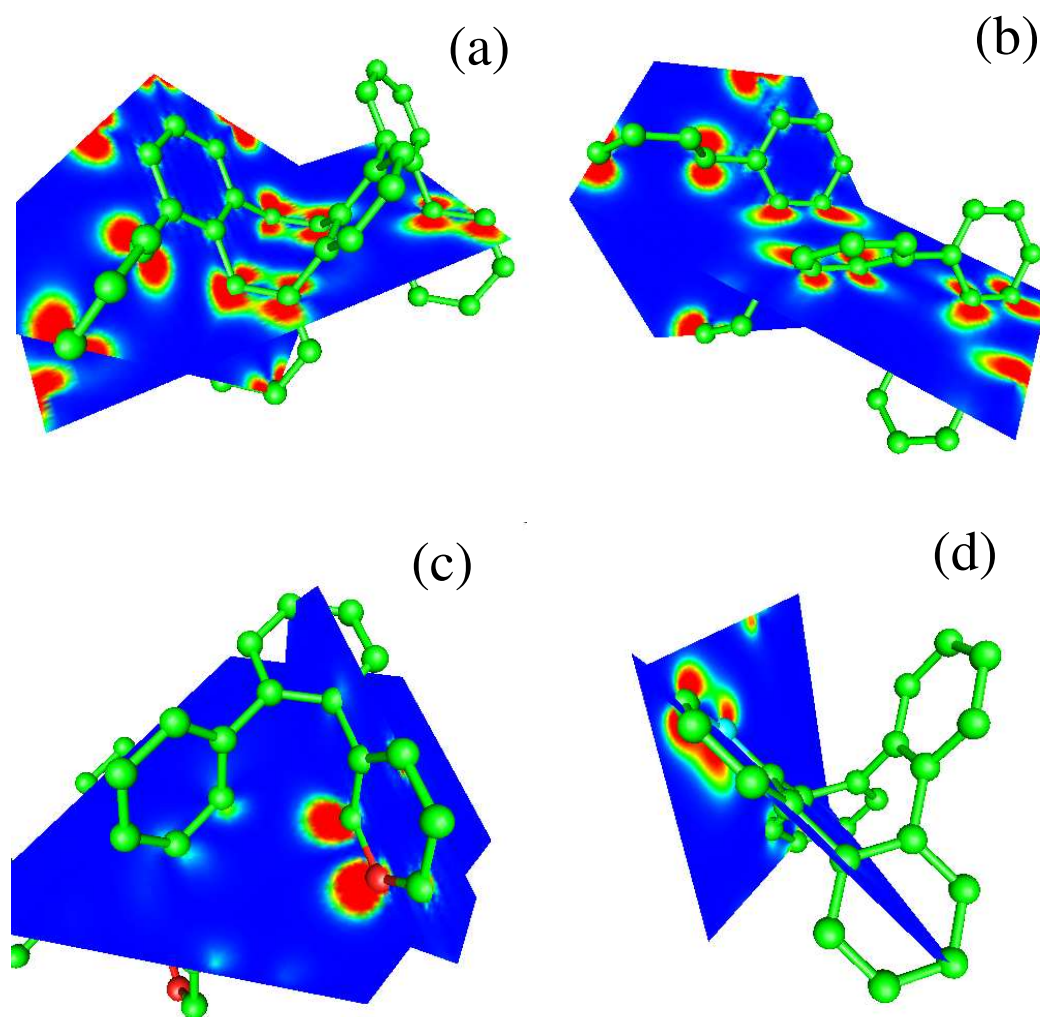


Figure 3.25: Representation of the HOMO (a) and LUMO (b) orbitals for the D688 structure, and orbitals near the Fermi level for the N enriched (c) and B enriched (species). In the color map, higher densities are colored in red.

The same analysis has been carried for the next smaller cells (G688 and P688 structures) with overall similar results. This fact reinforces the reliability of our tight-binding analysis, at least at qualitative levels.

We studied also the effects of substitutional doping on the D8BAL, P8BAL and NP8BAL structures. Those structures were selected because of their mechanical stability and their electronic band gaps. In each case, the internal coordinates remain unchanged by the relaxation procedure after doping, and the mechanical properties closely resemble those of the corresponding pristine pure carbon structures.

As shown in Fig. 3.26, where the electronic density of states for Nitrogen-doped structures is shown, Nitrogen substitutions in each case have the effect of including an additional electron, thus turning the structures into metals. As expected, larger e-dos near the Fermi level is obtained for P8BAL; this one exhibiting the larger gap in the original framework (no doping).

Let us consider the effect of pyridine-like substitutions, in which one carbon atom is removed and its three neighbors replaced by Nitrogen atoms. This structure is lacking of a valence electron, if compared to the original pure carbon counterpart. This kind of substitutions are also feasible experimentally in carbon nanostructures, and could also modify the chemical and electronic activity. Systems in the 688 family, including polybenzene, are not suitable for this replacement; because each carbon atom is shared by two octagons and pyridine-like substitution will result in distant nitrogen atoms. Mechanical stability would be seriously compromised under such conditions.

We have chosen the P8BAL and D8BAL as test systems because they have patches consisting of neighboring hexagons. Pyridine-like substitutions are, therefore, possible with Nitrogen atoms staying at reasonable distances, as shown in Fig. 3.27.

The mechanical properties can be significantly altered by the presence of the pyridine-like defect, as shown in figure 3.28. There the energy as function of lattice volume is shown for the defective D8BAL structure. The bulk modulus is slightly larger than in the pristine pure carbon structure (194GPa vs 174GPa), but at the cost of higher order terms in the Birch-Murnaham equation (up to order five terms

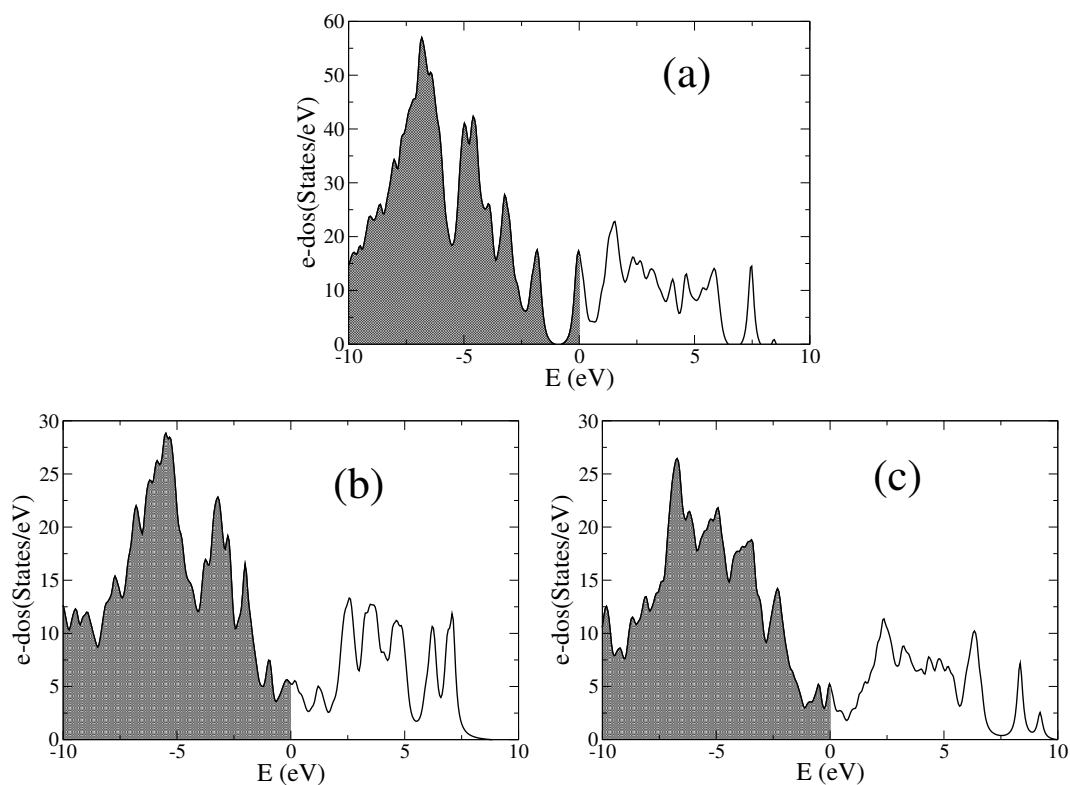


Figure 3.26: Electronic density of states (e-DOS) for P8BAL (a), NP8BAL (b) and D8BAL(c) with a Nitrogen in substitution, calculated with the Seifert parametrization [109]. The Fermi level is located at “0” energy.

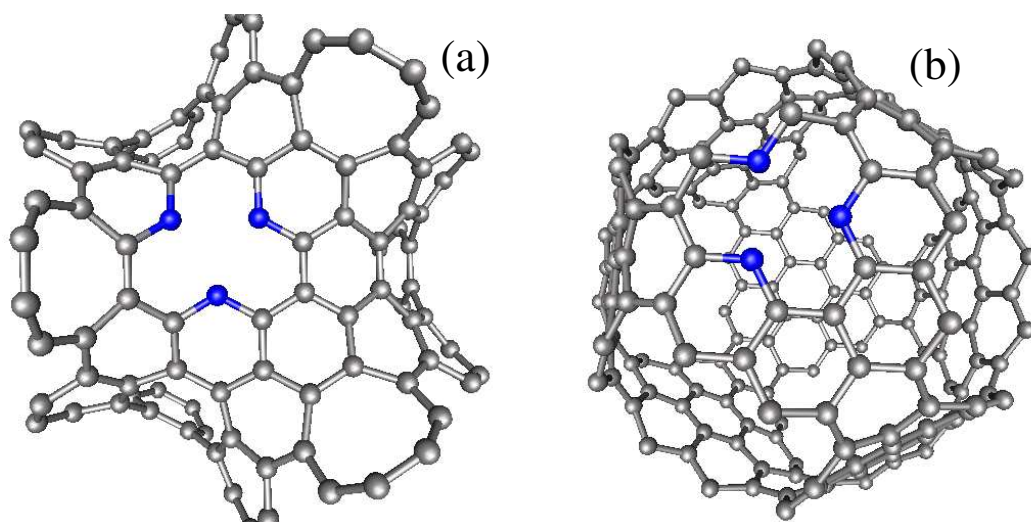


Figure 3.27: Molecular models for unrelaxed pyridine-like defect on the P8BAL (a), and D8BAL(b) frameworks.

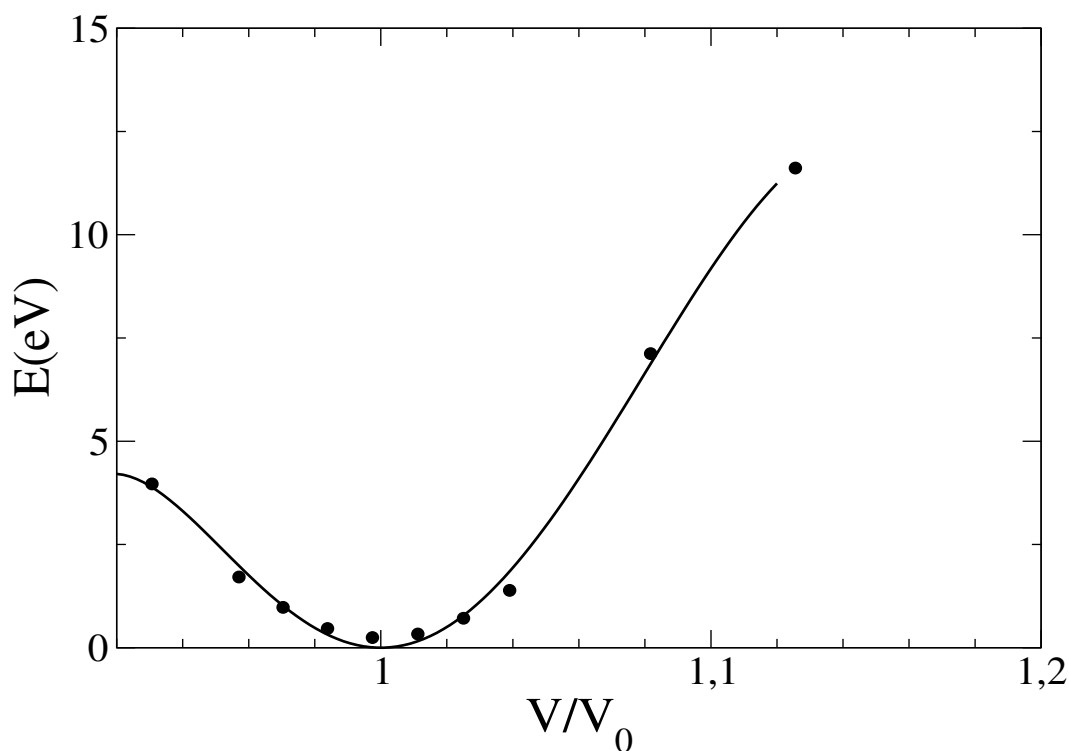


Figure 3.28: Energy vs. volume (normalized to the optimal volume) for the D8BAL structure with a pyridine-like defect. Points are the calculated data and the curve is a fit to the Birch-Murnaham equation.

were included in order to obtain the curve shown in figure 3.28).

Even for the 8BAL family, significant changes in the internal coordinates appear during the relaxation process, specially near the pyridine-like group; as can be seen when comparing the unrelaxed structures of figure 3.27 with the relaxed ones in figures 3.29 and 3.30. Note that the defective D8BAL structure was fully relaxed (both lattice parameters and internal coordinates), meanwhile in the case of P8BAL we have relaxed only the internal coordinates at the original lattice parameter. Considering that the observed change in the lattice parameter of the D8BAL structure was less than 1%, we do not think that lattice relaxation would induce large changes in the electronic structure of the pyridine-like doped P8BAL structure.

The influence of pyridine-like inclusions in the density of states is more significant than that of direct substitutions (figures 3.29 and 3.30). New states, arising from the Π -N contributions, appear in the *old* (no doping) conduction band.

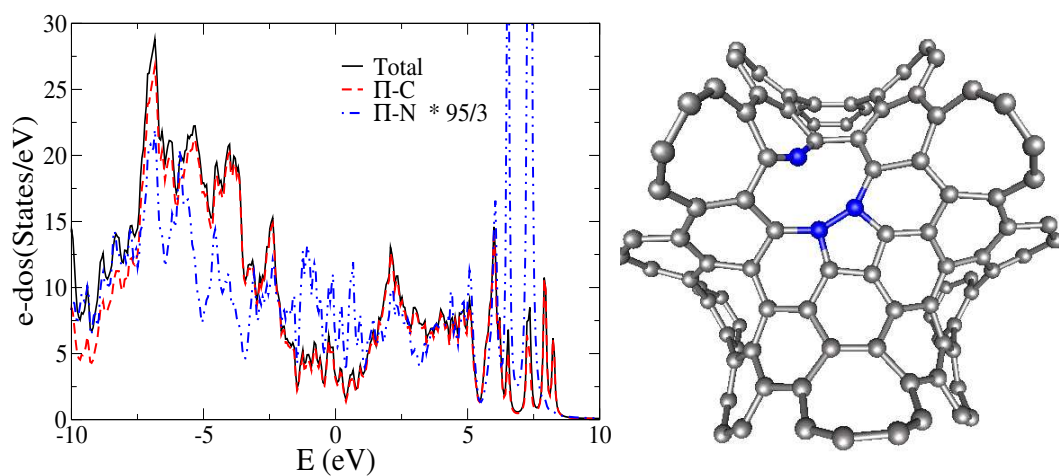


Figure 3.29: Left panel: Electronic density of states for the D8BAL structure with a pyridine-like defect, calculated using the Seifert parametrization. Partial contributions from the Π carbon and nitrogen states are also shown. Right panel: optimized geometry for this framework

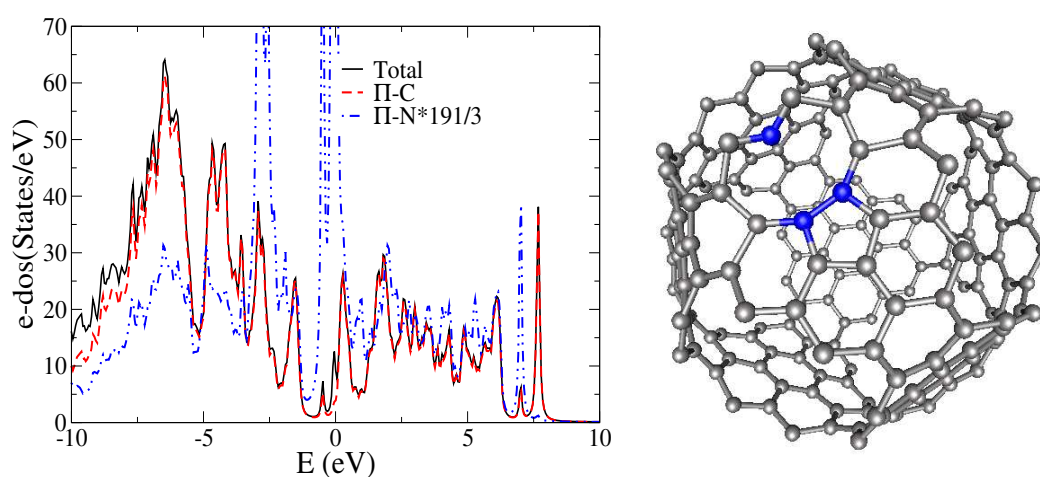


Figure 3.30: Same as figure 3.29 for the P8BAL framework.

In conclusion, effective doping with Nitrogen could be achieved in these Schwarzite frameworks using substitutional or pyridine-like inclusions. Substitutional inclusions do not affect the mechanical properties. Pyridine-like defects may compromise the mechanical strength, but they may be more chemically reactive. Further work on the chemical properties of pyridine-like substitutions is required. In the case of Boron substitutions, we noted that the systems were metallic with the Fermi level half-filled.

3.9 A note on synthesis attempts

We have performed some preliminary experimental works attempting to synthesize Schwarzite structures, at least as disordered phases. Our approach is based on the Chemical Vapor Deposition (CVD) method, and inspired by the results of Terasaki et. al. on nanoporous carbons [36]. The Na-Y and Z-14US Zeolites, were tested as templates. Impregnation of these molecular sieves with carbon precursors was attempted, dissolving the zeolites in a solution containing toluene (90%) and ferrocene (10%). The zeolite-toluene-ferrocene solutions were submerged in a sonic bath during 30 minutes, and subsequently left to dry at air. The resultant powder was pyrolysed during 15 min. at 800 degrees Celsius and 860 degrees Celsius in a powder-pyrolysis configuration. The results at this stage are far from conclusive, but we do believe that growth of carbon structures in such crystalline frameworks could lead to crystalline negatively curved structures.

Chapter 4

Laser pulses interacting with matter.

*I can see
what you mean
it just takes me longer...*
In the end, RUSH.

4.1 Overview.

There are various complexities associated to the theoretical description of the interaction between a material system and a strong laser pulse. The phenomena lie beyond the first order perturbation theory, and comprise highly non-thermal behavior. Due to the interaction with the electromagnetic fields, the material system is promoted to highly excited states. In the simple single-particle description (see appendix A), these excited states should be described by the promotion of a large fraction of electrons to virtual orbitals.

Attempts for describing this interaction by means of *state-of-the-art* theories like the Time Density Functional Theory, has been successful only for small sized systems interacting with highly coherent laser pulses. In this scenario, excitations occur mainly to one of the system's excited states [126]. The validity of former considerations, would be compromised in a wide variety of practical situations; real

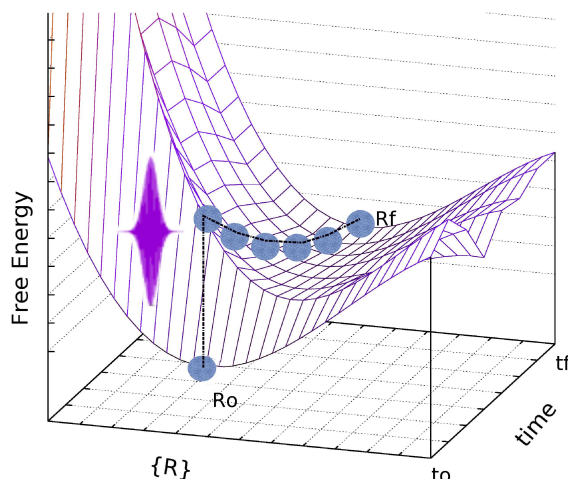


Figure 4.1: Schematic representation of the laser induced processes: the system is moving in a time dependent free energy surface which vary significantly during the pulse duration. Eventually, the system reaches a new equilibrium position.

femtosecond lasers create various electronic excitations, which then could interact among themselves, and with the atomic lattice, in a highly non-coherent fashion. In the single particle picture, electron-electron collisions, and electron-phonon interactions, should be taken into consideration.

We start this section by summarizing the main processes involved in the laser-matter interaction, within a single particle picture and the Born-Oppenheimer approximation:

1. The system is initially at an equilibrium configuration, as depicted in the simple representation of figure 4.1. The laser pulse excites the electronic system, populating various excited states.
2. The excited electron cloud provides the modified Potential Energy surface where the ions move.
3. Electron-electron collisions and electron-ion interactions take place.
4. The change in the ionic coordinates changes the external potential felt by the electrons.
5. The process from 2-4 continues until the system reaches a new equilibrium position.

4.2 A practical realization: Tight-binding modeling plus molecular dynamics.

A very appealing model for simulating laser induced transitions have been developed by Harald Jeschke and M. Garcia [127]. Their theoretical framework, is based upon a tight-binding description of the electronic states, provided that the electronic occupations are changed by the laser pulse. Molecular dynamics in the excited states Potential energy surface is then performed. In this section we review the original Garcia and Jeshcke scheme.

4.2.1 Evolution of the occupation numbers

The laser excitation is described by an increase in the occupation of virtual levels according to (see appendix F):

$$\frac{dn(e_m, t)}{dt} = \int_{-\infty}^{\infty} dw g(w, t - \Delta t) \{n(e_m - \hbar w, t - \Delta t) + n(e_m + \hbar w, t - \Delta t) + 2n(e_m, t)\} \quad (4.1)$$

where $g(w, t)$ is the laser's intensity distribution and $n(e_m, t)$ is the occupation number of the state with energy e_m . The above equation represents electrons going from a state e_m to a state with energy $e_m + \hbar w$, and electrons coming from $e_m - \hbar w$ to e_m .

The accurate description of the complex electron-electron collision processes lie beyond the scope of this work. Instead of a microscopic description, they are treated in a phenomenological way by means of a suitable relaxation time so that:

$$\frac{dn(e, t)}{dt} = -\frac{n(e, t) - n_T(e, T_{el})}{\tau_e} \quad (4.2)$$

where n_T is the thermal distribution to which electrons would approach in a given time.

This thermalized distribution is forced to preserve the number of electrons and the total electronic temperature, because it is defined as the equilibrium distribution that the system would reach if the remaining parameters were held constant (no

more laser irradiation or ionic motions). Therefore, the equilibrium distribution parameters T_{el} and μ_e are given by the conditions:

$$\begin{aligned} Ne &= \sum_{e_i} n(e_i, t) = \int \hat{n}(\varepsilon, T_{el}, \mu_e) d\varepsilon \\ E &= \sum_{e_i} e_i n(e_i, t) = \int \hat{n}(\varepsilon, T_{el}, \mu_e) \varepsilon d\varepsilon \end{aligned} \quad (4.3)$$

Finally, the lost of electronic energy due to interactions with the lattice vibrations is also described phenomenologically by means of the equilibration between electronic and lattice temperatures:

$$\frac{dT_{el}}{dt} = -\frac{T_{el} - T_{ions}}{\tau_2} \quad (4.4)$$

The philosophy behind this description has been discussed in detail in Refs. [44, 128, 129].

4.2.2 Free energy and ionic motion

The ionic dynamics is ruled by the free energy surface. This thermodynamic potential is defined through its general differentials:

$$\delta U = \delta E_{rep} + \mathbf{Tr}((\delta H_o)\rho) \quad (4.5)$$

where E_{rep} is a core-core repulsive term, ρ is the density matrix, and H_o is a tight-binding Hamiltonian with distance-dependent hopping matrix elements.

The k -th component of the force acting on the i -th ion, F_i^k , is computed, then, as:

$$F_i^k(t) = -\frac{\partial}{\partial x_i^k} U \quad (4.6)$$

with x_i^k being the k -th component of the position vector r_i , which is simply:

$$F_i^k(t) = -\mathbf{Tr}\left(\frac{\partial H_o}{\partial x_i^k} \rho\right) - \frac{\partial E_{rep}}{\partial x_i^k} \quad (4.7)$$

In the particular case of a Fermi-like distribution, the free energy can be written as:

$$U[\{r_{ij}\}, \{n_l(t)\}] = E_{rep} + \mathbf{Tr}H_o\rho - T_e S_e \quad (4.8)$$

where $n_l(t)$ are the electronic occupations of the electronic levels, T_e is the electronic temperature and S_e is the electronic entropy defined as [131]:

$$S_e = - \sum_l 2k_B (f_l \mathbf{log}(f_l) + (1 - f_l) \mathbf{log}(1 - f_l)) \quad (4.9)$$

with $f_l = n_l/2$.

As a matter of fact, for the definition given in Eq. 4.8

$$\begin{aligned} \delta U = & \delta \mathbf{Tr}(H\rho) - \delta E_{rep} + \delta T_e S_e \\ & \mathbf{Tr}(\delta H\rho) + \mathbf{Tr}(H_0\delta\rho) - \delta E_{rep} + \delta T_e S_e \\ & \mathbf{Tr}(\delta H\rho) + \mathbf{Tr}(H_0\delta\rho) - \delta E_{rep} + T_e \delta S_e \end{aligned} \quad (4.10)$$

The traces in the second and fourth terms on the last line can be easily evaluated in the eigenvector basis set with the implicit assumption that ρ is diagonal in that particular basis (as discussed in appendix F) and we have:

$$\begin{aligned} \mathbf{Tr}(H_0\delta\rho) &= \sum_l E_l \delta n_l \\ T_e \delta S_e &= \sum_l (E_l - \mu) \delta n_l \end{aligned} \quad (4.11)$$

Only neutral excitations occur, thus we should always have $\sum \frac{\partial n_l}{\partial x_i^k} = 0$. Consequently, the second and fourth terms in equation 4.10 cancel each other, and we obtain the condition stated in Eq. 4.5.

We did not attempt to calculate the exact form of the free energy and used Eq. 4.8 as an approximation for this thermodynamic potential in our analysis. As long as $e - e$ relaxation times are not very large, a sensible amount of electrons are promoted, electronic excitations are not highly localized in the energy axis, and because the conditions expressed in Eqs. 4.3 are imposed in each time step, this approximation is suitable for the studied systems.

The TB parameters have the form given by Pettifor et al. Ref. [132], which fits well for the molecular dynamics approach, and provide reliable results for electronic

properties (band structures and gaps). Within this parametrization, the hopping terms and repulsive potentials vary as function of the ionic separation r like:

$$\begin{aligned} \tau_{\delta\eta}(r) &= V_{\delta\eta} \left(\frac{r_0}{r}\right)^n \mathbf{exp} \left\{ n \left[-\left(\frac{r}{r_c}\right)^{n_c} + \left(\frac{r_0}{r_c}\right)^{n_c} \right] \right\} \\ \phi(r) &= \phi_0 \left(\frac{d_0}{r}\right)^m \mathbf{exp} \left\{ n \left[-\left(\frac{r}{d_c}\right)^{m_c} + \left(\frac{d_0}{d_c}\right)^{m_c} \right] \right\} \\ E_{rep} &= \sum_i F_{emb} \left(\sum_{j \neq i} \phi(r_{ij}) \right) \end{aligned} \quad (4.12)$$

and the derivatives of the hopping parameters and of the repulsive energy can be analytically evaluated.

4.2.3 The charge transfer problem

When we consider a multicomponent system like a multi-walled carbon nanotube or separated fullerenes, we face three problems leading to spurious charge transfers between them:

(i) The changes in the Hamiltonian matrix and eigenvectors induced by ionic motions lead to charge transfer as has already been discussed in the literature (see, for example [65]). Indeed, this problem stands also for covalently joined systems. However, for systems made of the same atomic species, this effect is usually very small both for periodic systems and for medium sized cluster. This point is related to the transferability of the tight-binding parameters, discussed in appendix C.

(ii) As we are within the Linear Combination of Atomic Orbitals framework, spatially separated systems should perform spatially separated eigenvectors. However, the transition probabilities appearing in eq. 4.1, depend only on the energy differences. Therefore, non-zero transfer rates could appear between eigenstates localized in separated regions of the space, leading again to unphysical charge transfer. This effect can be effectively corrected by the introduction of the dipolar matrix discussed in the next section.

(iii) The limit thermal distribution uses global parameters, and does not take into account the multicomponent character; any non-thermal occupation will be distributed across the entire system without considering the localized character of

the excited eigenvector. This is a rather complex issue, especially if we want to deal with non uniform multicomponent systems (as the multi-walled carbon nanotubes) and long simulation periods (so that electron thermalization cannot be simply disregarded). The standard procedure of including an energetic penalty for this process [134] is not very appealing, because it will not avoid unphysical charge transfer; instead, the geometrical configuration would change when electronic relaxation takes place. By imposing local charge neutrality [65], the calculation would also be very problematic; the physically meaningful laser-induced charge transfer would be forbidden. Taking all these considerations into account, this third point requires a major generalization of our simulation scheme, as will be discussed in the following sections.

4.3 Extending the model I: Polarization Effects

As we are mainly concerned with frequencies in the visible and ultraviolet region, direct coupling of the laser field with the ionic degrees of freedom is strongly hindered. Still, field polarization effects would appear in the interaction between the laser pulse and the electronic system.

In deriving equation 4.1, the Hamiltonian for the system in the presence of laser irradiation is assumed to be of the form (see appendix F):

$$H = H_o + H_I = \sum_m E_m \hat{c}_m^\dagger \hat{c}_m + \sum_{m,n} g_{mn} \hat{c}_m^\dagger \hat{c}_n \quad (4.13)$$

where \hat{c}_m^\dagger and \hat{c}_n^\dagger are creation operators corresponding to given eigenstates of the unperturbed Hamiltonian H_0 with energies E_m and E_n respectively. The operator g coupling different levels through the laser irradiation has the general form:

$$g_{mn} = E(t) X_{mn} \quad (4.14)$$

but the dipole matrix, X_{mn} , is assumed to be constant and equal to the unity for each (m, n) pair.

In order to account for polarization effects we have, as a first approach, to recall the dependence of the transition probabilities which depend on the eigenvectors

symmetry, and on the field polarization, i.e., we have to put back into play the X_{mn} matrix.

A consistent formula for the dipole matrix can be derived without resorting to external parameters starting from the Pierls substitution [135]. The original tight-binding Hamiltonian is given by:

$$H_0 = \sum_{i,\delta} \varepsilon_{i\delta} \hat{c}_{i\delta}^\dagger \hat{c}_{i\delta} + \sum_{i\delta j\eta} \tau_{\delta\eta} (R_i - R_j) \hat{c}_{i\delta}^\dagger \hat{c}_{j\eta} \quad (4.15)$$

where now we are working in the localized orbitals basis, i.e. $\hat{c}_{i\delta}^\dagger, \hat{c}_{j\eta}^\dagger$ create electrons in atomic orbitals localized at atoms i, j , and with orbital symmetries δ, η , $\varepsilon_{i\delta}$ are the onsite energies, and $\tau_{\delta\eta} (R_i - R_j)$ are the hopping parameters. The Hamiltonian under an electromagnetic field with potentials (Φ, \mathbf{A}) is transformed to:

$$H = \sum_{i,\delta} (\varepsilon_{i\delta} + e\Phi) \hat{c}_{i\delta}^\dagger \hat{c}_{i\delta} + \sum_{i\delta j\eta} \tau_{\delta\eta} (R_i - R_j) \times \exp\left(-\frac{ie}{2\hbar c} (R_i - R_j) \cdot [\mathbf{A}(R_i, t) + \mathbf{A}(R_j, t)]\right) \hat{c}_{i\delta}^\dagger \hat{c}_{j\eta} \quad (4.16)$$

In the dipole approximation, we take $\Phi = 0$ and assume that \mathbf{A} is small and does not depend on \mathbf{R} (i.e. we neglect the magnetic field effects). Then, we have:

$$H = \sum_{i,\delta} \varepsilon_{i\delta} \hat{c}_{i\delta}^\dagger \hat{c}_{i\delta} + \sum_{i\delta j\eta} \tau_{\nu\eta} (R_i - R_j) \times \left(1 - \frac{ie}{\hbar c} (R_i - R_j) \cdot \mathbf{A}(t) + \dots\right) \hat{c}_{i\delta}^\dagger \hat{c}_{j\eta} \quad (4.17)$$

Furthermore, the vector potential corresponding to a time dependent electric field in the direction of the polarization vector ε_p can be written as:

$$\mathbf{A}(t) = \vec{\varepsilon}_p A(t) \quad (4.18)$$

where $A(t)$ is now an scalar quantity. We should have then, in the dipolar approximation:

$$H = H_o + H_1 = H_0 - i \frac{e}{\hbar c} \sum_{i\delta j\eta} \tau_{\delta\eta} (R_i - R_j) \times (\vec{\varepsilon}_p \cdot (R_i - R_j) A(t)) \hat{c}_{i\delta}^\dagger \hat{c}_{j\eta} \quad (4.19)$$

So, by recalling equations 4.15 and 4.14, we can write the dipole matrix elements in the H_0 eigenvectors basis set as:

$$X_{mn} = \frac{-ie}{\hbar\omega} \sum_{i\delta j\eta} \tau_{\delta\mu}(R_i - R_j) \times (\vec{\epsilon}_p \cdot (R_i - R_j)) C_{i\delta}(m) C_{j\eta}^*(n) \quad (4.20)$$

where we have used the basis transformations between the localized orbitals and eigenvectors basis:

$$\hat{c}_m^\dagger = \sum_{i\delta} C_{i\delta} \hat{c}_{i\delta}^\dagger \quad (4.21)$$

Formula 4.20 can also be derived from the usual expression for the field-matter interaction in the dipole approximation:

$$H_I = \frac{-e\mathbf{A} \cdot \mathbf{p}}{m_0 c} \quad (4.22)$$

using a consistent formula for the momentum operator [135], taken from the $\mathbf{k} \cdot \mathbf{p}$ perturbation theory:

$$P_{i\nu j\eta} = \frac{m_0}{\hbar} \nabla_{\mathbf{k}} H_{i\nu, j\eta}(\mathbf{k}) \quad (4.23)$$

where the Hamiltonian at different points of the Brillouin zone of a periodic system is given by :

$$H_{i\nu j\nu}(\mathbf{k}) = \sum_L \mathbf{e}^{i\mathbf{k} \cdot (R_i + R_L - R_j)} \tau_{i\nu, j\mu}(R_i + R_L - R_j) + \varepsilon_{i\nu} \delta_{ij} \delta_{\mu\nu} \quad (4.24)$$

where R_L is a lattice vector, equation 4.23 yields then:

$$P_{i\nu j\nu}(\mathbf{k}) = \sum_L i(R_i + R_L - R_j) \mathbf{e}^{i\mathbf{k} \cdot (R_i + R_L - R_j)} \tau_{i\nu, j\mu}(R_i + R_L - R_j) \quad (4.25)$$

so that equation 4.22, provides the same definition for the dipole matrix as equation 4.20, when we consider $\mathbf{k} = 0$. As a matter of fact, the definition of the momentum operator 4.23 is inspired in the same kind of perturbative analysis which lead us to the derivation of formula 4.20 in the first place [135].

Following the same steps as in appendix F, we can write, for the evolution of the occupation as function of laser irradiation:

$$\frac{dn(e_m, t)}{dt} = \int_{-\infty}^{\infty} dw g(w, t - \Delta t) |X_{lm}|^2 \{n(e_m - \hbar w, t - \Delta t) + n(e_m + \hbar w, t - \Delta t) + 2n(e_m, t)\} \quad (4.26)$$

The dipolar operator can be further complemented with semi-empirical intra-atomic terms. Nevertheless, in the frequency ranges we are interested (visible and ultraviolet light), the terms coming from Eq. 4.20 dominate the absorption process; contributions arising from inter-atomic terms would represent small corrections.

It is convenient to consider the influence of this modification in a highly unphysical but simple to analyze system; a simple cubic carbon cluster consisting of 64 carbon atoms (see figure 4.2) with only two valence electrons by atom (hence, no hybridization on the bonds). This is a highly unstable system, so we have performed *frozen-ions* simulations; the atomic coordinates are held constant and the occupation numbers are free to evolve according to equation 4.26, in the presence of a laser pulse of fixed frequency and width. In order to make the test even simpler, occupancy thermalization is hindered by setting a large value for the decay time $\tau_{ee} = 4400 fs$. We measured the forces occurring in the system in absence of laser field \mathbf{F}_{i0} and follow the evolution of the excess forces

$$F_i(t) - F_{i0},$$

during the duration of the laser pulse (200 fs integrated in 0.1 fs steps).

It is clear from figure 4.2, where the final configuration of excess forces is shown for two polarization directions, that forces are larger in the direction of the applied field. The average force magnitude in the laser direction is about 30% larger than the perpendicular components (see figure 4.3).

The previous test demonstrates that equation 4.26 can lead to sensible differences in the ionic dynamics. However, in realistic systems, both symmetry, bond hybridization and thermalization may frustrate polarization effects. As a second test, we performed a simulation at low temperature ($T_0 = 14K$) for a small capped nanotube (110 atoms) with laser pulses parallel and perpendicular to the tube's main axis. We used again $\tau_{e-e} = 4400 fs$. The excess force configurations after laser irradiation obtained in a frozen calculation and the Velocity Autocorrelation Func-

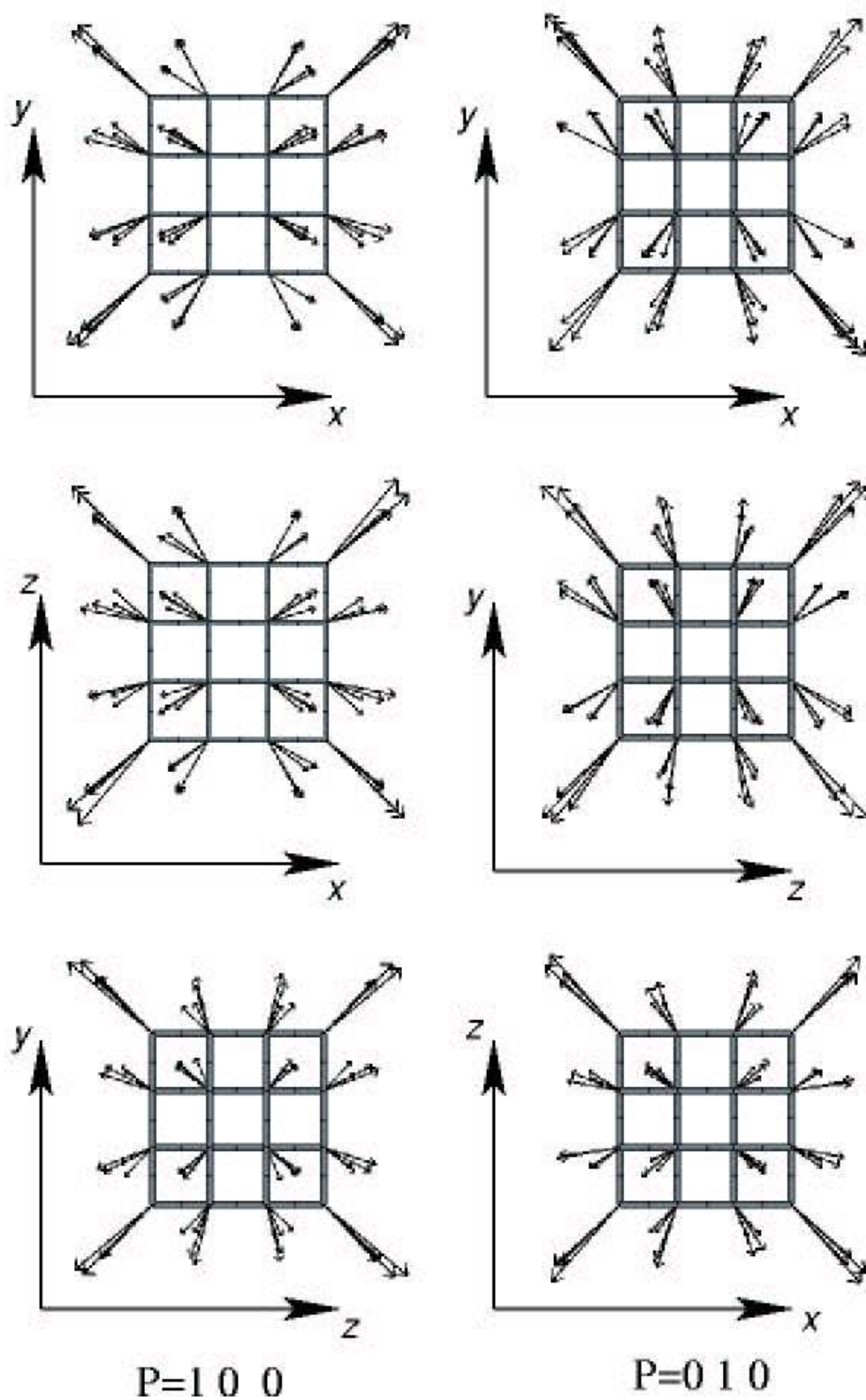


Figure 4.2: Excess force field configuration after laser irradiation in a simple cubic carbon cluster.

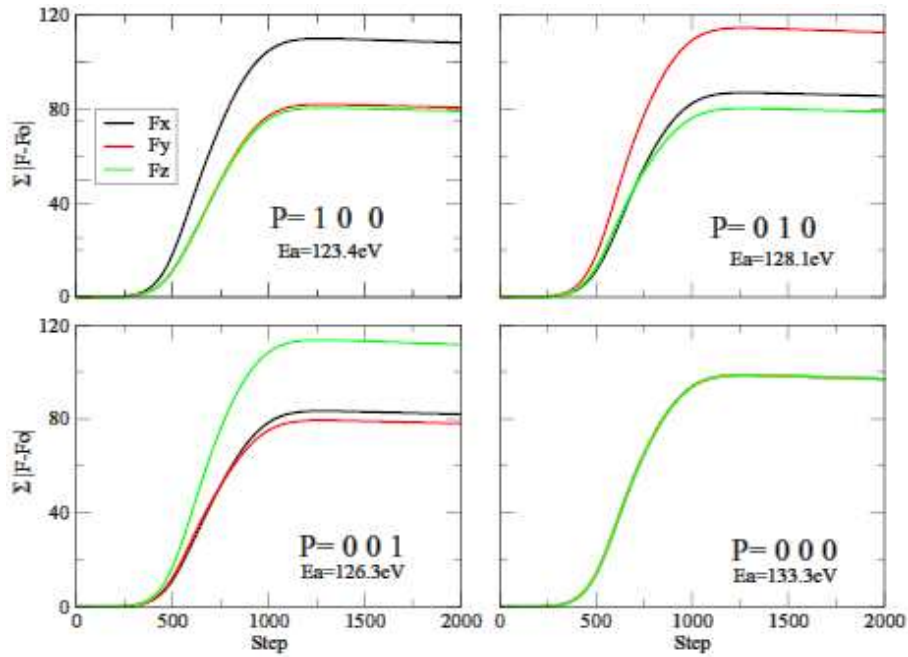


Figure 4.3: The overall excess force magnitude for different polarization directions in a cubic carbon cluster, $P=(0,0,0)$ stands for not-polarized light.

tion (VACF) obtained in a normal simulation, and calculated after laser irradiation are shown in figure 4.4.

Although the differences in the final force configurations are not as evident as in the simple cubic structure (a behavior that may be related to the orbital hybridization), it is still clear from the VACF that different vibrations have been activated in the system. It is also interesting to look at the atomic charge configuration in the frozen test, as they provide information on how the charge is moving when the laser is applied. In figure 4.5, we can clearly observe how for parallel fields, there is a clear charge transference from the center to the edges of the tube; something that we do not observe for perpendicular polarization.

A major effect of using equation 4.26, instead of Eq. 4.1 in real simulations (including thermalization effects), is witnessed in the amount of absorbed energy obtained with a given laser intensity. As a matter of fact, using Eq. 4.1, the absorption curve is described by the joint occupied-empty density of states

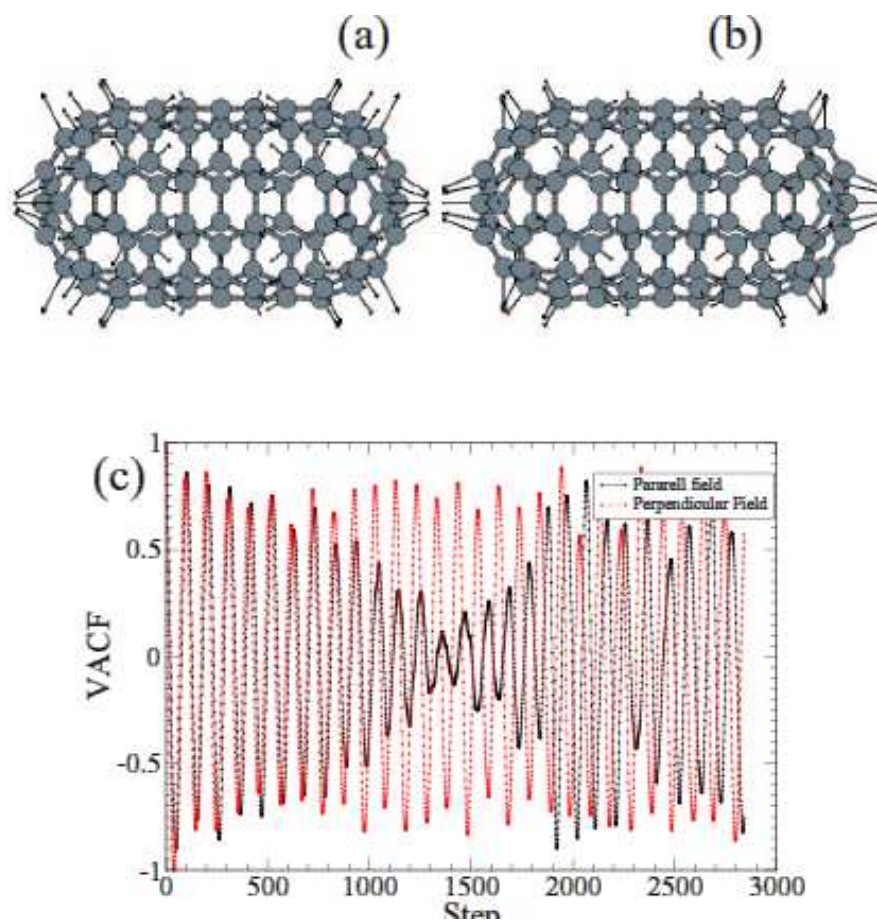


Figure 4.4: Top: Final force configuration for a capped nanotube for electric field parallel to the main axis (a), or perpendicular to it (b). Differences are significant only at the atoms bound to the pentagonal cap. Bottom: Velocity autocorrelation functions for both cases.

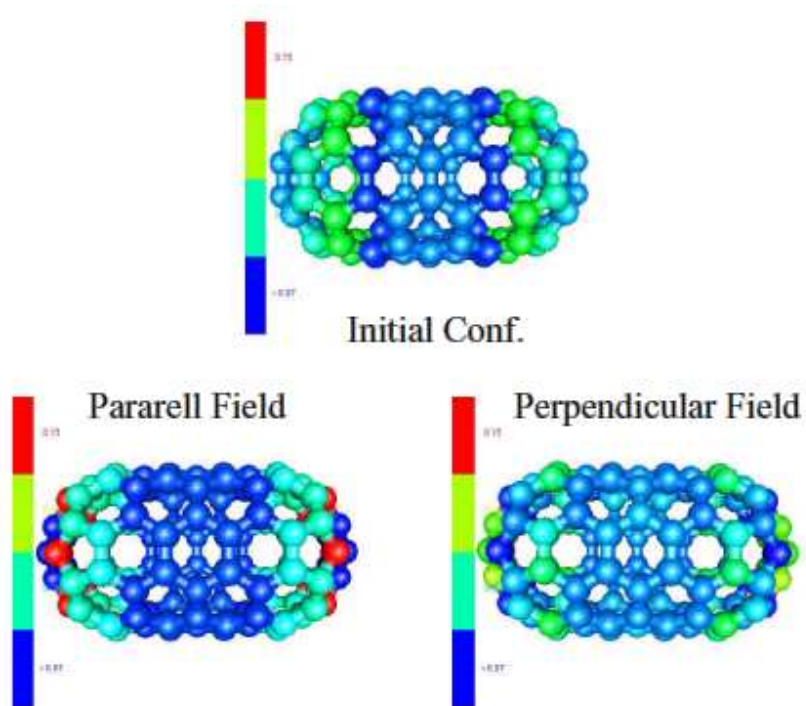


Figure 4.5: Initial and final charge configurations for a capped nanotube during with different directions of the electric field.

$$a(w) \sim \sum_{m=occ, n=empty} \delta(E_m - E_n + \hbar\omega) \quad (4.27)$$

meanwhile Eq. 4.26 relates the absorption to the RPA-like form of the imaginary part of the dielectric function:

$$a(w) \sim \sum_{m=occ, n=empty} \delta(E_m - E_n + \hbar\omega) P_{mn} \quad (4.28)$$

where P_{mn} is again the momentum operator. Whenever the differences between these two prescriptions are significant, in the relevant frequency range, the absorbed energy will be considerably different. Furthermore, the imposition of selection rules related to Eq. 4.28, leads to a significant reduction in the maximum amount of energy that the system could absorb.

The implementation of this kind of dipolar terms in the model, corrects partially the problem of unphysical charge transfer; transitions between eigenvectors localized on disconnected parts of the system are forbidden. It also provides valuable selection rules and makes the calculation scheme more flexible. The computational cost associated with this calculation is, unfortunately, high, as it involves large matrix multiplication. The major drawback is that it is a first order approach, and higher order processes leading to an increase of the effective transfer rate between eigenstates cannot be taken into account.

4.4 Extending the model II: Multiple atomic species

The molecular dynamic scheme described above can be extended, relatively easy to treat systems composed of multiple species (like binary semiconductors); provided that a set of tight-binding and repulsive energy terms of the form of Eqs. 4.12 is available for each pair of species. The parametrization tables can be constructed by following the methods described in refs. [65, 132, 134], but to the best of our knowledge, only Si-H and C-H interactions have been parametrized at present.

The C-H parametrization of ref. [65] would serve to illustrate the major point that must be taken into account when dealing with several atomic species; how to deal

with spurious charge transfers during the simulations. When different atomic species are considered, a significant amount of charge can be unphysically transferred from one site to another due to atomic motions. This problem is corrected by imposing Local Charge Neutrality (LCN), meaning that the Mulliken charge on each atom must be equal to the nominal valence of each atom:

$$Q_i = \sum_m \sum_\delta |C_{i\delta}(m)|^2 n(m) = N_i \quad (4.29)$$

where N_i is the number of valence electrons in the i -th atom. In order to achieve this condition, the onsite energy terms must be self-consistently shifted according to $\varepsilon_{i\delta} = \varepsilon_{i\delta} + \Delta\varepsilon_i$. As discussed in ref. [137], LCN is well justified for metallic and many semiconductor systems. When the condition is satisfied, the forces can be calculated just like in Eq. 4.7.

The relevance of LCN in this type of parametrization, especially for atoms with very different electron affinities (as is the case for Hydrogen and Carbon), can be easily inferred from figure 4.6, where the binding energy for methane with and without imposing LCN is shown. There it is clear that this particular tight-binding model, provides accurate results only when the LCN condition is satisfied.

As mentioned above, LCN is not very appealing when we consider laser irradiation. In particular if we want to consider processes such as fragmentation and dissociation, in which emission of charged ions may occur [138]. In this extreme case, the energy must also be extended in order to include the Madelung energy arising from Coulomb interactions between charged ions. Although other approximations are possible, it may be better to use a fully selfconsistent tight binding [139] when a significant ionic character is expected.

However, for binary semiconductors, and medium sized clusters, this may not constitute a major drawback. For these cases, only small charge transfer is expected for reasonable interatomic-distances. Therefore, it would be possible to construct reliable parametrizations, without resorting to the LCN condition, just as in the case of the carbon-carbon, and silicon-silicon, parameters [133].

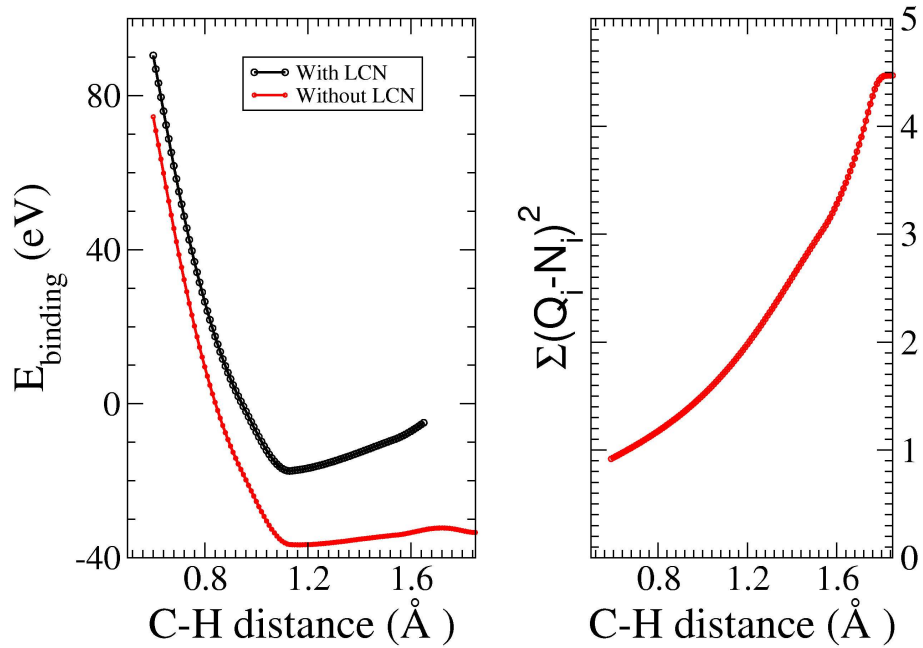


Figure 4.6: Binding energies for the methane molecule as function of the C-H bond length, calculated using the tight binding parametrization of ref. [65] with and without considering LCN.

4.5 Extending the model III: Full density matrix approach, *a modest proposition.*

The most appealing solution to the present drawbacks of our model is to move forward to a full density matrix description, meaning that we do not assume $\hat{\rho}$ to be diagonal in the eigenvectors basis. This step would require not only a major change in the used codes, but also much more computer resources. However, it would be possible to treat more general problems. As a matter of fact, by implementing a full density matrix approach, one could (i) go beyond the large wave approximation, and (ii) include strictly all the polarization effects. In the following subsections, we summarize our advances along this direction, as a guide for further development.

4.5.1 Basic equations for the time evolution of the reduced density matrix operator in the localized orbitals basis set

As discussed above, the effect of the electromagnetic field on the material system could be described via the Pierls substitution. In the basis set of localized orbitals, the transformed Hamiltonian takes the simple form stated in eq.4.16; a shift of the onsite terms, and a phase shift of the hopping interactions. Therefore, the equations describing the material's response to a laser pulse, may be more easily stated using this basis set. In addition, in the localized basis one could include a microscopical description of the e-e interaction (for instance, using the Hubbard approximation). Here we derive explicit formulas for the evolution of the density matrix, that could be useful for further works.

Let us start from the tight-binding Hamiltonian, written in the localized orbitals basis set 4.15, where the usual anticommutation rules for the creation and annihilation operators apply:

$$\left[\hat{c}_{i\delta}, \hat{c}_{k\beta}^\dagger \right]_+ = \delta_{i,k} \delta_{\delta,\beta}; \quad \left[\hat{c}_{i\delta}, \hat{c}_{k\beta} \right]_+ = \left[\hat{c}_{i\delta}^\dagger, \hat{c}_{k\beta}^\dagger \right]_+ = 0 \quad (4.30)$$

Interaction with the laser field is going to be described via Pierls substitutions, meaning that [135]:

$$\mathbf{t}_{ij}^{\delta\eta}(t) = \mathbf{t}^{\delta\eta}(R_i - R_j) * \exp\left(-\frac{ie}{\hbar c}(R_i - R_j) * [A(R_i, t) + A(R_j, t)]\right) \quad (4.31)$$

The scalar potential ϕ can be set to zero, by a convenient selection of the electromagnetic gauge.

Now we write the Liouville equation for the density matrix:

$$\frac{\partial \hat{\rho}}{\partial t} = -\frac{i}{\hbar} [H, \hat{\rho}] - \left[\frac{\partial \hat{\rho}}{\partial t} \right]_{col} \quad (4.32)$$

where the reduced (single particle) density matrix elements are given by:

$$\hat{\rho}_{l\alpha, k\beta} = \hat{c}_{l\alpha}^\dagger \hat{c}_{k\beta} \quad (4.33)$$

First we focus on the term $[H, \hat{\rho}_{l\alpha,k\beta}]$, which provide the coherent evolution of the density matrix elements. For the commutators in the diagonal part of the Hamiltonian, we have the following expressions:

$$\begin{aligned}\hat{c}_{i\delta}^\dagger \hat{c}_{i\delta} \hat{c}_{l\alpha}^\dagger \hat{c}_{k\beta} &= \hat{c}_{i\delta}^\dagger \left\{ \delta_{i,l} \delta_{\delta,\alpha} + \hat{c}_{l\alpha}^\dagger \hat{c}_{i\delta} \right\} \hat{c}_{k\beta} \\ &= \hat{\rho}_{i\delta,k\beta} \delta_{i,l} \delta_{\delta,\alpha} + \hat{c}_{i\delta}^\dagger \hat{c}_{l\alpha}^\dagger \hat{c}_{i\delta} \hat{c}_{k\beta} \\ &= \hat{\rho}_{i\delta,k\beta} \delta_{i,l} \delta_{\delta,\alpha} + \hat{c}_{l\alpha}^\dagger \hat{c}_{i\delta}^\dagger \hat{c}_{k\beta} \hat{c}_{i\delta}.\end{aligned}\quad (4.34)$$

and

$$\begin{aligned}\hat{c}_{l\alpha}^\dagger \hat{c}_{k\beta} \hat{c}_{i\delta}^\dagger \hat{c}_{i\delta} &= \hat{c}_{l\alpha}^\dagger \left\{ \delta_{k,i} \delta_{\beta,\delta} + \hat{c}_{i\delta}^\dagger \hat{c}_{k\beta} \right\} \hat{c}_{i\delta} \\ &= \hat{\rho}_{l\alpha,i\delta} \delta_{k,i} \delta_{\beta,\delta} + \hat{c}_{l\alpha}^\dagger \hat{c}_{i\delta}^\dagger \hat{c}_{k\beta} \hat{c}_{i\delta}\end{aligned}\quad (4.35)$$

So that subtracting the two terms in Eqs. 4.34 and 4.35, we obtain the first contribution:

$$\left[\sum_{i\delta} \varepsilon_{i\delta} \hat{c}_{i\delta}^\dagger \hat{c}_{i\delta}, \hat{\rho}_{l\alpha,k\beta} \right] = \hat{\rho}_{l\alpha,k\beta} (\varepsilon_{l\alpha} - \varepsilon_{k\beta}) \quad (4.36)$$

The following contribution comes from the hopping parameters, and we have to deal with:

$$\begin{aligned}\hat{c}_{i\delta}^\dagger \hat{c}_{j\eta} \hat{c}_{l\alpha}^\dagger \hat{c}_{k\beta} &= \hat{c}_{i\delta}^\dagger \left\{ \delta_{j,l} \delta_{\eta,\alpha} + \hat{c}_{l\alpha}^\dagger \hat{c}_{j\eta} \right\} \hat{c}_{k\beta} \\ &= \hat{\rho}_{i\delta,k\beta} \delta_{j,l} \delta_{\eta,\alpha} + \hat{c}_{i\delta}^\dagger \hat{c}_{l\alpha}^\dagger \hat{c}_{j\eta} \hat{c}_{k\beta} \\ &= \hat{\rho}_{i\delta,k\beta} \delta_{j,l} \delta_{\eta,\alpha} + \hat{c}_{l\alpha}^\dagger \hat{c}_{i\delta}^\dagger \hat{c}_{k\beta} \hat{c}_{j\eta}.\end{aligned}\quad (4.37)$$

And again for the other term in the commutator:

$$\begin{aligned}\hat{c}_{l\alpha}^\dagger \hat{c}_{k\beta} \hat{c}_{i\delta}^\dagger \hat{c}_{j\eta} &= \hat{c}_{l\alpha}^\dagger \left\{ \delta_{k,i} \delta_{\beta,\delta} + \hat{c}_{i\delta}^\dagger \hat{c}_{k\beta} \right\} \hat{c}_{j\eta} \\ &= \hat{\rho}_{l\alpha,j\eta} \delta_{k,i} \delta_{\beta,\delta} + \hat{c}_{l\alpha}^\dagger \hat{c}_{i\delta}^\dagger \hat{c}_{k\beta} \hat{c}_{j\eta}.\end{aligned}\quad (4.38)$$

So that by subtracting the two terms, we finally obtain the second contribution in the coherent evolution:

$$\left[\sum_{i\delta,j\eta} \mathbf{t}_{ij}^{\delta\eta}(t) \hat{c}_{i\delta}^\dagger \hat{c}_{j\eta}, \hat{\rho}_{l\alpha,k\beta} \right] = \sum_{i\delta} \mathbf{t}_{il}^{\delta\alpha}(t) \hat{\rho}_{i\delta,k\beta} - \sum_{j\eta} \mathbf{t}_{kj}^{\beta\eta}(t) \hat{\rho}_{l\alpha,j\eta} \quad (4.39)$$

Equation 4.32 , with the explicit formulae of Eqs. 4.36 and 4.39, provides the coherent part of the time evolution of the density matrix in the orbital basis set and, then, it is possible to write

$$\frac{\partial \hat{\rho}_{l\alpha,k\beta}}{\partial t} = -\frac{i}{\hbar} \hat{\rho}_{l\alpha,k\beta} (\varepsilon_{l\alpha} - \varepsilon_{k\beta}) - \frac{i}{\hbar} \left[\sum_{i\delta} \mathbf{t}_{il}^{\delta\alpha}(t) \hat{\rho}_{i\delta,k\beta} - \sum_{j\eta} \mathbf{t}_{kj}^{\beta\eta}(t) \hat{\rho}_{l\alpha,j\eta} \right] + \left[\frac{\partial \hat{\rho}}{\partial t} \right]_{col} \quad (4.40)$$

4.5.2 Collision Part

The second part in the Liouville equation represents the collision processes that electrons undergo due to their mutual interactions. As stated before, we may treat this part as a thermalization process that tends to cast the density matrix into a thermal (Fermi) distribution. This process will be described by certain decay times. So, in the eigenvectors basis we would have:

$$\left[\frac{\partial \hat{\rho}_{m,n}}{\partial t} \right]_{col} = \frac{\hat{\rho}_{m,n} - \hat{\rho}_{m,n}^o(\mu, T_{el})}{\tau_{mn}} \quad (4.41)$$

Where the diagonal elements of $\hat{\rho}_{m,n}^o(\mu, T_{el})$ are given by the Fermi distribution; calculated as before, and off diagonal elements are all Zero. Now, we need at least two decay times: one for the diagonal elements (in the eigenvector representation) related to the time scale in which electronic occupations go to the Fermi limit, and other for the non-diagonal elements related to the decoherence time of these excitations (a process that takes place in a shorter time scale):

$$\tau_{mn} = \begin{cases} \tau_{e-e} & \text{if } m=n \\ \tau_{decoh} & \text{if } m \neq n \end{cases} \quad (4.42)$$

The calculation of the electronic temperature could be achieved using the conditions stated in Eqs. 4.3.

This approach would still suffer of spurious charge transfer, but it would be possible to go far beyond the dipole approximation. Of course, as we are dealing with the full density matrix, electron collision could also be phenomenologically treated as diffusive processes by adding a term:

$$\left[\frac{\partial \hat{\rho}_{m,n}}{\partial t} \right]_c \text{ol} = -\mathbf{D} \nabla^2 \hat{\rho} \quad (4.43)$$

with some suitable diffusion matrix \mathbf{D} .

The difficulties inherent to either of those approaches; a larger number of parameters, the need to resort to the eigenvectors basis in order to define the thermal limit, the non-trivial supposition that Eqs. 4.43 and 4.41 provide the same evolution for connected clusters, make much more appealing the use of a microscopical description of the $e - e$ interaction such as the Hubbard model [136].

4.5.3 Energy and Forces

Equations 4.40 and a suitable collision part (phenomenological thermalization, diffusion, Hubbard model or other selected method), describe the evolution of the matrix density for a material system interaction with a laser pulse. With the density matrix, the expected value of the electronic energy, and the corresponding forces, are given by:

$$\vec{F}_{R_i} = \vec{\nabla}_{\vec{R}_i} U = Tr \left\{ \hat{\rho} \vec{\nabla}_{\vec{R}_i} H \right\} \quad (4.44)$$

Therefore, in principle we would not need to perform the Hamiltonian diagonalization, in order to obtain energy and forces, provided that a suitable (unitary and stable) algorithm, for the density matrix evolution is implemented.

4.5.4 Some Implementation Tips

In Eq. 4.40 we have $N(N - 1)/2$ equations to solve (one for each diagonal and lower diagonal term in the density matrix). The first issue to address is the stability of the integration of this equations of motion. It is important to remark that the evolution of the density matrix is now given by a complex Hamiltonian matrix, therefore the density operator should be represented by complex matrix.

Following the evolution of the density matrix given in equation 4.40 would require smaller time steps, when compared to those used in the actual implementation. Efficiency considerations lead us to believe that it could be better to restrict this

approach to the laser pulse duration (tens of femtoseconds, for ultrashort pulses), and keep the *old* evolution scheme for the subsequent evolution of the system.

We do not need matrix diagonalization for the forces and energies. However, before turning the laser pulse on, the density matrix should represent the occupation of the electronic levels, at the initial electronic temperature. Therefore, diagonalization would be required at least during the required thermalization steps.

If the electronic thermalization approach is to be used, the thermal limit $\hat{\rho}^o$ is only easy to define in the unperturbed eigenvectors basis, where it is given just by the Fermi distribution. In such approach, it would be necessary to calculate the unperturbed eigenvectors at certain time steps and transform the diagonal (in the eigenvectors basis) thermal limit, to the orbital basis set. Transformations to the orbital basis set must be performed every time we consider that the electronic temperature has changed. The Hamiltonian diagonalization would be required only when the ions are moved, thus changing the orbital and eigenstates basis.

In order to summarize the previously stated considerations, we propose a procedure that could be conveniently implemented:

1. If the laser is off, perform the dynamical evolution in the *old*, fast and trustable fashion
2. As soon as we turn the laser on, use the occupations and eigenvectors calculated in this time step to construct the density matrix (transform to the orbital basis).
3. At this time step (t_i), one should define a smaller time scale (dt_m) and evolve the density matrix according to equations 4.40, and a suitable description for the collision processes. This time step may be commensurable with the ionic time step. During this evolution we do not require the forces, neither further diagonalizations. If the e-e collisions are described by a phenomenological thermalization process, there are two possibilities.
 - 3a. If the electronic Temperature changes slowly enough (in the density matrix evolution time scale), one could assume it to be constant between one and the next ionic step. Under this condition, it would be

possible to evaluate the thermal limit of the density matrix only at the beginning of the matrix evolution loop. It would be important to keep track of the absorbed energy.

3b. Otherwise, it would be necessary to rewrite the thermal limit for each dt_m step, and perform the basis transformation.

4. At the end of the density matrix evolution loop, the system reaches the next ionic step t_{i+1} . At this time step, one should actualize the forces, positions, unperturbed eigenvector matrix, electronic temperature, and any other dynamical parameters depending upon the ionic-configuration.

5. Repeat again from step 3, until the laser pulse is shut down.

6. Look at the final density matrix in the instantaneous eigenvectors basis, if there are any remanent (hopefully small), nondiagonal terms switch them to zero and recast the problem in terms of the occupations.

7. Return to the *old* dynamics.

Chapter 5

Releasing strain and relaxing the curvature via a laser induced process.

... don't know what I want

but I know how to get it

Anarchy in U.K., Sex Pistols

5.1 Motivation.

While the quest for novel carbon-based nano-structures keeps going, a major concern with controlling the final products has arisen; defects appearing during the production stage have to be processed. The controlled introduction of structural defects may be useful in material engineering; however, undesired defects must be removed.

Recently, ultrafast laser irradiation has been shown to be a convenient way to induce structural modifications -ablation, fragmentation, dissociation, phase transitions - in graphitic and other covalent systems [41, 43, 140, 141], a fact that can be related to the change in the effective potential surface seen by the ions when the electrons get excited light beams [40, 45]. Even while typical laser's wavelengths are large at the nanometric scale, modifications at very short length scales can be

achieved and, for instance, the possibility of cleaning up certain kinds of defects in nanotubes have been proposed [142, 143].

The highest level of theory describing laser-matter interaction in solid state systems is the Time Dependent Density functional theory [142], which allows for an accurate treatment of electronic excitations. This approach, despite the increase in computational power, is very expensive when dealing with large systems and massive electronic excitations. Relatively cheaper static Density Functional methods with hot electron gases also provide satisfactory descriptions of massive excitations [42], but they are still quite expensive and, as the electron temperature is manually set up, the evolution of the system during the interaction time cannot be studied using those models.

The theoretical framework discussed in the previous chapter, by its side, allows for the description of larger system with affordable computational power. Reliable qualitative descriptions of several laser induced processes including laser melting of silicon, non-thermal fullerene fragmentation [145], selective phonon activation [144] and cap opening [44] in nanotubes, and diamond graphitization [146] have been obtained. Because of the rather large amount of excited electrons involved in these processes, the dynamics is mainly driven by the electronic entropy and thus, completely accurate description of the excited states is not crucial provided that a judicious selection of the pseudo empirical parameters is made.

In this chapter we use the method described in chapter 4 to study the ultrafast response of graphitic systems under laser irradiation. A novel mechanism for heptagon pentagon pair defects is found in nanotubes and fullerenes and damage thresholds are found to be generally reduced by the presence of these defects.

5.2 Ultrafast response of defective graphitic systems

In this contribution we focus on graphitic lattices modified by the $\frac{\pi}{2}$ rotation of one single dimer. This kind of structural modification, known as Generalized Stone-Wales (S-W) transformation [19, 120], introduces pentagon-heptagon pair defects

in otherwise homogeneous hexagonal lattices, like nanotubes or graphene layers, and, in general, changes the size of the carbon rings neighboring the rotated dimer in other graphitic structure. In the Buckminsterfullerene C_{60} an S-W mechanism transforms two pentagons into two hexagons and vice-versa. This 5-7 pair defects appear commonly in carbon nanostructures. The generalized S-W transformation, is believed to contribute to a wide variety of structural transformations including diffusion [120], hydrogen adsorption [121], coalescence in fullerenes [19, 120, 147] and nanotubes [148], and even in the annealing of general fullerene structures down to the Buckminsterfullerene [120, 150] .

The energetics of the S-W transformation in graphene, nanotubes and fullerenes has been intensively studied, and values for the barriers the systems have to overcome to go from pristine to defective forms have been determined to lie above ~ 5 eV [19, 120, 121, 150, 151] although catalysis with adsorbed carbon atoms (self-catalysis) can reduce the barriers significantly through Frenkel pairs generation [152]. The inverse transformation going back from a defective structure to the homogeneous one, has been less intensively studied. Under thermal conditions the systems could go back through the direct transition path overcoming transition barriers of about ~ 1.5 eV. Thermal processing may, nevertheless, induce other undesirable structural changes.

5.2.1 Graphene.

First we considered a S-W transformed graphene layer as shown in figure 5.1. In order to compare with the results from our simulations, the Minimum Energy Path (MEP) -the one that most contribute in a thermally activated transition- going from the defective to the perfect layer was calculated using the Climbing-Image Nudged Elastic Bands Method (CI-NEB) [153] within the DFT framework. CI-NEB allows for accurate determination of MEPs from a set of initial guesses -"images"- joining the two extremes of the path, the images are let to interact through virtual springs (hence they resemble an elastic band). We have used 16 images in our calculation, allowing for accurate enough outputs. The calculated MEP path does not differ fundamentally from the one proposed originally by Kaxiras et al [120] for the SW-

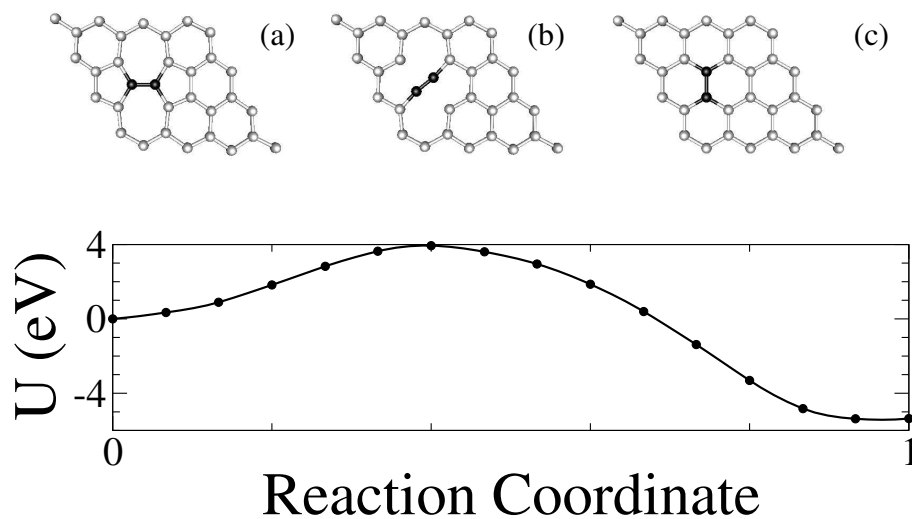


Figure 5.1: Top, snapshots of the Minimum Energy Path calculated for inverse SW transition in graphene using the CI-NEB. (a) The defective system with heptagon-pentagon pairs, (b) Transition State exhibiting sensible compression of the rotated dimer. (c) Perfect graphene layer. Bottom, the corresponding potential energy showing the barrier

transformation and it is characterized by a sensible compression of the dimer bond length providing an energetic barrier of about 4eV for the inverse SW-transition, a value that is also well within the typical ones reported in the literature between 3-4 eV.

This barrier height, provides metastability to the 5-7 pairs. It is usually remarked that out of plane motion of the dimer could reduce the transition barrier by reducing the C-C bond compression, this possibility was already discussed by Xu et al. [133] within a Tight Binding approach, revealing only minor changes for the inverse S-W transformation barrier. Annealing out of 5-7 pair defects was also suggested to occur for nanotubes in picosecond scales at temperatures around 4000K-5000K [155]. All into account, no evidence of inverse S-W transitions at room or moderated temperatures has been reported, to the best of our knowledge, and these defects are generally accepted as long lived species in that temperature regime, even further: the mostly in-plane paths and related barriers, like that in ref [120] and in the present

work, are widely used as sensible estimatives for the actual transition path [152,156] features and only small changes of the activation barrier may be expected from out of plane motions. In contrast, the highly non thermal processes observed in our simulations and that will be discussed below, occur at times below 1000fs after laser irradiation and with moderated values of the lattice temperatures (usually around 500 K).

Molecular dynamics simulations of the kind described in chapter 4 were performed on a graphene supercell containing 96 atoms. The thermalization parameters were taken as $\tau_{ee} = 50fs$ and $\tau_{el} = 44ps$, which are reasonable values according to pump-probe experimental data on carrier relaxation process in graphitic systems [157]. The central laser frequency is 1.96 eV and its width is 50 fs, values easily achieved in experimental setups, we did no attempt to tune in the laser frequency to any particular feature of the absorption spectra.

The laser spot is quite larger than the simulation cell and we have used (a) fixed supercell boundary conditions to simulate samples larger than the laser spot where expansion can only occur at the sound velocity and then no volume changes are expected during the simulated time, and (b) variable supercell conditions to simulate samples smaller than the laser spot that, hence, undergo rapid expansion. In each case the equations of motion are integrated using 0.1fs time steps.

Different laser intensities and, then, amounts of offered energy , were considered, and the energy absorbed by the system - a quantity that with fixed frequency and pulse width can be regarded from now on as a measure of the former- in a per atom basis ranges from 0.77eV to 1.32eV, which are below the threshold for laser ablation for the perfect lattice [128] . To this values of absorbed energy, a quite significative amount of electrons (between 4% and 6%) get promoted to excited states and, correspondingly, electronic temperatures go up to 20000K. This rather large fraction of excited electrons constitute a marked difference with the *First Principles* studies on photo-excitation of Stone Wales pairs in carbon nanotubes [142], where a single and well tuned electronic excitation is observed to induce strong vibrations at the rotated dimer neighborhood but without compromising the defect stability.

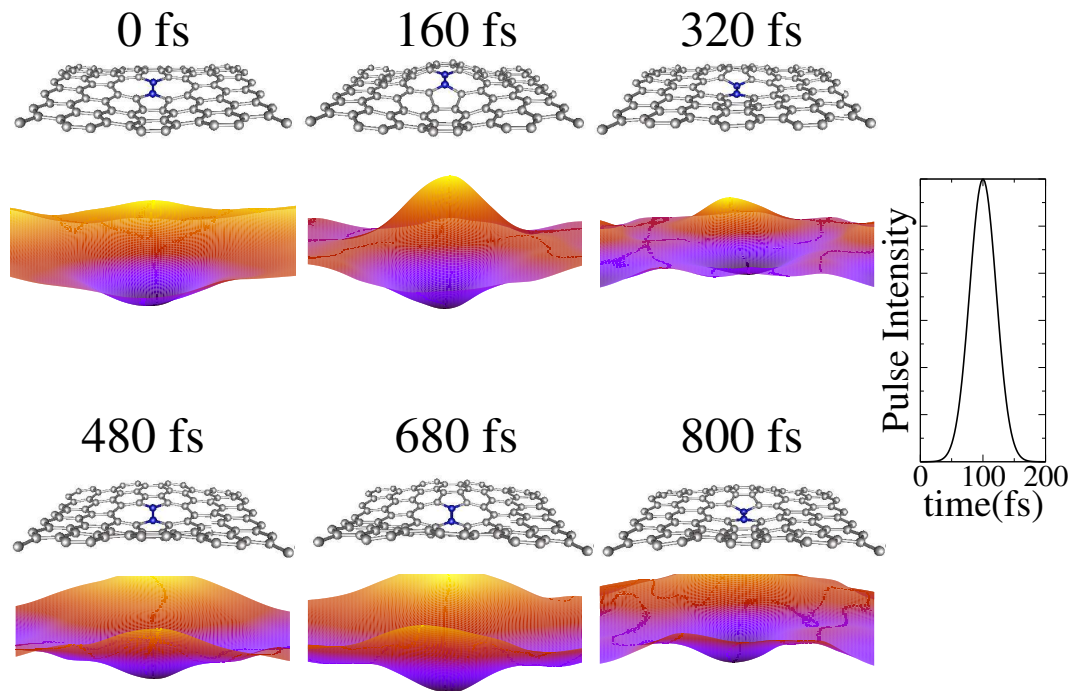


Figure 5.2: Snapshots of the graphene response to a laser pulse, the laser peak occurs at 100fs, and its intensity profile -envelope function- is shown to the right. The rotated dimer is shown in blue. When the absorbed energy is 0.77eV per atom (4% of the electrons are excited), low frequency vibrations are excited and strong motions near the defect are noticeable. Color mapped surfaces below each snapshot show the dramatized version of the Z-motion for the subjacent surface.

For the lower laser pulse intensities considered, the system undergoes strong motions in the direction perpendicular to the layer, as is also observed in the case of a perfect graphitic structure. Now, as shown in the snapshots of figure 5.2, especially strong movements are induced near the rotated dimer.

The fact that low frequency modes are activated by the laser pulse is better demonstrated by the evolution of the Power Spectra calculated from the Velocity Autocorrelation Function. We have calculated this quantity by looking at the VACF after laser irradiation as a function of laser intensity (absorbed energy). In order to get accurate enough results, we have followed the motion in rather large times (6700fs). Most of the spectra in the low frequency range comes from the z-velocities

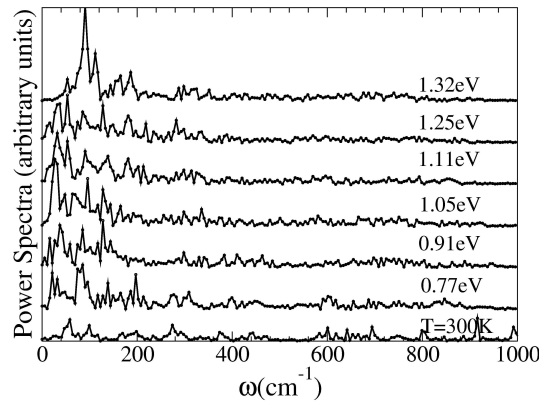


Figure 5.3: Power spectra calculated after laser irradiation for different absorbed energies. The spectrum for the thermalized sample is shown for comparison. The spectrums are normalized to 1 in the region between 0 cm^{-1} and 4000 cm^{-1} . Most of the spectral power for the thermalized case lies in the region above 1000 cm^{-1} where the laser irradiated samples do not exhibit any significant feature.

correlation, meaning that the relevant modes are out of plane vibrations.. As can be seen in figure 5.3 after irradiation several low frequency modes that were mostly inactive under thermal conditions get strongly excited. For the thermalized sample most of the spectral power is above the 1000 cm^{-1} region (not shown in figure 5.3) corresponding to the very local C-C stretching modes meanwhile the excited modes lie below 400 cm^{-1} . The last ones are most likely of the Z-Acoustic kind, their frequencies being way below those of optical modes.

It is also important to remark that not one but several modes are stimulated by the laser pulse. Indeed, the only spectra that is close to a single mode excitation is that 1.32eV energy, i.e. just where defect healing occur and the spectra is, then, mainly that of a clean graphene sheet.

Excitation of single vibrational modes, specifically bond stretching modes, has been shown to follow laser irradiation for defective nanotubes with low but tuned levels of excitation [142]. In our case, the laser pulse is not aimed to excite exclusively electronic states localized on the defect. Consequently, the dimer bond length exhibit large frequency oscillations (about 1650 cm^{-1}), which could be related to those discussed in ref. [142], but those vibrations are mixed with the low frequency

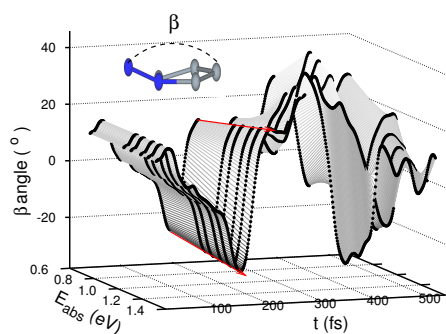


Figure 5.4: Evolution of the dihedral angle between the rotated dimer and an adjacent pentagon with time and absorbed energy. Dark points are the calculated data and the smooth surface is a guide to the eye. Arrows are used to emphasize the quite linear dependency between the value of the angle's minimum (maximum) just before (after) laser irradiation and the absorbed energy.

modes.

Still, the variety of excited vibrational modes summons and allows for rather localized motion with the out of plane components near the defect being larger than in the remaining cell. This out of plane motion of the Stone-Wales defect can be nicely characterized by measuring a dihedral angle β between the dimer and two carbon atoms in one neighboring pentagon (if the pentagon were to stay planar that would just be the angle between the dimer and the pentagon plane). Following the evolution of this angle with the absorbed energy we can see (fig 5.4) how the height of the first value reached just after laser irradiation (around 220fs) changes almost linearly with the laser intensity. When the angle reaches a certain critical value after laser irradiation, one of the pentagon's edges is broken and the inverse Stone Wales transition proceeds. After defect healing (about 420 fs) smooth oscillations of this angle can be seen related to the clear mode excitations observed in the Power Spectra.

Some key steps in the inverse transition path are depicted in figure 5.5: strong motions around the defective region are induced after the laser pulse peak (time near 160 fs) in a very similar fashion that for lower intensities , out of plane motion of the

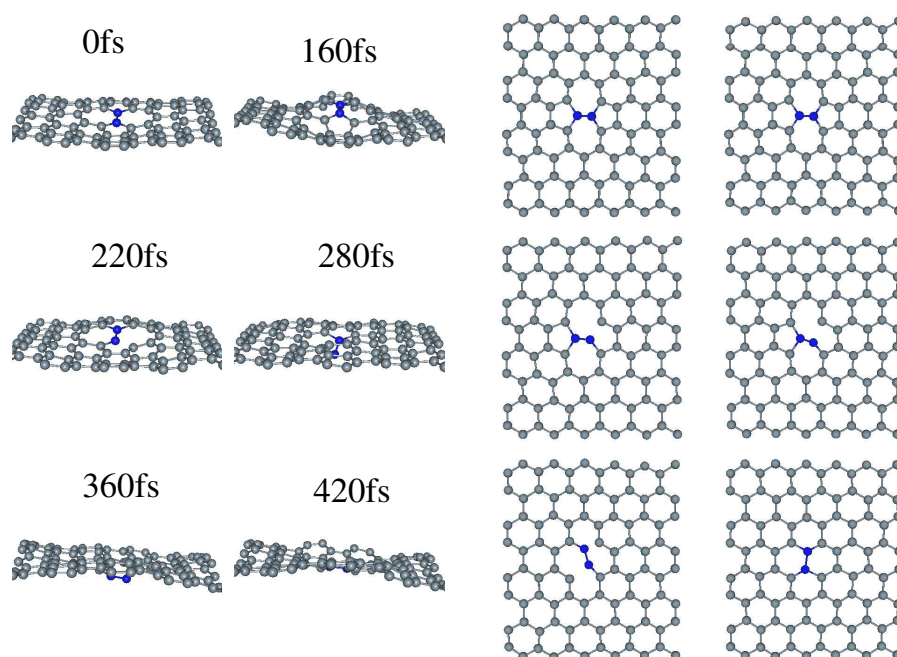


Figure 5.5: Frontal and lateral snapshots for the laser induced S-W transition. When 1.32eV per atom are absorbed (6% of the electrons are excited) the strong motions are followed by bond breaking, out of plane rotation and, finally defect healing. The rotated dimer is shown in blue.

dimer leads to the “liberation” of one the dimer’s end (time near 220fs), dimer moves even deeper and β reaches its maximum value (around 280fs), dimer out of plane rotation leads to a configuration closely resembling the intimate Interstitial-Vacancy defect in graphite [152] (around 360fs), finally the defect is cleared up and a perfect graphitic lattice is obtained (around 420fs). After defect healing the graphite layer keeps moving in a rather well defined vibrational mode, as discussed above.

The out of plane trajectory followed during this laser induced transition would be quite unlikely under normal thermal conditions, performing an energy barrier (within the Tight Binding scheme) of about 12.4 eV, related to sensible bond stretching during the initial expansion, if the electrons were to remain in their ground state. As shown in figure 5.6 this trajectory performs an even harder barrier than the CI-NEB path (with the energies now re-calculated within Tight Binding in order to make direct comparison). The fact that the change in the electronic occupation ends up cleaning the barrier through the contribution of the electronic entropy to

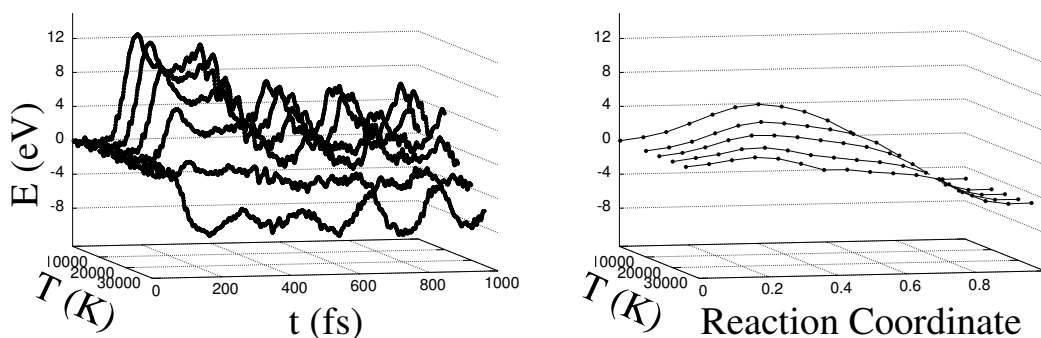


Figure 5.6: The free energy U , that ions would feel moving along the inverse SW transition paths at several electronic temperatures. To the left: the laser induced path; to the right: the CI-NEB path with energies calculated in the Tight Binding approach.

the free energy has been discussed earlier in relation to the healing of 5-7 pairs in carbon nanotubes [143].

The free energy on figure 5.6 exhibit some rather well defined oscillations after healing is completed. Although the simulation time is not large enough to achieve an accurate measurement, the period in this first peaks is about 380 fs, which would closely correspond to the peak observed in the in the power spectra.

5.2.2 Single Walled Carbon nanotubes.

It is important to see whether curvature affects the healing mechanism found for graphene layers. We have, therefore, performed a series of theoretical simulations within the same spirit of the previous subsection considering 5-7 pair defects in SWNTs ¹.

We performed calculations on zigzag and armchair CNTs (these being both semiconductor and metallic, respectively) with at least 240 atoms in a supercell geometry.

¹The original simulations demonstrating the possibility of 5-7 pair defects healing in carbon nanotubes, were performed by A. H. Romero and H. Jeschke. The subsequent detailed study of the inverse transformation mechanism in graphitic structures, has been developed by F. Valencia, A. H. Romero, H. Jeschke and M. Garcia [158]

We considered a SWNT possessing an individual 5-7-5-7 defect within the supercell. As in the case of graphene, once this defect is formed, an energy of the order of 4-6 eV is required to return to the perfect hexagonal lattice tubule [120,133].

The laser pulse and thermalization parameters are the same as the ones used for graphene.

In Fig. 5.7, we show snapshots of the structural transformation of a (7,7) armchair CNT upon excitation with a 50 fs pulse of Gaussian shape. The energy absorbed by the CNT was 1.7 eV/atom. The first remarkable feature in the time evolution of the CNT upon excitation is the presence of a coherent phonon, corresponding to a large amplitude radial breathing mode [44]. During the first 400 fs, this vibration leads to a reversible bond breaking/reconstruction processes around the 5-7-5-7 defect (see upper panel of Fig. 5.7 (b)). Then, the laser induced change of the potential landscape U starts to be noticeable, in particular in the defect region. The two atoms building the dimer between the two heptagons moves together, keeping their interatomic distance approximately constant, and breaking their bonds with the surrounding atoms. During this process, which starts at ca. 400 fs after the maximum of the pulse, the dimer performs a complex motion with one component in the direction perpendicular to the nanotube wall, and another component "in-plane". This motion ends up with the healing of the CNT and the elimination of the 5-7-5-7 defect via a Stone-Wales type rotation with a component out of the plane. The final result of the trajectory of the dimer is a 90 degree rotation in the wall (Stone-Wales-type transformation). Therefore, an ultrafast inverse SW transition has occurred, induced by the femtosecond laser excitation (Fig. 5.7 (c)).

We have calculated the electronic density of states (DOS) and we obtained the same features reported in Ref. [170], which indicates that we are dealing with the same type of defect (2 heptagons with 2 pentagons). It is very important to stress out that the bonding and antibonding states, related to the SW transformations, are well described within our tight-binding approach, as can be seen from figure 5.8 where the electronic densities of states are reported for the same dynamical steps chosen for the snapshots. This fact, i.e. that our tight-binding approach can deal with the electronic structure all along the calculated trajectory, is of uttermost

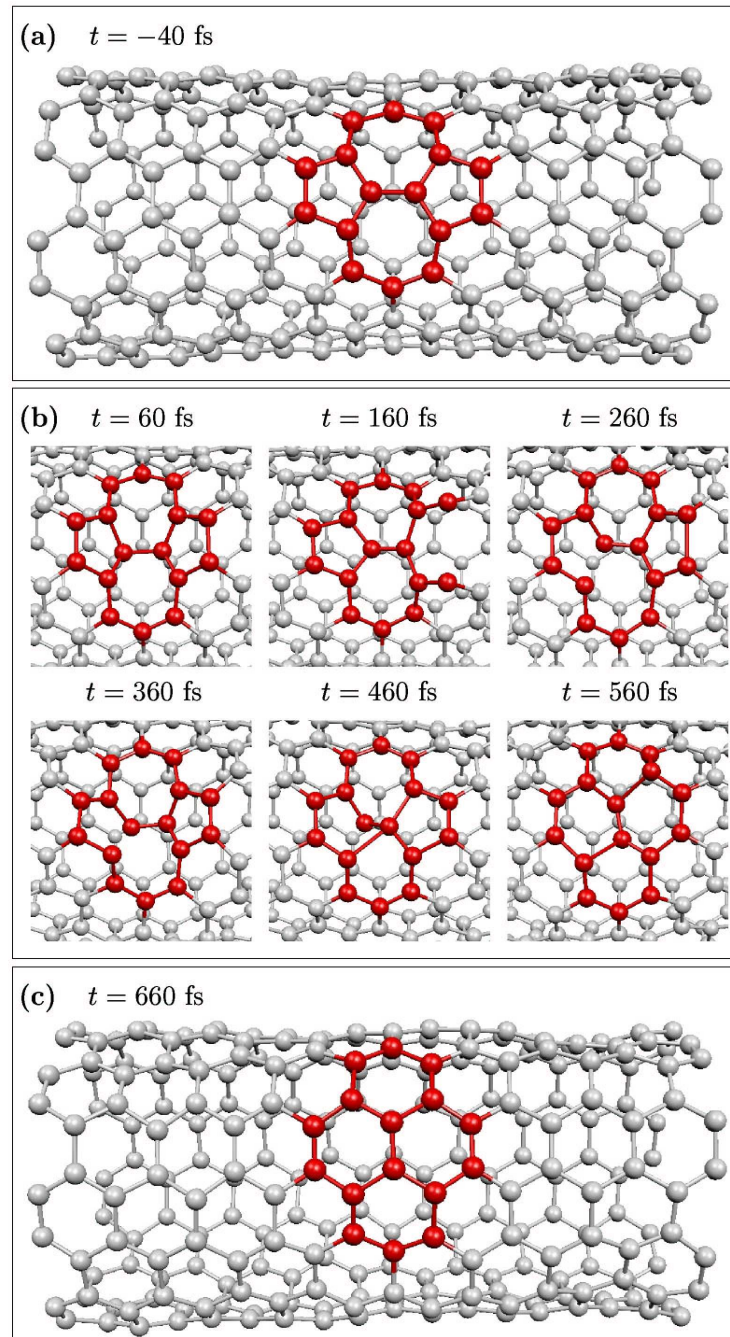


Figure 5.7: Snapshots of the response of a (7,7)-CNT to a femtosecond laser pulse leading to the healing of the SW defect. The relevant processes and the times at which they happen (measured with respect to the maximum of the pulse) are indicated.

importance for our interpretation.

The mechanism driving this non thermal structural change comprises several steps: 1. Activation of the molecular breathing mode, leading bonds breaking around the 5-7-5-7 defect.

2. The large increase in the electronic temperature driven by the laser pulse: at an electronic temperature larger than 20000 K, the radial expansion does not cost energy.

3. The 5-7-5-7 defect becomes unstable because of the population of the anti-bonding states.

4. Dimer motion with a significative out-of-plane (the plane is defined by the surrounding bonds) component.

5. Suppression of the energetic barrier driven by the increase in the electronic entropy.

5. Ultrafast annealing of the defect into hexagons.

As in the case of graphene, the mechanism is very different from what one can expect in a thermally driven process. Calculations of the reaction path going from the defective to the perfect tube within the Climbing Image Nudged Elastic Bands Method (CI-NEB) method [153],² reveal a very different reaction path where the 5-7 defect goes through a transition state with an energy of 6.04 eV with respect to the initial state, this configuration corresponds to the stabilization of a carbon dimer with very small carbon-carbon distance (1.22Å) in the plane of the structure. After crossing this transition, the dimer strain is relaxed by rotating it around its axis and converting it to a perfect hexagonal tube. It is important to mention that the dimer goes through a rotation in the same plane most of the time, which makes the laser induced transition a characteristic one with respect to the transition geometry, because it occurs via a 3D dimer rotation.

It is interesting to focus in the activation of the breathing mode prior to the

²*ab initio* calculations have been carried out using the Car-Parrinello approach [159] in the framework of the density functional theory (DFT), using gradient corrections in the BLYP implementation [160]. The Γ point only in the Brillouin zone has been considered, and we used norm-conserving pseudopotentials [77] with s and p nonlocality for C and s for H

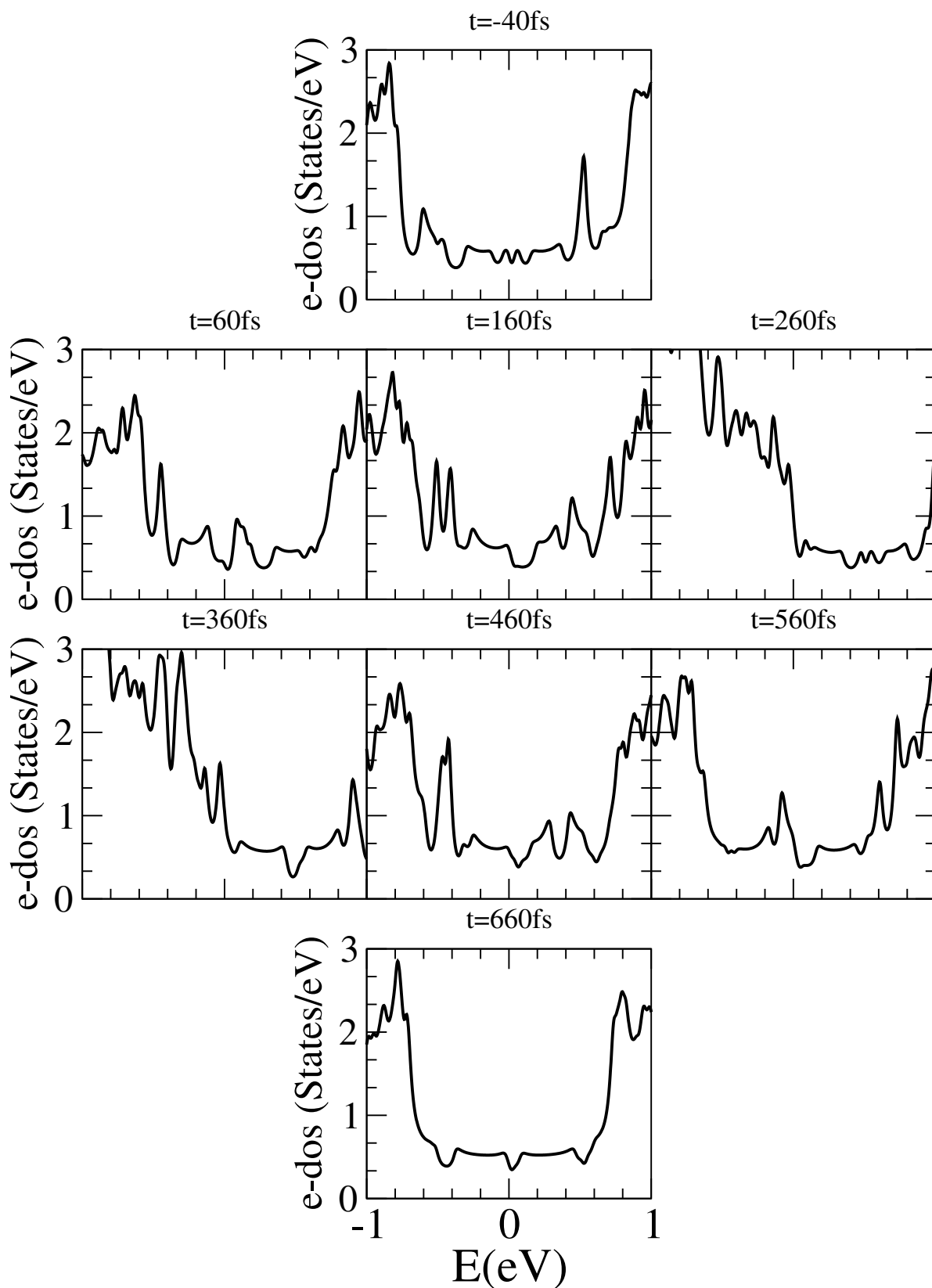


Figure 5.8: The calculated electronic densities of states along the trajectory points selected for the snapshots in figure 5.7. The initial and final steps show clearly the expected behavior for a defective and perfect nanotube. The Fermi level is located at “0” energy.

22nd June 2005

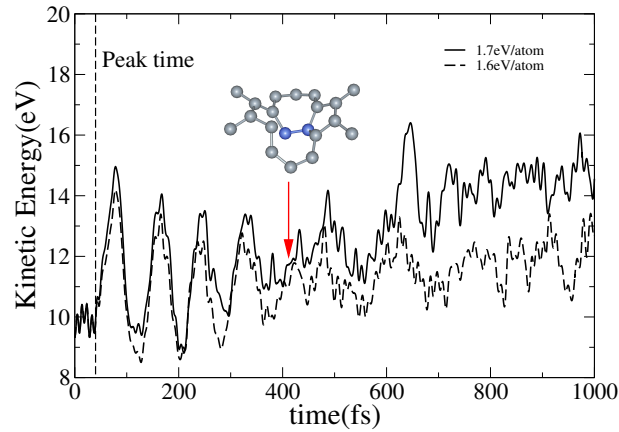


Figure 5.9: Kinetic energy evolution during the simulation time for a (7,7) nanotube under laser irradiation for two different values of the absorbed energy. At 1.7eV/atom the inverse SW transition occurs. At 1.6eV/atom the system reaches a metastable state with the dimer pushed into the tube. The configuration of the defect neighborhood at the point where the initial vibrations disappear is also displayed

transformation, as it plays a very important role in the subsequent structural response. In figure 5.9 the evolution of the kinetic energy during the simulation time for a defective (7,7) nanotube is shown. From the fluctuations it is clear that the expansion observed in the simulations just after the laser pulse peaks (ref [143]) do correspond to excitation of a vibrational mode with a frequency around 193 cm^{-1} . Again, this is not a pristine mode excitation as can be seen from the variation in the fluctuation amplitudes. For times above 400 fs this mode is no longer supported by the samples. As a matter of fact, around 400 fs the out of wall component of the SW dimer reaches its maximum value and the dimer gets free from one of the pentagons, this point can be considered the onset for the inverse SW transition.

When the absorbed energy is not enough to efficiently smooth the barriers between the break point, around 400 fs, and the perfect nanotube, the system do not undergo ultrafast transformation and get stuck in a metastable (in the simulation time scales of thousand femtoseconds) state with the dimer pointing inwards. The barrier separating this state from the perfect nanotube should be somewhere below 5 eV (value with $T_{el}=300\text{K}$) and it is still possible for the system to go to the perfect

lattice even if not performing an sub-picosecond transition.

The intermediate steps in the laser induced inverse S-W transitions are qualitatively the same as those found for graphite despite the differences in curvature. Simulations on a (12,0) zig-zag nanotube revealed the same behavior [158].

5.2.3 SW transformations in Fullerenes

The ability of femtosecond laser pulses to induce structural transformations in carbon fullerenes has been already shown in the literature [43, 127, 162]. Now, one would like to know if it is possible to observe the same kind of laser healing as that witnessed for carbon nanotubes and graphene layers.

First, we have considered the ideal Buckminster fullerene C_{60} molecule in which we performed a generalized S-W transformation, as shown in the figure 5.10.

This transformation leads to the formation of 5-5 pairs in two sites of the molecule, this C_{60} isomer, a C_{2v} fullerene, is a generally believe to be a fundamental step in the transformation from any of the 1812 C_{60} fullerenes into the most stable Buckminster fullerene, a barrier of about 4 eV for the inverse transformation could be expected according to the analysis of ref [150]. Then, the question about laser healing is related to efficient annealing of C_{60} isomers down to Buckminster fullerenes.

We thermalized the system at 300 K and 600 K, and it is shown to be stable at these temperatures.

Then, we applied laser pulses with different intensities. The absorbed energies go from 1.1eV/atom to 1.8eV/atom (for the 300K ionic temperature), and to 1.6 eV/atom (for the 600 K temperature). The duration of the laser pulse was 50 fs, and its frequency was 1.9eV. The output of this simulations is that the only mechanism in which the relaxes the stress of the 5-5 pairs is by fragmentation of the molecule, thus emitting one atom from each 5/5 pair and then form octagonal rings. This can be easily achieved with laser pulses intensities of 1.7eV/atom (at 300K initial ionic temperature) and 1.6eV/atom (at 600 K initial ionic temperature). The ionic temperatures remain relatively low (close to the initial values) during the simulations. Subsequently, the absence of healing was observed in this type of

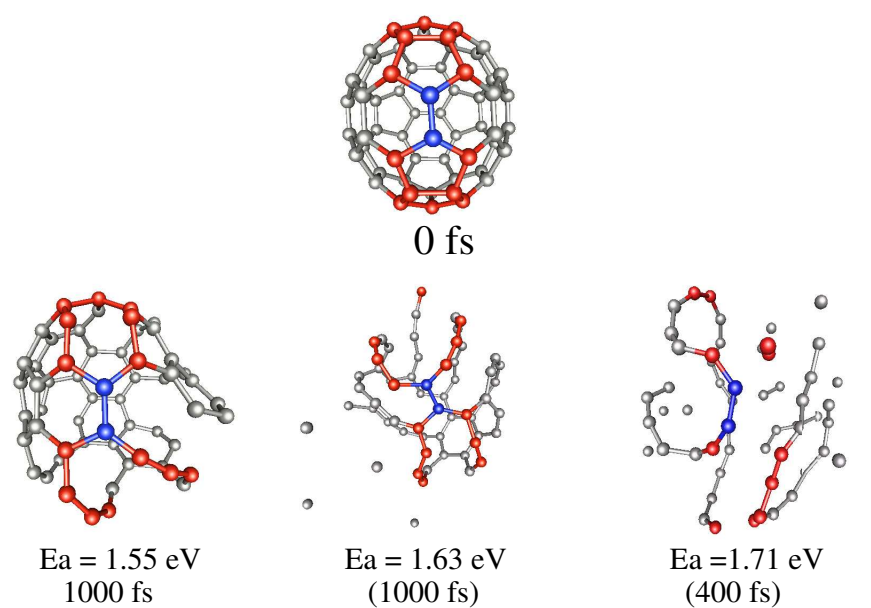
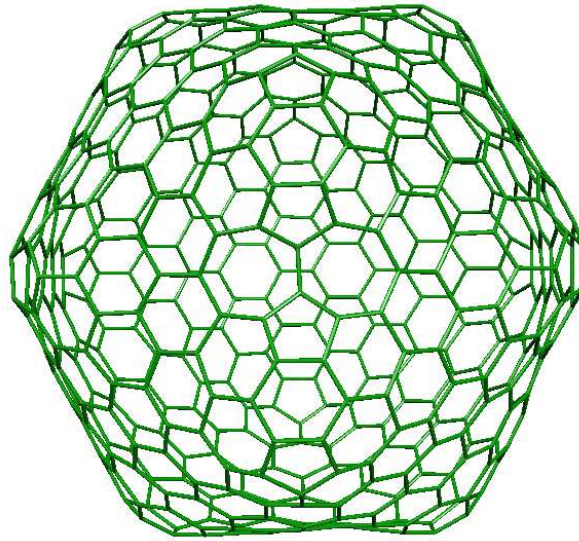


Figure 5.10: Snapshots from the response of a C_{2v} fullerene to a laser pulse. Initial lattice temperature is 300 K. Configurations after laser irradiation are shown at different absorbed energy values. The rotated dimer is shown in blue and pentagons in red.



defective fullerenes. The fragmentation process is lead by strong excitations of the molecular breathing mode.

We also looked for 5-7-5-7 transformations in a larger fullerene: C_{500} (see figure 5.2.3). In this case we observed at $1.15\text{eV}/\text{atom}$, some of the steps of the inverse SW transformations described earlier: coupling with the breathing mode, bond breaking near the SW transformed dimer and out of plane rotation of the SW transformed dimer. Nevertheless, the dimer stays in a metastable state (formation of octagonal rings) during a rather large time (in the simulation time scale), and then returns to the 5-7-5-7 configuration. Electronic temperatures reach values above 20000K , meanwhile ionic temperatures remain relatively low (about 500K). At smaller radiation doses, the system just breath. At higher doses fragmentation was observed; atoms belonging to heptagonal rings are emitted at about 1.18eV . Therefore, the energy window for laser induced inverse S-W transformations would be very narrow.

5.3 Ultrafast response of fullerenes inside nanotubes.

Finally, we looked for the possibility of laser assisted annealing of fullerene molecules encapsulated inside a nanotube (peas in a pod). The interaction of the fullerenes with the nanotube, was simulated by a Lennard Jones potential wall, with constant mass density set at a fixed radius. The resulting confining potential as function of the polar coordinate ρ was introduced within the molecular dynamics cycle.

The forces do not strongly depend upon the relative orientation of the fullerenes. Therefore, the C_{60} molecules are free to rotate, a fact that was observed during the thermalization steps. We have considered several initial conditions for the laser pulse irradiation: facing pentagons, facing hexagons and facing bonds. The initial distances between the fullerenes are set to 3.1\AA . We have used a periodic model with three c_{60} molecules per cell, and a cluster model with two fullerenes. The laser pulse duration is set to 20fs and the frequency is 1.96eV. We used laser intensities below, but close to, the damage thresholds of 2.1eV [43]. In that absorbed energy range we can expect the generation of several dangling bonds in each fullerene, a necessary step for the annealing process. Initial lattice temperatures of 600K and 300K were used in the simulations. Although configurations with several dangling bonds were achieved, no annealing of the fullerenes was observed in the periodic model. The dangling bonds are not symmetrically generated, thus hindering the annealing process. As a matter of fact, the non-thermal fragmentation mechanisms observed for the C_{60} fullerene [43], consisting mostly of segregation of chains, does not seem to be particularly suited for the annealing process.

The results for the cluster model are summarized in the snapshots of figure 5.11. It is possible to establish a bridge between the two fullerenes, starting from a configuration with a bond shared by an heptagon and an hexagon, in the first fullerene, is faced to a bond shared by two hexagons in the second fullerene. The bridge involves the formation of an heptagonal and an octagonal ring, containing two atoms of the second fullerene. This effect is seen at times c.a. 680fs after laser irradiation, and requires c.a. 1.7eV/atom. At times c.a. 1000fs, there remains

two dangling bonds in one of the fullerenes, and no dangling bonds in the other. Subsequent re-arrangement of the bonds occur until an stable dimer is formed (c.a. 2500 fs). Molecular dynamics at constant temperatures up to 1000K were performed on the resultant dimer, and the structure shows to be metastable.

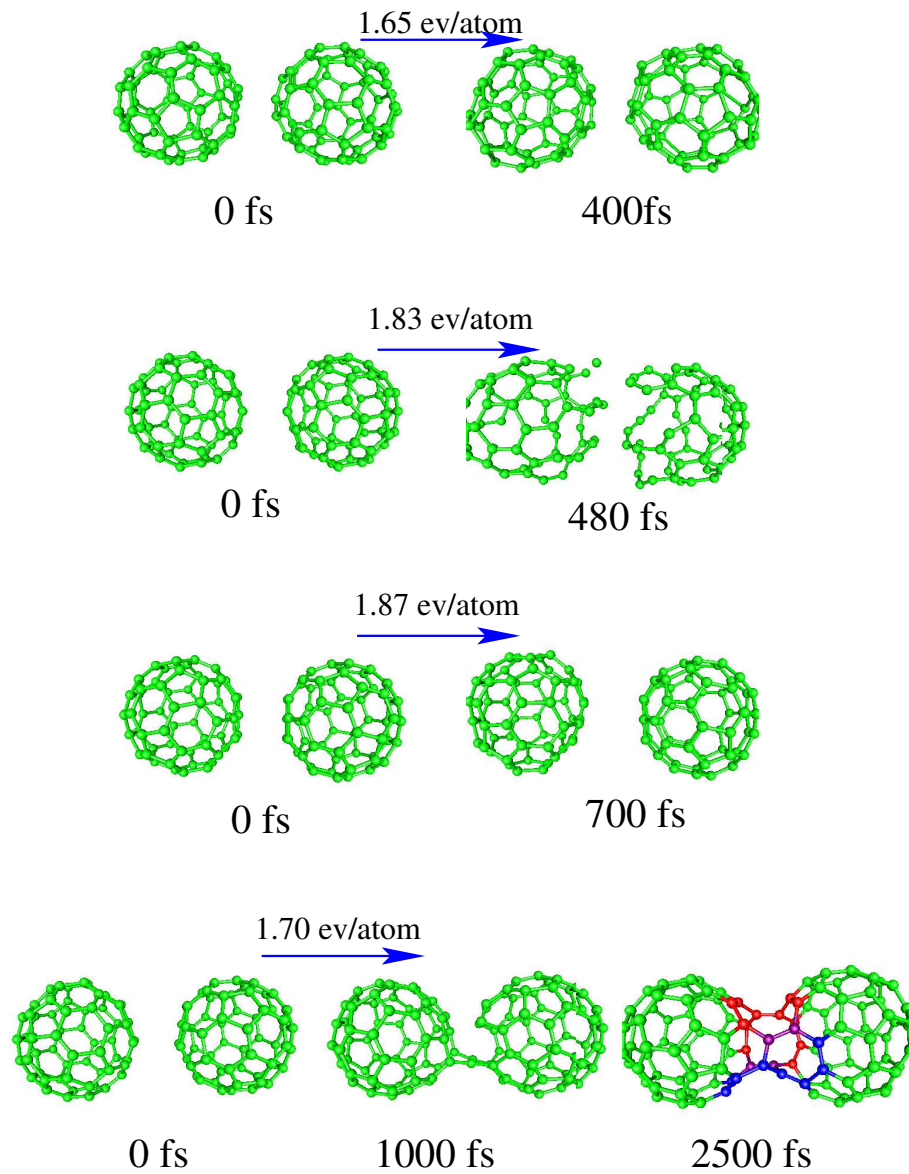


Figure 5.11: Snapshots of the ultrafast response of two neighboring fullerenes under the action of a 20fs and 1.96eV laser pulse. The results shown are for $T_{init}=300\text{K}$. Several facing conditions are examined. In the bottom panel, 7- and 9- membered rings appearing in the dimer, are colored in blue and red, respectively.

Chapter 6

Conclusions and outlook

The geometrical structure and electronic properties of cubane chains (polycubanes) have been investigated. In general, these chains exhibit, large electronic band gaps. The stability of two dimensional cubane networks was also studied, and a reduction of the electronic band-gap was observed. When doping polycubanes with hydrocarbon and nitrogen groups, narrower electronic band gaps appeared, without altering significantly the mechanical stability. In the case of NO and NS groups as dopants, half-filled valence bands were observed. However, the effective masses for holes in the valence band, and electrons in the conduction band, would be large (between 1.5 to 17 times the electron mass), because of the molecular character of these polymers.

We studied crystalline arrangements consisting of negatively curved carbon atoms. The energetics and electronic properties of these systems were calculated. These are strongly dependent on curvature. However, the presence of 7-, 8-, and 5- membered rings, leads to clear differences between these curved structures. The local topology of these structures could be modified by performing relatively small atomic re-arrangement, which resulted in modifications of their electronic properties. In this context, we demonstrated the relevance of calculating a proper relaxation of these negatively curved carbon structures.

The possibility of doping these crystals with either Nitrogen or Boron, was also investigated. We conclude that doping may be achieved by direct atomic substitution of carbon atoms with stoichiometries below $1/24$. The shape of the electronic DOS of the doped systems is inherited from that of the pure carbon framework.

Addition of Boron or Nitrogen, changes the number of valence electrons in the system. Therefore, the electronic properties of these doped crystals are dramatically different. The introduction of pyridine-like groups was shown to be possible in open Schwarzite frameworks. This doping induces significant variations in the geometrical structure near the pyridine inclusion, and notorious differences in the electronic structure. These results should be of relevance in the study of spongy and reactive carbons, for which the topology of Schwarzite structures has been experimentally observed [35].

In the context of experimental identification of these curved structures, the vibrational and EEL spectra were calculated, thus providing useful.

The investigation of femtosecond laser induced transitions in carbon nanostructures, revealed the possibility of healing of 5-7-5-7 defects into hexagonal rings in graphitic structures. This healing mechanism could be activated with experimentally available laser pulses (durations ~ 50 fs, frequencies ~ 2 eV, and energies ~ 1.5 eV/atom). This transition could be related to the experimental observations reported in ref. [168], on laser irradiated nanotubes. The laser-induced inverse generalized S-W transformation (conversion of 5-7-5-7 defects into 6-6-6-6 rings) proceeds in a characteristic fashion. Here, we noted strong out-of-plane components of the rotated dimer motion are required prior to the dimer's rotation, and the formation of 6-6-6-6 rings.

The laser induced fragmentation mechanisms of C_{2V} fullerenes (the Buckminster fullerene with a generalized S-W transformation), were also studied. The fragmentation was observed to start from the atoms shared by two pentagons.

For a larger (C_{500}) fullerene with a generalized S-W transformation, we witnessed some of the steps observed for defect annealing in graphite and nanotubes. However, the absorbed energy required for laser healing, seems to be very close to the fragmentation threshold of the system, a condition that does not favor the possibility of laser induced inverse S-W transformations.

The possibility of laser induced dimerization of fullerenes encapsulated in a carbon nanotube was also demonstrated. The resultant dimer is bridged by 7- and 9-membered rings. This dimer is metastable, and no further annealing was observed

for temperatures up to 1000K.

We have extended the framework for the description of laser-matter interactions, in order to include polarization effects, and the possibility to deal with multi-species systems (binary semiconductors, for instance).

6.1 Further work

6.1.1 Polycubane polymers.

Cubane based polymers still requires further studies. The growth of different patterns, and the evolution of the physical and chemical properties would be of experimental interest. The identification of paths leading to the 3D-supercubane structure [67] could also be of technological relevance.

The effects of substituting the hydrogen terminations with functional groups, could be investigated; especially the electronic properties, and the solubility of the polymer chains.

The interaction of polycubane polymers with biological systems, would be relevant for the pharmaceutical industry. Therefore, alternative methods for studying these system should be developed.

6.1.2 Negatively curved carbon structures.

Additional theoretical characterization, aimed to the experimental identification of Schwarzites structures is required. The calculation of Raman and Infrared spectra, may be relevant in this context.

The study of the chemical and catalytic properties of Schwarzites structures, should also be investigated in detail.

The potential use of these structures for the fabrication of gas storage devices is also an interesting issue. Molecular dynamics simulations may help to establish their adsorption capability.

The synthesis of disordered Schwarzites have been experimentally achieved [35]. Therefore, it is also important to clarify the effects of disorder in the electronic

properties of the Schwarzites.

6.1.3 Laser-matter interaction.

The tight-binding, non adiabatic molecular dynamics framework used in this work, could now be applied to a large variety of atomic systems. Therefore, novel nano-systems could be studied in this context.

Further improvements to the theoretical framework, especially the generalization to a full density-matrix formalism, should be developed, but this may be worth of a Ph. D. research.

The potential use of laser irradiation in the synthesis of novel carbon structures (for instance Schwarzite crystals), should also be addressed.

6.1.4 Synthetic paths for Schwarzite structures

The witnessed laser induced dimerization of fullerenes, suggest the possibility of achieving negatively curved carbon structures using laser annealing of fullerite crystals.

The templated pyrolysis of carbon precursors, especially using templates with the topology of minimal surfaces (zeolites), may also lead to periodic minimal surfaces.

Bibliography

- [1] H.W. Kroto *et al*, C_{60} : BUCKMINSTERFULLERENE *Nature* (London) 318, 162 (1985).
- [2] H. Ibach and H. Lüth, SOLID STATE PHYSICS, AN INTRODUCTION TO THEORY AND EXPERIMENT, Springer-Verlag, Berlin (1991).
- [3] P. E. Eaton, T.E. Cole Jr. , CUBANE, *J. Am. Chem. Soc.* 86, 3157 (1964) .
- [4] T. J. Katz, N. Acton, SYNTHESIS OF PRISMANE *J. Am. Chem. Soc.*, 95(8), 2738-2739 (1973).
- [5] Maier, Pfriem, Scäfer, Matusch, *Angew. Chemie, Int. Ed. Engl.* 17, 520 (1978).
- [6] G. K. S. Prakash, V. V. Krishnamurthy, R. Herges, R. Bau, H. Yuan, G. A. Olah, W. D. Fessner, H. Prinzbach, STABLE CARBOCATIONS. 273. [1.1.1.1]- AND [2.2.1.1]PAGODANE DICATIONS: FROZEN TWO-ELECTRON WOODWARD-HOFFMANN TRANSITION-STATE MODELS, *J. Am. Chem. Soc.*, 110(3), 7764-7772 (1988).
- [7] P. E. Eaton, Y. S. Or, S. J. Branca, PENTAPRISMANE *J. Am. Chem. Soc.* 103(8), 2134-2136 (1981).
- [8] H. Dodziuk, UNUSUAL SATURATED HYDROCARBONS : INTERACTION BETWEEN THEORETICAL AND SYNTHETIC CHEMISTRY, *Top. Stereochem.*, 21, 351 (1994).
- [9] K. Sorger, P. v. R. Schleyer, D. Stalke, DIMERIC [3,3-DIMETHYL-2-(TRIMETHYLSILYL)CYCLOPROPENYL]LITHIUM- TETRAMETHYLETHYLENE-DIAMINE: DISTORTION OF THE CYCLOPROPENYL GEOMETRY DUE TO

- STRONG REHYBRIDIZATION AT THE LITHIATED CARBON, *J. Am. Chem. Soc.* 118, 1086-1091 (1996).
- [10] A. Albinati, S. Brückner, G. Allegra, STRUCTURAL STUDIES OF HIGHLY STRAINED HYDROCARBONS. II. THE A-C'-C STEREOISOMER OF DODECAHYDROTRIPTYCENE, *Acta Cryst.*, B33, 229-231 (1977).
- [11] T. Yildirim, P. M. Gehring, D. A. Neumann, P. E. Eaton, T. Emrick, UNUSUAL STRUCTURE, PHASE TRANSITION, AND DYNAMICS OF SOLID CUBANE, *Phys. Rev. Lett.* 78, 4938 (1997).
- [12] T. Yildirim, Ç. Kiliç, S. Ciraci, P. M. Gehring, D. A. Neumann, P. E. Eaton, T. Emrick, VIBRATIONS OF THE CUBANE MOLECULE: INELASTIC NEUTRON SCATTERING STUDY AND THEORY, *Chem. Phys. Lett.* 309, 234 (1999).
- [13] T. Yildirim, P. M. Gehring, D. A. Neumann, P. E. Eaton, T. Emrick, NEUTRON-SCATTERING INVESTIGATION OF MOLECULAR REORIENTATIONS IN SOLID CUBANE, *Phys. Rev. B* 60, 314 (1999).
- [14] P. E. Eaton, CUBANES: STARTING MATERIALS FOR THE CHEMISTRY OF THE 1990S AND THE NEW CENTURY, *Angew. Chem.* 31, 1421 (1992).
- [15] P. E. Zhang, OCTANITROCUBANE: A NEW NITROCARBON. *Propellants, Explosives, Pyrotechnics* 27, 1 - 6 (2002).
- [16] M-X Zhang, P.E. Eaton, R. Gilardi, HEPTA- AND OCTANITROCUBANES, *Angew. Chem. Intl. ed.* 39 401 (2000).
- [17] P. E. Eaton, K. Pramod, T. Emrick, R. Gilardi, BUILDING WITH CUBANE-1,4-DIYL. SYNTHESIS OF ARYL-SUBSTITUTED CUBANES, P-[N]CUBYLS, AND CUBANE-SEPARATED BIS(ARENES), *J. Am. Chem. Soc.* 121, 4111 (1999).
- [18] D. A. Hrovat, W.T. Borden, P. E. Eaton, and B. Kahr, A COMPUTATIONAL STUDY OF THE INTERACTIONS AMONG THE NITRO GROUPS IN OCTANITROCUBANE, *J. Am. Chem. Soc.* 123, 1289-1293 (2000).

- [19] A. J. Stone and D. J. Wales, THEORETICAL STUDIES OF ICOSAHEDRAL C₆₀ AND SOME RELATED SPECIES, *Chem. Phys. Lett.* 128, 501 (1986).
- [20] S. L. Richardson, J. L. Martins, AB INITIO STUDIES OF THE STRUCTURAL AND ELECTRONIC PROPERTIES OF SOLID CUBANE, *Phys. Rev. B* 58, 15307 (1998).
- [21] P. M. V. B. Barone, A. Camilo Jr., D. S. Galvão, THEORETICAL CHARACTERIZATION OF OLIGOCUBANE, *Synthetic Metals* 102, 1410 (1999).
- [22] J. Gryko, P. F. MacMillan, R. F. Marzke, G. K. Ramachandran, D. Patton, S. K. Deb and O. T. Sankey, LOW-DENSITY FRAMEWORK FORM OF CRYSTALLINE SILICON WITH A WIDE OPTICAL BAND GAP, *Phys. Rev. B.* 62, 7707(2000).
- [23] K. Allen and F. Hellman, SPECIFIC HEAT OF ENDOHEDRAL AND HIGHER FULLERENE THIN FILMS, *J. Chem. Phys.* 111 5291)(1999).
- [24] R. Saito, M. Fujita, G. Dresselhaus, and M. S Dresselhaus, ELECTRONIC STRUCTURE OF CHIRAL GRAPHENE TUBULES *Appl. Phys. Lett.*, 60(18), 2204 (1992).
- [25] A. L. MacKay and H. Terrones, DIAMOND FROM GRAPHITE *Nature* (London) 352, 762(1991).
- [26] H. Terrones and A.L. Mackay, THE GEOMETRY OF HYPOTHETICAL CURVED GRAPHITE STRUCTURES *Carbon* 30 No. 8, 1251 (1992).
- [27] H. Terrones and A.L. Mackay, TRIPLY PERIODIC MINIMAL SURFACES DECORATED WITH CURVED GRAPHITE, *Chem. Phys. Lett.* 207, 45 (1993).
- [28] A. H. Schoen, INFINITE PERIODIC MINIMAL SURFACES WITHOUT SELF-INTERSECTIONS, NASA Techn. note no. D-5541 (1970).
- [29] M. O' Keeffe, G. Adams, O. F. Sankey , PREDICTED NEW LOW ENERGY FORMS OF CARBON *Phys. Rev. Let* 68, 2325 (1992)

- [30] R. Philips, D. A. Drabold, Thomas Lenosky, G. B. Adams and O. F. Sankey, ELECTRONIC STRUCTURE OF SCHWARZITE, *Phys. Rev. B.* 46 1941(1992).
- [31] D. Vanderbilt, J. Tersoff, NEGATIVE-CURVATURE FULLERENE ANALOG OF C60, *Phys. Rev. Lett.* 68, 511 (1992)
- [32] M. Z. Huang and W. Y. Ching (1993) ELECTRONIC PROPERTIES OF NEGATIVE-CURVATURE PERIODIC GRAPHITIC CARBON SURFACES , *Phys. Rev. B* 47 1593 (1993) .
- [33] H. Aoki, M. Koshino, D. Takeda, M. Morise, ELECTRONIC STRUCTURE OF PERIODIC CURVED SURFACES: TOPOLOGICAL BAND STRUCTURE, *Phys. Rev. B.*,65, 035102 (2001).
- [34] Townsend *et al*, NEGATIVELY CURVED GRAPHITE SHEET MODEL OF AMORPHOUS CARBON, *Phys. Rev. Lett.*, 69 921 (1992).
- [35] Barborine, Piseli, Milani, Benedek,Dukati and Robertson, NEGATIVELY CURVED SPONGY CARBON, *Appl. Phys. Lett*, 81, 3359 (2002).
- [36] Z. Ma, T. Kyotani, Z. Liu, O. Terasaki and A. Tomita, VERY HIGH SURFACE AREA MICROPOROUS CARBON WITH A THREE-DIMENSIONAL NANO-ARRAY STRUCTURE: SYNTHESIS AND ITS MOLECULAR STRUCTURE, *Chem. Mater.* 13 4413 (2001) .
- [37] N. Park *et. al.*, MAGNETISM IN ALL-CARBON NANOSTRUCTURES WITH NEGATIVE GAUSSIAN CURVATURE,*Phys. Rev. Lett.* 91, 7204 (2003).
- [38] Y. Kopelevich, R. R. da Silva, J. H. S. Torres, A. Penicaud and T. Kyotani, LOCAL FERROMAGNETISM IN MICROPOROUS CARBON WITH THE STRUCTURAL REGUARILY OF ZEOLITE Y, *Phys. Rev. B* 68 092408 (2003).
- [39] L. Bartels,F. Wang, D. Möller, E. Knoesel, T. F. Heinz, REAL-SPACE OBSERVATION OF MOLECULAR MOTION INDUCED BY FEMTOSECOND LASER PULSES, *Science*, 305, 648-651 (2004).

- [40] M. Dûr, A. Biedermann, Z. Hu, U. Hôfer, T. F. Heinz , PROBING HIGH-BARRIER PATHWAYS OF SURFACE REACTIONS BY SCANNING TUNNELING MICROSCOPY, *Science* 296 1838 (2002).
- [41] K. Sokolowski-Tinten et al. TRANSIENT STATES OF MATTER DURING SHORT PULSE LASER ABLATION, *Phys. Rev. Lett.* **81** 224 (1998)
- [42] M. Bonn et. al., PHONON- VERSUS ELECTRON-MEDIATED DESORPTION AND OXIDATION OF CO ON RU(0001) , *Science* 285 1042 (1999).
- [43] H. O. Jeschke, M. E. Garcia, J. A. Alonso, NONTHERMAL FRAGMENTACION OF C₆O, *Chem. Phys. Lett.* 352 (2002).
- [44] T. Dumitrica, M. E. Garcia, H. O. Jeschke and B. I. Yakobson, SELECTIVE CAP OPENING IN CARBON NANOTUBES DRIVEN BY LASER-INDUCED COHERENT PHONONS , *Phys. Rev. Lett.*, 92 7401 (2004).
- [45] H. O. Jeschke et. al. MICROSCOPIC ANALYSIS OF THE LASER-INDUCED FEMTOSECOND GRAPHITIZATION OF DIAMOND , *Phys. Rev. B.* 60 R3701 (1999).
- [46] Q. Zhao, M. B. Nardelli and J. Bernholc, ULTIMATE STRENGTH OF CARBON NANOTUBES: A THEORETICAL STUDY, *Phys. Rev. B* 65, 144105-1 (2002).
- [47] T. Yildirim, S. Ciraci, Ç Kiliç, A. Buldum, FIRST-PRINCIPLES INVESTIGATION OF STRUCTURAL AND ELECTRONIC PROPERTIES OF SOLID CUBANE AND ITS DOPED DERIVATIVES *Phys. Rev. B* 62, 7625 (2000) .
- [48] T. Yildirim, LATTICE DYNAMICS OF SOLID CUBANE WITHIN THE QUASI-HARMONIC APPROXIMATION .*Solid State Comm* 124, 449 (2002).
- [49] K. Miaskiewicz, D. A. Smith, COMPUTATIONAL DENSITY FUNCTIONAL THEORY VIBRATIONAL SPECTRA OF CUBANE, *Chem. Phys. Lett* , 270, 376 (1999).
- [50] J. M. Schulman, C. R. Fischer, P. Solomon and T. J. Venanzi, THEORETICAL STUDIES OF THE CUBANE MOLECULE, *J. Am. Chem. Soc.* 100 2949 (1978).
- [51] J. Almlöf, T. Jonvik, THE MOLECULAR STRUCTURE AND SPECTRA OF CUBANE. AN AB INITIO INVESTIGATION , *Chem. Phys. Lett.* 92, 267 (1982).

- [52] B. Herrera, A. Toro-Labbé, THEORETICAL STUDY OF THE INTERNAL ROTATION OF CUBYLCUBANE AND CUBYLCUBANE DIFLUORIDE *Chem. Phys. Lett.* 344, 193 (2001) .
- [53] A. S. Pine, A.G. Maki, A. G. Robiette, B.J. Krohn, J.G. Watson. Th. Urbanek, TUNABLE LASER SPECTRA OF THE INFRARED-ACTIVE FUNDAMENTALS OF CUBANE, *J. Am. Chem. Soc.* 106, 891 (1984).
- [54] E. B. Fleishcer, X-RAY STRUCTURE DETERMINATION OF CUBANE, *J. Am. Chem. Soc.* 86, 3889 (1964).
- [55] J. C. Facelli, A. M. Orendt, M.S. Solum, G. Depke, D. M. Grant, J. Michl, LOW-TEMPERATURE CARBON-13 MAGNETIC RESONANCE IN SOLIDS. 6. METHINE CARBONS, *J. Am. Chem. Soc.* 108, 4268 (1986).
- [56] C. A. Scamehorn, S. N. M. Hermiller, R. M. Pitzar, ELECTRONIC STRUCTURE OF POLYHEDRAL ALKANES *J. Chem. Phys.* 84, 833 (1986).
- [57] J. P. Perdew, J. A. Chevari, S. H. Vosko, K. A. Jackson, M. R. Pederson, D. J. Singh, F. Carlos, ATOMS, MOLECULES, SOLIDS, AND SURFACES: APPLICATIONS OF THE GENERALIZED GRADIENT APPROXIMATION FOR EXCHANGE AND CORRELATION *Phys. Rev. B.* 46 6671 (1992).
- [58] D. Vanderbilt, SOFT SELF-CONSISTENT PSEUDOPOTENTIALS IN A GENERALIZED EIGENVALUE FORMALISM, *Phys. Rev. B.* , 41 (Rapid Communications) , 7892 (1991).
- [59] B. Herrera, F. Valencia, A. H. Romero, M. Kiwi, R. Ramírez and A. Toro-Labbé, A DENSITY FUNCTIONAL THEORY STUDY OF CUBANE OLIGOMERS, *in preparation*.
- [60] D. F. Shanno *Mathematics of Computation*, 24, 647 (1970). See also summary in: D. F. Shanno, *J. of Optimization Theory and Applications*, 46(1), 87 (1985).

- [61] F. Valencia, A. H. Romero, M. Kiwi, R. Ramirez, A. Toro-Labbé, AB INITIO STUDY OF CUBYL CHAINS AND NETWORKS, *J. Chem. Phys.*, **121**, 9172 (2004).
- [62] A. D. Becke. DENSITY-FUNCTIONAL EXCHANGE-ENERGY APPROXIMATION WITH CORRECT ASYMPTOTIC BEHAVIOR *Phys. Rev. A*, **38**, 3098 (1988).
- [63] C. Lee; W. Yang; R. G. Parr. DEVELOPMENT OF THE COLLE-SALVETTI CORRELATION-ENERGY FORMULA INTO A FUNCTIONAL OF THE ELECTRON DENSITY *Phys. Rev. B* **37** 785 (1988).
- [64] GAUSSIAN 98, REVISION A.7, M. J. Frisch, G. W. Trucks, H. B. Schlegel, G. E. Scuseria, M. A. Robb, J. R. Cheeseman, V. G. Zakrzewski, J. A. Montgomery, Jr., R. E. Stratmann, J. C. Burant, S. Dapprich, J. M. Millam, A. D. Daniels, K. N. Kudin, M. C. Strain, O. Farkas, J. Tomasi, V. Barone, M. Cossi, R. Cammi, B. Mennucci, C. Pomelli, C. Adamo, S. Clifford, J. Ochterski, G. A. Petersson, P. Y. Ayala, Q. Cui, K. Morokuma, D. K. Malick, A. D. Rabuck, K. Raghavachari, J. B. Foresman, J. Cioslowski, J. V. Ortiz, A. G. Baboul, B. B. Stefanov, G. Liu, A. Liashenko, P. Piskorz, I. Komaromi, R. Gomperts, R. L. Martin, D. J. Fox, T. Keith, M. A. Al-Laham, C. Y. Peng, A. Nanayakkara, C. Gonzalez, M. Challacombe, P. M. W. Gill, B. Johnson, W. Chen, M. W. Wong, J. L. Andres, C. Gonzalez, M. Head-Gordon, E. S. Replogle, and J. A. Pople, Gaussian, Inc., Pittsburgh PA, **1998**.
- [65] A. P. Horsfield, P. D. Godwin, D. G. Pettifor, P. Sutton, COMPUTATIONAL MATERIALS SYNTHESIS. I. A TIGHT-BINDING SCHEME FOR HYDROCARBONS, *Phys. Rev. B.* , **54**, 15773 (1996).
- [66] H. Müller, H. G. Fritsche, and L. Skala, CLUSTERS OF ATOMS AND MOLECULES I, Chap. ANALYTIC CLUSTER MODELS AND INTERPOLATION FORMULAE FOR CLUSTER PROPERTIES, p. 114, Springer-Verlag, Berlin **1995**.

- [67] B. Winkler, V. Milman, STRUCTURE AND PROPERTIES OF SUPERCUBANE FROM DENSITY FUNCTIONAL CALCULATIONS, *J. Chem. Phys.* **108** 5506 (1998)
- [68] U. H. F. Bunz, SYNTHESIS OF NOVEL LIQUID CRYSTALLINE ORGANOMETALLIC POLYMERS, *Pure & Appl. Chem.* **68**(2) 309-312, (1996).
- [69] H. L. Anderson, BUILDING MOLECULAR WIRES FROM THE COLOURS OF LIFE: CONJUGATED PORPHYRIN OLIGOMERS, *Chem. Comm.* 1999 2323-2330 (1999).
- [70] C. Kitamura, S. Kakuya; M. Nakagawa, M. Ouchi, A. Yoneda, Y. Yamashita, SYNTHESIS AND PROPERTIES OF A NEW ETHYNE-LINKED DONOR/ACCEPTOR PENTAMER, *Tetrahedron Lett.* **43**(18) 3373-3376 (2002).
- [71] J. J. Pak, O. S. Darwish, T.J.R. Weakley, M. M. Haley, SYNTHESIS AND CRYSTALLOGRAPHIC CHARACTERIZATION OF A PALLADADEHYDROBENZO[19]ANNULENE, *Journal of Organometallic Chemistry* **683** 430 (2003).
- [72] P. P. Ghoroghchian *et al.*, NEAR-INFRARED-EMISSIVE POLYMERSOMES: SELF-ASSEMBLED SOFT MATTER FOR IN VIVO OPTICAL IMAGING, *PNAS* **102**(8) 2922-2927 (2005).
- [73] P. Manini, W. Amrein, V. Gramlich, F. Diederich, EXPANDED CUBANE: SYNTHESIS OF A CAGE COMPOUND WITH A C₅₆ CORE BY ACETYLENIC SCAFFOLDING AND GAS-PHASE TRANSFORMATIONS INTO FULLERENES *Angew. Chem.* **114**(22) 4515 - 4519 (2002).
- [74] V. V. Walatka, M. M. Labes and J. H. Perlstein, POLYSULFUR NITRIDE- A ONE-DIMENSIONAL CHAIN WITH A METALLIC GROUND STATE *Phys. Rev. Lett.* **31** 1139 (1973).
- [75] P. E. Eaton, R. L. Gilardi, M-X. Zhang, POLYNITROCUBANES: ADVANCED HIGH-DENSITY, HIGH-ENERGY MATERIALS, *Adv. Mater.* **12**, 1143 (2000).

- [76] Savin, A.; Becke, A. D.; Flad, J.; Nesper, R.; Preuss, H.; von Schnering, A
NEW LOOK AT ELECTRON LOCALIZATION, *Angew. Chem. Intl. Edition* 30 409-412 (1991)
- [77] N. Troullier and J. Martins, EFFICIENT PSEUDOPOTENTIALS FOR PLANE-WAVE CALCULATIONS, *Phys. Rev. B* 43, 1993 (1991).
- [78] J. Lee, S. Yoo, T. Hyeon, S. M. Oh and K. Bum Kim, SYNTHESIS OF A NEW MESOPOROUS CARBON AND ITS APPLICATION TO ELECTROCHEMICAL DOUBLE-LAYER CAPACITORS, *Chem. Comm.* 1999(21) 2177 (1999).
- [79] R. Ryo, S. H. Joo and S. J. Jun, SYNTHESIS OF HIGHLY ORDERED CARBON MOLECULAR SIEVES VIA TEMPLATE-MEDIATED STRUCTURAL TRANSFORMATION *J. Phys. Chem. B* 103(37) 7743 (1999) .
- [80] J. Lee, S. Yoon, S. M. Oh, C. H. Shin and T. Hyeon, DEVELOPMENT OF A NEW MESOPOROUS CARBON USING AN HMS ALUMINOSILICATE TEMPLATE *Adv. Mater.* 12 No.5 359 (2000) .
- [81] S. Jun, S.H Joo, R. Ryoo, M. Kruk, M. Jaroniec, Z. Liu, T. Ohsuna and O. Terasaki, SYNTHESIS OF NEW, NANOPOROUS CARBON WITH HEXAGONALLY ORDERED MESOSTRUCTURE, *J. Am. Chem. Soc.* 122 10712 (2000).
- [82] S. H. Joo, S. Jun and R. Ryoo, SYNTHESIS OF ORDERED MESOPOROUS CARBON MOLECULAR SIEVES CMK-1, *Microporous and Mesoporous Materials* 44-45 153 (2001).
- [83] Z. K. Tang, H. D. Sun, J. Wang, J. Chen and G. Li, MONOSIZED SINGLE WALL CARBON NANOTUBES FORMED IN CHANNELS OF AlPO_4 -5 SINGLE CRYSTALS, *Appl. Phys. Lett.* 73 2287 (1998).
- [84] S. Han, S. Kim, H. Lim, W. Choi, H. Park, J. Yoon, T. Hyeon, NEW NANOPOROUS CARBON MATERIALS WITH HIGH ADSORPTION CAPACITY AND RAPID ADSORPTION KINETICS FOR REMOVING HUMIC ACIDS, *Microporous and Mesoporous Materials* 58 131-135 (2003).

- [85] S. Han, M. Kim, T. Hyeon, DIRECT FABRICATION OF MESOPOROUS CARBON USING IN-SITU POLIMERIZED SILICA GEL NETWORKS AS A TEMPLATE. *Carbon* 41 1525 (2005).
- [86] J. H. Jang, S. Han, T. Hyeon, S. M. Oh ELECTROCHEMICAL CAPACITOR PERFORMANCE OF HYDROUS RUTHENIUM OXIDE/MESOPOROUS CARBON COMPOSITE ELECTRODES, *Journal of Power Sources* 123 ,79 (2003).
- [87] M. Kim, K. Sohn, H. Bin Na, T. Hyeon, SYNTHESIS OF NANORATTLES COMPOSED OF GOLD NANOPARTICLES ENCAPSULATED IN MESOPOROUS CARBON AND POLYMER SHELLS, *Nano Letters* 2 No. 12 1383 (2002).
- [88] S. B. Yoon, J. Y. Kim and J-S. Yu, SYNTHESIS OF HIGHLY ORDERED NANOPOROUS CARBON MOLECULAR SIEVES FROM SILYLATED MCM-48 USING DIVINYLBENZENE AS PRECURSOR *Chem. Comm.* 2001(6) 559 (2001).
- [89] S. B. Yoon, J. Y. Kim and J-S. Yu, A DIRECT TEMPLATE SYNTHESIS OF NANOPOROUS CARBONS WITH HIGH MECHANICAL STABILITY USING ASSYNTHESIZED MCM-48 HOSTS *Chem. Comm.* 2001 (14) 1536 (2002) .
- [90] S. Shiraishi, H. Kurihara and A. Oya, PREPARATION AND ELECTRIC DOUBLE CAPACITANCE OF MESOPOROUS CARBON, *Carbon Science* 1 No. 3, 133 (2001).
- [91] T. Heine, P. W. Fowler, G. Seifert, C_{36} : FROM DIMER TO BULK, *Solid State Comm.* 111, 19 (1999).
- [92] R. Nesper , K. P. E. Vogel, P. E. Blchl, HYPOTHETICAL CARBON MODIFICATIONS DERIVED FROM ZEOLITE FRAMEWORKS, *Angew. Chem. Int'l Ed. engl* 32 ,701-703 (1993).
- [93] C. T. Kresge, M. E. Leonowicz, W. J. Roth, J. C. Vartuli, and J. S. Beck, ORDERED MESOPOROUS MOLECULAR SIEVES SYNTHESIZED BY A LIQUID CRYSTAL TEMPLATE MECHANISM., *Nature* 359 710-712 (1992).

- [94] A. H. Nevidomsky, G. Santiyi, M. C. Payne, CHEMICAL ACTIVE SUBSTITUTIONAL NITROGEN IMPURITY IN CARBON NANOTUBES, *Phys. Rev. Lett.* **91**, 5502 (2003).
- [95] E. Raymundo-Pinẽro *et. al.*, STRUCTURAL CHARACTERIZATION OF N CONTAINING ACTIVATED CARBON FIBERS PREPARED FROM A LOW SOFTENING POINT PETROLEUM PITCH AND MELAMINE RESINE, *Carbon* **40** 597 (2002).
- [96] V. Petkovf, R. G. DiFrancesco, S. L. Billinge, M. Acharya, H.C. Foley, LOCAL STRUCTURE OF NANOPOROUS CARBONS, *Philosophical Magazine B* **10**, 1519 (1999).
- [97] S. Baroni, A. Dal Corso, S. de Gironcoli, and P. Giannozzi, <http://www.pwscf.org>.
- [98] M.C. Payne *et. al.*, ITERATIVE MINIMIZATION TECHNIQUES FOR AB INITIO TOTAL-ENERGY CALCULATIONS: MOLECULAR DYNAMICS AND CONJUGATE GRADIENTS, *Rev. Mod. Phys.* **64**, 1045 (1992).
- [99] H. Terrones MATHEMATICAL SURFACES AND INVARIANTS IN THE STUDY OF ATOMIC STRUCTURES, Ph.D. Thesis, University of London, 1992.
- [100] S.T. Hyde, THE TOPOLOGY AND GEOMETRY OF INFINITE PERIODIC SURFACES *Z. fur. Kristallogr.* **187**, 165-185 , (1989) .
- [101] S. Andersson, S.T. Hyde, K. Larsson, and S. Lidin, MINIMAL SURFACES AND STRUCTURES: FROM INORGANIC AND METAL CRYSTALS TO CELL MEMBRANES AND BIOPOLYMERS, *Chem. Rev.* **88**, 221-241 (1988) .
- [102] H. Terrones, J. Fayos and J. L. Aragón, GEOMETRICAL AND PHYSICAL PROPERTIES OF HYPOTHETICAL PERIODIC AND APERIODIC GRAPHITIC STRUCTURES, *Acta Metallurgica et Materialia* **42**, 2687-2700 (1994).
- [103] M. J. Mehl , B.M. Klein and D. A. Papaconstantopoulos, FIRST PRINCIPLES CALCULATIONS OF ELASTIC PROPERTIES OF METALS, in: *Intermetallic Compounds: Principles and Practice* Volume I, Ch. 9. pp 195-210, J.H. Westbrook and R. L. Fleischer, eds. , John Wiley & Sons (London, 1995).

- [104] Z. Ma, T. Kyotani, Z. Liu, O. Terasaki and A. Tomita, VERY HIGH SURFACE AREA MICROPOROUS CARBON WITH A THREE-DIMENSIONAL NANO-ARRAY STRUCTURE: SYNTHESIS AND ITS MOLECULAR STRUCTURE, *Chem. Mater.* 13, 4413 (2001)
- [105] P J F Harris, STRUCTURE OF NON-GRAPHITIZING CARBONS, *Int. Mater. Rev* 42 206-218(1997) .
- [106] G. Benedek, H. Vahedi-Tafreshi, E. Barborini, P. Piseri, P. Milani, C. Ducati and J. Robertson, THE STRUCTURE OF NEGATIVELY CURVED SPONGY CARBON, *Diamond and Related Materials* 12 768 (2003).
- [107] R. Rurali, E. Hernández, TROCADERO: A MULTIPLE-ALGORITHM MULTIPLE-MODEL ATOMISTIC SIMULATION PROGRAM, *Comput. Mat. Sci.* 28, 85 (2003).
- [108] J. Widany, Th. Frauenheim, Th. Khler, M. Stenberg , D Porezag and G. Jungnickel, DENSITY-FUNCTIONAL-BASED CONSTRUCTION OF TRANSFERABLE NONORTHOGONAL TIGHT-BINDING POTENTIALS FOR B, N, BN, BH, AND NH, *Phys. Rev. B.* 53, 4443 (1996).
- [109] Th. Frauenheim *et. al.*, SELF-CONSISTENT CHARGE DENSITY-FUNCTIONAL BASED TIGHT-BINDING METHOD FOR PREDICTIVE MATERIALS SIMULATIONS IN PHYSICS, CHEMISTRY AND BIOLOGY, *physica status solidi (b)*, 217(1) 41 (2000).
- [110] H. J. Monkhorst and J. D. Pack, SPECIAL POINTS FOR BRILLOUIN-ZONE INTEGRATIONS, *Phys. Rev. B* 13, 5188 (1976).
- [111] J. P. Perdew and A. Zunger, SELF-INTERACTION CORRECTION TO DENSITY-FUNCTIONAL APPROXIMATIONS FOR MANY-ELECTRON SYSTEMS *Phys. Rev. B* 23, 5048 (1981) .
- [112] For a short review of this pseudopotential generation method see, for example, A. Dal Corso, S. Baroni , R. Resta and S. de Gironcoli AB INITIO CALCULA-

- TION OF PHONON DISPERSIONS IN II-VI SEMICONDUCTORS, *Phys Rev B*. 47 3588 (1993) .
- [113] D. L. Page, Y. Sun, A. F. Koschan, J. Paik, M. A. Abidi, NORMAL VECTOR VOTING: CREASE DETECTION AND CURVATURE ESTIMATION ON LARGE, NOISY MESHES, *Graphical Models*,64, 199 (2002), and references therein.
- [114] D. Zorin, TOPICS IN COMPUTER GRAPHICS, LECTURE NOTES, lecture #8: *Mesh smoothing. Discrete Laplacian and related smoothing methods. Discrete curvature and geodesics*, New York University, spring 2004. Available from <http://mrl.nyu.edu/~dzorin/geom04/lectures/lect08.pdf>
- .
- [115] M. L. Connolly, SOLVENT ACCESSIBLE SURFACES OF PROTEINS AND NUCLEIC ACIDS, *Science* 221, 709 713 (1983).
- [116] M. F. Sanner, A. J. Olson, and J. C. Spehner, REDUCED SURFACE: AN EFFICIENT WAY TO COMPUTE MOLECULAR SURFACES, *Biopolymers* 38,305 (1996).
- [117] E. F. Pettersen, T. D. Goddard, C. C. Huang, G. S. Couch, D. M. Greenblatt, E. C. Meng, and T. E. Ferrin, UCSF CHIMERA - A VISUALIZATION SYSTEM FOR EXPLORATORY RESEARCH AND ANALYSIS., *J. Comput. Chem.* 25, 1605-1612 (2004).
- [118] H. K. Chae *et. al.*, A ROUTE TO HIGH SURFACE AREA, POROSITY AND INCLUSION OF LARGE MOLECULES IN CRYSTALS, *Nature*, 427, 523-527 (2004).
- [119] MOLEKEL 4.0, P. Flkger, H.P. Lti, S. Portmann, J. Weber, *Swiss Center for Scientific Computing*, Manno (Switzerland), 2000.
- [120] E. Kaxiras and K. C. Pandey, ENERGETICS OF DEFECTS AND DIFFUSION MECHANISMS IN GRAPHITE, *Phys. Rev. Lett.* 61, 2693 (1988).

- [121] E. J. Duplock, M. Scheffler, P. J. D. Lindan, HALLMARK FOR PERFECT GRAPHITE *Phys. Rev. Lett.* **92** 225502 (2004).
- [122] A. Braun *et. al.*, ADVANTAGES OF SOFT X-RAY ABSORPTION OVER TEM-EELS FOR SOLID CARBON STUDIES A COMPARATIVE STUDY ON DIESEL SOOT WITH EELS AND NEXAFS, *Carbon*, 43, 117 (2005).
- [123] X. Weng, P. Rez, O. F. Sankey, PSEUDO-ATOMIC ORBITAL BAND THEORY APPLIED TO ELECTRON-ENERGY-LOSS NEAR-EDGE STRUCTURES, *Phys. Rev. B.*, 40, 5694 (1989).
- [124] E. K. U. Gross, LECTURE NOTES : DFT - I AND II - TDDFT - I AND II, lectures held during the *Spring College on electronic structure approaches to the physics of Material*, (19 May 9 June 2000), The Abdus Salam International Center for Theoretical Physics. Available through the agenda service:

http://cdsagenda5.ictp.trieste.it/full_display.php?ida=a02080#s1t1

.
- [125] M. Bockrath *et. al.*, CHEMICAL DOPING OF INDIVIDUAL SEMICONDUCTING CARBON-NANOTUBE ROPES, *Phys. Rev. B* 61 (Rapid Communication) 10606 (2000).
- [126] A. Castro, M.A.L. Marques, J.A Alonso, G.F. Bertsch, and A. Rubio , EXCITED STATES DYNAMICS IN TIME-DEPENDENT DENSITY FUNCTIONAL THEORY HIGH-FIELD MOLECULAR DISSOCIATION AND HARMONIC GENERATION, *European Physical Journal D* 28, 211-218 (2004).
- [127] H. Jeschke, THEORY FOR OPTICALLY CREATED NONEQUILIBRIUM IN COVALENT SOLIDS, ph.D. Thesis, Physics Department of the Freie Universitat, Berlin , 2000.
- [128] H. O. Jeschke, M. E. Garcia and K. H. Bennemann, THEORY FOR THE ULTRAFAST ABLATION OF GRAPHITE FILMS , *Phys. Rev. Lett.* 87, 015003 (2001).

- [129] H. O. Jeschke and M. E. Garcia, THEORETICAL DESCRIPTION OF THE ULTRA-FAST ABLATION OF DIAMOND AND GRAPHITE: DEPENDENCE OF THRESHOLDS ON PULSE DURATION *Appl. Surf. Sci.* 197-198, 107-113 (2002).
- [130] M. E. Garcia and H. O. Jeschke, THEORETICAL APPROACH TO THE LASER-INDUCED MELTING OF GRAPHITE UNDER DIFFERENT PRESSURE CONDITIONS *Appl. Surf. Sci.* 208-209, 61 (2003).
- [131] M. D. Mermin, THERMAL PROPERTIES OF THE INHOMOGENEOUS ELECTRON GAS *Phys. Rev.* 137 A1441 (1965).
- [132] C. H. Xu, C. Z. Wang, C. T. Chan und K. M. Ho, A TRANSFERABLE TIGHT-BINDING POTENTIAL FOR CARBON, *J. Phys. Condens. Matter* 4, 6047 (1992).
- [133] C. H. Xu, C. L. Fu and D. F. Pedraza, SIMULATIONS OF POINT-DEFECT PROPERTIES IN GRAPHITE BY A TIGHT-BINDING-FORCE MODEL *Phys. Rev. B* 48, 13273 (1993).
- [134] B. N. Davidson and W. E. Pickett , TIGHT BINDING STUDY OF HYDROGEN ON THE C(111), C(100) AND C(110) DIAMOND SURFACES *Phys. Rev. B.* 46 11253 (1994).
- [135] M. Graf and P. Vogl, *Physics. Rev. B*, ELECTROMAGNETIC FIELDS AND DIELECTRIC RESPONSE IN EMPIRICAL TIGHT-BINDING THEORY 51, 4940 (1995).
- [136] E. K. U. Gross, E. Runge and O. Heinonen, MANY-PARTICLE THEORY, Adam Hilger Eds., Bristol, England, (1991).
- [137] P. Sutton, M. W. Finnis, D. G. Pettifor, Y. Ohta, THE TIGHT BINDING BOND MODEL, *J. Phys. C.:Solid State Phys.* 21 35-66 (1988).
- [138] S. Shimizu, et al, COULOMB EXPLOSION OF BENZENE INDUCED BY AN INTENSE LASER FIELD *Journal of Chemical Physics* 117 3180 (2002).

- [139] M. Kohyama, S. Kose, M. Kinoshita, and R. Yamamoto, THE SELF-CONSISTENT TIGHT-BINDING METHOD:APPLICATION TO SILICON AND SILICON CARBIDE *J. Phys.: Condes. Matter* 2 7791-7808 (1990).
- [140] D. H. Reitze *et. al.*, OPTICAL PROPERTIES OF LIQUID CARBON MEASURED BY FEMTOSECOND SPECTROSCOPY, *Phys. Rev. B.* 45 2677 (1992).
- [141] P. L. Silvestrelli and M. Parrinello, AB INITIO MOLECULAR DYNAMICS SIMULATION OF LASER MELTING OF GRAPHITE, *J. Appl. Phys.* 83, 2478 (1998).
- [142] Y. Miyamoto *et. al.*, CAN PHOTO EXCITATIONS HEAL DEFECTS IN CARBON NANOTUBES? *Chem. Phys. Lett.* **392** 209 (2004).
- [143] A.H. Romero, M. Garcia, H. Jeschke, F. Valencia, H. Terrones, M. Terrones, FEMTOSECOND LASER NANOSURGERY OF DEFECTS IN CARBON NANOTUBES **to be published in:** *Nanoletters* (2005).
- [144] M. E. Garcia, T. Dumitrica, H. O. Jeschke LASER-INDUCED COHERENT PHONONS IN GRAPHITE AND CARBON NANOTUBES: MODEL AND SIMULATIONS, *Appl. Phys. A.* **79** 855 (2004).
- [145] H. Jeschke, M. Garcia, J. A. Alonso, *Chem. Phys. Lett.* **352** 154 (2002).
- [146] C. Z. Wang, K. M. Ho, M. D. Shirk, and P. A. Molian, LASER-INDUCED GRAPHITIZATION ON A DIAMOND (111) SURFACE, *Phys. Rev. Lett.* 85, 4092 (2000).
- [147] J. Zhao, B. Yakobson, R. E. Smalley, DYNAMIC TOPOLOGY OF FULLERENE COALESCENCE, *Phys. Rev. Lett.* 88 185501 (2002).
- [148] M. Terrones, F. Banhart, N. Grobert, J. C. Charlier, H. Terrones, P. M. Ajayan, MOLECULAR JUNCTIONS BY JOINING SINGLE WALLED CARBON NANOTUBES , *Phys. Rev. Lett.* 89, 075505 (2002).
- [149] M. Yoon, S. Han, G. Kim, S. B. Lee, S. Bever, E. Osawa, J. Ihm, M. Terrones, F. Banhart, J. C. Charlier, N. Grobert, H. Terrones, P. M. Ajayan,

- D. Tománek, ZIPPER MECHANISM OF NANOTUBE FUSION: THEORY AND EXPERIMENT, *Phys. Rev. Lett.*, 92, 75504 (2004) .
- [150] P.A. Marcos, M.J. Lopez, A. Rubio, J.A. Alonso, THERMAL ROAD FOR FULLERENE ANNEALING, *Chem. Phys. Lett.* 273 367 (1997).
- [151] A. Perez-Garrido *J. Phys: Condens. Matter.* **14** 5077 (2002).
- [152] C.P. Ewels et al. METASTABLE FRENKEL PAIR DEFECT IN GRAPHITE: SOURCE OF WIGNER ENERGY?, *Phys. Rev. Lett.* **91** 25505 (2003).
- [153] G. Henkelman, B. P. Uberuaga, H. Jónsson, A CLIMBING IMAGE NUDGED ELASTIC BAND METHOD FOR FINDING SADDLE POINTS AND MINIMUM ENERGY PATHS, *J. Chem. Phys.* 113, 9901 (2000); G. Henkelman and H. Jónsson, IMPROVED TANGENT ESTIMATE IN THE NUDGED ELASTIC BAND METHOD FOR FINDING MINIMUM ENERGY PATHS AND SADDLE POINTS, *J. Chem. Phys.* 113, 9978 (2000).
- [154] K. Sokolowski-Tinten, C. Blome, J. Blums, A. Cavalleri, C. Dietrich, A. Tarasevitch, I. Uschmann, E. Förster, M. Kammler, M. Horn-von-Hoegen, D. von der Linde, FEMTOSECOND X-RAY MEASUREMENT OF COHERENT LATTICE VIBRATIONS NEAR THE LINDEMANN STABILITY LIMIT *Nature (London)*, 422, 287 (2003).
- [155] V.H. Crespi, M.L. Cohen and A. Rubio, IN SITU BAND GAP ENGINEERING OF CARBON NANOTUBES, *Phys. Rev. Lett.* **79** 2093 (1997) and reference therein.
- [156] B.C. Pan, W.S. Yang and J. Yang, FORMATION ENERGIES OF TOPOLOGICAL DEFECTS IN CARBON NANOTUBES, *Phys. Rev. B.* **62** 12652 (2000).
- [157] J. Kono et. al., ULTRA-FAST OPTICAL SPECTROSCOPY OF MICELLE-SUSPENDED SINGLE-WALLED CARBON NANOTUBES *Appl. Phys. A.* **78** 1093 (2004).

- [158] F. Valencia, A. H. Romero, H. Jeschke, and M. Garcia, ULTRAFAST RESPONSE OF DEFECTIVE GRAPHITIC SYSTEMS: LASER INDUCED VIBRATIONS AND INVERSE STONE-WALES TRANSITIONS, *In preparation*, (2005).
- [159] R. Car and M. Parrinello, UNIFIED APPROACH FOR MOLECULAR DYNAMICS AND DENSITY-FUNCTIONAL THEORY, *Phys. Rev. Lett.* 55, 2471 (1985); we have used the code CPMD developed by J. Hutter *et al.*, at MPI für Festkörperforschung and IBM Research Laboratory (1990-2001).
- [160] A. D. Becke, DENSITY-FUNCTIONAL EXCHANGE-ENERGY APPROXIMATION WITH CORRECT ASYMPTOTIC BEHAVIOR, *Phys. Rev. A* 38, 3098 (1988);
C. Lee, W. Yang, and R. C. Parr, DEVELOPMENT OF THE COLLE-SALVETTI CORRELATION-ENERGY FORMULA INTO A FUNCTIONAL OF THE ELECTRON DENSITY, *Phys. Rev. B* 37, 785 (1988).
- [161] D. S. Ivanov and L. V. Zhigilei, EFFECT OF PRESSURE RELAXATION ON THE MECHANISM OF SHORT-PULSE LASER MELTING, *Phys. Rev. Lett* 91, 105701-1 (2003).
- [162] R. Mitzner, B. Winter, C. Kusch, E. E. B. Campbell, V. Hertel, COALESCENCE REACTIONS IN LASER-INDUCED FULLERENE DESORPTION: THE ROLE OF FRAGMENTS, *Z. Physik. D* 37 No.1 89 (1996)
- [163] T. Mitani, K. Matsuishi, S. Onari, PHOTO-INDUCED STRUCTURAL TRANSFORMATION OF C[60] SINGLE CRYSTALS UNDER HIGH PRESSURE, *Physica statu solidi (b)* 223 495 (2001).
- [164] J. Steinbeck, G. Braunstein, M. S. Dresselhaus, T. Venkatesan and D. C. Jacobson, A MODEL FOR PULSED LASER MELTING OF GRAPHITE, *J. Appl. Phys.* 58, 4374 (1985).
- [165] A. Cavalleri, Cs. Tóth, C. W. Siders, J. A. Squier, F. Ráksi, P. Forget, and J. C. Kieffer, FEMTOSECOND STRUCTURAL DYNAMICS IN VO₂ DURING AN ULTRAFAST SOLID-SOLID PHASE TRANSITION *Phys. Rev. Lett.* 87, 237401 (2001).

- [166] A. Rousse, C. Rischel, S. Fournaux, I. Uschmann, S. Sebban, G. Grillon, P. Balcou, E. Förster, J. P. Gelndre, P. Audebert, J. C. Gauthier and D. Hulin, NON-THERMAL MELTING IN SEMICONDUCTORS MEASURED AT FEMTOSECOND RESOLUTION *Nature* (London) 410, 65 (2001).
- [167] A. H. Romero, J. O. Jeschke, M. E. Garcia and A. Rubio, *Appl. Surf. Sci.* submitted (2004).
- [168] P. Corio, P. S. Santos, M. A. Pimenta and M. S. Dresselhaus, EVOLUTION OF THE MOLECULAR STRUCTURE OF METALLIC AND SEMICONDUCTING CARBON NANOTUBES UNDER LASER IRRADIATION , *Chem. Phys. Lett.*, 360, 557 (2002).
- [169] M. Terrones, SCIENCE AND TECHNOLOGY OF THE TWENTY-FIRST CENTURY: SYNTHESIS, PROPERTIES, AND APPLICATIONS OF CARBON NANOTUBES, *Ann. Rev. Mater. Sci.* 33, 413 (2003).
- [170] H. J. Choi, J. Ihm, S. G. Louie and M. L. Cohen, DEFECTS, QUASIBOUND STATES, AND QUANTUM CONDUCTANCE IN METALLIC CARBON NANOTUBES, *Phys. Rev. Lett* 84 2917 (2000).
- [171] J. Dorantes-Dávila, G. M. Pastor, ALTERNATIVE LOCAL APPROACH TO NONORTHOGONAL TIGHT-BINDING THEORY: ENVIRONMENT DEPENDENCE OF THE INTERACTION PARAMETERS IN AN ORTHOGONAL BASIS, *Phys. Rev. B.*, 51, 16627, (1995).

Appendix A

Essentials on many electrons physics.

*I'm a soldier of freedom in the army of man
We are the chosen, we're the partisan
The cause it is noble and the cause it is just
We are ready to pay with our lives if we must.
Ride across the river, Dire Straits.*

A.1 The many body problem of condensed matter.

I love the style of those great classical text books such as Pine's *Elementary excitations in solids* so let me begin with the usual equations. A system of N atomic species of charge Z_i with $i \in (1, N)$ is described by the Hamiltonian operator:

$$H = H_{ion} + H_{electron} + H_{electron-ion} \quad (\text{A.1.1})$$

where

$$H_{ion} = \sum_{i=1}^N \frac{1}{2M_i} P_i^2 + \frac{1}{2} \sum_{i \neq j}^N V(R_i - R_j) \quad (\text{A.1.2})$$

$$H_{electron} = \sum_i^{N_{el}} \frac{p_i^2}{2m_e} + \frac{1}{2} \sum_{i \neq j}^{N_{el}} \frac{e^2}{|r_i - r_j|} \quad (\text{A.1.3})$$

$$H_{electron-ion} = \sum_{i,j} v(r_i - R_j) \quad (\text{A.1.4})$$

R_i are the ionic coordinates and r_i the electronic ones. The number of electrons in the system is, in principle $N_{el} = \sum_i Z_i$. The ion-ion interaction (V), and the ion-electron interaction (v), are just equal to the Coulomb interaction if all the electrons in the systems are considered. The full system, at zero temperature, is described by a many body wave function with both ionic and electronic coordinates as degrees of freedom, and which satisfies the Schrödinger equation:

$$H\Psi(R_1, \dots, R_N, r_1, \dots, r_{N_{el}}) = E\Psi(R_1, \dots, R_N, r_1, \dots, r_{N_{el}}) \quad (\text{A.1.5})$$

We must not, in general, attempt to solve exactly equation A.1.5 as it describes an absolutely formidable problem, even though it does not consider the full problem of a material; we have neglected ionic internal degrees of freedom and relativistic effects and restricted ourselves to the zero temperature limit so that the system is described by a wave function and not by an statistical mixture.

Let us recall the usual approximation hierarchy that lead us to complex but solvable systems.

In quantum mechanics, the space of solutions of a multi particle system is constructed from the Hilbert spaces corresponding to each particle, via the tensorial product. This means that the Hilbert space to which the wavefunction Ψ belongs is a subspace of the product between the Hilbert space for the ions and the Hilbert space for electrons:

$$\mathcal{H}_{material} = \mathcal{H}_{electrons} \otimes \mathcal{H}_{ions} \quad (\text{A.1.6})$$

meaning that the wavefunction is a superposition of waves with separated electronic and ionic degrees of freedom:

$$\Psi(R_1, \dots, R_N, r_1, \dots, r_{N_{el}}) = \sum_{\lambda} C_{\lambda} \psi_{\lambda}(R_1, \dots, R_N) * \Phi_{\lambda}(r_1, \dots, r_{N_{el}}) \quad (\text{A.1.7})$$

Where λ runs over a suitable collection of indexes.

A.2 Un-coupling the fast electrons from the slow ions: The adiabatic approximation.

If the electron-ion interaction is switched off, the Hamiltonian would be separable in ionic and electronic coordinates. Suitable solutions of the Schrödinger equation could be found with a single term in the sum A.1.7. It would be tempting, then, to treat the $v(r - R)$ interaction within a perturbative scheme and derive the wavefunctions from the un-coupled terms. Nevertheless, the electron-ion potential is far from being a perturbative term, so that this approach would not make sense from the physical point of view. Another approximation scheme, named the adiabatic approximation, is still available and can lead us to a different kind of *separability* of the wavefunction. Let us now consider this method in more detail because it will lead to the well known Born-Oppenheimer approximation ¹, one of the most widely used approaches in solid state physics and quantum chemistry, and whose validity is assumed throughout this work.

First of all, nuclear masses are much larger than electronic masses (by a factor of at least 1/10000), meanwhile the electrostatic potentials felt by nuclei and electrons are mainly of the same order of magnitude. This means that, typically, electronic velocities are much larger than nuclear velocities by the same nuclear mass to electronic mass ratio. Then, from the point of view of electrons, nuclei move very slowly and they can follow closely any changes in the nuclear positions. We now propose a separation of the wavefunction into *slow and fast* changing parts:

$$\Psi = \Phi(r, R)\psi(R) \tag{A.2.8}$$

¹Indeed there are some differences between the Born-Oppenheimer and the adiabatic approximation, at least in their original form, but now it is becoming customary to use the same name for both of them, and as long as this is not a book on quantum mechanics, we will follow this convention

where we have omitted the sub-indices for the nuclear and electronic coordinates just for simplicity. The dynamically slow part (ψ) depends only upon the nuclear degrees of freedom, meanwhile Φ depends both upon the electronic degrees of freedom and *parametrically* on the nuclear coordinates. It is important to recall that Eq. A.2.8 is not a separation into *electronic and nuclear* coordinates, a separation that we have already dismissed. The difference between the time scales associated with electronic and nuclear motions, makes reasonable this slow/fast separation proposal. With this separation, the dynamical evolution is given by the two coupled equations:

$$i\hbar\frac{\partial\Phi}{dt} = (H_{electron} + H_{electron-ion})\Phi \quad (\text{A.2.9})$$

and

$$i\hbar\frac{\partial\psi}{\partial t} = H_{eff}\psi \quad (\text{A.2.10})$$

where

$$H_{eff} = H_{ion} + \langle\Phi|H_{electron} + H_{electron-ion}|\Phi\rangle \quad (\text{A.2.11})$$

In the first evolution equation, the ionic coordinates are treated as parameters, not as degrees of freedom. Equations A.2.9 to A.2.11 forms the already mentioned Born-Oppenheimer scheme. In simple words, these equations represent electrons moving in the presence of slow nuclei and, at the same time, provide an effective potential surface for the nuclei to move. In this sense, equation A.2.9 could be regarded as the *electronic part* of the system and the corresponding Hamiltonian could be referred as an *electronic Hamiltonian*, even though there was never a strict separation of the corresponding degrees of freedom (note that nuclear coordinates appear still in the electronic Hamiltonian, although only in a parametric way).

When the nuclei are slow and massive enough, the system of equations A.2.9 to A.2.11 can be further simplified, so that the nuclei can be treated in a classical way. Therefore equation A.2.10 can be replaced by:

$$\frac{d^2 R}{dt^2} = -\frac{\partial}{\partial R}(H_{eff}) \quad (\text{A.2.12})$$

Equations A.2.9 and A.2.12 constitute the framework of the well known Molecular Mechanics, and are widely used in solid state physics. In particular, our studied systems can be described within this regime.

Unfortunately² we have still to solve the many electrons problem of equation A.2.9, and this implies still more approximations, some of which we will discuss in the following paragraphs.

A.3 General description of the electronic sub-system

The electronic wavefunction belongs to the tensor product space of N_{el} single particle's Hilbert spaces

$$\mathcal{H}_{electrons} \subset \mathcal{H}(N_{el}) = \mathcal{H}_1 \otimes \mathcal{H}_2 \otimes \cdots \otimes \mathcal{H}_{N_{el}} \quad (\text{A.3.13})$$

Because electrons are identical particles, particularly fermionic particles, their associated wavefunctions must be antisymmetric under the interchange of any two particles:

$$\Phi_{el}(P(r_1, \dots, r_{N_{el}})) = (-1)^p \Phi_{el}(r_1, \dots, r_{N_{el}}) \quad (\text{A.3.14})$$

where P is any permutation and p is the parity of P . So that $\mathcal{H}_{electrons}$ is a subspace generated by the anti-symmetrized wavefunctions usually referred as Slater Determinants. Given a N_{el} -tuple of ordered indexes

$$c = (c_1, c_2, \dots, c_{N_{el}})$$

and a set of single particle's wavefunctions $\{\phi_\nu\}$ indexed by an ordered³ set $\{\nu\}$, we define the slater determinant corresponding to the N-tuple c of indexes as:

²Maybe fortunately. The richness of phenomena associated with, and theoretical approximations related to, the solution of the many electrons systems is worthy of headaches that such a complex problem brings to physicists!

³Order is only required to avoid sign ambiguity in the electronic wavefunctions

$$\begin{aligned}
\Phi_c^A &= \mathcal{A}(\phi_{c_1}(x_1)\phi_{c_2}(x_2)\dots\phi_{c_{N_{el}}}(x_{N_{el}})) = \\
&= \frac{1}{\sqrt{N_{el}!}} \sum_{P \in S_{N_{el}}} (-1)^P P[\phi_{c_1}(x_1)\phi_{c_2}(x_2)\dots\phi_{c_{N_{el}}}(x_{N_{el}})] \\
&\equiv \frac{1}{\sqrt{N_{el}!}} \det[\phi_{c_i}(x_{c_j})]
\end{aligned} \tag{A.3.15}$$

where where \mathcal{A} is the anti-symmetrization operator, $S_{N_{el}}$ is the set of permutations of the N_{el} indexes in c , and x_i stands for spin and position coordinates of each particle. One of the most important properties of the Slater determinants is that whenever more than one instance of a given orbital appears in the sum A.3.15 the output is identically null (the Fermi exclusion principle).

The anti-symmetrization operator \mathcal{A} is a projector in the space of identical particles and the Hilbert space for electrons is then the image under \mathcal{A} of $\mathcal{H}(N)$:

$$\mathcal{H}_{electrons} = \mathcal{A}[\mathcal{H}(N_{el})] \tag{A.3.16}$$

If the set $\{\phi_\nu\}$ is a basis for the Hilbert space of a single particle H_i , then the set of Slater determinants, $\{\Phi_c^A\}$ with every possible N_{el} - *tuples* $\{c\}$ of indexes in $\{\nu\}$, is a basis for $\mathcal{H}_{electrons}$. Even further, if $\{\{\phi_\nu\}\}$ is an orthonormal basis so it is the $\{\{\Phi_c^A\}$ basis.

Because in several situations (ionization, for instance) the number of electrons in the system changes, it is comfortable to work not in the Hilbert space of N_{el} electrons by in a general Hilbert space for any number of particles:

$$\mathcal{F} = \bigotimes_{n_{el}=1}^{\infty} \mathcal{H}_{electrons}(n_{el}) \tag{A.3.17}$$

This space is known as the Fock space. In \mathcal{F} we define a linear operator \hat{c}_k that we call *annihilation operator* through its action on the element of the basis (Slater determinants):

$$\begin{aligned}
\hat{c}_k \Phi_{(c_1, \dots, c_n)}^A &= 0, & \text{if } k \notin (c_1, \dots, c_n) \\
&= (-1)^{j-1} \Phi_{(c_1, \dots, c_{j-1}, c_{j+1}, \dots, c_n)}^A, & \text{if } k = c_j
\end{aligned} \tag{A.3.18}$$

The annihilation operator, therefore, crosses out the orbital ϕ_k from the Slater determinant, or destroy the wavefunction if ϕ_k was not in the Slater determinant. Its

adjoint operator \hat{c}_k^\dagger is called the *creation operator*. From the definition of adjoint, we have that given the n -tuple $c = (c_1, \dots, c_n)$ and the $(n+1)$ -tuple $b = (b_1, \dots, b_{n+1})$,

$$\begin{aligned} \langle \hat{c}_k^\dagger \Phi_c^A | \Phi_b^A \rangle &= \langle \Phi_c^A | c_k \Phi_b^A \rangle \\ &= (-1)^{j-1} \langle \Phi_c^A | \Phi_{(b_1, \dots, b_{j-1}, b_{j+1}, \dots, b_{n+1})}^A \rangle && \text{if } k = b_j \\ &= 0 && \text{otherwise} \end{aligned}$$

As stated above, if $\{\phi_\nu\}$ is an orthogonal basis the slater determinants are also orthogonal and the output vanishes unless the n -tuples c and $\bar{b} = (b_1, \dots, b_{j-1}, b_{j+1}, \dots, b_{n+1})$ are the same. If $k \in c$ the product will always vanish: if $k \notin b$ the annihilation operator vanishes the Φ_b^A , if $k \in b$ there is not possible that $c = \hat{b}$. When $k \notin c$, the result will depend on whether the two n -tuples are the same. If $c = \bar{b}$ it is also true that $b = \bar{c}$ where \bar{c} is the $(n+1)$ -tuple $c + \{k\}$. Therefore we can write:

$$\begin{aligned} \langle \hat{c}_k^\dagger \Phi_c^A | \Phi_b^A \rangle &= 0 && \text{if } k \in c \\ &= (-1)^{j-1} \langle \Phi_{\bar{c}}^A | \Phi_b^A \rangle && \text{otherwise} \end{aligned}$$

Where j is the position of k in the ordered $(n+1)$ -tuple $\bar{c} = c + \{k\}$. This means that :

$$\begin{aligned} \hat{c}_k^\dagger \Phi_c^A &= 0 && \text{if } k \in c \\ &= (-1)^{j-1} \Phi_{\bar{c}}^A && \text{otherwise} \end{aligned}$$

Therefore, the action of the creation operator is to introduce a new orbital ϕ_k in the slater determinant. As both creation and annihilation operators are linear by definition, their action on an arbitrary wavefunction is given as a superposition of their actions on slater determinants expanding the wavefunction.

The most important algebraic properties of creation-annihilation operators are their anticommutation relationships:

$$\begin{aligned} [\hat{c}_k, \hat{c}_{k'}]_+ &= [\hat{c}_k^\dagger, \hat{c}_{k'}^\dagger]_+ = 0 \\ [\hat{c}_k, \hat{c}_{k'}^\dagger]_+ &= \delta_{kk'} \end{aligned} \tag{A.3.19}$$

which can be easily proved from their action on slater determinants, and are the fermionic counterparts to the harmonic oscillator algebra. From those operators, we

can also define the *number operators*:

$$\hat{n}_k = \hat{c}_k^\dagger \hat{c}_k,$$

whose action on any Slater determinant is given by:

$$\begin{aligned} \hat{n}_k \Phi_c^A &= \Phi_c^A & \text{if } k \in c \\ &= 0 & \text{if } k \notin c, \end{aligned}$$

therefore, n_k measures the number of times that the orbital ϕ_k is in the Slater determinant, which, as stated before, can only be 0 or 1. The Slater wavefunctions can, therefore, be seen as eigenvectors of the number operators:

$$\Phi_c^A = |n_1, n_2, n_3, n_4, \dots, n_{N_{el}} \rangle$$

where $n_i = 0$ if $i \notin c$ and $n_i = 1$ for $i \in c$. We define the *vacuum state*

$$|0 \rangle = |0, 0, 0, \dots, 0 \rangle$$

as the state with zero occupied orbitals, i.e. with $n_i = 0 \forall i$. This state must not be confused with the null vector 0. Obviously, the action of any destruction operator on the vacuum level is the null vector.

$$\hat{c}_k |0 \rangle = 0$$

If an unitary basis change is performed in the single-particle's basis set so that:

$$\chi_k(x) = \sum_j D_{jk}^* \phi_j(x)$$

the creation operators related to the new basis set $\{\chi_k\}$ can be easily shown to be given by:

$$\hat{a}_k^\dagger = \sum_j D_{jk}^* \hat{c}_j^\dagger$$

and the corresponding hermitic adjoint expression for the annihilation operators. The anticommutation relationships are preserved through this unitary transformation.

A.4. Single particles in an effective field: the Hartree-Fock method. 174

Any observable can be written in terms of the creation annihilation operators, in particular for one- and two-particle's operators:

$$\begin{aligned}\hat{O} &= \sum_{i=1}^{N_{el}} \hat{o}(x_i) = \sum_{i,j=1}^{N_{el}} \langle \phi_i | \hat{o} | \phi_j \rangle \hat{c}_i^\dagger \hat{c}_j \\ \hat{V} &= \sum_{i,j=1, i \neq j}^{N_{el}} \hat{v}(x_i, x_j) = \sum_{i,j,k,l}^{N_{el}} (\langle \phi_i | \otimes \langle \phi_j |) \hat{v}(|\phi_k \rangle \otimes |\phi_l \rangle) \hat{c}_i^\dagger \hat{c}_j^\dagger \hat{c}_l \hat{c}_k,\end{aligned}\tag{A.3.20}$$

results that can be obtained by straightforward application of the formulas at the R.H.S of A.3.20 on the Slater determinant's basis. When all the operators are written in terms of the creation and annihilation operators, the problem is said to be written in *second quantized* form. This denomination stands from the fact that for the particular case when the basis functions for the single-particle's space are the eigenvectors of the position operator, the associated creation-annihilation operators $\hat{\chi}_i^\dagger(x)$ and $\hat{\chi}_i(x)$ (known as *field operators*) create and destroy particles localized at a given spatial point. Single particle's operators, for instance, can be written in terms of the field operators as:

$$\hat{O} = \int dx \hat{\chi}_i^\dagger(x) \hat{o}(x) \hat{\chi}_j^\dagger(x),\tag{A.3.21}$$

an expression that certainly looks like the usual expression in quantum mechanics but with the wavefunctions treated like operators. Second quantization is a very helpful tool in the many body problem, as it allows for fancy formulations of, for instance, perturbative expressions and treatment of addition-removal of electrons within the same framework.

A.4 Single particles in an effective field: the Hartree-Fock method.

A major breakthrough in the solution of the many electrons problem A.2.9 is the Hartree-Fock proposal. This assumes that the wavefunction can be described by a single Slater determinant, i.e. that the system of interacting fermions can be mapped into an effective system of non interacting ones, and then find the best

A.4. Single particles in an effective field: the Hartree-Fock method. 175

effective non-interacting system to describe the problem using the system of equations:

$$H_{HF} = \sum_{i=1}^{N_{el}} \left(\frac{1}{2m_e} p_i^2 + v_{HF}^i(r) \right) \quad (\text{A.4.22})$$

$$H_{HF}\Phi = E\Phi \quad (\text{A.4.23})$$

$$\Phi = \Phi_c^A = \frac{1}{\sqrt{N_{el}!}} \det[\varphi_{c_i}(r_{c_j})] \quad (\text{A.4.24})$$

Both the Hartree-Fock (v_{HF}) potential and single particle wavefunctions φ_i are unknown. By imposing the condition that the energy (i.e. expected value of the exact electronic Hamiltonian) in the non-interacting wavefunction must be minimal, the variational condition is expressed by:

$$\frac{\delta}{\delta\varphi_i} (\langle \Phi | H | \Phi \rangle + \sum_{i=1}^{N_{el}} \varepsilon_i \int \varphi_i^*(r) \varphi_i(r)) = 0 \quad (\text{A.4.25})$$

where the Lagrangian multipliers ε_i fix the normalization condition, one can, then, arrive to the Hartree-Fock equations :

$$\left[\frac{\hbar^2}{2m_e} \nabla^2 + V_{ext}(r) \varphi_i + \sum_{j=1}^{N_{el}} \int d^3r' n(r', r') \frac{e^2}{|r' - r|} \right] \varphi_i - \int dr' n(r, r') \frac{e^2}{|r' - r|} \varphi_i(r') = \varepsilon_i \varphi_i(r) \quad (\text{A.4.26})$$

the density matrix is given by:

$$n(r, r') = \sum_{i=1}^{N_{el}} \varphi_i^*(r) \varphi_i(r')$$

The external potential in equation A.4.26 comprises both the electron-ion potential and any other local external force. The last, non-local term in the LHS comes from the anti-symmetrization and is usually referred as the *exchange* potential. This term is related to the energy required to exchange the position of a given (i) particle with each one of the remaining particles in the system (j). In the Hartree-Fock approach, each particle feels the same potential, arising from the interactions among all the particles in the system, that is the reason for referring to HF as a *Mean Field* method.

A.4. Single particles in an effective field: the Hartree-Fock method. 176

Equation A.4.26 do also provide an explicit method to construct the Hartree Fock potential, but for accomplishing this step, we need the single particle solutions which, in turn, require knowledge of the potential. In order to solve this problem, we must resort to an iterative method; a set of trial single particles wavefunctions is chosen, from them it is possible to calculate the Hartree-Fock potential and recalculate the wavefunctions. The process continues until the new wavefunctions/potentials are the same as the old ones. For this reason, Hartree-Fock is called a *Self Consistent Method*.

The total energy of the system in a given Slater determinant is given by:

$$E = \langle \Phi_c^A | H | \Phi_c^A \rangle = \sum_i^{N_{el}} \varepsilon_{c_i}$$

The ground state of the electronic system is constructed by selecting from the, in general infinitely many, solutions of the single particle equation, the N_{el} with lowest energies

$$\Phi_{GS}(N_{el}) = \Phi_{c_0}^A$$

where c_0 is the N_{el} - *tuple* of indexes for the orbitals with lowest energies. The states in this ground state slater determinant are referred as *occupied orbitals*, and those with higher energies as *empty* or *virtual orbitals*.

Hartree-Fock is a very useful method, and a really beautiful work of physics (at least in our opinion). It provides, within simple and physically clean roots, the best description for a system of interacting N_{el} electrons using a non-interacting electronic wavefunction, validated by the total energy minimization principle.

When a Ionization process takes place and one electron is extracted from the system, and if we assume that the H-F orbitals does not change due to the remotion of one electron (an approximation that is reasonable when the number of electrons is large enough) the ground state wavefunction for the cation could be approximated by:

$$\Phi_{GS}(N_{el} - 1) = \Phi_{c-\{k\}}^A = (-1)^{k-1} \hat{c}_k \Phi_{GS}(N_{el}) \quad (\text{A.4.27})$$

A.4. Single particles in an effective field: the Hartree-Fock method. 177

where k is one of the orbitals in the ground state wavefunction of the original system. The Ionization Potentials (\mathbf{I}_k), i.e. the differences in energy between the cation and the neutral system would be given under this approximation by:

$$\mathbf{I}_k = -\varepsilon_k$$

So that the H-F eigenenergies can be regarded as the various Ionization potentials of the system. Under the same approximations (that the H-F orbitals do not change due to the presence of an extra electron) electron affinities \mathbf{A} , would be given by:

$$\mathbf{A}_k = \varepsilon_j,$$

where the ϕ_j orbital was not in the neutral system wavefunction. This results for Ionization Potentials and Electron Affinities are known as *Koopman's Theorem*. This also means, when the assumption that the orbitals for the N_{el} and $(N_{el} \pm 1)$ systems are the same, that the excitation energies of the system can be taken to be the energies needed to clear out an orbital ϕ_k from the ground state Slater determinant and introduce the orbital ϕ_j :

$$\varepsilon_{kj} = \varepsilon_k - \varepsilon_j$$

then, excitations of the system can be interpreted, within this approach, as promotion of electrons from occupied states ϕ_k to virtual states ϕ_j .

In general H-F yields accurate results for Ionization Potentials, but poor approximations for Electron Affinities. Better approximations to these potentials can be achieved by using ΔSCF calculations: i.e., by solving the H-F equations for the systems with N , $(N + 1)$ and $(N - 1)$ so that effects of orbital relaxation are taken into account. These ΔSCF calculations are useful for medium sized systems.

At this point it is interesting to summarize the typical measurable quantities in a many-electron system and their relationship with the full many-electron and H-F wavefunctions, this step would evidence the convenience of the independent particle's description, especially in the definition of a simple language:

Removal energies the energies needed to extract one electron from the system are measured by photoemission: the system absorbs a photon of energy $h\nu$ and

A.4. Single particles in an effective field: the Hartree-Fock method. 178

ejects an electron with kinetic energy K , this kinetic energy would be given by the differences between the system with N and $(N - 1)$ electrons:

$$K = \langle \Phi_{GS}(N) | H(N) | \Phi_{GS} \rangle + h\nu - \langle \Phi_I(N - 1) | H(N - 1) | \Phi_I(N - 1) \rangle$$

Where we have assumed the easiest case where the initial state is the ground state of the corresponding N electrons system. The distribution of kinetic energies is a measure of the distribution of energies for the various possible (ground or excited) states of the $(N - 1)$ electrons system Φ_I (note that only the number of electrons is changed, ion-electron potentials being fixed). In the Hartree-Fock approximation this energies would be given by the various energies of the occupied orbitals ε_k , and the distribution of energies is then referred as the *density of occupied states*.

Addition energies when an electron of given kinetic energy K is captured by the system. Several processes can lead to this capture. In what follows we suppose that we are dealing with inverse photoemission processes where the capture is accompanied by emission of photons of energy $h\nu$, the energies of the emitted photons will be given by

$$h\nu = K + \langle \Phi_{GS}(N) | H(N) | \Phi_{GS} \rangle + h\nu - \langle \Phi_{GS}(N + 1) | H(N + 1) | \Phi_{GS}(N + 1) \rangle$$

The distribution of photon energies measures the distribution of energies for the available $(N + 1)$ states. Again in H-F, this would be just related to the available empty orbitals, and this distribution of energies is named *density of empty states*.

Absorption energies Photons of energy $h\nu$ are absorbed by the system without ejection of electrons, therefore the final state of the system is one of the excited states of the N electrons system. The photon energy must satisfy, then,

$$h\nu = K + \langle \Phi_{GS}(N) | H(N) | \Phi_{GS} \rangle + h\nu - \langle \Phi_I(N) | H(N) | \Phi_I(N) \rangle$$

Where the Φ_I are the excited states of the system. The distribution of absorbed energy is a measure of the transition probabilities between the ground state and the

various excited states. These probabilities are given, within first order of perturbation theory by

$$P(GS \rightarrow I) \sim \langle \Phi_{GS} | \mathbf{P} \cdot \mathbf{A} | \Phi_I \rangle$$

where \mathbf{P} is the total momentum operator and \mathbf{A} is the potential vector for the electromagnetic field. In the case of independent particles, these probabilities can be mapped to the transition rates between single particle's states:

$$P(GS \rightarrow I) \sim \langle \phi_j | \mathbf{p} \cdot \mathbf{A} | \phi_i \rangle$$

where we assume that the excited states are given by:

$$\Phi_I = \hat{c}_i^\dagger \hat{c}_j \Phi_{GS}$$

so that the orbitals themselves, and not only their energies, have physical meaning in the H-F approximation.

Response functions to other excitations can be constructed in a similar way, and their profiles related to transition probabilities between orbitals in the H-F approximation.

Therefore, in the H-F approximation, electronic states can be discussed in terms of empty or occupied orbitals, which physical content can be directly mapped to the real many-electron system response. Terms such as *densities of states* and *promotion of electrons to excited levels*, have their full physical meaning within this context ⁴.

Actual interacting electrons, however, have *correlated* motion and do not occupy well defined orbitals; the wavefunction is always a superposition of several Slater determinants. These correlation effects, neglected in Hartree-Fock⁵, happen to be significant in most of the condensed matter systems, so that methods to describe

⁴It is important to remark that this terminology concerning orbitals and electronic promotions only has got full meaning within the context of non-interacting-particles pictures such as Hartree-Fock. However, it has become kind of common language in solid state physics, sometimes very unluckily.

⁵As a matter of fact, the practical definition of correlation energy is the difference between the Hartree-Fock and the real energy

them are required. One of those methods, suitable for not very strongly correlated systems, the Density Functional Theory, is used through this work, and will be explained in appendix B.

A.5 Beyond Hartree-Fock: Particle's correlation.

Going beyond the Hartree-Fock scheme in order to include electronic correlations is, in principle, straightforward. Hartree-Fock provides the best zero-th and first order perturbative approach to the correlated wavefunctions and energies. Higher order perturbative schemes, such as second order Möller-Plesset, allow for better description of correlation effects. However higher order in the perturbative expansion are progressively expensive and practical calculations rarely go beyond fourth order. Even further, there are many situations in which second or fourth order perturbative results are poorer than the first order approximation (Hartree-Fock).

Superposing several Slater determinants constructed from H-F orbitals and using them in a full variational calculation (the Configuration Interaction method, CI) provides, in our opinion, the best solution of the many-electrons problem. Increasing the basis size and the number of considered Slater determinants, progressively better approximations can be constructed. Both ground state and excited wavefunctions are available in CI. Provided unrestricted availability of computational power, CI gives a transparent physical framework allowing arbitrary accuracy thresholds.

The only question with Configuration Interaction is just the “*unrestricted computational power*”. As a matter of fact, CI is heavily time and resources consuming, and practical calculations are restricted to small molecular systems.

In the next section we will proceed to the definition of the very useful concept of *quasiparticles* which allow for inclusion of correlation effects yet preserving most of the conveniences of the independent particle's description.

A.6 Quasiparticles

In order to introduce the concept of quasiparticles, let us look at a free particle propagating in the vacuum in a one dimensional space. In this simple case the spin of the particle cannot change and we omit spin indexes. It is useful now to move to the Heisenberg picture where the operators, and not the wave function, vary. The probability amplitude to measure (destroy) a particle at a time t in the point x after it was created in x' at a time t' is given by:

$$g(xt, x't') = \langle 0 | \hat{\phi}(x, t) \hat{\phi}^\dagger(x', t') | 0 \rangle, \quad t > t' \quad (\text{A.6.28})$$

where $|0\rangle$ is the vacuum state (no particles), and the field operators $\hat{\phi}(x, t)$ and $\hat{\phi}^\dagger(x', t')$ destroy at (x, t) the particle created at (x', t') . In order to generalize the expression for any times (t, t') , it is necessary to introduce the time ordered product of operators:

$$\begin{aligned} T(\hat{O}_1(t), \hat{O}_2(t')) &= \hat{O}_1(t) \hat{O}_2(t') && \text{if } t > t' \\ &= -\hat{O}_2(t') \hat{O}_1(t) && \text{if } t' > t \end{aligned} \quad (\text{A.6.29})$$

and then we rewrite

$$g(xt, x't') = \langle 0 | T[\hat{\phi}(x, t) \hat{\phi}^\dagger(x', t')] | 0 \rangle \quad (\text{A.6.30})$$

From this quantity we define the *Green's function* or *propagator* for the system as:

$$G(xt, x't') = -i \langle 0 | T[\hat{\phi}(x, t) \hat{\phi}^\dagger(x', t')] | 0 \rangle \quad (\text{A.6.31})$$

where the imaginary number i is introduced for convenience, especially because now we can state that the green function is the matrix element in the position eigenvectors of the evolution operator, and that the time development of any wavefunction from an initial state $\Phi(x, t)$ is given by:

$$\Phi(x, t) = \int G(xt, x't') \Phi(x', t') dx'$$

Using the basis transformation leading from position representation to momentum representation:

$$\hat{\phi}^\dagger(x, t) = \int \frac{1}{\sqrt{2\pi}} e^{-ikx} \hat{c}^\dagger(k, t) dk,$$

where now $\hat{c}^\dagger(k, t)$ creates a particle with a given momentum $p = \hbar k$, we can write for the Green's function (for the sake of economy we restrict again to the case $t > t'$)

$$G(xt, x't') = -i \frac{1}{\Pi} \int_k \int_{k'} e^{i(kx - k'x')} \times \langle 0 | \hat{c}(k, t) \hat{c}^\dagger(k', t') | 0 \rangle dk dk' \quad (\text{A.6.32})$$

Because we are considering a free particle, the evolution of the operators is given by the kinetic energy operator $K = \frac{p^2}{2m}$. From the evolution of the momentum eigenvectors in the wavefunction representation, it is easily seen that:

$$\hat{c}^\dagger(k, t) = e^{-i \frac{\hbar k^2}{2m} t} \hat{c}^\dagger(k, 0)$$

and the corresponding adjoint expression for the annihilation operators. So that we have for the Green's function:

$$G(xt, x't') = -i \frac{1}{2\Pi} \int \int e^{-i(\frac{\hbar k^2}{2m} t + kx - \frac{\hbar k'^2}{2m} t' - k'x')} \times \langle 0 | \hat{c}(k, 0) \hat{c}^\dagger(k', 0) | 0 \rangle dk dk' \quad (\text{A.6.33})$$

Because of the anticommutation relationships, $\hat{c}(k, 0) \hat{c}^\dagger(k', 0) = \delta(k - k') - \hat{c}^\dagger(k, 0) \hat{c}(k', 0)$, but the action of the destruction operator $\hat{c}^\dagger(k, 0)$ on the vacuum state is the null vector, so we have:

$$G(xt, x't') = -i \frac{1}{2\Pi} \int e^{-i(\frac{\hbar k^2}{2m}(t-t') + k(x-x'))} dk$$

which can be easily integrated computed by completion of squares to give:

$$G(xt, x't') = -i \frac{\sqrt{im_e}}{\sqrt{\hbar 2\Pi(t-t')}} e^{\frac{im_e(x-x')^2}{2\hbar(t-t')}} \quad (\text{A.6.34})$$

The green function for the free particle depends only on the time and position differences, a result that can be generalized to any system where the Hamiltonian

does not depend explicitly on time and commutes with the total momentum operator (for instance translational invariant systems). Fourier transforming again we can write in the momentum basis:

$$G(k, (t - t')) = \mathbf{e}^{\frac{\hbar k^2}{2m_e}(t-t')} = \mathbf{e}^{\frac{\varepsilon(k)(t-t')}{\hbar}}, \quad (\text{A.6.35})$$

where $\varepsilon(k)$ is the energy for a particle with well defined momentum k . For this trivial case, the Green's function could have been obtained easily by direct bracketing of the evolution operator $\hat{U} = \mathbf{exp}(-i\hat{p}^2/(2m_e\hbar))$ with the momentum eigenvectors. Fourier transforming in time, we can write:

$$G(k, w) = \frac{1}{2\Pi} \delta(w - w_k), \quad (\text{A.6.36})$$

and we can see that the green function is related to the available energies. These results can be extended for a system of interacting fermions. We define the *single-particle Green's Function*, by analogy with our definition for the free particle, to be:

$$G_{ss'}(xt, x't') = -i \langle \Phi_{GS} | T[\hat{\phi}_s(x, t) \hat{\phi}_{s'}^\dagger(x', t')] | \Phi_{GS} \rangle \quad (\text{A.6.37})$$

where s and s' stands for the spin. This Green's function is said to describe the propagation of a *field quantum*, or in terms of particles, the propagation of a test particle appearing in the system at the space-time point (x', t') and measured at (x, t) . It can be shown that knowing the single-particle Green's function it is possible to calculate the ground state expectation value of any single-particle operator:

$$\langle \hat{O} \rangle = -i \int d^3r \lim_{r \rightarrow r'} Tr(O(r))G(rt, r't')$$

where the trace is over the spin variables. The ground state energy is also available through:

$$E_0 = \langle \hat{H} \rangle = -\frac{i}{2} \int d^3r \lim_{t' \rightarrow t} \lim_{r' \rightarrow r} \left(i \frac{\partial}{\partial t} - \frac{\nabla_r^2}{2m} \right) Tr[G_{ss'}(rt, r't')]$$

Even further, the single-particle Green's function has its poles at the exact excitation energies of a system with $(N - 1)$ and $(N + 1)$ electrons: i.e., the exact addition and removal energies.

For a system of N non-interacting fermions (i.e. a Fermi gas), the single-particle's green function can be easily calculated following the same steps that for the free particle's propagator. In fact, the non-interacting Green Function resembles very closely it's free particle's counterpart:

$$G_{s,s'}^0(\vec{k}, (t-t')) = -i\delta_{ss'} e^{-i\varepsilon(k)(t-t')} (\theta(t-t')\theta(k-k_f) - \theta(t'-t)\theta(k_f-k)) \quad (\text{A.6.38})$$

where \vec{k} is the wave-number, k being the norm of the former, θ is the step function and k_f is the Fermi level (norm of the last occupied orbital), and $\varepsilon(k)$ is the energy associated to a particle with fixed momentum (which, of course, depends on the ionic and other external potentials).

Then, both for a free particle and for non-interacting particles, the time evolution of the single-particle Green's function is given by a term of the form $e^{-i\varepsilon(k)(t-t')/\hbar}$. The functional dependence of the energies ε with k is referred as the *dispersion relationship* in analogy with classical electrodynamics.

Note that in cases where k is not a good quantum number (when the total momentum of the electronic subsystem is not conserved), a similar analysis can still be performed using instead of k other suitable quantum numbers, for instance, the l and m angular momentum numbers for a central potential or the crystal momentum for periodic systems.

The results on Green's function for the free particle and for non-interacting particles suggest the proposition of the time evolution $e^{-i\varepsilon(k)(t-t')/\hbar}$ as the fingerprint for the propagation of free particles a many fermions system. By analogy if we have that the single-particle Green's function evolves in time according to:

$$G(\vec{k}, t) \sim e^{(-i\varepsilon(k)t - \Gamma(k)t)} \quad (\text{A.6.39})$$

we say that a particle-like object with a life time $1/\Gamma(k)$ is propagating in the system. Such objects (or such excitations) are referred as *quasiparticles*. A perturbative analysis of the Green's function reveals that it can be written, for translationally invariant and not explicitly time dependent systems, as:

$$G(\vec{k}, w) = \frac{1}{w - \varepsilon^0(k) - M(k, w)} \quad (\text{A.6.40})$$

where $\varepsilon^0(k)$ are the energies for non-interacting particles and $M(k, w)$ is the *Irreducible Self Energy* and is related to the electronic interaction. Its value within a given framework is related to the perturbative approximations used. If

$$M(k, w) = \mathbf{Real}(M(k, w)) + \mathbf{Im}(M(k, w))$$

it can be seen that for a sharp enough Green's function, the time evolution of the Green's function will follow approximately the prescription A.6.39, with a modified dispersion relationship given by:

$$w - \mathbf{Real}(M(k, w)) - \varepsilon^0(k) = 0$$

and lifetimes given by $1/\Gamma = \mathbf{Im}(M(k, w))$. For an object to be considered a feasible quasiparticle, the lifetimes must be much longer than the associated excitation energy, a restriction imposed by the energy uncertainty relationship. Quasiparticles can be, in general, found whenever converged perturbative analysis are feasible, for low enough excitation energies. It is usually said that quasiparticles are *dressed* particles because effects of the mutual interactions are reflected in their propagation.

Quasi-particle's amplitudes are defined through the field operators:

$$f(x) = \langle N - 1 | \hat{\phi} | N \rangle$$

which are the counterparts of the normal orbitals for non-interacting systems.

Hartree-Fock electrons are, indeed, quasiparticles with an infinite lifetime. In that case, the quasiparticle's amplitudes are just the H-F orbitals. As mentioned above, they do correspond to the zeroth and second order level of perturbation theory starting from non-interacting particles in the external atomic potential. Spectral properties of solids such as densities of states, band structures, addition and removal energies, are also mapped to quasiparticles's spectra (in this case dressed electrons and holes).

We close this overview of many-electron physics with a final note: most of the solid state physics is constructed in quasiparticles's descriptions. Electrons, holes,

cooper pairs, excitons, are all examples of many-body excitations that are usually dealt with by reducing the full many-body problem to a system of non-interacting electrons. Further inclusion of many body effects is usually achieved by perturbative approaches.

Further Reading

Many-body physics: E. K. U. Gross, E. Runge and O. Heinonen, MANY-PARTICLE THEORY, Adam Hilger Eds., Bristol, England, (1991).

J.W. Negele and H. Orland, QUANTUM MANY-PARTICLE SYSTEMS, Addison-Wesley, New York (1988).

D. Pines, ELEMENTARY EXCITATIONS IN SOLIDS : LECTURES ON PHONONS, ELECTRONS, AND PLASMONS Westview Press, (1966),

Fundamental quantum mechanics:

B. Holstein, TOPICS IN ADVANCED QUANTUM MECHANICS, Addison-Wesley Publishing Co., Redwood City, (1992).

Green's functions:

E. N. Economou, GREEN'S FUNCTIONS IN QUANTUM PHYSICS 2nd. edn, Springer, Berlin (1983).

Appendix B

Density Functional Theory.

*When I'm drivin' in my car
And that man comes on the radio
He's tellin' me more and more
About some useless information
Supposed to fire my imagination
I can't get no, oh no no no
Hey hey hey, that's what I say
Satisfaction, The Rolling Stones.*

B.1 The Basic concepts and principles.

Density Functional Theory (DFT) is based on the electronic density rather than the full wavefunction. This is equivalent to the total neglect of wavefunction's phases which, as we will see below, provides a satisfactory description of the ground state properties in various materials; but behaves rather poorly when electronic fluctuations are relevant (meaning that effects like Van der Waals forces can not be studied using DFT).

Let us consider the ground state energy:

$$E_g = \langle \Phi_g | H | \Phi_g \rangle \tag{B.1.1}$$

where H is from now on the electronic Hamiltonian in the sense of section A.2, which is of the form already assumed when discussing the Hartree-Fock approach:

$$H = T + U + V_{ext}$$

where T is the kinetic energy operator, U is the coulombic electronic interaction and V_{ext} is the potential exerted by the nuclei and any other external local potential. Therefore, we can write the external potential as a sum of one body operators :

$$V_{ext} = \sum_i v(r_i) \quad (\text{B.1.2})$$

The ground state electron density, defined as usual in Many body, theory is:

$$n(r) = \langle \Phi | \hat{n}(r) | \Phi \rangle \quad (\text{B.1.3})$$

with the density operator being :

$$\hat{n}(r) = \sum_{i=1}^{N_{el}} \delta(r - r_i) \quad (\text{B.1.4})$$

where $\delta(r - r_i)$ are Dirac delta functions.

It is clear that if the ground state is non-degenerate¹, the external potential $v(r)$ uniquely determines the ground state wavefunction Φ and, then, the ground state density $n(r)$. Within the same assumption of non degeneracy, it is possible to show the reciprocal; there is only one external potential giving a certain density $n(r)$ for the ground state of N_{el} interacting electrons. This is the first Hohenberg and Kohn theorem. For proving this theorem, we need to recall the convexity of the total energy as function of the external potential, meaning that if we have two different potentials v_o and v_1 and connect them by a parametric family:

¹I acknowledge a tough discussion with Professor R. Lopez Sandoval, concerning this assumption of non-degenerate ground states. As a matter of fact, and as he already pointed out, a system of interacting fermions is more likely to behave like a highly degenerate system. Nevertheless, in many interesting systems the external potential provided by the nuclei and any other external forces cooperate to lift up degeneracies in the ground state, when the number of particles increases, in the same way it does for small molecular systems.

$$v_\lambda = v_o(r) + \lambda(v_i(r) - v_o(r)) = v_o(r) + \lambda\Delta v = (1 - \lambda)v_o(r) + \lambda v_1(r) \quad (\text{B.1.5})$$

so that $\lambda = 0$ correspond v_o and $\lambda = 1$ to v_1 , the ground state energy is a strictly convex function of λ :

$$E_g(\lambda) > (1 - \lambda)E_g(0) + \lambda E_g(1) \quad (\text{B.1.6})$$

Convexity can be easily proved by standard perturbation theory for the ground state. As a matter of fact, up to second order in perturbation theory, the energy can be written, expanding about any given λ value:

$$E_g(\lambda + d\lambda) = E_g(\lambda) + d\lambda \langle \Phi_o(\lambda) | \Delta v | \Phi_o(\lambda) \rangle + d\lambda^2 \sum_{n \neq 0} \frac{|\langle \Phi_o(\lambda) | \Delta v | \Phi_n(\lambda) \rangle|^2}{E_g(\lambda) - E_n(\lambda)} + \mathcal{O}(3) \quad (\text{B.1.7})$$

where the parametric dependence of energies and wavefunctions on λ has been explicitly stressed. The second derivative of the energy as function of λ is just twice the sum in the third term of Eq. B.1.7 , and as we have $E_n(\lambda) > E_g(\lambda)$ for each n , this second derivative is strictly negative, unless $\langle \Phi_o(\lambda) | \Delta v | \Phi_n(\lambda) \rangle = 0$, which is true only if Δv is a trivial constant term. This is a sufficient and necessary condition for $E_g(\lambda)$ to be strictly convex. Convexity also implies that the first derivative is a strictly decreasing function so that:

$$\frac{\partial}{\partial \lambda} E_g(\lambda) |_{\lambda=1} < \frac{\partial}{\partial \lambda} E_g(\lambda) |_{\lambda=0}$$

From the perturbative expression B.1.7, it is clear that at $\lambda = 0$ the derivative is $\langle \Phi_o(0) | \Delta v | \Phi_o(0) \rangle$, and at $\lambda = 1$ it is $\langle \Phi_o(1) | \Delta v | \Phi_o(1) \rangle$, so that convexity implies:

$$\langle \Phi_o(1) | \Delta v | \Phi_o(1) \rangle < \langle \Phi_o(0) | \Delta v | \Phi_o(0) \rangle$$

Because of the form of Δv (a sum over one particle's operators), these expectation values can be easily written as functions of the corresponding densities, in the form:

$$\int dr \Delta v(r) n_1(r) < \int dr \Delta v(r) n_0(r) \quad (\text{B.1.8})$$

where n_1 is the density corresponding to the potential v_1 and n_0 that corresponding to v_0 . This inequality obviously cannot be fulfilled if $n_1 = n_0$ and that proves our point: different potentials give rise to different densities, so that the density uniquely determines the external potential up to an arbitrary constant term. So, we can state the first Hohenberg and Kohn theorem²:

- **There is a one to one relationship between the ground state density and the external potential, and then, between the density and the wavefunction of the system -up to an undetermined phase-. Therefore the expected value of any operator in the ground state, is a functional of the density.**

Now that we have established this theorem, it is quite easy to show that the ground state energy must be variationally minimal with respect to the density. As a matter of fact, let us consider two wavefunctions Φ and Φ' which are, correspondingly, ground state wavefunctions for two different external potentials v and v' . The usual Rayleigh-Ritz variational principle tell us that the ground state energy E_g corresponding to the external potential v is minimal so that:

$$E_g \leq \langle \Phi' | T + U + V_{ext} | \Phi' \rangle \quad (\text{B.1.9})$$

but, as stated above, the expected value of the external potential evaluated at Φ' can be expressed as an integral over the space of the one body potential $v(r)$ times density associated with Φ' , that is n' . The expected value $\langle T + U \rangle$ is also a functional of the density that we shall call, from now on *the universal functional* $F[n(r)]$, with this in mind we could write:

²The previous discussion has been restricted to an even number of electrons without spin polarization. Extensions of the result, can be made to include spin polarization but since this is not really a book on Density Functional Theory, I will kindly refer the reader to the corresponding literature.

$$E_g[n(r)] \leq \int dr v(r)n'(r) + F[n'] \quad (\text{B.1.10})$$

And the equality holds only if $n = n'$. The squared brackets are the standard notation for functional dependence. Equation B.1.10 is just the variational principle of Density Functional Theory, and is the second Hohenberg and Kohn Theorem:

- **The ground state energy associated with a given external potential $v(\mathbf{r})$, $E_g(n)$, is variationally minimal at the right density $n(r)$, with $v(r)$ and the number of electrons held fixed.**

Note that the demonstration relies upon the fact that both Φ and Φ' are ground state solutions for some given potentials. This condition usually referred as *v-representability of the wavefunctions and densities*, restricts the variational space in which equation B.1.10 must be used. Though not trivial at all, *v-representability* is not such a strong condition and most of the reasonable trial densities lie within this space.

B.2 Solving the equations, the Kohn-Sham method.

When solving the variational problem of equation B.1.10 it is customary to separate the universal functional $F[n]$ in two parts. The first part ($T_o[n]$), is defined to be the kinetic energy operator of a system of non-interacting electrons displaying the same density as the actual problem in its ground state; the remaining contributions to $F[n]$ are grouped in the second part, i.e:

$$F[n] = T_o[n] + (F[n] - T_o[n]) = T_o[n] + \{(T + U)[n] - T_o[n]\}$$

With this notation, the variational principle B.1.10 reads:

$$0 = \int dr \left\{ v(r) + \frac{\delta T_o}{\delta n(r)} + \frac{\delta}{\delta n(r)} ((T + U)[n] - T_o) - \mu \right\} \delta n(r) \quad (\text{B.2.11})$$

where the usual convention for variational derivatives has been used, $\delta n(r)$ are arbitrary variations in the density and the Lagrange multiplier μ has been introduced

to fix the number of electrons. As the density variations are arbitrary, the variational equation requires the bracketed term to be null:

$$\frac{\delta T_o}{\delta n(r)} + v(r) + \frac{\delta}{\delta n(r)}((T + U)[n] - T_o) = \mu \quad (\text{B.2.12})$$

This last expression is just the corresponding Euler equation for our variational principle. Obviously, the only difference between this Euler equation and its noninteracting (both U and $T - T_o$ equal to zero) counterpart is the functional derivative in the last term at the LHS. So, if one could obtain an expression for that functional derivative, the equation will be the same as that for non-interacting particles in the presence of an effective potential:

$$V_{eff} = v(r) + \frac{\delta}{\delta n(r)} ((T + U)[n] - T_o)$$

We also assume that the actual density $n(r)$ can be written as a sum over non-interacting particle's densities:

$$n(r) = \sum_i \psi_i^* \psi_i \quad (\text{B.2.13})$$

The existence of this effective potential and the possibility of writing the density as in Eq. B.2.13, are not guaranteed by any physical principle, so we have again to assume both facts, this latter condition is referred as *non interacting v-representability of the density* and is fulfilled for many physically meaningful densities (see the discussion on the suggested readings). We could follow the procedure discussed in many standard quantum mechanics text books when deriving the Schrödinger equation from variational principles, and arrive to the following Schrödinger-like equations for the ψ_i functions:

$$-\frac{\hbar^2}{2m_e} \nabla^2 \psi_i + V_{eff} \psi_i = \varepsilon_i \psi_i \quad (\text{B.2.14})$$

The system of equations B.2.14 are known as the Kohn-Sham (K-S) equations, and constitute a practical recipe to obtain the ground state properties of a multi-electronic system. The K-S method is only useful provided one has the functional form of the effective potential for the problem at hand, but in most of the real

systems this is not the case. Let us rewrite the effective potential by taking apart the well-known Hartree and external potentials:

$$V_{eff} = v_{ext}(r) + e^2 \int dr \frac{n(r)}{|r - r'|} + \frac{\delta}{\delta n} E_{xc}[n] \quad (\text{B.2.15})$$

where the meaning of the exchange correlation energy E_{xc} must be obvious if one writes it explicitly as:

$$E_{xc}[n] = \langle T + U \rangle - \langle T_o \rangle - e^2 \int dr \frac{n(r)}{|r - r'|} \quad (\text{B.2.16})$$

Then the exchange correlation energy is the part of the energy left when subtracting both the independent particle's kinetic energy, the coulombic Hartree potential and the external interactions. Therefore it is related to the correlated motion of the particles and to exchange terms in the sense defined in Hartree-Fock theory. The variational derivative appearing in equation B.2.15 has been named exchange-correlation potential:

$$V_{xc} = \frac{\delta}{\delta n} E_{xc}[n] \quad (\text{B.2.17})$$

and most of the Density Functional theory (and *black magic*) is related to the construction of physically meaningful approximations to this exchange correlation terms. Indeed, each approximation constitute a flavor of DFT. In sections B.5 and B.6, we will review some of those approximations, restricting ourselves, of course, to those who are referred in our calculations.

For the rest of this appendix we will be engaged with a new hierarchy of approximations, although they are based on important physical considerations, most of them share a certain *technical* character as they are concerned on how to write the potentials or express the orbitals. For this reason, it would be useful to review the major physical approximations we have already made, and the related limitations of the DFT framework. Let us remember what we are dealing with:

The non relativistic limit: It is not really essential, and relativistic corrections can be included within the theory.

The adiabatic approximation: Extensions to include non-adiabatic processes have been reported in DFT, but we will not be concerned with non-adiabatic processes in this thesis.

Molecular mechanics limit: This is not a hard constrain, ions can be also treated in a quantum mechanical way, but again, we will only be concerned with systems where a classical treatment of the ions is justified.

Ground state non degeneracy: As mentioned above, this is not a trivial assumption, and, to the best of our knowledge, there is no straightforward way to test it for each system, unless full quantum calculations (in the spirit of CI or quantum Montecarlo) are performed. In our case, we just assume this supposition to be valid.

No spin polarization: Again this is not an essential limitation, DFT can be extended to polarized cases just by introducing two densities : one for spin up and other for spin down electrons. Most of the discussion above is still valid with this separation.

V-representability: This is not really a trouble, we just restrict our variational space to physically meaning densities: if a density is *v-representable*, it could be the solution of a physical problem, and vice versa. Extensions of the theory have been made to include a larger class of densities, those that are *N-representable* meaning they can be calculated as the densities corresponding to any N particles many body wavefunction.

Non interacting v-representability: That is a key point. The whole K-S scheme would not be valid if this assumption is broken. To the best of our knowledge, again there is nor a simple way to check the validity of this assumption, neither a systematic definition of problems which cannot be treated due to a violation of it. The reader is strongly recommended to consult the suggested readings in the issue of density representability.

B.3 Applications of DFT

What could, then, be performed using DFT? Well, within the discussed limits, DFT is in principle able to deal with the ground state density of a system of interacting fermions, with a judicious choice of the exchange correlation kernel, this technique is at least comparable with other correlated methods such CI, Möller-Plösset perturbation theory and even quantum Montecarlo, demanding much less computational resources.

As long as many interesting properties of solids and molecules such as optimal geometries, vibrational frequencies, atomic forces, and chemical reactivities are mainly determined by the ground state behavior, this ground state description accurately accomplish a large amount of problems.

DFT can not account for properties which are related to fluctuations in the charge densities such as Van der Wals forces, nor with physically meaningful phases (Berry phases) or currents in periodic systems.

Neither it can, at least directly, account for an orbital (quasiparticle) description of the atomic states in the sense of H-F theory, because the Kohn Sham orbitals are constructed just to resemble the density of the real system. However, it is customary to state the quasiparticle and orbital discussion in terms of the Kohn Sham orbitals, and we already use this kind of approach in this work. It has also been seen that Kohn-Sham orbitals are good starting points for perturbative analysis of the Green's function. The question on the interpretation of the K-S orbitals is further discussed in the next section.

B.4 Interpretation of the Kohn-Sham orbitals

As stated above, Kohn-Sham's orbitals have no relationship with any approximation of the many body wavefunction. Therefore, they can not be used in an single-particle description of the many body problem, and their energies do not correspond to addition, removal or excitation energies. Even further, as Kohn-Sham's orbitals are introduced as auxiliary objects, their shapes depend upon the actual DFT used.

It is possible, however, to show that for finite systems in which DFT is applicable

(non-degenerate ground state) the energy of the last occupied K-S orbital (HOMO level) gives the exact first Ionization Potential, and the asymptotical behavior of the HOMO orbital for large distances is the same as that of a corresponding quasiparticle. The demonstration follows from the fact that the asymptotic behavior of the charge density in finite systems is driven by the first ionization potential, meanwhile it is driven by the HOMO energy in DFT theory. As exact DFT should give the exact density, the energy of the Kohn-Sham HOMO level should be equal to the first Ionization Potential. The actual demonstration is not given here because it lies far from the scope of our work.

Similarly, for a solid surface, the energy of the last occupied Kohn-Sham orbital with respect to the Kohn-Sham energy far from the surface gives the right chemical potential. In actual calculations, the level of approximation between HOMO levels and ionizations potentials, depends upon the quality of the approximation to the exchange-correlation used.

The interpretation of the remaining energies as addition or removal energies is, in general, not justified. The similarities between the Hartree-Fock and the Kohn-Sham equations explains the fact that, in many situations, the trends in DFT calculated electronic band gaps follows the same trends observed experimentally. The same is true for orbital symmetries, which in many situations happen to be similar to the quasiparticle's amplitudes. All into account, the accumulated experience is the only precedent you can use to justify the use of Kohn-Sham's orbitals and orbital's energies as approximations to the quasiparticle's amplitudes and excitation energies.

B.5 The Local Density Approximation.

The functional form of the exchange-correlation energy appearing in the Kohn-Sham's equations is in general unknown. The simpler approximation to this functional, is to assume that the energy contribution at a given point has the same value as the exact exchange correlation energy for an uniform electron system with the same density:

$$E_{xc} = \int d^3x \epsilon_{xc}(\rho(\vec{x})) \quad (\text{B.5.18})$$

Where the simplification comes from the fact that the exchange-correlation energy for the homogeneous electron gas with a given density $\epsilon_{xc}(\rho)$ is a relatively well known object. The exchange part of the exchange correlation energy is:

$$\epsilon_{exchange}(\rho) = \frac{3}{4\pi} (3\Phi^2 \rho)^{1/3}$$

that can be calculated within the Hartree-Fock theory. Correlation energies can be calculated using, for instance, quantum Monte-Carlo methods and then parametrized as a functional of the density. Common parametrization schemes for the correlations are the Perdew and Zunger (PZ) parametrization and the Perdew and Wang (PW) parametrization.

This approximation is known as *Local Density Approximation* (LDA) and has proved to yield excellent results for systems where the charge density is rather uniform. LDA can be regarded as an extension to the Thomas Fermi model.

LDA is known to, in general, overestimate the binding between atoms and then, underestimate interatomic distances. When used for electronic structure calculations, gaps are seen to be also significantly underestimated.

B.6 Generalized Gradient Approximations.

In the Generalized-Gradient Approximation (GGA) the exchange correlation energy is assumed to depend both on the local density and its gradient:

$$E_{xc} = \int d^3x \epsilon_{xc-GGA}(\rho(\vec{x}), |\nabla\rho(\vec{x})|) \quad (\text{B.6.19})$$

Several flavors of GGA approximations exist. Some of the most commonly used are the Perdew and Wang functional (PW91), the Perdew, Burke and Ernzerhof functional (PBE) and the Becke formula for exchange with the Lee, Yang and Parr formula for the correlation energy (BLYP). The reader is referred to the suggested readings for further information on each formula.

In cases where spatial variations of the densities play a sensible role, GGA's are expected to yield better results than LDA. In general GGA's underestimate the bond strengths and, therefore, overestimate the lattice parameters.

B.7 Basis sets for the one-electron wavefunction.

In order to solve the Kohn-Sham equations it is necessary to expand the Kohn-Sham orbitals in a given basis set, transforming the problem in a matrix diagonalization problem. The commonly used basis sets can be classified as : localized, delocalized and mixed.

Localized basis sets are wavefunctions centered on atoms (or, in the case of periodic structures, Bloch functions constructed from localized functions). The most popular localized functions are: atomic-like orbitals, gaussian-type orbitals and Muffin-Tin orbitals (functions which die out above a certain cutoff distance). Typically, localized orbitals perform very well in finite systems. There are, however, several issues with them , specially the fact that there is no systematic way to improve convergence in terms of the basis size. They are also usually harder to implement because basis elements are in general not orthonormal.

Delocalized basis sets, particularly Plane Waves (PW) basis sets, are particularly well suited for periodic systems. The wavefunctions for each \vec{k} vector in the band structure are expanded in functions of the form:

$$\phi_{\vec{k}+\vec{G}}(\vec{r}) = e^{i(\vec{k}+\vec{G})\cdot\vec{r}}, \quad \text{with} \quad \frac{\hbar^2}{2m}|\vec{k} + \vec{G}| \leq E_{cut}$$

with \vec{G} being a vector in the reciprocal space. E_{cut} is referred as the *cutoff energy*. The basis elements are orthogonal to each other. In general more basis elements are needed in a Plane Waves calculation than in localized basis sets. The cutoff energy provides a systematic way to increase the basis size improving convergence.

Mixed basis sets combine features of localized and delocalized basis sets. The most commonly employed are the Linearized Augmented Plane Waves (LAPW) and the Projector Augmented Plane Waves (PAW).

B.8 Pseudopotentials.

It can be seen, from elementary Fourier analysis, the the number of plane waves needed in a PW calculation can be very large if core states (those states closer to the ions and that do not change during the chemical binding) are to be treated. The length scale in which an object varies, determines the number of Fourier components needed to correctly describe it. For example, the length scale for a $1s$ state in carbon is about 0.1 a.u, so that the c.a 250.000 PWs would be needed for a simple calculation of diamond's electronic structure.

In order to make practical PW calculations, it is needed to get rid of the core states. Even more, due to the orthogonality of electronic states, the valence states also exhibit rapid oscillations in the core region, which have also to be excluded for efficient PWs calculations. Here is where *pseudopotentials* appear. A pseudopotential is a smooth effective potential that reproduces the effect of the nucleus plus the core states on the valence states, starting from a given cutoff radius.

A good pseudopotential must be: (i) *transferable* i.e. it should yield the same results as a full electron calculation for various chemical environments, transferability can be improved by decreasing to cutoff radius. And (ii) *soft* in the sense that as few as possible plane waves are needed to describe the variations of the pseudo-atomic wavefunctions. Those two properties are usually conflicting.

Typical flavors of pseudopotentials are *norm conserving* and *ultra-soft* pseudopotentials.

Norm conserving pseudopotentials are constructed from a given atomic reference state, requiring that the total charge in the core region for the pseudo wavefunctions is the same that for the full electron counterparts. The pseudo and all-electron wavefunctions and their logarithmic derivatives must agree beyond the cutoff radius. The pseudopotentials are constructed as semi-local operators with dependency on the angular momentum:

$$\langle \vec{r} | \hat{V}_{ps} | \vec{r}' \rangle = V^{local}(\vec{r}) \delta(\vec{r} - \vec{r}') + \sum_{l=0}^{l_{max}} \sum_{m=-l}^l \mathbf{Y}_{lm}^*(\Omega_{\vec{r}}) \delta V_l^{ps}(r) \frac{\delta(\vec{r} - \vec{r}')}{r^2} \mathbf{Y}_{lm}(\Omega_{\vec{r}'})$$

where $\Omega_{\vec{r}}$ is the solid angle subtended by the position vector and \mathbf{Y}_{lm} are the spher-

ical harmonics. The steps involved in the pseudopotential construction are:

- (1) Calculate the electronic structure for the atom using a full-electron calculation.
- (2) Construct the pseudo-wavefunctions and pseudo-potentials according to the conditions on the functions, their logarithmic derivatives and norms.
- (3) Un-screen the pseudo-potential: i.e. remove the contributions from the valence electrons from the pseudo-potential.
- (4) Test the softness and transferability properties.

Various recipes for generating smooth norm-conserving pseudo-potentials can be constructed. The Martins-Troulliers method being one of the most widely used.

Ultrasoft pseudopotentials do not impose norm-conservation, and allows for smaller kinetic energy cutoffs. The construction procedure is, not counting the normalization, similar to the construction of norm-conserving pseudo-potentials. The Vanderbilt recipe for ultrasoft pseudopotential has been widely used.

Further Reading

DFT Theory: E. K. U. Gross, LECTURE NOTES : DFT - I AND II - TDDFT - I AND II, lectures held during the *Spring College on electronic structure approaches to the physics of Material*, (19 May 9 June 2000), The Abdus Salam International Center for Theoretical Physics. Available through the agenda service:

http://cdsagenda5.ictp.trieste.it/full_display.php?ida=a02080#s1t1

.

Representability:

M. Levy, ELECTRONIC DENSITIES IN SEARCH OF HAMILTONIAN, *Phys. Rev. A* 26 1200 (1982).

W. Kohn, v-REPRESENTABILITY AND DENSITY FUNCTIONAL THEORY, *Phys. Rev. B.*, 51 1596, (1983)

W. Yang, P. W. Ayers, and Q. Wu, POTENTIAL FUNCTIONALS: DUAL TO DENSITY FUNCTIONALS AND SOLUTION TO THE v-REPRESENTABILITY PROBLEM, *Phys. Rev. Lett.* 92 146404 (2004).

Koopman's theorem and interpretation of Kohn-Sham's orbital energies:
22nd June 2005

A Nagy, and H Adachi, TOTAL ENERGY VERSUS ONE-ELECTRON ENERGY DIFFERENCES IN THE EXCITED-STATE DENSITY FUNCTIONAL THEORY , *J. Phys. B: At. Mol. Opt. Phys.* 33 L585 (2000).

C-O. Almbladh and U. von. Barth, EXACT RESULTS FOR THE CHARGE AND SPIN DENSITIES, EXCHANGE CORRELATION POTENTIALS AND DENSITY FUNCTIONAL EIGENVALUES, *Phys. Rev. B.* 31, 3231 (1985).

Exchange correlation functionals:

LDA-PZ: J. P. Perdew, A. Zunger, SELF-INTERACTION CORRECTION TO DENSITY-FUNCTIONAL APPROXIMATIONS FOR MANY-ELECTRON SYSTEMS, *Phys. Rev. B* 23 5048 (1981).

LDA-PW: J. P. Perdew; W. Y. Wang, ACCURATE AND SIMPLE ANALYTIC REPRESENTATION OF THE ELECTRON-GAS CORRELATION ENERGY, *Phys. Rev. B*, 45, 13244 (1992).

GGA-PW91: K. Burke, J. P. Perdew, and Y. Wang, DERIVATION OF A GENERALIZED GRADIENT APPROXIMATION: THE PW91 DENSITY FUNCTIONAL, in *Electronic Density Functional Theory: Recent Progress and New Directions* edited by J. F. Dobson, G. Vignale and M. P. Das, pages 81-121, (1997).

GGA-PBE: J. P. Perdew, K. Burke, and M. Ernzerhof, GENERALIZED GRADIENT APPROXIMATION MADE SIMPLE, *Phys. Rev. Lett.* 77 3865 (1996).

GGA-BLYP: A. D. Becke. DENSITY-FUNCTIONAL EXCHANGE-ENERGY APPROXIMATION WITH CORRECT ASYMPTOTIC BEHAVIOR *Phys. Rev. A*, 38, 3098 (1988).

C. Lee; W. Yang; R. G. Parr. DEVELOPMENT OF THE COLLE-SALVETTI CORRELATION-ENERGY FORMULA INTO A FUNCTIONAL OF THE ELECTRON DENSITY *Phys. Rev. B* 37 785 (1988).

Pseudopotentials

N. Troullier, J. L. Martins, EFFICIENT PSEUDOPOTENTIALS FOR PLANE WAVES CALCULATIONS, *Phys. Rev. B* 43 1993 (1991).

D. Vanderbilt, SOFT SELF-CONSISTENT PSEUDOPOTENTIALS IN A GENERALIZED EIGENVALUE FORMALISM, *Phys. Rev. B* 41(Rapid Communication) 7892 (1990) .

Appendix C

Tight-binding modeling.

*Cops with cars, the topless bars
never saw a woman, so alone
so alone!*

L.A. Woman, The Doors.

Despite the availability of increasingly faster computers and relatively cheaper frameworks for *ab initio* calculations, atomistic studies for many interesting systems (particularly nano-sized systems) would be prohibitively expensive if they were to be carried out by fully first principles approaches. Whenever chemical bonds are involved it is important to preserve the quantum description of the forces acting in each atom, in other words: classical simulations are not particularly appealing in these situations. Although the number of atoms that can be treated within first principles methods depend strongly on the research budget, there will always be systems calling for simpler approximations.

The semiempirical tight-binding method bridges the gap between state of the art *ab initio* calculations and purely classical approximations. It is constructed in a quasiparticle's spirit and retains most of the quantum character of chemical forces. Tight-binding calculations can even compete with, for instance, DFT methods under certain circumstances, but their dependence on semiempirical parameters represents a major drawback. In this section we will discuss the basics of the tight-binding approach to the electronic structure of matter.

C.1 Essentials.

We start as usual recalling the the Schrödinger equation for a system of electrons embedded in an external potential:

$$E|\Phi \rangle = H\Phi \rangle = \sum_i h_i |\Phi \rangle = \left\{ \sum_i \frac{\vec{p}_i^2}{2m} + \sum_i v_i \sum_i u_i \right\} |\Phi \rangle \quad (\text{C.1.1})$$

where v_i is an external potential and u_i is the electron-electron interaction. It is obvious from the former expression that the many body problem has been implicitly assumed to be mapped into an effective non-interacting particles system. The tight-binding method attempts to find an approximation to the energy of this system under the following two assumptions:

(i) The wavefunction Φ is given by an Slater determinant, just as in H-F:

$$\Phi = \frac{1}{\sqrt{N!}} \det(\chi_i(x_j))$$

already implicit in equation C.1.1.

(2) The single-particle's wavefunctions used in the construction of the Slater determinant are linear superpositions of atomic-like orbitals (hence the alternative denomination of LCAO: Linear Combination of Atomic Orbitals):

$$\chi_i(x) = \sum_{I,\alpha} C_{I\alpha}(i) \phi_{I\alpha}(x) \quad (\text{C.1.2})$$

where the index I stands for the atomic sites and α for the various symmetries of the atomic orbitals considered. The $\phi_{I\alpha}$ orbitals are atomic-like in the sense that they have the same symmetries associated to some specific atomic orbitals.

The problem at hand is, then, to solve the set of single-particle's equations:

$$h_i |\chi_i \rangle = \varepsilon_i |\chi_i \rangle,$$

recalling the form of the eigenvectors C.1.2, we can write:

$$h_i \sum_{I,\alpha} C_{I\alpha}(i) |\phi_{I\alpha} \rangle = \varepsilon_i \sum_{I,\alpha} C_{I\alpha}(i) |\phi_{I\alpha} \rangle,$$

bracketing with a given atomic-like orbital $|\phi_{I'\alpha'} \rangle$ give us:

$$\sum_{I,\alpha} \langle \phi_{I'\alpha'} | h_i | \phi_{I\alpha} \rangle C_{I\alpha} = \varepsilon_i \sum_{I,\alpha} C_{I\alpha} \langle \phi_{I'\alpha'} | \phi_{I\alpha} \rangle,$$

or just:

$$\sum_{I,\alpha} H_{I'\alpha'}^{I\alpha} C_{I\alpha}(i) = \varepsilon_i \sum_{I,\alpha} S_{I'\alpha'}^{I\alpha} C_{I\alpha} \quad (\text{C.1.3})$$

where $S_{I'\alpha'}^{I\alpha}$ is the overlap matrix $\langle \phi_{I'\alpha'} | \phi_{I\alpha} \rangle$. Equation C.1.3 represents a generalized eigenvectors problem:

$$[h]\vec{C}(i) = \varepsilon_i [S]\vec{C}(i),$$

with $\vec{C}(i)$ being the vectors representing the possible single-particle's states. The diagonal elements of the Hamiltonian matrix are usually referred as *onsite energies* and the off-diagonal elements as *hopping parameters*.

From a given set of atomic-like orbitals it is possible to construct a set of orthogonal functions with the same symmetries of the original set by using the Löwdin transformation:

$$\psi_{I,\alpha} = \sum_{I',\alpha'} (S_{I',\alpha'}^{I,\alpha})^{(1/2)} \phi_{I',\alpha'}$$

using these Löwdin functions as basis, the problem would be that of a standard diagonalization. Most of the traditional tight-binding schemes assume the use of Löwdin function, these are referred as *orthogonal tight-binding methods* because basis functions are taken as orthogonal. Parametrizations where the overlap is explicitly taken into account are referred as *non orthogonal tight-binding methods*.

The major simplification in tight binding, and what makes it so computationally efficient, is to consider the matrix elements $H_{I'\alpha'}^{I\alpha}$ and $S_{I'\alpha'}^{I\alpha}$ as parameters which depend only on the interatomic distance $|R_I - R_{I'}|$, and the orbital's symmetries (therefore, on the corresponding angular momentums and relative orientations). The ionic and electronic potentials depend, obviously, on the position of all the atoms, and the supposition that matrix elements depend only on the distances between two sites, is referred as the *two center approximation* because only two center integrals are considered.

Note that all the relevant information is contained in the parametrized matrices, therefore the basis functions themselves are not needed. Once the matrix equation has been solved, the electronic energy is the sum of the energies for the occupied levels:

$$E_{elec} = \sum_{i=occ} \varepsilon_i$$

Despite all the approximations involved, tight-binding based calculations can be remarkably successful provided that a good enough parametrization is used. In general, however, there is not an absolute measure of the quality of a parametrization, usually each set of parameters is suited for a given atomic environment (the original author's goal) .

In order to perform tight-binding based molecular dynamics simulations, the dependence of the matrix elements with distance must be known. It is also necessary to have access to the total energy and not only to the electronic contribution. It was shown that in a broad variety of situations, the total energy can be expressed as a sum of the electronic energy and a repulsive pair potential function:

$$E_{Tot} = E_{elec} + \sum_{I,I'} V_{rep}(R_I, R_{I'})$$

The latter approach has been widely employed. The inclusion of this repulsive term allows also to include by hand some correlation effects as the differences between the tight-binding and some correlated calculation *Total energy* methods in which the energy is given directly by the electronic energy have also been developed.

C.2 Transferability of the tight-binding parameters.

As mentioned above, typical tight-binding parametrizations are intended to work in a very well defined atomic environment. The parameters in the seminal paper of Slater and Koster, for instance, are intended to study the band structure of binary semiconductors with fixed geometries. When molecular dynamics is in mind, it is

important to know to what extent the set of parameters is able to describe accurately the various configurations appearing during the dynamical evolution. The capability of a given parametrization to yield accurate results for atomic environments other than the ones used during the construction of the tight-binding tables, is referred as transferability.

Two different goals are usually attempted by a tight-binding calculation: a good description of the total energies and a good description of the electronic properties. Many times, these two goals conspire one against the other and compromises between them must be established.

Several strategies have been used to assure transferability of tight-binding parametrizations at least within reasonable configurations.

The first and most important step is to choose a chemically appealing set of atomic-like orbitals: a tight-binding table including one *s-like* and two *p-like* orbitals for carbon may work as long as sp^2 hybridized species are considered but it would necessary fail as soon as tetrahedral configurations appear. Increasing the size of the atomic-like basis set increase the required computational resources but, for certain systems, improves the transferability of the parametrization, specially in terms of electronic properties.

A physically sensible selection of the distance dependence of the parameters is also crucial. Functional forms or numerical tables can be used to follow the evolution of the onsite and hopping parameters with varying distances. It is also possible to choose between fixed or environment dependent onsite parameters.

Non-orthogonal methods usually exhibit improved transferability contrasted with orthogonal ones. Orthogonal parametrizations with environment dependent parameters could also significantly improve the transferability [171].

However, and as a final note, tight-binding schemes will always fail at some point, and it is, to a large extent, responsibility of the researcher to check for the limits of a particular method.

Further Reading

The uppermost relevant historical reference: P. C. Slater and G. F. Koster, SIMPLIFIED LCAO METHOD FOR THE PERIODIC POTENTIAL PROBLEM, *Phys. Rev.* 94 1498, (1954).

Compressive reviews :

W. A. Harrison, ELECTRONIC STRUCTURE AND THE PROPERTIES OF SOLIDS, C.A:Freeman, San Fransico, (1985).

C. M. Goringe and D. R. Bowler and E. Hernandez, TIGHT-BINDING MODELING OF MATERIALS, *Reports on Progress in Physics*, 60, 1447-1512 (1997).

The introduction of repulsive pair-potentials:

A. P. Sutton, M. W. Finnis, D. G. Pettifor and Y. Otha, THE TIGHT-BINDING BOND MODEL, *J. Phys. C.: Solid State Phys.* 21, 35-66 (1988).

Appendix D

Periodic systems.

Truth is the most valuable thing we have – so let us economize it.

Mark Twain

From the many approximations made in solid state physics, only a few can compete in popularity, physical appeal or historical relevance with the one transforming a system of $\sim 10^{22}$ atoms into one with a few (typically less than a hundred and in some cases only one) atoms. From the philosophical point of view, it is reasonable to assume that in infinitely large pieces of matter, the ground state of the system is such that each atom sees the same local environment. The observation of regularity in various properties, specially *X – ray* spectrums, for a large family of solid materials, together with the previously stated heuristic argument, lead to the statement of a fundamental premise: the atomic structure of solid systems is that of simple motifs periodically repeated in the three-dimensional space space. This arrangement is referred as a *crystal lattice* and the underlying property as *crystallinity*. The ideal solids, within this context, are then periodic arrays in the space or, plainly, *periodic systems*

Similarity of local environment for atomic species can also be achieved by using a different idealization: solids are made from similar, space filling, motifs, just like in the oriental mosaics, a concept that nowadays has gained lots of attention, particularly with the identification of what are referred as quasi-crystalline structures obeying this premise but not that of standard crystallinity. Although this last statement is much more general, the amount of interesting crystalline solids, and

the accumulated *know-how* on crystal structures, keep the lattice crystal model in the front-line of materials description. In this chapter we give a brief overview of the characteristics associated to crystalline solids and some simplifications in the description of their properties arising from the periodical character.

D.1 A review on basic concepts.

The periodicity paradigm implies that the atoms, or the atomic motifs forming a solid, occupy all the sites of a three-dimensional array of points formed by translating the arbitrary origin an entire number of times in each direction. Then, the atomic motifs are located at points:

$$\vec{R}_n = \vec{0} + n_1\vec{a}_1 + n_2\vec{a}_2 + n_3\vec{a}_3, \quad n_1, n_2, n_3 \in \mathcal{Z} \quad (\text{D.1.1})$$

The set of points in D.1.1 constitute a *lattice*. The vectors $\vec{a}_1, \vec{a}_2, \vec{a}_3$ spanning this lattice are called *basis vectors* and each vector R_n in the set is referred as a *lattice vector*. There are 7 different groups of basis systems, depending on the relative orientations and lengths of the lattice vectors. Including the possibility of different centerings of the atomic motifs 14 different types of lattices can be constructed, these are known as the *Bravais lattices*. The atomic motifs themselves can have certain symmetry properties, known as *point symmetries*. When point symmetries and translational symmetries are considered, there are 230 possible symmetry groups, known as the *point groups*. Each crystalline solid, therefore, belongs to one of the possible point groups, a fact that provide a powerful classification scheme.

The polyhedron formed by the basis vectors, and the atomic motifs within this polyhedron are referred as *the unit cell*.

Because atoms are periodically arranged, atomic densities and any other local properties of the system must have the same periodicity that the underlying lattice.

Associated with the lattice D.1.1 there is a *reciprocal lattice*

$$\vec{G}_n = \vec{0} + n_1\vec{g}_1 + n_2\vec{g}_2 + n_3\vec{g}_3, \quad \text{with} \quad g_i \cdot a_j = \delta_{ij}, \quad (\text{D.1.2})$$

the spatial Fourier transform of any object with the periodicity of the lattice contains only terms with $\vec{k} = \vec{G}_n$. Reciprocally, any function defined as a Fourier sum containing only reciprocal vectors has necessarily the periodicity of the lattice.

An important example showing the significance of the reciprocal lattice arises in the diffraction theory: the intensity of scattered X-rays can be approximated (in the first Born approximation that we are not going to discuss here) by:

$$I(\vec{k}_0 - \vec{k}_f) = \left| \int (\vec{r}) e^{i(\vec{k}_i - \vec{k}_f) \cdot \vec{r}} \right|^2$$

where \vec{k}_0 and \vec{k}_f are the wave-vectors of the incident and scattered light pulses, respectively, and (\vec{r}) is the scattering density. (\vec{r}) must have the symmetry of the lattice, therefore, as stated above, its Fourier transform contains only contributions from vectors in the reciprocal space. Then, we must have

$$\vec{k}_i - \vec{k}_f = \vec{G}_n$$

which is known as the *Laue condition* for X-ray diffraction. The smallest polyhedron centered in the origin of the reciprocal space and enclosed by \vec{k} vectors satisfying the Laue condition is called the *first Brillouin zone*. This region is, then, the zone of space which is closer to the origin than to any other reciprocal vector. Any vector in the space is then the sum of a vector in the first Brillouin zone plus a reciprocal lattice vector.

D.2 Single particle equations in the periodic system: the Bloch's Theorem.

If we assumed that the many-electron problem has been reduced to a single-particle description, the electronic orbitals should obey a Schrödinger equation of the form:

$$H\Phi_i = \left\{ \frac{\vec{p}^2}{2m} + V(\vec{r}) \right\} \Psi_i(\vec{r}) = E_i \Psi_i(\vec{r}).$$

Because the atoms are periodically arranged, the potential V must have the periodicity of the lattice and then:

$$V(\vec{r}) = \sum_{\vec{G}_n} V(\vec{G}_n) e^{i\vec{G}_n \cdot \vec{r}}$$

expanding the wavefunctions in plane waves:

$$\Psi_i(\vec{r}) = \int C_i(\vec{k}) e^{i\vec{k} \cdot \vec{r}} d\vec{k}$$

we find that the Schrödinger equation is transformed to:

$$\int e^{i\vec{k} \cdot \vec{r}} \left\{ \left(\frac{\hbar^2 k^2}{2m} - E \right) C_i(\vec{k}) + \sum_{\vec{G}_n} V(\vec{G}_n) C_i(\vec{k} - \vec{G}_n) \right\} = 0,$$

a condition that can not be fulfilled unless it is true for each Fourier component.

Then, we must have

$$\left(\frac{\hbar^2 k^2}{2m} - E \right) C_i(\vec{k}) + \sum_{\vec{G}_n} V(\vec{G}_n) C_i(\vec{k} - \vec{G}_n) = 0 \quad (\text{D.2.3})$$

In the former system of equations, each \vec{k} is coupled only to its translations by reciprocal vectors, the solutions for the eigen-energies can, therefore, be labeled by the vector \vec{k} , $E_i = E(\vec{k})$, consequently the eigen-vectors can be labeled as $\Psi_i = \Psi_{\vec{k}}$. The diagonalization problem has, then, a block form where each block contains a given \vec{k} vector and its periodic images, and the eigen-vectors are given by the solutions of equation D.2.3 for each \vec{k} . The plane waves expansion of each eigenvector is then of the form

$$\Psi_{\vec{k}}(\vec{r}) = \sum_{\vec{G}_n} e^{i(\vec{k} + \vec{G}_n) \cdot \vec{r}} C(\vec{k} + \vec{G}_n) \quad (\text{D.2.4})$$

Note, however, that the labeling of energies and eigenvectors by the \vec{k} vectors does not mean that the wavefunctions are eigen-functions of the momentum operator: each wavefunction is a superposition of several (in principle an infinite number) of plane waves differing by reciprocal lattice vectors as in equation D.2.4.

Equation D.2.4 can be written as:

$$\Psi_{\vec{k}}(\vec{r}) = e^{i\vec{k} \cdot \vec{r}} \sum_{\vec{G}_n} e^{i\vec{G}_n \cdot \vec{r}} C(\vec{k} + \vec{G}_n) \quad (\text{D.2.5})$$

the summation in D.2.5 runs over each reciprocal vector. It has, therefore, the translational symmetry of the spatial lattice and we can finally write:

$$\Psi_{\vec{k}}(\vec{r}) = e^{i\vec{k}\cdot\vec{r}}u(\vec{r}) \quad \text{with} \quad u(\vec{r} + \vec{R}_n) = u(\vec{r}), \quad (\text{D.2.6})$$

a result that is known as *the Bloch's theorem*: the single-particle's orbitals in a periodic lattice have the form of plane waves times a function with the periodicity of the lattice. The wavefunctions of D.2.6 are called *Bloch's waves*.

D.3 The band-structure of solids and the density of states.

The Bloch's waves represented in equation D.2.6 provide a convenient way to characterize the electronic structure. To each \vec{k} value there can be several associated energies and wavefunctions. The collection of 4-dimensional surfaces representing the energies as function of the wave-vectors is called *the band structure*, and it is an extension of the concept of energy levels in a finite system. Bloch's electrons are also quasiparticles, because they carry on both the information of the lattice periodicity and the electronic interactions that are implicit in the effective Schrödinger equation. Their energies can, therefore, be considered as approximations to the several addition, removal or absorption energies.

It is important to review some properties of the Bloch's waves in order to understand the full significance of the band structure:

Bloch's waves are periodical in the reciprocal space, in fact we have that:

$$\begin{aligned} \Psi(\vec{k} + \vec{G}_m)(\vec{r}) &= e^{i(\vec{k} + \vec{G}_m)\cdot\vec{r}} \sum_{G_n} e^{i\vec{G}_n\cdot\vec{r}} C(\vec{k} + \vec{G}_m + \vec{G}_n) \\ &= e^{i\vec{k}\cdot\vec{r}} \sum_{G_n} e^{i(\vec{G}_n + \vec{G}_m)\cdot\vec{r}} C(\vec{k} + \vec{G}_m + \vec{G}_n) \\ &= e^{i\vec{k}\cdot\vec{r}} \sum_{G_l} e^{i\vec{G}_l\cdot\vec{r}} C(\vec{k} + \vec{G}_l), \quad \text{with} \quad \vec{G}_l = \vec{G}_m + \vec{G}_n \\ &= \Psi(\vec{k}), \end{aligned} \quad (\text{D.3.7})$$

consequently, the energies are also periodical in the reciprocal space:

$$E(\vec{k} + \vec{G}) = E(\vec{k}),$$

meaning that we only need to know the dispersion relationship in the first Brillouin's zone. The transition probability between two Bloch's waves mediated by an interaction potential varying as $e^{i(\vec{q}\cdot\vec{r} + \omega(q)t)}$ (electromagnetic fields, interaction with fast electrons, and several other phenomena) are given, in first order perturbation theory by:

$$S_{\vec{k},\vec{k}'} \sim \int e^{i(\vec{k}-\vec{k}'+\vec{q})\cdot\vec{r}} u_{\vec{k}}(\vec{r}) u_{\vec{k}'}^*(\vec{r}),$$

because the $u_{\vec{k}}(\vec{r}) u_{\vec{k}'}^*(\vec{r})$ term has the periodicity of the lattice, we can write:

$$u_{\vec{k}}(\vec{r}) u_{\vec{k}'}^*(\vec{r}) = \sum_{G_n} f_{\vec{k},\vec{k}'} e^{i\vec{G}_n\cdot\vec{r}}$$

and then the transition probabilities are given by:

$$S_{\vec{k},\vec{k}'} \sim f_{\vec{k},\vec{k}'} \sum_{G_n} \delta(\vec{k} - \vec{k}' + \vec{q}) \tag{D.3.8}$$

conservation of energy requires, by other hand:

$$E_{\vec{k}} - E_{\vec{k}'} = \hbar\omega(q) \tag{D.3.9}$$

For photons, the wave-vector \vec{q} is usually negligible compared to the reciprocal lattice vectors and, then, photon mediated processes are recalled as elastic collisions. The relationships D.3.8 and D.3.9 are also valid for the transitions between a Bloch's wave and a free plane wave (electron emission). The band structure can be measured, then, in photoemission experiments by measuring the momentum vector of the ejected electron (Angle-Resolved Photoemission).

The amount of available states within a given energy range is called the *Density of electronic states*, and it is the quantity measured by the total photoemission power. In terms of the band structure it can be written:

$$\mathbf{D}(E) = \int d\vec{k} \sum_i \delta(E_i(\vec{k}) - E) \tag{D.3.10}$$

where the $E_i(\vec{k})$ are the various energies that can, in general, correspond to the same Bloch's wave vector. In terms of the band structure the former can also be written as a surface integral on the k -space

$$\mathbf{D}(E)dE = \frac{1}{(2\pi)^3} \left(\int_{e_k=const} \frac{dS_E}{|\nabla E(k)|} \right) dE. \quad (\text{D.3.11})$$

D.4 Lattice dynamics: phonons.

In the spirit of the Born-Oppenheimer approximation and within the molecular mechanics limit, the potential felt by a given ion in the crystal, located at a given position $\vec{r}_{n\alpha i} = \vec{R}_n + \vec{r}_{\alpha i}$ where \vec{R}_n is a lattice vector and $\vec{r}_{\alpha i}$ is the position in the unit cell, is given by the total energy of the crystal. If we perform a Taylor expansion near the equilibrium position we have:

$$E(\vec{r}_{n\alpha i} + \vec{s}_{n\alpha i}) = E(\vec{r}_{n\alpha i}) + \frac{1}{2} \sum_{n\alpha i, m\beta j} \frac{\partial^2 E}{\partial r_{n\alpha i} \partial r_{m\beta j}} s_{n\alpha i} s_{m\beta j} + \dots \quad (\text{D.4.12})$$

where the $s_{n\alpha i}$ are the displacements with respect to the equilibrium position. If we keep only the first two terms in the Taylor expansion (i.e. we make an harmonic approximation) the equations of motion for the ions will look like:

$$M_\alpha s_{n\alpha i}'' + \sum_{m\beta j} \Phi_{n\alpha i}^{m\beta j} s_{m\beta j} = 0 \quad (\text{D.4.13})$$

where M_α is the mass of the corresponding ion and the $\Phi_{n\alpha i}^{m\beta j}$ elements are the harmonic coefficients:

$$\Phi_{n\alpha i}^{m\beta j} = \frac{\partial^2 E}{\partial r_{n\alpha i} \partial r_{m\beta j}}$$

In principle, we have to deal with a formidably large system of coupled oscillations, as the number of atoms is large (remember : about 10^{22} in a typical solid sample). It is possible, however to decouple the equations using the ansatz:

$$s_{n\alpha i} = \frac{1}{\sqrt{M_\alpha}} u_{\alpha i}(\vec{q}) e^{i(\vec{q} \cdot \vec{R}_n - \omega t)}$$

which is similar to a plane wave but it is only defined on the lattice points R_n . This ansatz lead to :

$$-w^2 u_{\alpha i}(\vec{q}) + \sum_{\beta j} \sum_m \frac{1}{\sqrt{M_\alpha M_\beta}} \Phi_{n\alpha i}^{m\beta j} e^{i\vec{q}(\vec{R}_m - \vec{R}_n)} u_{\beta j}(q) = 0 \quad (\text{D.4.14})$$

Because of the lattice periodicity, the summation over lattice vectors R_m does not depend upon the origin R_n , we now define the *dynamical matrix* elements to be:

$$D_{\alpha i}^{\beta j}(\vec{q}) = \sum_m \frac{1}{\sqrt{M_\alpha M_\beta}} \Phi_{n\alpha i}^{m\beta j} e^{i\vec{q}(\vec{R}_m - \vec{R}_n)},$$

and rewrite the system of equations as:

$$-w^2 u_{\alpha i}(\vec{q}) + \sum_{\beta j} D_{\alpha i}^{\beta j}(\vec{q}) u_{\beta j}(q) = 0 \quad (\text{D.4.15})$$

which is just a diagonalization problem with matrices of $3n_I \times 3n_I$, with n_I being the number of ions in the unit cell.

Equation D.4.15 gives the normal modes of vibration for the solid system. They represent a system of harmonic oscillators, if those oscillators are quantized, the related field quantum is called *phonon*.

The relationship between the corresponding frequencies $w(\vec{q})$ (or energies) and the wave vectors \vec{q} is also referred as *dispersion relationship*. $3n_I$ different solutions are possible for each \vec{q} , and these various solutions are referred as *branches* of the dispersion relationship. Inelastic scattering of light (Raman Spectroscopy), electrons or neutrons (the most traditional) can be used to measure the dispersion relationships.

We close this section by remarking that although anharmonic motions play a significant role in important processes, for instance structural transitions, most of the thermal properties of solids can be understood by studying the phonon relationships.

Further reading

General solid state physics:

H. Ibach and H. Lüth, SOLID STATE PHYSICS, AN INTRODUCTION TO THEORY AND EXPERIMENT, Springer-Verlag, Berlin (1991).

N. W. Ashcroft and N. D. Mermin, **SOLID STATE PHYSICS**, Brooks Cole; 1 edition (1976).

Appendix E

Optical response.

.. The name of the song is called 'Haddock's Eyes'!

"Oh, that's the name of the song, is it?" Alice said, trying to feel interested.

"No, you don't understand," the Knight said, looking a little vexed.

"That's what the name is called.

Through the Looking Glass, Lewis Carrol.

E.1 Microscopic description of the interaction with external fields. Linear Regime

Let us consider a system subject to a time dependent external potential V_{ext} activated at a given time $t \geq t_o$, assuming that at t_o the system was in the ground state, the electronic density functional $n(V_{ext})$ can be formally written in a Taylor expansion:

$$n(r, t) - n_o(r) = n_1(r, t) + n_2(r, t) + \dots \quad (\text{E.1.1})$$

where the indexes 1,2,3... stands for the order in the external potential V_{ext} . The response at first order is given by:

$$n_1 = \int dt' \int d^3r' \chi(r, t, r', t') V_{ext}(r', t') \quad (\text{E.1.2})$$

Which defines the first order density-density response function χ . Using the standard first order perturbation theory, we can write

$$\chi(r, t, t', t') = \sum_m \frac{\langle 0 | n_H(r) | n \rangle \langle m | n_H(r') | 0 \rangle}{\hbar\omega - (E_m - E_o) + i\delta} - \frac{\langle 0 | n_H(r') | m \rangle \langle n | n_H(r) | 0 \rangle}{\hbar\omega + (E_m - E_o) + i\delta} \quad (\text{E.1.3})$$

where n_H is the density operator in the Heisenberg representation, δ is an positive infinitesimal introduced to assure causality, $|0 \rangle$ is the ground state and the $\{|m \rangle\}$ stands for the excited states of the system and $\{E_m\}$ for their energies.

If the system is supposed to be described by a time-dependent Hartree-Fock wavefunction, the response function can be calculated through the Hartree-Fock orbitals and orbital's energies:

$$\chi(r, t, t', t') = \sum_{i,j} \frac{n_i - n_j}{-\hbar\omega + \varepsilon_i - \varepsilon_j - i\delta} f_{ij}(r) f_{ij}(r')^* \quad (\text{E.1.4})$$

with

$$f_{ij}(r) = \phi_i(r) \phi_i^*(r),$$

ϕ_i being the SCF-orbitals and ε_i their respective energies. This approximation is referred as the *Random Phase Approximation* (RPA).

In terms of the potentials, the response of the system to the external potential is written as:

$$V_{tot} = \int dr' \epsilon^{-1}(r, r', \omega) V_{ext}(r', \omega) \quad (\text{E.1.5})$$

where we have make the time Fourier transform, using the Poisson equation for the induced potential in terms of the induced density is easily seen that:

$$\epsilon(r, r', \omega) = \delta(r, r') + \int dr'' \frac{\chi(r, r'', \omega)}{|r - r''|} \quad (\text{E.1.6})$$

E.2 The dielectric function in a Tight-Binding Approximation.

We have calculated the dielectric response following the Graf and Vogl [135] prescription that will be briefly described here. A tight-binding-like momentum operator is defined as:

$$P_{n,n'}(k) = \langle nk | \nabla_{k'} H(k') | n'k \rangle \quad (\text{E.2.7})$$

where $|nk\rangle$ are the system eigenvectors. From the expression for the Hamiltonian in the reciprocal space in terms of the localized orbitals, one can write:

$$\nabla_{k'} H_{\alpha'I',\alpha I}(k') = \sum_l (R_{\alpha'I'l} - R_{\alpha I}) e^{ik'(R_{\alpha'I'l} - R_{\alpha})} * t_{\alpha'I'l,\alpha I}(R_{\alpha'I'l} - R_{\alpha}) \quad (\text{E.2.8})$$

where l stands for the corresponding periodic cell, I is the atomic index in the unit cell, and α stands for the kind of atomic orbital. The eigenvectors are a superposition of Bloch states constructed with the molecular orbitals:

$$|nk\rangle = \sum_{\alpha I} C_{\alpha I}(nk) * |\alpha I, k\rangle \quad (\text{E.2.9})$$

where the Bloch orbitals used as basis are given by:

$$|\alpha I k\rangle = \sum_l e^{ik * R_{\alpha I l}} |\alpha, I, L\rangle$$

then, in terms of the vectors representing the eigenstates in the Bloch states basis, we obtain:

$$P_{n,n'}(k) = C^\dagger(nk) * \nabla_{k'} H_{\alpha'I',\alpha I}(k) * C(n'k) \quad (\text{E.2.10})$$

this is the appropriate tight-binding momentum operator that appears in the typical RPA expression for the transversal dielectric function. For a non-metal (only full band occupation, so it is also valid for graphene where the valence band is fully occupied) we have:

E.3. Dielectric Loss of fast electrons passing through a material system 220

$$Im(\varepsilon_{ij}) = \frac{4e^2 \Pi^2}{w^2 \hbar m_o^2 V_o} \sum_{n,m,k} P_{nm}^i * P_{mn}^j (f_n(k) - f_m(k)) * \delta(w - (E_m(k) - E_n(k))/\hbar) \quad (\text{E.2.11})$$

The real part of the dielectric function can be calculated from the Kramers-Kronig relationships.

Implementation in the TROCADERO code

In the Tight-Binding TROCADERO code, the matrix $\nabla_{k'} H_{\alpha' l', \alpha l}$ can be easily calculated in analogy to the squared forms of the Hamiltonian matrix, (`construct_k_point_matrices` subroutine, in the TROCADERO code) within the `DFTB_module.f90` and `PETTIFOR_module.f90` (a module that we have implemented for the orthogonal Pettifor parametrization). We have chosen the Pettifor parametrization for the dielectric function parametrization because it yields a better description of the empty states (the ones more relevant for the optical response). It is only necessary to include the corresponding cofactors ($R_i - R_j$) within the respective routines. It is important to recall that calculating dielectric functions require a large number of k-points (a good result for diamond requires a 32x32x32 Monkhorst-Pack cell)

The Kramers-Kronig relationships are evaluated by a tetrahedral integration.

E.3 Dielectric Loss of fast electrons passing through a material system.

When a fast electron interacts with a material system with a certain dielectric function, the interaction potential is given by:

$$V_{int}(r) = e^2 \int dr' \frac{n(r')}{|r - r'|} \quad (\text{E.3.12})$$

where n is the total density within the material and r is the external electron position. Transforming to the momentum space:

$$V_{int}(r) = \int dk \frac{4\Pi}{k^2} e^2 n_k e^{ikr} \quad (\text{E.3.13})$$

E.3. Dielectric Loss of fast electrons passing through a material system 221

If the electron is moving fast enough so that the Born approximation is valid, the probability per unit of time $W(k, w)$ of having a momentum transfer $\hbar k$ and energy transfer $\hbar w$ is given by:

$$W(k, w) = \frac{2\Pi}{\hbar} \left(\frac{4\Pi e^2}{k^2} \right)^2 \sum_m \langle 0|n_k|m \rangle \langle m|n_k|0 \rangle \delta(w - w_m) \quad (\text{E.3.14})$$

regarding the expression for the density-density response function E.1.3 and for the dielectric function, one can see that the energy loss can be characterized by a Loss function:

$$L(w)\alpha - \text{Im} \left(\int dr dr' e^{-ikr} \chi(r, r', w) e^{ikr} \right) \quad (\text{E.3.15})$$

that is, it is determined by the Fourier transform of χ or, even more and according to the relationship between χ and ϵ :

$$L(k, w) = -\frac{8\Pi}{\hbar k^2} \text{Im}(\epsilon^{-1}(k, k, w)) \quad (\text{E.3.16})$$

that, in the case of small k vectors is just given by the inverse of the macroscopic dielectric function.

In a typical Tight-Binding or pseudopotentials approach, the core states are fully neglected, so that energy transfer to core electrons can not be described by the thereof calculated dielectric function. The core energy loss can, nevertheless, be approximated if one neglects the final state effects (no electron-hole interaction), assumes also that the core bands are quite flat (a rather reasonable approximation, or at least one consistent with the tight-binding or pseudopotentials approach). This technique also considers that the initial state is localized on a single atom (that is, after all, why one consider them core states!). Then, the core energy loss will be given by the projected density of states and the corresponding selection rules. For example, for the carbon K-shell, the initial state is *s-like* so that the core energy is roughly given by the *p-projected* density of states.

Further reading

Optical response of material systems

D. Pines, ELEMENTARY EXCITATIONS IN SOLIDS : LECTURES ON PHONONS, ELECTRONS, AND PLASMONS Westview Press, (1966),

G. Onnida, L. Reining, A. Rubio, ELECTRONIC EXCITATIONS: DENSITY FUNCTIONAL VERSUS MANY-BODY GREEN'S FUNCTIONS APPROACH,

Electromagnetic fields in tight-binding models:

M. Graf and P. Vogl, *Physics. Rev. B*, ELECTROMAGNETIC FIELDS AND DIELECTRIC RESPONSE IN EMPIRICAL TIGHT-BINDING G THEORY 51, 4940 (1995).

Appendix F

Simplified evolution of the occupation number in a tight-binding approach

*Everybody guess
that baby can't be blessed
till she finally finds that
she is like all the rest*

Like a woman, Bob Dylan.

In this appendix, we show the derivation of equation 4.1 for the evolution of the occupation number of a system described in a tight-binding approach and interaction with a laser field. We start from the Hamiltonian in the Schrödinger representation:

$$H = H_0 + H_1 = \sum_m \epsilon_m c_m^\dagger c_m + \sum_{mn} g_{mn} c_m^\dagger c_n \quad (\text{F.0.1})$$

where c_m^\dagger and c_m correspond to creation and annihilation operators of electrons in the tight-binding orbital m with given energy ϵ_m . As there is no place here for confusion with the notation, we omit the hats we have used in other chapters to distinguish the operators. These operators obey anti-commutation relations $[c_m, c_n]_+ = [c_m^\dagger, c_n^\dagger]_+$ and $[c_m, c_n^\dagger]_+ = \delta_{mn}$. Switching to the interaction representation we transform the

annihilation operator according to

$$\begin{aligned}\tilde{c}_m &= U^{-1}c_mU && \text{with } U = e^{-\frac{i}{\hbar}H_0t} \\ &= e^{\frac{i}{\hbar}H_0t}c_me^{-\frac{i}{\hbar}H_0t} = e^{\alpha c_m^\dagger c_m}c_me^{-\alpha c_m^\dagger c_m} && \text{with } \alpha = \frac{i}{\hbar}\epsilon_mt \\ &= e^{-\alpha}c_m.\end{aligned}\quad (\text{F.0.2})$$

For the creation operator this means

$$\tilde{c}_m^\dagger = e^\alpha c_m^\dagger, \quad (\text{F.0.3})$$

and we find for the interaction part of the Hamiltonian

$$\tilde{H}_I = U^{-1}H_IU = \sum_{mn} g_{mn}U^{-1}c_m^\dagger UU^{-1}c_nU = \sum_{mn} g_{mn}e^{\frac{i}{\hbar}(\epsilon_m - \epsilon_n)t}\tilde{c}_m^\dagger\tilde{c}_n. \quad (\text{F.0.4})$$

Thus, in the interaction representation the Hamiltonian reads

$$\tilde{H} = \sum_m \epsilon_m \tilde{c}_m^\dagger \tilde{c}_m + \sum_{mn} g'_{mn} \tilde{c}_m^\dagger \tilde{c}_n \quad \text{with } g'_{mn} = g_{mn} e^{\frac{i}{\hbar}(\epsilon_m - \epsilon_n)t} \quad (\text{F.0.5})$$

From now on, we drop the tilde as we perform all calculations in interaction representation.

We are interested in the time dependence of the density matrix $\hat{\rho}$ which obeys the equation of motion

$$i\hbar \frac{\partial \hat{\rho}}{\partial t} = [H_I, \hat{\rho}], \quad (\text{F.0.6})$$

where $\hat{\rho}_{ll'} = c_l^\dagger c_{l'}$ in the single-particle approximation. In addition to Eq. F.0.6 we impose the Pauli principle by ensuring $\langle \hat{\rho}_{ll'} \rangle \leq 2$ as the equations are written independent of spin. First, we determine the value of various commutators:

$$[c_m^\dagger c_n, c_l] = c_m^\dagger [c_n, c_l] + [c_m^\dagger, c_l] c_n = 2c_m^\dagger c_n c_l + 2c_m^\dagger c_l c_n - \delta_{lm} c_n, \quad (\text{F.0.7})$$

$$[c_m^\dagger c_n, c_l^\dagger] = c_m^\dagger [c_n, c_l^\dagger] + [c_m^\dagger, c_l^\dagger] c_n = 2c_m^\dagger c_n c_l^\dagger + 2c_m^\dagger c_l^\dagger c_n - \delta_{ln} c_m^\dagger, \quad (\text{F.0.8})$$

where $[c_n, c_l] = c_n c_l - c_l c_n = 2c_n c_l$ and $[c_m^\dagger, c_l] = c_m^\dagger c_l - c_l^\dagger c_m = 2c_m^\dagger c_l - \delta_{lm}$ was used. With this expression we find

$$\begin{aligned}[c_m^\dagger c_n, c_l^\dagger c_{l'}] &= [c_m^\dagger c_n, c_l^\dagger] c_{l'} + c_l^\dagger [c_m^\dagger c_n, c_{l'}] \\ &= 2c_m^\dagger c_n c_l^\dagger c_{l'} + 2c_m^\dagger c_l^\dagger c_n c_{l'} - \delta_{ln} c_m^\dagger c_{l'} + 2c_l^\dagger c_m^\dagger c_n c_{l'} + 2c_l^\dagger c_m^\dagger c_{l'} c_n - \delta_{l'm} c_l^\dagger c_n \\ &= 2\delta_{ln} c_m^\dagger c_{l'} - \delta_{ln} c_m^\dagger c_{l'} - \delta_{l'm} c_l^\dagger c_n \\ &= \delta_{ln} c_m^\dagger c_{l'} - \delta_{l'm} c_l^\dagger c_n = \delta_{ln} \hat{\rho}_{ml'} - \delta_{l'm} \hat{\rho}_{ln}.\end{aligned}\quad (\text{F.0.9})$$

Thus, Eq. F.0.6 yields

$$i\hbar \frac{\partial \hat{\rho}_{ll'}}{\partial t} = \sum_{mn} g'_{mn} (\delta_{ln} \hat{\rho}_{ml'} - \delta_{l'm} \hat{\rho}_{ln}) = \sum_m (g'_{ml} \hat{\rho}_{ml'} - g'_{l'm} \hat{\rho}_{lm}). \quad (\text{F.0.10})$$

The diagonal part of this is

$$i\hbar \frac{\partial \hat{\rho}_{ll}}{\partial t} = \sum_m (g'_{ml} \hat{\rho}_{ml} - g'_{lm} \hat{\rho}_{lm}). \quad (\text{F.0.11})$$

Integrating Eq. F.0.10 we find

$$\hat{\rho}_{kk'} = \hat{\rho}_{kk'}(t - \Delta t) - \frac{i}{\hbar} \int_{t-\Delta t}^t dt' \sum_n (g'_{nk} \hat{\rho}_{nk'} - g'_{k'n} \hat{\rho}_{kn}) \quad (\text{F.0.12})$$

Introducing this into Eq. F.0.11 yields

$$i\hbar \frac{\partial \hat{\rho}_{ll}}{\partial t} = \sum_m \left\{ g'_{ml} \hat{\rho}_{ml}(t - \Delta t) - \frac{i}{\hbar} g'_{ml} \int_{t-\Delta t}^t dt' \sum_n (g'_{nm} \hat{\rho}_{nl} - g'_{ln} \hat{\rho}_{mn}) \right. \\ \left. - g'_{lm} \hat{\rho}_{lm}(t - \Delta t) + \frac{i}{\hbar} g'_{lm} \int_{t-\Delta t}^t dt' \sum_n (g'_{nl} \hat{\rho}_{nm} - g'_{mn} \hat{\rho}_{ln}) \right\}. \quad (\text{F.0.13})$$

Assuming that the nondiagonal elements of $\hat{\rho}$ vanish instantaneously, we find

$$i\hbar \frac{\partial \hat{\rho}_{ll}}{\partial t} = \frac{i}{\hbar} \sum_m \left\{ g'_{ml} \int_{t-\Delta t}^t dt' (-g'_{lm} \hat{\rho}_{ll} + g'_{lm} \hat{\rho}_{mm}) + g'_{lm} \int_{t-\Delta t}^t dt' (g'_{ml} \hat{\rho}_{mm} - g'_{ml} \hat{\rho}_{ll}) \right\}, \quad (\text{F.0.14})$$

and considering that $g'^*_{ml} = g'_{lm}$

$$\hbar^2 \frac{\partial \hat{\rho}_{ll}}{\partial t} = 2\text{Re} \left\{ \sum_m g'_{ml} \int_{t-\Delta t}^t dt' g'_{lm} (\hat{\rho}_{mm} - \hat{\rho}_{ll}) \right\}. \quad (\text{F.0.15})$$

Introducing the full form of g'_{lm}

$$g'_{lm} = e^{i\omega_{lm}t} \frac{E(t)}{2} [e^{i\omega t} + e^{-i\omega t}] x_{lm} \quad \text{with} \quad \omega_{lm} = \frac{\epsilon_l - \epsilon_m}{\hbar}, \quad (\text{F.0.16})$$

Eq. F.0.15 reads

$$\hbar^2 \frac{\partial \hat{\rho}_{ll}}{\partial t} = \text{Re} \left\{ \sum_m |x_{lm}|^2 E(t) [e^{i(\omega_{lm} + \omega)t} + e^{i(\omega_{lm} - \omega)t}] \times \right. \\ \left. \times \int_{t-\Delta t}^t dt' E(t') [e^{i(\omega_{lm} + \omega)t'} + e^{i(\omega_{lm} - \omega)t'}] [\hat{\rho}_{mm}(t') - \hat{\rho}_{ll}(t')] \right\}. \quad (\text{F.0.17})$$

Introducing the Fourier transform of the pulse envelope via $E(t) = \int_{-\infty}^{\infty} d\omega' g^0(\omega') e^{i\omega' t}$, we find

$$\begin{aligned} \hbar^2 \frac{\partial \hat{\rho}_{ll}}{\partial t} = \text{Re} \left\{ \sum_m |x_{lm}|^2 E(t) \left[e^{i(\omega_{ml} + \omega)t} + e^{i(\omega_{ml} - \omega)t} \right] \times \right. \\ \left. \times \int_{t-\Delta t}^t dt' \int_{-\infty}^{\infty} d\omega' g^0(\omega') \left[e^{i(\omega_{lm} + \omega + \omega')t'} + e^{i(\omega_{lm} - \omega + \omega')t'} \right] \left[\hat{\rho}_{mm}(t') - \hat{\rho}_{ll}(t') \right] \right\}. \end{aligned} \quad (\text{F.0.18})$$

We now approximate Eq. F.0.18 assuming that the time Δt for which we want to integrate the equation is small with respect to slowly varying functions and large with respect to rapidly oscillating functions (coarse integration). Thus, we find

$$\begin{aligned} \hbar^2 \frac{\partial \hat{\rho}_{ll}}{\partial t} = \text{Re} \left\{ \sum_{m=1}^{l-1} |x_{lm}|^2 E(t) e^{i(\omega_{ml} + \omega)t} \int_{-\infty}^{\infty} d\omega' g^0(\omega') \left[\hat{\rho}_{mm}(t) - \hat{\rho}_{ll}(t) \right] \delta(\omega_{lm} - \omega + \omega') \right. \\ \left. + \sum_{m=l+1}^M |x_{lm}|^2 E(t) e^{i(\omega_{ml} - \omega)t} \int_{-\infty}^{\infty} d\omega' g^0(\omega') \left[\hat{\rho}_{mm}(t) - \hat{\rho}_{ll}(t) \right] \delta(\omega_{lm} + \omega + \omega') \right\}. \end{aligned} \quad (\text{F.0.19})$$

Assuming the energy levels to be numerous, we transform the sums (\sum_m) to integrals, introducing the density of states $N(\epsilon)$

$$\begin{aligned} \hbar^2 \frac{\partial \hat{\rho}_{\epsilon l}}{\partial t} = \text{Re} \left\{ \int_{\epsilon_1}^{\epsilon_{l-1}} d\epsilon N(\epsilon) |x(\epsilon_l, \epsilon)|^2 E(t) e^{i(\epsilon - \epsilon_l + \omega)t} \int_{-\infty}^{\infty} d\omega' g^0(\omega') \left[\hat{\rho}_{\epsilon}(t) - \hat{\rho}_{\epsilon_l}(t) \right] \delta(\epsilon_l - \epsilon - \omega + \omega') \right. \\ \left. + \int_{\epsilon_{l+1}}^{\epsilon_M} d\epsilon N(\epsilon) |x(\epsilon_l, \epsilon)|^2 E(t) e^{i(\epsilon - \epsilon_l - \omega)t} \int_{-\infty}^{\infty} d\omega' g^0(\omega') \left[\hat{\rho}_{\epsilon}(t) - \hat{\rho}_{\epsilon_l}(t) \right] \delta(\epsilon_l - \epsilon + \omega + \omega') \right\}. \end{aligned} \quad (\text{F.0.20})$$

and evaluating the δ functions we obtain

$$\begin{aligned} \hbar^2 \frac{\partial \hat{\rho}_{\epsilon l}}{\partial t} = \text{Re} \left\{ \int_{-\infty}^{\infty} d\omega' e^{i\omega' t} E(t) g^0(\omega') \left[N(\epsilon_l - \omega + \omega') |x(\epsilon_l, \epsilon_l - \omega + \omega')|^2 \left[\hat{\rho}_{\epsilon_l - \omega + \omega'}(t) - \hat{\rho}_{\epsilon_l}(t) \right] \right. \right. \\ \left. \left. + N(\epsilon_l + \omega + \omega') |x(\epsilon_l, \epsilon_l + \omega + \omega')|^2 \left[\hat{\rho}_{\epsilon_l + \omega + \omega'}(t) - \hat{\rho}_{\epsilon_l}(t) \right] \right] \right\}. \end{aligned} \quad (\text{F.0.21})$$

Assuming that the dipole matrix elements are constant ($X_{lm} = x_0$) and taking into account that the density of states $N(\epsilon_l - \omega + \omega')$ is properly included if we sum over all TB energy levels, we obtain after evaluating the operator equation in the tight-binding basis

$$\frac{\partial n_{\epsilon_l}}{\partial t} = \int_{-\infty}^{\infty} d\omega' g(\omega', t) \left[n_{\epsilon_l - \omega + \omega'}(t) - n_{\epsilon_l}(t) + n_{\epsilon_l + \omega + \omega'}(t) - n_{\epsilon_l}(t) \right], \quad (\text{F.0.22})$$

where we have abbreviated $g(\omega', t) = \cos(\omega't)E(t)g^0(\omega')|x_0|^2/\hbar^2$, and $n_{\epsilon_l}(t)$ is the occupation of the state l .

This last equation is just the same as Eq. 4.1.

Papers

THEORETICAL CHARACTERIZATION OF SEVERAL MODELS OF NANOPOROUS CARBON, **F. Valencia**, A. H. Romero, E. Hernandez, M. Terrones, and H. Terrones, *New Journal of Physics*, 3, 123 (2003).

AB INITIO STUDY OF CUBYL CHAINS AND NETWORKS, **F. Valencia**, A. H. Romero, M. Kiwi, R. Ramirez, A. Toro-Labbé, *J. Chem. Phys.*, 121, 9172 (2004).

POLYCUBANES LINKED WITH C₂, N₂, NO AND NS: FROM INSULATING TO METALLIC BEHAVIOR, **F. Valencia**, A. H. Romero, M. Kiwi, R. Ramirez, A. Toro-Labbé, *Phys. Rev. B.* 71, 033410 (2005).

FEMTOSECOND LASER NANOSURGERY OF DEFECTS IN CARBON NANOTUBES, A. H. Romero, M. E. García, H. O. Jeschke, **F. Valencia**, H. Terrones, M. Terrones, *accepted for publication in Nanoletters*, 2005.

A DENSITY FUNCTIONAL THEORY STUDY OF CUBANE OLIGOMERS, B. Herrera, **F. Valencia**, A. H. Romero, M. Kiwi, R. Ramirez, A. Toro-Labbé, *to be submitted to Chemical Physics Letters* 2005.